# Integration of photochemical reactions in microreactors with infrared optical sensors

Zur Erlangung des akademischen Grades eines

DOKTORS DER INGENIEURWISSENSCHAFTEN (Dr.-Ing.)

von der KIT-Fakultät für Chemieingenieurwesen und Verfahrenstechnik des
Karlsruher Instituts für Technologie (KIT)
genehmigte

DISSERTATION

von

M. Sc. Jun Li

aus Zhejiang, VR China

Tag der mündlichen Prüfung: 19.06.2024

Erstgutachter: Prof. Dr.-Ing. Roland Dittmeyer

Zweitgutachter: Prof. Dr. Matthias Franzreb

# Erklärung

Die vorliegende Arbeit wurde im Zeitraum vom 1. Oktober 2019 bis 31. August 2023 am Institut für Mikroverfahrenstechnik (IMVT) am Karlsruher Institut für Technologie (KIT) unter der Leitung von Prof. Dr. Roland Dittmeyer angefertigt.

---

Hiermit versichere ich, die vorliegende Arbeit selbstständig verfasst und keine anderen als die angegebenen Quellen und Hilfsmittel verwendet sowie Zitate kenntlich gemacht zu haben.

Ich versichere, dass die hier vorliegende Dissertation mit dem eingereichten und genehmigten Prüfungsexemplar der Doktorarbeit übereinstimmt. Die Dissertation wurde bisher an keiner anderen Hochschule oder Universität eingereicht.

Karlsruhe,

---------------------------------- ---------------------------------

Jun Li Ort und Datum

# Acknowledgements

First of all, I would like to thank my supervisor Prof. Dr. Roland Dittmeyer for his continuous support, valuable guidance, adequate patience, and enthusiastic encouragement during my Ph.D. study, who offered me an excellent chance to do my research following my own idea at the institute of micro process engineering (IMVT), KIT. Besides, I would like to thank my previous group leader and advisor Prof. Bradley P. Ladewig, for insightful thoughts, meaningful discussions, and valuable instructions during my first two years stay of study. His rich and impressive knowledge has greatly helped the successful implementation of my doctoral study. Meanwhile, I would like to thank his kind support in helping me settle down in Karlsruhe. Moreover, I would like to thank my present group leader Dr. Peter Holtappels for his kind support in my last stay in IMVT. Although he is not an expert in this field, he enthusiastically participated in the project discussion, conducted excellent discussions, and gave valuable suggestions.

I would like to express my thankfulness to my colleagues Helena from IBCS-FMS, KIT, and David from IMTEK, Freiburg for their enthusiasm and cooperation in the ProMiSe project. In particular, I would like to thank Helena for her help in experimental designs and NMR measurements. I would like to appreciate our super supportive technicians Ms. Cornelia Schorle and Mr. Conrad Grehl for their wonderful help with my test rig. I would thank Dipl.-Ing. Heinz Lambach, Mr. Matthias Schöffler, Mrs. Sabine Schweikert-Joß, and Ms. Cornelia Schorle for their help with the design, fabrication, and maintenance of the photoreactor. I want to express my thanks to our secretary Mrs. Karin Krämer for her patience and indispensable help in my participation in scientific activities. Mr. Xiang Zhan and Dr. Dongxu Xie are gratefully thanked for their kind care during my stay at KIT, no matter in study or life. I want to thank Dr. Paul Kant for his great help and excellent discussion in photon flux calibration experiments, microreactor conceptual design, and radiative transfer modelling. In addition, many thanks to all my colleagues from IMVT for the support, encouragement, and sharing experiences during my doctoral stay.

I want to thank my friends Dr. Tian Ke and Mr. Yukai Jin, who gave me lots of help and consolation during my study. Moreover, I would like to express my gratitude to my girlfriend Zihan Xia for her endless love and support, who helped me go through the ups and downs during my stay in Karlsruhe. Finally, I would like to sincerely thank my family,

especially my parents and sister, for their unconditional support and care during my study abroad days.

# Abstract

Sensor-integrated microfluidic systems for process intensification and control have received increasing attention from the scientific and industrial communities in recent years. The integration of process analytical technologies with microreactors can provide real-time information representative of the degree of process realization, while also offering the opportunity to capture transient intermediates in the transformation. Some examples show the feasibility of monitoring chemical reactions with *in situ* optical sensors, but there is no literature regarding their implementation in flow photochemistry. As the penetration depth of the light can be tailored to the dimension of the microchannels used, the photon attenuation effect in microfluidic photoreactors is greatly mitigated, making flow photochemistry a promising application for industrial production. Among all the available optical sensors, FTIR would be the most suitable technique that can be integrated with flow photoreactors because it has outstanding advantages of portability and wide detection ranges. Moreover, miniaturized infrared sensors have been reported, which greatly increases the possibility of their integration with microfluidic reactors. In this context, a novel microfluidic photoreactor design should be proposed to enable this integration.

In this dissertation, a compact microfluidic photoreactor (PHO-μR) containing three reaction areas and four sensing areas has been fabricated, taking both photoreaction and infrared sensing into consideration. Transmission FTIR is adopted in the PHO-μR design, and the infrared sensor employed has four different bandwidths, capable of covering the entire infrared spectrum used for conventional offline measurements. The design here is to make the reactor compatible with all photochemical reactions, as the characteristic absorption peaks of their infrared spectra are not fixed and are highly dependent on the photoreaction itself. Also, for process intensification and control purposes, a simple capillary microreactor (CAP-μR) was fabricated to get the kinetic parameters of the chosen photoreaction and aid with the development of the reaction model. Consequently, two standardized microfluidic photochemical reaction platforms have been constructed. The photon fluxes received by the photoreactor were systematically studied by solving the 1D Monte Carlo method. The actual optical path was analyzed in detail according to whether significant reflection occurs in the reactor. Several parameters representing the performance of the photoreactors built were evaluated and compared.

In this study, the visible-light-induced photocyclization of an F-tagged aniline derivative to prepare the 3-acylindole product was chosen as the probe reaction. Kinetic study of the photoreaction was performed in the CAP-μR to access kinetic parameters. The effects of residence time and light intensity on NMR yield were studied, using optimal photocatalyst loading disclosed in the literature. The reaction order and apparent rate constants under different light intensities were evaluated and regressed with the algorithm in MATLAB. The constants were found to be linearly dependent on the light intensity received, indicating the weak photon absorption conditions in the CAP-μR. The quantum yield of the photoreaction was found to correlate with the reaction progress, and photon competition between the photocatalyst and indole product was confirmed. On the basis of the findings in the kinetic study, a 2D axisymmetric model was employed to replicate the process and help to build the reaction model. The intrinsic rate constant independent of photon flux and reactor geometry was proposed in the reaction model. The photochemical process was assumed to be uniform, and a transversal irradiance profile was used to simplify the simulation. A simplified reactor model was adopted to describe the process and the transient study corresponding to the actual operation was performed. The parity plot shows that the simulation results match well with experiments. Some predictions are, however, biased due to mass transfer limitation and photon competition occurring in the process.

Subsequently, the discrete ordinate method (DOM) was used to solve the radiative transfer equation (RTE) and to propose the optimal LED configuration for the PHO-μR by assessing the radiation field of the microchannel. An iterative method based on the results from photon flux calibration was adopted for the RTE simulation. Material-based photon reflections were also considered here. The irradiance level, energy efficiency, and irradiation homogeneity over the microchannel were analyzed to find the most suitable LED configurations. With the obtained radiation field in hand, 3D spatially resolved reaction simulation using the intrinsic rate constant from the previous kinetic study was performed. The concentration field was found to be highly dependent on the radiation field where a higher local concentration could be observed near the optical and reflective sides. The simulation can capture well the nature of the fluid dynamics, reaction kinetics, and photon reflection inside the channel. It has been found that if the same reaction is carried out in a non-reflective microchannel, the effect of the velocity field on the concentration field is negligible. Meanwhile, the reaction simulation was validated with experiments under weak photon absorption conditions. The deviation between

simulations and experiments remains within 5% tolerance. The successful validation of the reaction simulation, in turn, shows the correctness of the RTE simulation. Thus, a generic reaction kinetic model was proposed and successfully applied to two different photochemical platforms. Moreover, productivity tests of the PHO-µR were performed at the maximum power available, which demonstrated a significant enhancement in photoreactor performance due to light reflection and a substantial reduction in energy consumption required. At the same time, with the help of reaction simulation, a suitable operating condition using dry acetone as solvent was found.

Last but not least, a 3D-printed infrared sensor bracket was designed and built with the help of modulation in Autodesk Inventor, thereby enabling the integration of the infrared sensor with the PHO-µR. The physical structure of the constructed support does not conflict with the LED configuration obtained from the RTE simulation, thus enabling the smallest possible energy consumption and maximum energy efficiency and productivity of the PHO-µR. Several multifunctional software packages were developed to control the system, thus achieving process control and exempting manual operation. Finally, the proof-of-concept "*in situ* infrared sensing of photoreactions in microfluidic photoreactor" was theoretically demonstrated to be feasible and has been realized.

# Zusammenfassung

Sensorintegrierte mikrofluidische Systeme zur Prozessintensivierung und -kontrolle haben in den letzten Jahren in Wissenschaft und Industrie zunehmend an Aufmerksamkeit gewonnen. Die Integration von Prozessanalysewerkzeugen in Mikroreaktoren kann Echtzeitinformationen liefern, die für den Grad der Prozessrealisierung repräsentativ sind, und bietet gleichzeitig die Möglichkeit, vorübergehende Zwischenprodukte bei der Umwandlung zu erfassen. Einige Beispiele zeigen die Durchführbarkeit der Überwachung chemischer Reaktionen mit optischen In-situ-Sensoren, aber es gibt keine Literatur über deren Einsatz in der Durchflussphotochemie. Da die Eindringtiefe des Lichts auf die Größe der verwendeten Mikrokanäle zugeschnitten werden kann, wird der Photonenabschwächungseffekt in mikrofluidischen Photoreaktoren stark abgeschwächt, was die Durchflussphotochemie zu einer vielversprechenden Anwendung für die industrielle Produktion macht. Unter allen verfügbaren optischen Sensoren erscheint FTIR als die am besten geeignete Technik, die in Durchfluss-Photoreaktoren integriert werden kann, da sie herausragendem Vorteile hinsichtlich Portabilität und großem Erfassungsbereich aufweist. Darüber hinaus wurde bereits über miniaturisierte Infrarotsensoren berichtet, was die Möglichkeit deren Integration in mikrofluidische Reaktoren mit sich bringt. In diesem Zusammenhang sollte ein neuartiges mikrofluidisches Photoreaktordesign vorgeschlagen werden, um diese Integration zu ermöglichen.

In dieser Dissertation wurde ein kompakter mikrofluidischer Photoreaktor (PHO-µR) mit drei Reaktionsbereichen und vier Sensorbereichen hergestellt, wobei sowohl die Photoreaktion als auch die Infrarotsensorik berücksichtigt wurden. Bei der Konstruktion des PHO-µR wird die FTIR-Transmission eingesetzt, und der verwendete Infrarotsensor hat vier verschiedene Bandbreiten, die das gesamte Infrarotspektrum abdecken, das für herkömmliche Offline-Messungen verwendet wird. Damit soll der Reaktor mit allen photochemischen Reaktionen kompatibel sein, da die charakteristischen Absorptionsspitzen ihrer Infrarotspektren nicht von vorne herein feststehen sondern stark von der Photoreaktion selbst abhängen. Zur Prozessintensivierung und -kontrolle wurde außerdem ein einfacher Kapillarmikroreaktor (CAP-µR) aufgesamt, um die kinetischen Parameter der gewählten Photoreaktion zu bestimmen und die Entwicklung des Reaktionsmodells zu unterstützen. Im Anschluss wurden zwei standardisierte mikrofluidische photochemische Reaktionsplattformen konstruiert. Die vom

Photoreaktor empfangenen Photonenflüsse wurden systematisch mit Hilfe der 1D Monte Carlo Methode untersucht. Der tatsächliche optische Pfad wurde detailliert analysiert, um festzustellen, ob das Phänomen der Reflexion im Reaktor auftritt. Mehrere Parameter, die die Leistung der gebauten Photoreaktoren darstellen, wurden bewertet und verglichen.

In dieser Studie wurde die durch sichtbares Licht induzierte Photocyclisierung eines Fluor-markierten Anilinderivats zur Herstellung des 3-Azylindolprodukts als Testreaktion gewählt. Die kinetische Studie der Photoreaktion wurde im CAP-µR durchgeführt, um kinetische Parameter zu ermitteln. Die Auswirkungen der Verweilzeit und der Lichtintensität auf die NMR-Ausbeute wurden untersucht, wobei die in der Literatur angegebene optimale Photokatalysatorbeladung verwendet wurde. Die Reaktionsordnung und die scheinbaren Geschwindigkeitskonstanten bei verschiedenen Lichtintensitäten wurden bestimmt und in MATLAB einer Regression unterworfen. Es wurde festgestellt, dass die Konstanten linear von der empfangenen Lichtintensität abhängen, was auf eine schwache Photonenabsorption im CAP-µR hinweist. Es wurde weiterhin festgestellt, dass die Quantenausbeute der Photoreaktion mit dem Reaktionsfortschritt korreliert, und die Photonenkonkurrenz zwischen dem Photokatalysator und dem Indolprodukt wurde bestätigt. Auf der Grundlage der Ergebnisse der kinetischen Studie wurde ein achsensymmetrisches 2D-Modell verwendet, um den Prozess abzubilden und ein Reaktionsmodell zu erstellen. Die intrinsische Geschwindigkeitskonstante, die vom Photonenfluss und der Reaktorgeometrie unabhängig ist, wurde im Reaktionsmodell ermittelt. Der photochemische Prozess wurde als gleichförmig angenommen und zur Vereinfachung der Simulation wurde ein transversales Bestrahlungsstärkeprofil verwendet. Zur Beschreibung des Prozesses wurde ein vereinfachtes Reaktormodell gewählt, und es wurde eine transiente Studie durchgeführt, die dem tatsächlichen Betrieb entspricht. Das Polaritätsdiagramm zeigt, dass die simulierten Ergebnisse gut mit den Experimenten übereinstimmen. Einige Vorhersagen sind jedoch aufgrund der Begrenzung des Stofftransport und Konkurrierender Photonen- Umsetzungspfade im Prozess verzerrt.

Anschließend wurde die diskrete Ordinatenmethode (DOM) verwendet, um die Strahlungstransportgleichung (RTE) zu lösen und die optimale LED-Konfiguration für den PHO-µR vorzuschlagen, indem das Strahlungsfeld des Mikrokanals bewertet wurde. Für die RTE-Simulation wurde eine iterative Methode verwendet, die auf den Ergebnissen der Photonenflusskalibrierung basiert. Dabei wurden auch materialbedingte

Photonenreflexionen berücksichtigt. Die Bestrahlungsstärke, der Photonenwirkungsgrad und die Homogenität der Bestrahlung über den Mikrokanal wurden analysiert, um die am besten geeigneten LED-Konfigurationen zu finden. Mit dem erhaltenen Strahlungsfeld in der Hand wurde eine räumlich aufgelöste 3D-Reaktionssimulation unter Verwendung der intrinsischen Geschwindigkeitskonstante aus der vorherigen kinetischen Studie durchgeführt. Es wurde festgestellt, dass das Konzentrationsfeld stark vom Strahlungsfeld abhängt, wobei in der Nähe der optischen und reflektierenden Seite eine höhere lokale Konzentration zu beobachten war. Die Simulation kann die Fluiddynamik, die Reaktionskinetik und die Photonenreflexion innerhalb des Kanals gut erfassen. Es hat sich gezeigt, dass die Auswirkungen des Geschwindigkeitsfeldes auf das Konzentrationsfeld vernachlässigbar sind, wenn die Reaktion in einem nicht reflektierenden Mikrokanal durchgeführt wird. Inzwischen wurde die Reaktionssimulation mit Experimenten unter schwachen Photonenabsorptionsbedingungen validiert. Die Abweichung zwischen Simulationen und Experimenten liegt innerhalb einer Toleranz von 5 %. Die erfolgreiche Validierung der Reaktionssimulation zeigt wiederum die Korrektheit der RTE-Simulation. Somit wurde ein allgemeines reaktionskinetisches Modell vorgeschlagen und erfolgreich auf zwei verschiedene photochemische Plattformen angewendet. Darüber hinaus wurden Produktivitätstests des PHO-µR mit der maximal verfügbaren Leistung durchgeführt, die eine erhebliche Verbesserung der Photoreaktorleistung aufgrund der Lichtreflexion und eine erhebliche Verringerung des erforderlichen Energieverbrauchs zeigten. Gleichzeitig wurden mit Hilfe der Reaktionssimulation geeignete Betriebsbedingungen unter Verwendung von trockenem Aceton als Lösungsmittel gefunden.

Zu guter Letzt wurde eine 3D-gedruckte Halterung für den Infrarotsensor entworfen und mit Hilfe der Modulation in Autodesk Inventor gebaut, wodurch die Integration des Infrarotsensors in den PHO-µR ermöglicht wurde. Die physische Struktur der konstruierten Halterung steht nicht im Widerspruch zu der aus der RTE-Simulation gewonnenen LED-Konfiguration, wodurch ein möglichst geringer Energieverbrauch und eine maximale Energieeffizienz und Produktivität des PHO-µR ermöglicht werden. Zur Steuerung des Systems wurden mehrere multifunktionale Softwarepakete entwickelt, die eine Prozesssteuerung ermöglichen und die manuelle Bedienung überflüssig machen. Schließlich wurde die Machbarkeit des Konzepts "In-situ-Infrarotsensorik von Photoreaktionen in einem mikrofluidischen Photoreaktor" theoretisch nachgewiesen und realisiert.

Parts of this dissertation have been published in:

**Jun Li**, Helena Šimek, David Ilioae, Nicole Jung, Stefan Bräse, Hans Zappe, Roland, Dittmeyer, Bradley P. Ladewig. In situ sensors for flow reactors-a review. React. Chem. Eng., 2021,6, 1497−1507. (Front cover)

**Jun Li**, Patrick Hodapp, Ladewig P. Ladewig, Nicole Jung, Roland Dittmeyer. A batch photoreactor for small-scale laboratory research - a technical note. ChemRxiv. Cambridge: Cambridge Open Engage; 2022.

**Jun Li**, Helena Šimek, Bradley P. Ladewig, Nicole Jung, Stefan Bräse, Roland Dittmeyer. Extraction of the intrinsic rate constant for a photocyclization reaction in capillary microreactors using a simplified reactor model. React. Chem. Eng., 2024, DOI: 10.1039/d4re00087k.

Content reproduced with the permission of Royal Society of Chemistry, and ChemRxiv®.

# Contents

# Abbreviations

| | |
|---|---|
| PAT | Process analytical technology |
| RTRT | Real-time release testing |
| API | Active pharmaceutical ingredient |
| NMR | Nuclear magnetic resonance |
| MS | Mass spectrometry |
| IR | Infrared spectroscopy |
| FTIR | Fourier-transform infrared |
| ATR | Attenuated Total Reflection |
| DRIFTS | Diffuse reflectance infrared fourier transform spectroscopy |
| XAS | X-ray absorption spectroscopy |
| PTFE | Polytetrafluoroethylene |
| FEP | Fluorinated ethylene propylene |
| PFA | Perfluoroalkoxy alkane |
| PDMS | Polydimethylsiloxane |
| IMTEK | Department of Microsystems Engineering, University of Freiburg |
| SS | Stainless steel |
| SSB | Stainless-steel board |
| MSSB | Milled stainless-steel board |
| CFD | Computational Fluid Dynamics |
| LED | Light-emitting diode |
| CAP-µR | Capillary microreactor |
| PHO-µR | *In situ* infrared microfluidic photoreactor |
| DMSO | Dimethyl sulfoxide |
| STY | Space-time yield |
| MSRA | Mean surface rate of photon absorption |
| LVRPA | Local Photon Absorption Volume Rate |

| | |
|---|---|
| RTE | Radiative Transfer Equation |
| DOM | Discrete Ordinate Method |
| PSTY | Photochemical space time yield |
| IBCS | Institute of Biological and Chemical Systems,<br>Karlsruhe Institute of Technology |
| PWM | Pulse-Width Modulation |
| RTD | Resistance temperature detector |

# 1 Introduction

## 1.1 Background and motivation

Over the last decades, thanks to the rapid developments in additive manufacturing [1-5] and the emergence of new construction materials [6-9], microfluidic reactors have become increasingly sophisticated, from initial conceptual designs to the formation of realistic, compact, and even automated platforms. Typical microfluidic reaction systems can be constructed by microfabrication and fine-machining techniques and have been considered one of the most attractive new approaches in the natural sciences, involving chemistry, biochemistry, materials sciences, and the pharmaceutical industry, etc. [10-16]. The resulting systems, typically with dimensions of the inner channels in the range of 100 nanometers to several hundred micrometers, exhibit features like enhanced mass and heat transport, improved safety, decreased reaction time, enhanced selectivity, the potential for high-throughput drug screening [17] and material discovery [18], and integration of optical sensors for systematic monitoring in microfluidics [19-22]. Sensors that visualize changes of indicators in the process have endowed these microfluidic devices with unexpectedly versatile and multifunctional utilization compared to that of conventional batch synthesis, thereby making closed-loop optimization and on-demand synthesis possible [23]. In the meantime, the adoption of microfluidics for scientific studies is further encouraged by reported economic and eco-friendly metrics [24].

Progress in microfluidic synthesis technology has also triggered novel demands in characterization and measurement. Calls for improving the performance of process analytical technology (PAT), which is termed as a unique system available to analyze, control, and optimize the critical product quality in a manufacturing process, have drawn considerable attention as highly sensitive and accurate analytics evolved half a century ago. Attempts to combine state-of-the-art analytical technology with microfluidic reactors for real-time measurements have promoted enhancements in flow chemistry, opening up a new avenue to conduct kinetic and mechanistic studies in milliseconds to picoseconds processes [25]. Prior to that, traditional offline analytical methods (e.g., UV, IR, MS, NMR) were extensively used by the chemical community in batch and flow synthesis due to intermittent manual operations for separation and purification in the post-processing. This scenario is particularly common in organic synthesis, as evaporation, distillation, crystallization, and column chromatography require a lot of effort and are mostly time-consuming. Indeed, in the case of long-term running fabrication with a comparatively short time for characterization, offline manipulations for sampling and analyzing become affordable and acceptable. For instance, some photochemical transformations in flask vessels demand response times from hours to days in some cases [26]. However, the improvements in effective conversion rate and the overall yield in a short period of time suggest that time-efficient flow chemistry is more constructive for industrial production. In addition, smart strategies such as solution-based approaches, continuous separation and distillation as well as incorporating solid-supported scavengers make multi-step organic flow synthesis practical and competitive [27]. In this context, additional preparations for sampling and analyzing are not well-matched with the inherent conveniences featured by flow reactors. On the other hand, the accuracy of offline operations heavily relies on the professional skills of the operator. In addition to inevitable differentiation caused by the defects of analytic machines, the extra risks that may occur in manual processes may increase artificial errors and compromise results, such as incomplete reaction quenching, or unpredictable contaminations in post-processing. Exempting sample analysis from manual operations and reducing exposure to the natural environment can minimize external influences and maintain the greatest extent of primitive working conditions. To free the process from expensive offline sampling, it is essential to integrate innovative analytical techniques capable of exempting transferring samples and manual handling [28-30].

In the meantime, many valuable concepts have been introduced in flow manufacturing, indicating future requirements regarding process control. Price and co-workers summarized the scope and potential for coupling manual-free analytics with flow analysis in an excellent review where the notions of process analytical technology (PAT) and real-time release testing (RTRT) are presented [31]. Correspondingly, the conceptual definitions aim to interrogate the process to guarantee high-quality production in arbitrary time intervals over the entire continuous manufacturing. Additionally, evaluating the state of flow feeds and materials produced in continuous operations as well as optimizing parameters that affect the final results, are the ultimate objectives for transforming flow chemistry from cutting-edge science into realistic industrial application [29]. The integration of optical sensors and process-intensification techniques with microfluidics would be a good option to achieve this goal. The proposed combination could be able to assemble an algorithm-modified automation platform with feedback mechanisms and self-regulation functions [32], enabling continuous synthesis for potential automated industrial applications [33, 34]. Consequently, interval-free reaction-to-analysis processes envisaged with concepts of inline, online, and *in situ* measurements, tailored to the intrinsic nature of process control within flow reactors, contribute greatly to academia and industry.

The callings of innovations in process intensification show the great importance of the integration of real-time sensors with flow reactors for challenging academic and industrial purposes. A suitable case in this combination was introduced by Kappe's group [35]. They designed a real-time analytical platform for the multi-step synthesis of mesalazine, an active pharmaceutical ingredient (API), with three distinct steps: nitration, hydrolysis, and hydrogenation, adopting four PAT tools (inline NMR, UV/vis, and IR for three respective synthetic routines and online UHPLC for final quantification) as well as three inline separations. Moreover, the combination of inline and online analytical methods with microreactors to constitute algorithm-assisted platforms was reviewed by Sans et al. [32], giving a profound overview of linking feedback algorithms and microreactor-embeddable inline/online analytics. Likewise, Baumann summarised and enumerated several cases of combining in-line purification and analysis techniques in telescoped multi-step sequences [36]. It is true that inline and online measurements are available to acquire data in continuous manufacturing for process evaluation. However, the data obtained by sensors may not be able to reflect the real situation inside the reactor due to inconsistent physical parameters between the signaling device and the reaction site. In contrast, *in situ* measurements, i.e., detection and analysis conducted in the primitive position where active intermediate or unstable species can be monitored, are considered one of the top priorities in the characterization of chemistry and chemistry-related disciplines [37]. A graphical outline of the different measurement approaches is shown in Fig. 1-1 [38].

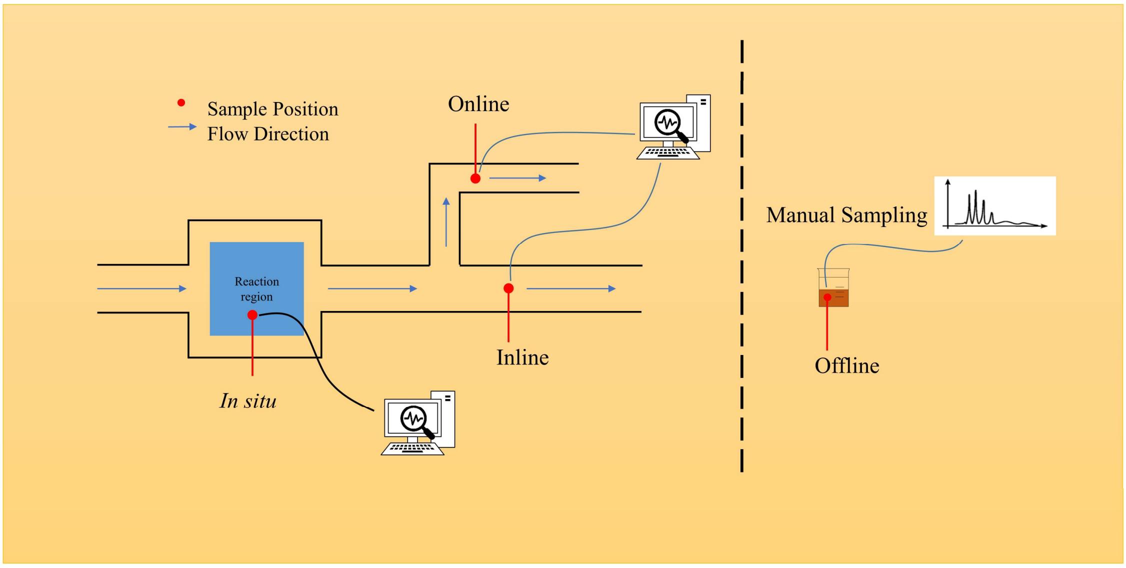

Figure 1-1 Schematic illustration of *in situ*, inline, online and offline measurements. (adapted from ref. [38] Copyright 2021 The Royal Society of Chemistry)

By comparison, deep insight research might be compromised by difficulties in the capture of active intermediates or the differentiation of significant transient signals from noisy backgrounds immediately when employing comparatively time-lagged techniques. Similarly, the precision and accuracy of inline sensors and online sensors vary. As stated in a previous article, “inline strategies, when integrated to a suitable controller for automation, can qualify as an online PAT tool for flow analysis.” [31] Demands for insight studying and precisely controlled fabrication encourage the marriage of *in situ* sensors and microfluidic systems. The study is being advocated for the transition from online analysis tools to the monitoring of the real flow manufacturing process. The integration of *in situ* sensors with flow reactors to assemble an automated system is more applicable to profoundly rapid mechanistic and kinetic insights, favouring reaction optimization and repeatability [39]. Some applications in the literature show the urgency and necessity of *in situ* sensing. For instance, the monitoring and identification of transient radical intermediates at electrode-electrolyte interfaces are challenging but attainable and can be realized by the coupling of electrochemistry and *in situ* liquid secondary ion mass spectrometry (SIMS) for a vacuum-compatible microfluidic electrochemical device, providing molecular evidence of a mechanism for the electrochemical oxidation reaction [37]. Likewise, governing the nucleation and growth process is crucial to produce the controllable size and shape of Au NPs (nanoparticles), in which procedures are usually accomplished in a fleeting period (2 to 20 ms) [14]. The marriage of such cooperation leverages the ability to extract local information of transient species without time delay. The ability to capture transient species during a chemical process makes insightful research accessible, helping scientists gain a better understanding of how it went through and why this happened from a microscopic perspective.

However, studies on the state-of-the-art cooperation between *in situ* sensors and flow reactors for chemical transformations, which would become one of the attractive and hot-discussed topics in future flow chemistry, are scarce. Overall, *in situ* studies of chemical transformations in flow reactors take remarkable benefits by comparison of the traditional offline methods with the following strengths:

It is possible to distinguish on-site changes during the chemical transformation process, thereby providing higher accuracy and reliability of the data and results analysis.

It can dynamically monitor changes in any progress at a given location (time- and spatially- resolved) in the reaction process, giving “real-time” feedback and invaluable information.

It provides the opportunity to observe the process during the non-equilibrium phase, where intermediate species may generate *in situ* and their presence may not be captured due to the unavoidable time lag in other analytical techniques.

It significantly reduces the workload of condition screening since the preparation of samples for analysis is no longer necessary and operating conditions can be appointed based on the feedback from the values of external indicators.

It has great potential to be integrated into an algorithm-assisted closed-loop synthesis process, making automated synthesis possible through automatic feedback of signal conditioning.

## 1.2 State-of-the-art in reaction probing with in-situ analysis technology

The use of *in situ* sensors allows different research priorities to be explored. The following subsections give an overview of recent discoveries with a particular focus on enabling *in situ* monitoring within microreactors for chemical transformations.

### 1.2.1 Reaction probing with in-situ NMR spectroscopy

Nuclear magnetic resonance spectroscopy (NMR) is a potent, non-invasive, and by far the most information-rich analysis technique for molecular structure determination. It is nevertheless essential to improve the inherent limited sensitivity and line broadening in NMR instruments caused by magnetic susceptibility inhomogeneities [40]. Another issue is its implementation for small sample volumes, which can be addressed by decreasing the diameter of the detection coil raising the possibilities for *in situ* measurements in microfluidic assemblies as the sensitivity per amount of spins increases. The aforementioned strategies function well and show good compatibility with microfluidic NMR. Stripline-design chips, for instance, are studied as good alternatives under an unperturbed flow state for both liquid and solid samples, resulting in higher sensitivity and good resolution, as well as facilitating microfluidic NMR for fast reaction kinetic studies [41, 42]. Other methods like adopting diamond quantum sensors [43] and combing the parahydrogen-induced hyperpolarization (PHIP) tactics are also implemented into microfluidic NMR systems for liquid analytes ranging from tens of picolitres to several microliters [44]. The integration of designed micro coils into microfluidic devices allows for specific optimization of materials, architectures and read-out [45-48].

Examples for exploiting *in situ* NMR as an analytical tool for microflow chemical synthesis are hitherto seldom. As elucidated by an earlier case, Bart et al. proposed a stripline-shape flow probe for real-time reaction kinetics study of the acylation of benzyl alcohol with acetyl chloride, tackling the incompatibility between spectral resolution and the distortion of the static magnetic field [41]. The peak broadening and N,N-diisopropylethylamine (DIPEA) signals, as well as the absence of the 2.40 ppm peak that should be present in general NMR tests, showed strong evidence in tracing intermittent species. Further, the ability of microfluidic stripline NMR chips was extended from 1H signals into gathering 1D and 2D 1H, 13C, and heteronuclear spectra when modified stripline chips were introduced (Fig. 1-2) [42]. The inlet and outlet located on the top and bottom of the chip as well as the glued-fused silica (FS) capillaries for mass-limited NMR characterization enable a convenient microfluidic connection. However, due to the simple glue fixation of FS capillaries, the system is not appropriate to be figured as a “compact” one. Therefore, the degree of leakage of these three chips is different; hence, the results cannot be assessed at the same level. Some technical sealing problems seem inevitable and often challenging when trying to incorporate the fragile chips into flow systems.

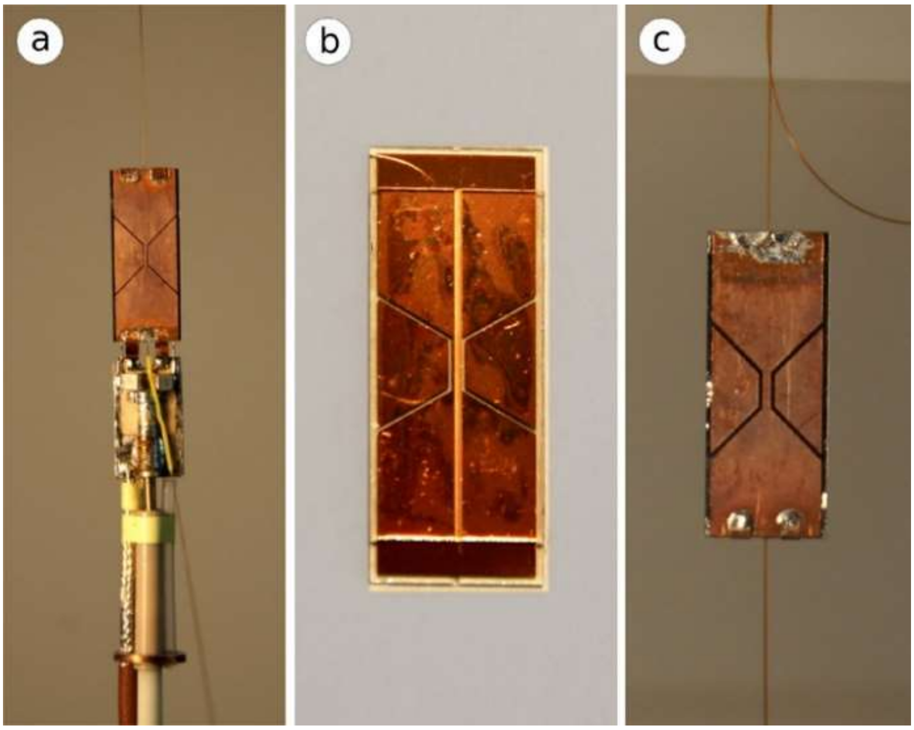

Figure 1-2 Schematic view of three modified stripline chips for microfluidic flow NMR spectroscopy including 1D, 2D, and heteronuclear signals. (a) 100 µm D263T borosilicate-made 165 nL volume chip with optimal resolution and sensitivity (b) 500 µm fused silica-made 145 nL volume chip, preferable for small volume samples (c) borosilicate-made chip with a maximum volume of 215 nL similar design as (a) (adapted from ref. [42] Copyright 2017 American Chemical Society)

Ahmed-Omer and co-workers demonstrated the use of benchtop NMR spectroscopy for *in situ* monitoring of hypervalent iodine(III)-initiated cyclopropanation of styrenes [49]. An innovative approach was developed to effectively differentiate the features between reactants and products, in which an inline solvent switching device allowing the switch from reaction to an analytical medium was incorporated for accessing spectra in a deuterium-enriched media. The robust and compact continuous platforms equipped with the function of evaporation, concentrating, and solvent switching are easily fabricated from commercially available elements (Fig. 1-3). Mass spectrometry was also combined with this system to contribute additional evidence and a multidimensional perspective to process control and real-time monitoring. The built platform is versatile, facilitating downstream processing with the strategy of online monitoring of the reaction progress over time. It also shows satisfactory adaptability of realizing the interaction with the MNOVA software to profile the reaction progress and record species resonance at a specific chemical shift. Since the monitoring is not accomplished in its original position, it does not strictly follow the notion of *in situ* NMR measurement, even though the strategy is capable of acquiring real-time data approximately.

Figure 1-3 Robust platform for *in situ* reaction monitoring of a cyclopropanation reaction with Spinsolve benchtop NMR spectroscopy. (A) Vapourtec R2+ pump unit. (B) Vapourtec R4 reactor unit. (C) Flow stream input. (D) Benchtop NMR. (E) Flow stream output. (F) Glass NMR cell (adapted from ref. [49] Copyright 2016 American Chemical Society)

A step forward in this regard was provided by Gomez et al., [50] who assembled a novel kit with integrated planar-spiral transceiver coils for *in situ* NMR monitoring of UV-Vis assisted reductive dehalogenation of α-bromoacetophenone in the nanoliter scale. The described process solves the plight of low photonic efficiency encountered with large-scale photochemistry and makes reduced dimension analysis feasible (Fig. 1-4). The light-induced photocatalytic dehalogenation of α-bromoacetophenone and the photoconversion of o-nitrobenzaldehyde to nitrosobenzoic acid were chosen as probe reactions under stopped-flow conditions, using LEDs (525 nm) and laser diodes (405 nm) as the light sources, respectively. The obvious evolution of the chemical process can be visualized by the disappearance of α-bromoacetophenone at 4.93 ppm and the formation of acetophenone at 2.57 ppm as well as the chemical shift of the oxidized form of diethyl-2,6-dimethyl-1,4-dihydropyridine-3,5-dicarboxylate at 4.32 ppm. Kinetic data from the photoconversion of o-nitrobenzaldehyde to nitrosobenzoic acid showed good agreement with literature. These reactions can be performed in small NMR detection volumes of 25 nL and can be evenly irradiated by diverse low-power light sources with non-invasive optic fibers, enabling high photon flux. The attempts of implementing uniform UV-Vis illumination in a traditional NMR device are always confronted with excessive irradiative heating, drastic decay of light strength, etc. Although the methodology presented here partially advocates a new path of problem handling to tackle difficulties listed before, the predicaments of irradiation are still to be met when the sample volume comes to a microliter scale, particularly when trying to scale up photocatalytic reactions in microfluidics.

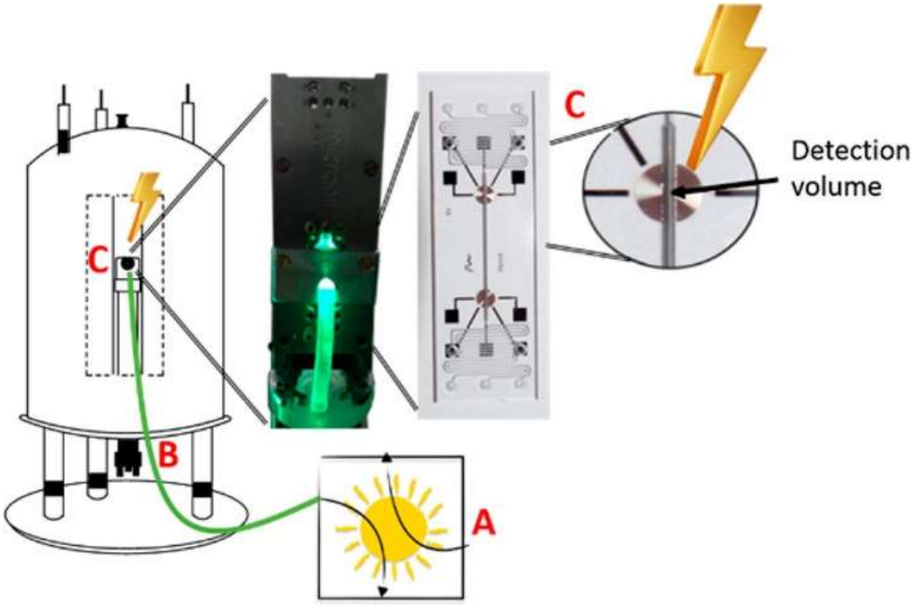

Figure 1-4 Graphic representation of the assembly of nanolitre-*in situ*-NMR microfluidic chips. (A) used UV-vis light source. (B) non-contact-sample optical fiber. (C) sampling zone. (adapted from ref. [50] Copyright 2018 American Chemical Society)

### 1.2.2 Reaction probing with in-situ infrared spectroscopy

The utilization of infrared (IR) spectroscopy as a non-invasive analytical technique to obtain spectral information has been proven to be reliable and effective [51]. IR spectroscopy offers an abundant capacity of spectroscopic information of interrogated chemicals due to activated molecular vibration in the range of near-IR to mid-IR. The implementation of three different FTIR techniques, diffuse reflectance (DR), attenuated total reflectance (ATR), and transmission mode, has promoted the advancement of IR detection in chemical process inspection. Furthermore, the coupling of microfluidics and mid-IR spectroscopy can be successfully applied to trace analytics and enables access to spatially resolved spectra with a good signal-to-noise ratio (SNR). Simultaneously, the prototype of integrating FT-IR imagining with microfluidic apparatus was confirmed to be achievable, in which transmission mode results in superior sensitivity while the ATR mode contributes a preferable choice for quantitative analysis [52]. Hence, it is practical to monitor a chemical process with IR detection in a flow reactor. An excellent review for combing microfluidics with FTIR spectroscopy was provided by Perro et al., where the potentialities, strategies, and challenges are well generalized, giving a tutorial guide to constructing innovative devices for real-time IR mapping [51].

Examples concerning stand-alone *in situ* IR reaction imaging are scarce. In most cases, it is only regarded as an ancillary detection method and cannot be analyzed independently to support quantitative transformations because of fragmented structural information provided. Indeed, the complexity of incorporating external analytical tools like mass spectrometry and NMR spectroscopy interferes in some cases with *in situ* IR implementation for chemical synthesis. There is, however, no better solution to date to circumvent these limitations. In the first case, Gross et al. [53] reported a flow system equipped with micron synchrotron IR and X-ray beams in a small cell with 2 cm length. This apparatus can associate the functions of analyzing reaction transformation and observation of species evolution from vinyl ester **I**, as a consequence providing strong evidence of the presence of a short-lived intermediate, the allenic aldehyde **II** (Fig. 1-5). The yield and selectivity of products can be modified by altering the residence time of the raw feed. The results show a decreased flow rate by 50-fold compared to the original one (from 10 $mL·h^{-1}$ to 0.2 $mL·h^{-1}$) contributed a dramatic increase of conversion (elevated from 20% to 75%), and high chemo-selectivity to give the acetal product **III** was achieved. Confirmation of the conclusion deduced from *in situ* IR measurement needs data from gas chromatography and NMR-spectroscopy. The plot of the species distribution provided insights into kinetic studies with a high spatial resolution of 15 μm. This pioneering analytic technique depicts the blueprint of *in situ* reaction mapping of organic synthesis, clearing the mist in the field of combining microfluidics with *in situ* IR measurements.

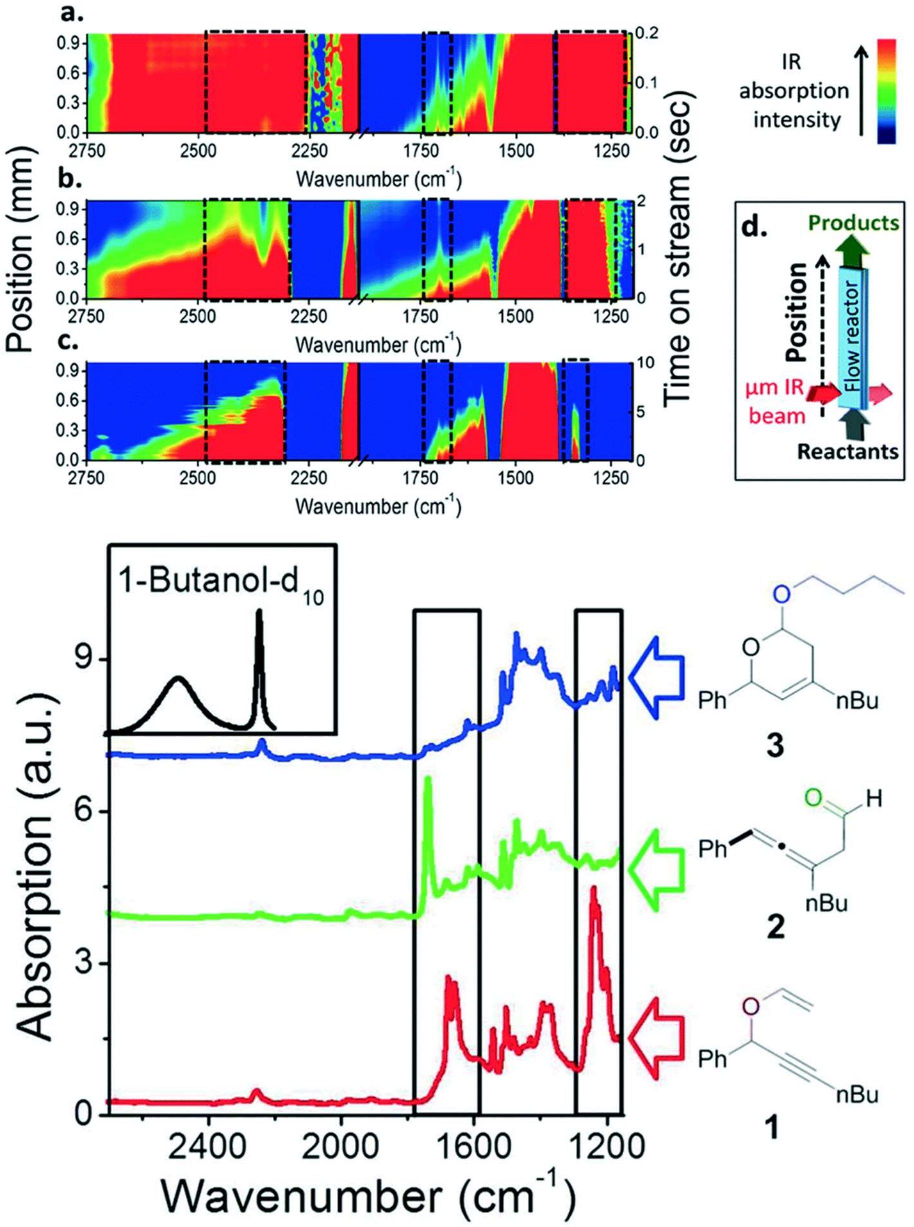

Figure 1-5 Top: spatially resolved IR spectroscopic imaging along a flow reactor with various flow rates, 10 (a), 1 (b), 0.2 (c) mL/h, respectively. (d) scheme of a microreactor for *in situ* IR and X-ray microspectroscopy measurements. Bottom: FTIR spectra of reactant, vinyl ether **I** (red), allenic aldehyde **II** (green), and acetal **III** (blue) (adapted from ref. [53] Copyright 2014 American Chemical Society).

Following, Zhang et al. [54] studied heterogeneous catalytic asymmetric hydrogenation of an α-amino ester over a cinchonidine (CD)-modified palladium catalyst with several home-made *in situ* FTIR experimental apparatuses that enable various function-oriented characterizations (Fig. 1-6). The same overall shape, together with trifling distinction among three FTIR spectra depicts the evolution of the hydrogenation process very well: the transmission model corroborated the formation of OH–O and NH–N hydrogenation bonding between CD and the amino ester, while DR and ATR gave support in monitoring the degree of interface hydrogenation. The first incorporation of diffuse reflectance infrared Fourier transform spectroscopic (DRIFTS) with a microfluidic platform offers a better option of inspecting CD-morphology on the transition-metal catalyst surface with changeable coverages, exempting from new catalyst bed preparation and reducing the waste of essential resources significantly. The described method can be used for the exploration of the morphology of a catalyst's surface in the process of heterogeneous catalysis, exploiting *in situ* IR analysis and microflow systems.

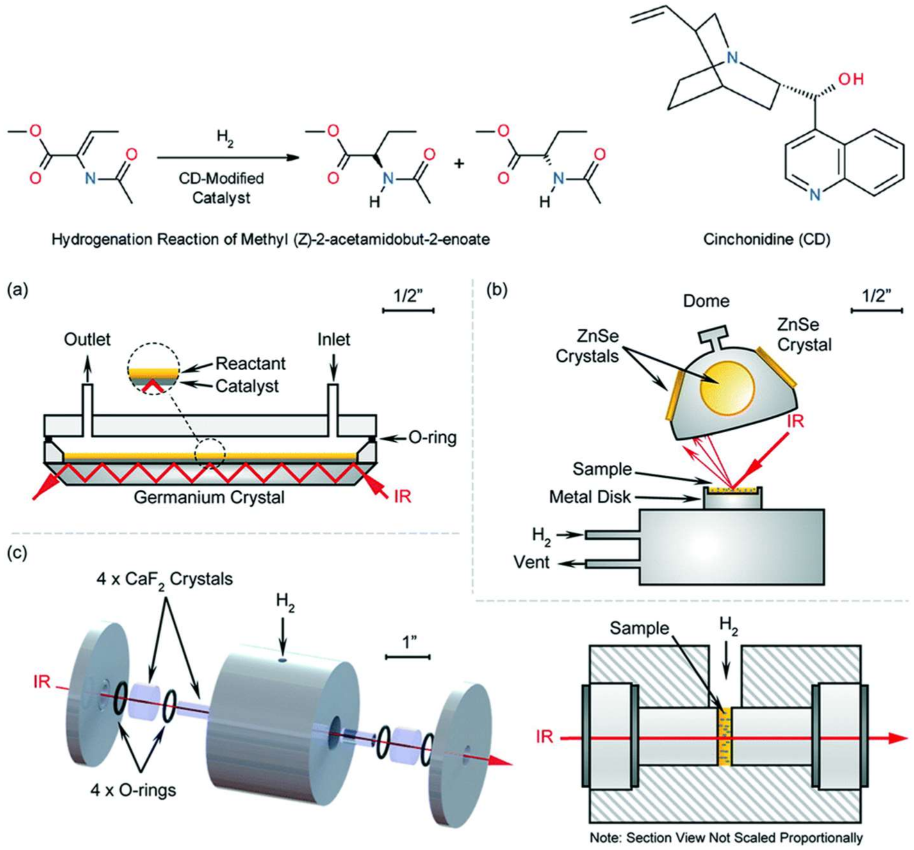

Figure 1-6 Top: the hydrogenation of methyl (Z)-2-acetamidobut-2-enoate with a CD-doped Pd catalyst. Bottom: detailed views of the in-situ IR-microfluidics setup, (a) ATR infrared cell assembled by Ge crystal, (b) DRIFTS cell, (c) transmission FTIR structure (adapted from ref. [54] Copyright 2016 American Chemical Society).

Another case reported recently was pertinent to the improvement of a hydrosilylation reaction in a microflow system using *in situ* IR monitoring [55]. Fig. 1-7 shows an example of *in situ* IR analysis of a hydrosilylation when adopting a microfluidic reactor, achieving nearly 100% Si-H conversion of 1,1,1,3,5,5,5-heptamethyltrisiloxane (HMTS) and 1-octene with only 1 minute residence time and a very low concentration of catalyst usage. The apparent disappearance of the Si–H bond during the conversion process of the raw materials makes *in situ* IR analytics accessible to acquire real-time information. The conversion can be calculated from the reducing area of the Si–H vibration band around 915 $cm^{-1}$ since the intensity of the signal is proportional to the concentration of reactants based on the Beer–Lambert law. Although results from *in situ* IR showed a lower yield in comparison to data from gas chromatography, the swift detection makes it an ideal tool for observing the hydrosilylation. The plug-in contact measurements of ReactIR 15 for the record of IR data make it flexible and portable, but it can only reflect the state of specific local points rather than give an overview of the fluid state.

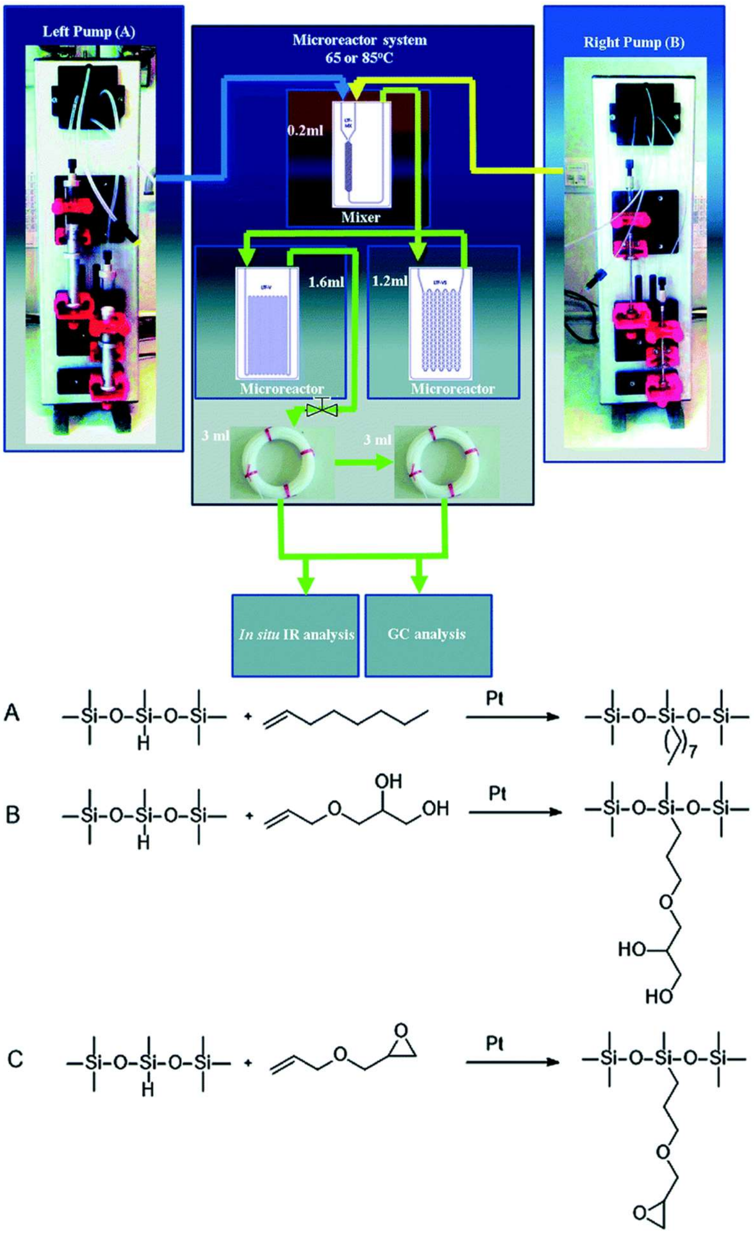

Figure 1-7 Setup of *in situ* IR detection in flow reactors (upper) and hydrosilylation of different olefins (below). (adapted from ref. [55] Copyright 2018 The Royal Society of Chemistry)

To sum up, the integration of IR microspectroscopy with flow reactors for real-time monitoring of the reaction progress can be beneficial, but the requirements for differentiation between reactants and test samples as well as acquiring accurate quantitative results remain challenging.

### 1.2.3 Reaction probing with in-situ Raman spectroscopy

Raman spectroscopy can compensate for some of the drawbacks that come along with IR measurements such as the sensitivity to water and inaccessibility of the low wavelength spectral range that bears structural information for hydroxyl groups and metal-connected bonds [56, 57]. Practicing rapid and damage-free identification of test samples as well as *in situ* progress monitoring of chemical reactions with Raman techniques is strongly recommended in flow chemistry [58]. Low scattering sensitivity confronted with surface-enhanced Raman spectroscopy (SERS) can be addressed by the addition of rough noble metal nanoparticles to accomplish several orders of magnitude increase in the analyte's Raman signals. The bridge of Raman spectroscopy and microflow setup requires developing custom-tailored flow cells and reliable probes for sensing.

An initial attempt to combining *in situ* Raman spectroscopy for rapid condition optimization of organic synthesis was presented in 2007. Leadbeater et al. [59] chose a microwave-assisted simple esterification reaction of acetic acid with butanol as a model reaction in an automated stop-flow instrument that revealed the attractive potential of quality control for organic transformations. Another example of Raman spectroscopic studies was presented with Au–Pd bimetallic-supported TiO2 for catalytic oxidation of benzyl alcohol in silicon-glass micro-packed-bed reactors (MPBRs) [60]. The microreactor design and laboratory setup are shown in Fig. 1-8. Due to the characteristic CO stretching of benzaldehyde in the Raman spectrum at 1700 $\mathrm{cm}^{-1}$, the authors succeeded in quantitative determination of the product and screening of different reaction parameters. External calibration was established by gas chromatography, in which the results show good accordance with the Raman measurements. An optimized reaction condition resulted in 95% conversion of benzyl alcohol with 78% selectivity towards benzaldehyde.

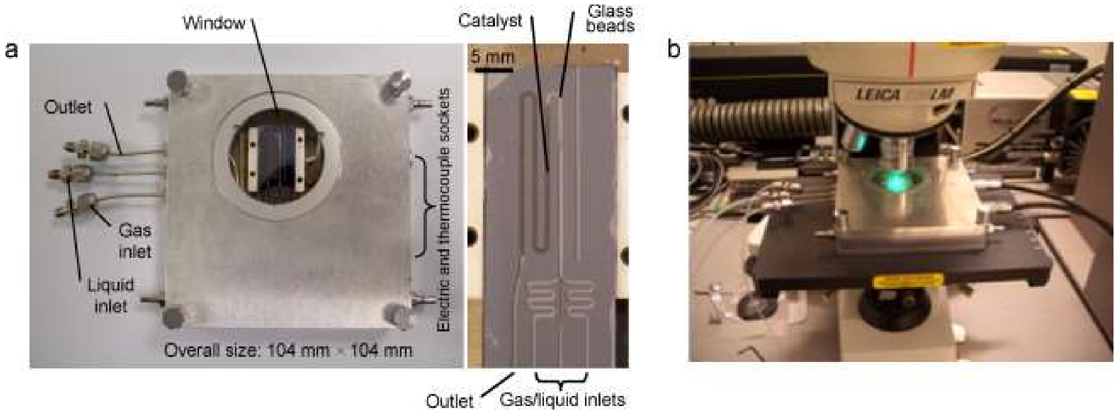

Figure 1-8 Microreactor set-up and assembly with Raman microscope (adapted from ref. [60] Copyright 2011 Elsevier)

More complex chemical conversions are demonstrated in a multichannel microfluidic chip fabricated from PDMS/glass with the method of moulding and plasma bonding, which approves nanolitre-scale organic synthesis for Raman imagining of dynamic flowing droplets in microchannels (Fig. 1-9) [58]. The Hantzsch syntheses of 2-aminothiazoles were chosen as model reactions, and an acquisition time of 500 ms was adopted to realize considerable SNR. Suitable indicative Raman bands characterized with apparent discrepancy between starting materials and final products were selected for spectroscopically single droplets tracing, which correspond to the dynamic view of the reaction progress. Silver nanoparticles were involved for enhancing the Raman signal with the strategy of introducing them downstream before arriving at the acquisition points. This research paves the way to qualitative analysis of high-throughput screening of organic reactions in flow.

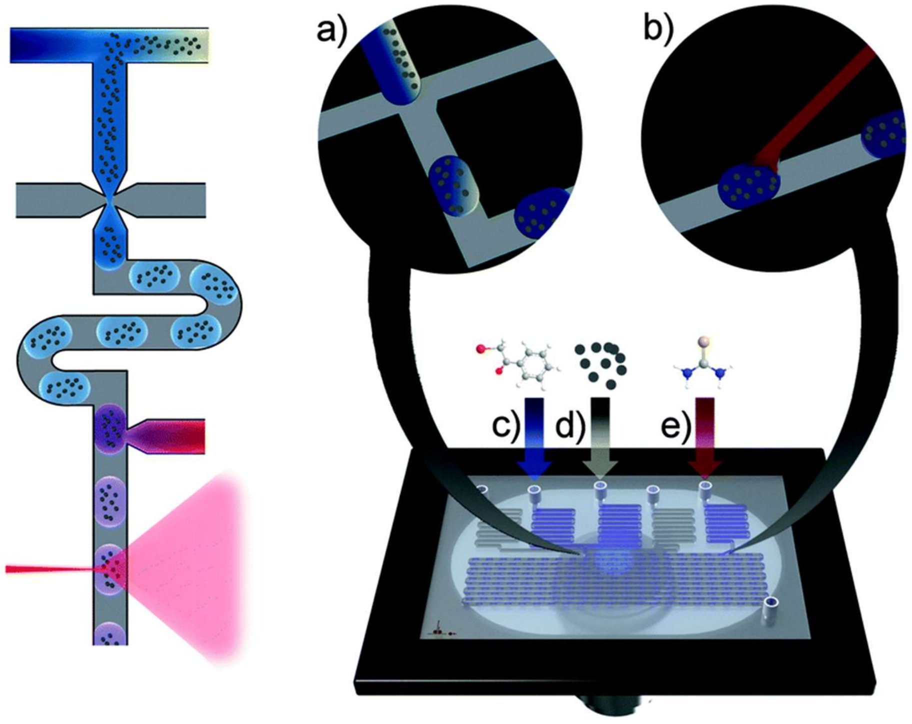

Figure 1-9 Schematic diagram of *in situ* Raman detection (left) and multichannel microfluidic chip (right) (adapted from ref. [58] Copyright 2015 The Royal Society of Chemistry).

Latterly, the first example of utilizing microfluidics with Raman spectroscopy for conducting mechanism and kinetic study of palladium-catalyzed cross-coupling was elucidated by Rizkin and co-workers (Fig. 1-10) [61], who proved that the process of $PdCl_2(CH_3CN)_2$ conversion into an active $Pd_0L_2$ complex proceeds only in the interface of aqueous and organic phases. The Raman data integrated with calibration curves were used for concentration and mole fraction determination of each species. Chemical kinetics showed that neither carbopalladation nor ionic mechanisms are involved in the cross-coupling reaction while cationic and anionic deprotonation mechanisms were found to contribute. The binding of a palladium atom with ligands endows the ability of catalytic activation, which in turn promotes the chemical transformation. Such discovery supports inspirations for ubiquitous functionalization reactions in organic chemistry that resemble cross-coupling reactions.

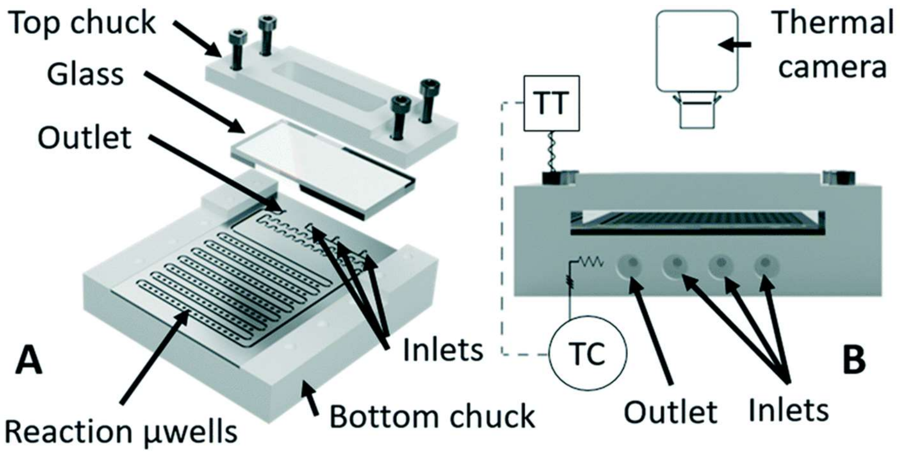

Figure 1-10 Microreactor design adopted in Pd-catalyst assisted cross-linking reaction and relative mechanism study (adapted from ref. [61] Copyright 2018 The Royal Society of Chemistry)

### 1.2.4 Reaction probing with in-situ UV-Vis spectroscopy

The first paradigm of *in situ* UV-Vis investigation in continuous-flow was led by Jiang et al., [62] who coupled 13C MAS NMR and UV-Vis spectroscopy to evaluate a catalytic methanol-to-olefins (MTO) process on silicoaluminophosphate H-SAPO-34 in a 7 mm MAS NMR rotor reactor. Evidence from *in situ* NMR and UV-Vis spectroscopy under continuous-flow conditions discloses that dimethyl ether (DME) is the MTO's primary product at a low working temperature of 473 K and 523 K. A further increase in temperature is conducive to the simultaneous generation of smaller olefins and carbenium ions. The selectivity of propylene and ethylene can be manipulated with different catalyst working temperatures of 573 K and 623 K, respectively. Also, the resulting olefins may progressively react with the carbenium ions to generate larger aromatic deposits and larger carbenium ions, which in turn is detrimental to MTO and results in catalyst deactivation at 673 K (the formed polycyclic aromatics act as coke deposit).

Reports showed oxidative catalyst states and their reactivities are highly dependent on the touching gas atmosphere, and some reversible changes in catalyst state are not maintainable without suitable reaction conditions. These make a direct interrogation the relationship between oxidation states of the catalyst and the corresponding reactivity inaccessible. The issue can be tackled with *in situ* UV-Vis spectroscopy and continuous handling in flow operation. Bu et al. carried out another study dealing with microgram Cu-catalyst dynamics and CO-oxidation kinetics. They incorporated a pocket microreactor with *in situ* UV-Vis and MS (see Fig. 1-11). [63] Over a reduction to a stepwise oxidation process, the designed approach can visualize the Cu-catalyst in different valences, from metallic state to Cu(II), among which metallic Cu was found to be catalytically active. Deactivation occurred due to irreversible oxidation of the metallic Cu. Also, XPS is included for providing supplementary evidence as well.

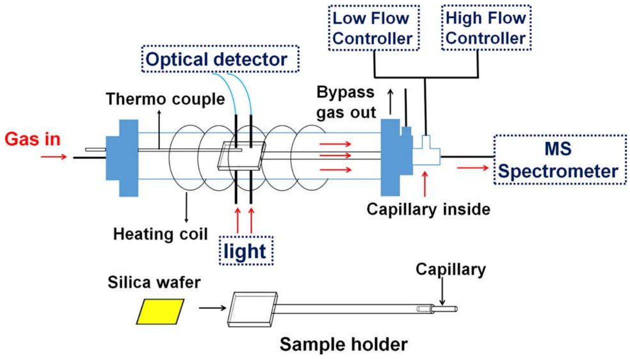

Figure 1-11 The design of a microreactor integrated with an optical spectroscopic apparatus and a sampling capillary. (adapted from ref. [63] Copyright 2015 American Chemical Society)

The adoption of *in situ* UV-Vis into microfluidic reactors for organic synthesis monitoring is still far from mature. Currently, applications of UV-Vis in microfluidics focus on morphology changes on a catalyst's surface or spectral differentiations between metals in different valence states, rather than the chemical transformation itself. Besides, for reaction monitoring purpose, the chosen analytes need to possess a suitable chromophore [64].

### 1.2.5 Overview of different in-situ sensing methods used in microfluidic reactors

Mass spectroscopy is commonly used for online measurements of microfluidic analysis. However, illustrative cases regarding *in situ* application in microfluidics are very few [37, 65, 66]. Electrochemical readout combined with other spectroscopic techniques such as NMR allows for the rapid dissemination of redox processes *in situ* [47].

Other *in situ* optical analytics like fluorescence spectroscopy and X-ray absorption spectra (XAS) have been extensively utilized in non-interference kinetic studies of integrated microfluidic synthesis. The production of metal nanoparticles (Au-NPs, $In_2O_3$-NPs, $Pt_3Ti$-NPs, etc.) [67-69], colloidal semiconductor nanocrystals (NCs), and quantum dots (QDs) [70] has revealed the early stage of rapid nanostructure growth and nucleation processes and corroborates the process mechanism that completes in a few milliseconds. Likewise, their applications are, however, more for material science. Studies related to reaction probing are limited and have not been described yet. Table 1-1 summarises the advantages and disadvantages of various *in situ* sensors coupled with flow reactors.

Table 1-1 Comparison of *in situ* sensors coupled with flow reactors

| *In situ* analytics | Advantages | Disadvantages |
|---|---|---|
| NMR | Most informative, robust scope, independent | Bulky main body, expensive, solvent-switch |
| IR | Broad scope, portable, easy to miniaturize | Water-limited, material limitation dependent |
| Raman | Broad scope, good resolution | Expensive laser required |
| UV/vis | Suitable for catalyst studies | Limited scope |
| XAS | Suitable for nano-synthesis | Limited scope |

NMR has the most powerful capabilities in the assay, but the problems of bulky size, expensive instrumentation, and the need for a solvent-switch system served for the deuteration process seems to be insurmountable. IR has subordinate application scope and shows ascendency in portability, flexibility, and cost-effectiveness in microfluidic applications, but some applications were restricted in aqueous solution and the fingerprint region of an infrared spectrum. The material challenges are confronted with inadequate wavelength coverage in the detection area of interest and high prices in some optical glasses. At the same time, additional analytical instruments are required to fulfill quantitative evaluation. Raman can compensate flaws in IR, while the costly laser is necessary for the determination. Meanwhile, the clogging of microchannels should be carefully addressed if rough metal nanoparticles are employed to achieve good resolution. A common drawback associated with IR and Raman probing is that they cannot be used independently and the choice of chemicals in a study should be decided by a sophisticated chemist to achieve good discrimination in the obtained resultant spectra, as these spectra provide only partial structural information. UV-Vis and XAS are suitable for kinetic studies in distinct fields. The adoption of these methods in chemical synthesis should be further explored.

The achievement of integrating *in situ* optical analysis with microfluidics technology has shown an impact to extract real-time information for in-depth dynamics and mechanism research, thereby reducing the gap between theoretical and realistic processes. Challenges with *in situ* optical analysis using microfluidics, however, remain daunting. Difficulties in the miniaturization of NMR, dependence, and sensitivity of infrared, Raman, as well as UV-vis spectrometry, should not be neglected [71], even though spectrometers with ever-smaller footprints capable of *in situ* mapping were fabricated and field-resolved infrared spectroscopy for biological systems with a plethora of water absorptions was introduced [25].

### 1.2.6 In-situ IR analysis of photocatalysis in flow reactors

Photocatalysis has been shown to be a green and sustainable synthetic method for the chemical conversion of many high-value-added products under mild conditions [72-75]. However, problems with engineering scale-up are inevitable when using large, conventional batch reactors. To address this issue and to take full advantage of the benefits associated with the sustainability of photoredox reactions, the existing methodologies should be adapted to large-scale production. This requires the mitigation of the light penetration effect in reactors. Flow chemistry and associated PAT tools are therefore ideal for carrying out photoredox reactions whilst controlling the quality of the product in real time [76]. Furthermore, a breakthrough has been made in the miniaturization of infrared sensors, which have been successfully integrated with microreactors to detect the concentration of the photolysis solution of 2-azidobenzoic acid, which provides both spectral and spatial resolution for monitoring reaction chemistry (Fig. 1-12) [77].

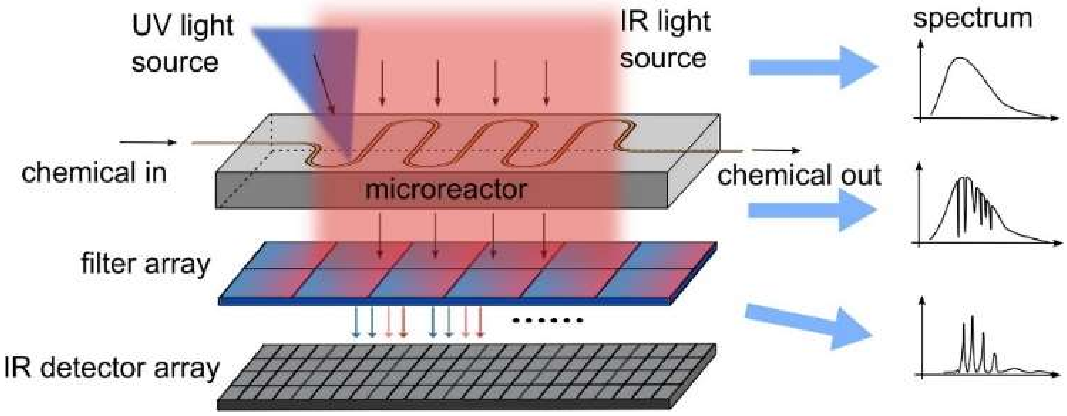

Figure 1-12 Proof-of-the concept: integration of miniaturized infrared sensors to detect the solution concentration after photolysis of 2-azidobenzoic acid. (adapted from ref. [77] Copyright 2020 Elsevier)

With the increasing number of photochemical studies showing great success in microfluidic devices and the ease of integration of infrared sensors into microfluidic devices, further investigation may focus on *in situ* IR monitoring of photochemistry in flow.

## 1.3 Objectives of this dissertation

Integrating microfluidic reactors and PAT tools is fascinating and shows great potential in product quality control. Of all the optical sensors currently available in the literature, infrared would be the most competitive candidate because of its wide detection range and already achieved miniaturization. The microreactors can therefore be combined with infrared sensors to build up a portable benchtop system. Simultaneously, the development of *in situ* infrared micro photoreactors for the application in reaction probing and scaling up production would be an important topic in the near future. However, such a combination is still in its infancy and far from mature. Even though Wang et al. [77] have shown the concept that their miniaturized infrared sensor has improved integratability with microreactors, the optical path length of both the reaction and sensing region is 100 μm. A limited light path is detrimental to photoreactions as it results in a large proportion of light not being absorbed by the reaction medium, thus wasting energy. To maximize the use of light and make full use of infrared sensing, an innovative reactor design is required that takes both photoreaction and infrared detection into account. The designed microreactor should be able to be used for *in situ* IR sensing of a wide range of photocatalytic reactions.

The dissertation includes part of the results from the DFG research unit “Assessing and Controlling Dynamic Local Process Conditions in Microreactors via Novel Integrated Microsensors” (ProMiSe Phase II), whose research interest is on measurements and control of dynamic local process states in microreactors through novel in-situ sensor technologies [78]. In the present dissertation, the main contribution focuses on designing a sensor-integrated micro photoreactor for reaction probing and mounting the miniaturized infrared sensors from the University of Freiburg (the continuation work of Wang [77]) with the proposed microfluidic reactor to build up a compact and robust flow system for *in situ* sensing applications and real-time process control. In addition, the chemical kinetic parameters of the chosen photoreaction will be extracted to develop a generic reaction model to reproduce the process in the proposed flow system. Computational Fluid Dynamics (CFD) multiphysics simulation of the photoreaction will be carried out to gain insight into the process and identify the limiting factors of the reaction, and ultimately use simulation results to obtain suitable operating conditions for process intensification.

The research objectives of the thesis are the following:

1. Development of microreactor test systems for evaluation and chemical kinetic

measurements. The reaction kinetics of the chosen photoreaction should be determined. Variable reaction parameters such as residence time, light intensity, the concentration of feed solution, and catalyst loading are required to extract the kinetic parameters of the reaction.

2. Modelling and simulation of the chosen photochemical reactions in flow microreactors. CFD tools are employed to build up a model to reproduce the process and help to obtain detailed scientific understanding of the process and the reactor behavior from a micro perspective. The proposed model starts with the simplest example and gradually increases in complexity to cover all features of the flow systems. Moreover, the system model plays an important role in process control since a generic model can be used to predict the conversion of the reaction with arbitrary process parameters as inputs. The different operating parameters are assessed to find the most suitable operating conditions. Meanwhile, the mass transport resistance within the reactor channel is evaluated for different operating parameters.

3. Integration of spatially resolved chemical composition measurements with the designed flow photoreactor. Building a compact and portable microfluidic system to perform spatially resolved reaction probing. The system should be constructed so that the infrared light source is aligned with the infrared sensors to minimize systematic errors in each measurement. The illumination system and corresponding cooling system should be incorporated into the constructed experimental test bench to ensure that the photoreaction is independent of temperature. Finally using the optimized reaction and process conditions previously established, the optical sensors are used to complete the real-time composition measurements.

# 2 Development of photoreactor test benches for detailed kinetic studies and process control

## 2.1 Fundamentals in photoreactor design

The application of visible-light photoredox catalysis for the synthesis of high-value-added chemicals has contributed to great prosperity in the chemical community. As a result, a surge of studies relating to this field has been disclosed over the last few decades [79-82]. The success in photocatalytic practice has naturally given rise to the requirement to propose new photoreactor designs to exploit their possibilities and maximize their potential. In this scenario, a dizzying array of photochemical test benches have been introduced by different research groups [83-86], yet no explicit standardization is disclosed. Only a few words describing the type of LED used and its distance from the borosilicate vial and tube are available. Despite the rapid development of photocatalysis, these achievements face some problems of reproducibility and inconsistent results due to the use of traceless "photons" as reagent and the fact that the test benches on which the experiments performed are not often exactly specified. The discrepancies are often a result of missing detailed descriptions with respect to the photoreactor setup. Important information such as the actual incident light intensity received is not explicitly stated and only a vague macroscopic indicator of irradiated power is provided as an alternative. In fact, the rate of a chemical reaction is related to the actual incident light intensity [87]. It is true that using more powerful light sources to initiate the reaction is an easy-to-follow way of speeding up the reaction while reducing production time. However, on one hand, according to the basic principle of radiative transfer, only a portion of the light will be absorbed by the reaction mixture, while a considerable fraction of incident light will be scattered, transmitted, or even reflected [88, 89]. On the other hand, as stated by the Grotthuss–Draper law, only the absorbed light will be able to propel chemical reactions, whose intensity attenuates exponentially with the penetration depth (or light path) in a given reaction medium as dictated by the Bouguer-Lambert-Beer law [90]. The same principle applies to other spectroscopic methods, such as UV-Vis and infrared, etc. For a lateral illumination case (Fig. 2-1), the actual penetration depth that experiences irradiation within the photoreactor is very limited (normally below 2 mm), therefore only a small fraction of the photocatalyst proximal to the optical side is activated and able to initiate photoreactions [91]. The majority of the bulk solution remains in the “dark zone”, where few photons will be dispersed. As a result, it is hard to achieve homogeneous irradiation in batch syntheses where the reaction screening usually takes place in flasks or vials. Consequently, long exposure times are inevitable in batch synthesis to achieve satisfactory yields because of low photon efficiency [92-94]. This engineering hindrance makes photon attenuation effects become non-negligible when researchers attempt to transfer their findings into different scales (i.e., from gram-scale to kilogram- and even ton-scale) [87, 95].

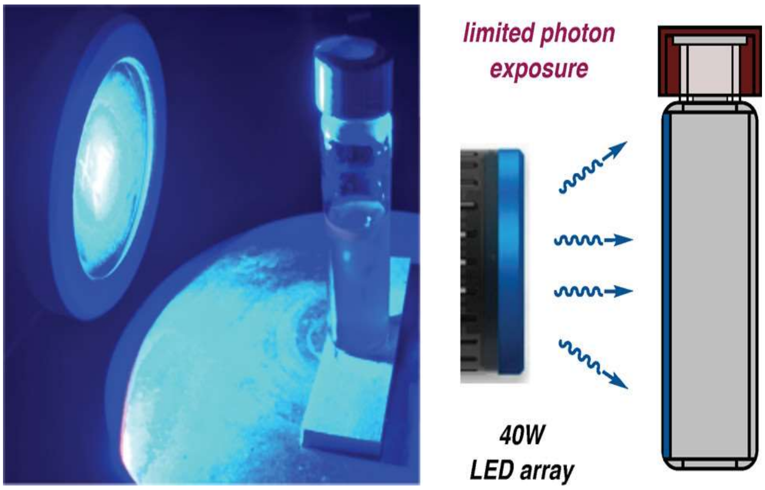

Figure 2-1 Light attenuation in a lateral illumination case. (adapted from ref. [91] copyright 2017 American Chemical Society)

In contrast, significant acceleration can be observed when photochemical reactions are transferred to microfluidic reactors. The use of microreactors for photochemical syntheses takes advantage of the unique benefits offered by rapidly evolving micro technologies, such as larger surface-to-volume ratios, more efficient mass and heat transport, and higher productivity, which leads to higher selectivity and reduced reaction times [26]. Moreover, the illumination in the microreactor will become more uniform as the penetration depth can be well matched by the reactor's geometry. As a result, incident photons can be utilized to the maximum, thus greatly accelerating photoreactions. These merits make the flow reactor versatile to accommodate various photochemical transformations. To construct a robust flow system for photochemical study, suitable light sources should be determined to match the optical property of the photocatalyst [96]. The narrow emission spectrum can maximize the overlap between the emission spectrum of the light source and the absorption spectrum of the photocatalyst, thereby avoiding waste of energy. Among commercially available light sources, the light-emitting diode (LED) becomes a competitive candidate for this purpose. The rapid advances of LED show great compatibility with flow systems as high photon flux density, low power consumption, narrow emission spectrum (pseudo-monochromatic features), satisfactory photoelectric efficiency, high irradiance, and long lifespan can be achieved [97]. Moreover, the miniaturized LED's flexibility allows it to be perfectly integrated into flow reactors [98]. However, heat sinks should be properly introduced into the system as side effects accompanying peripheral heating in the vicinity of the light source may have an impact on the thermal path of the photoreaction, leading to a possible increase in the proportion of by-products and impaired selectivity [99]. In addition, air or liquid cooling is an effective aid to keep the LEDs in the reaction system working at a given temperature, thus effectively avoiding the spectrum shift, and controlling the internal temperature of the system effectively as well.

In general, the light source used for microfluidic photoreactors should be positioned at a given distance from the microchannel to ensure a consistent photon flux received by the microreactor and to improve the reproducibility of the results. However, building a flow system for photocatalysis is not simply a matter of combining light sources with microreactors. This requires standardization of the flow system, and the establishment of a standardized photochemical microfluidic system is imperative. Hone and Kappe have summarized some of the relevant key points with respect to flow system standardization [100], albeit specifications for the standardized photochemical microfluidic system have not yet been enumerated. Luckily, some of the specific requirements can be found in the proposals for the standardization of batch photoreactors [101-103]. Likewise, a standardized photochemical microfluidic system should follow these requirements. It is also essential to modularize the components that build the reaction system. Standardization of the photocatalytic flow system is facilitated by componentizing the modules and then assembling them according to certain rules.

## 2.2 Construction of a capillary-based photoreactor (CAP-µR) for chemical kinetics studies

The design and construction of an *in situ* infrared photoreactor will require a lot of effort. As an alternative, kinetic experiments on photoreactions can be carried out in simpler capillary microreactors. In the practice of flow photocatalysis, some fluoropolymer-based materials such as polytetrafluoroethylene (PTFE), fluorinated ethylene propylene (FEP), perfluoroalkoxy alkane (PFA), etc. have shown good chemical resistance as well as good transmittance in the UV-Visible range. Small tubings prepared from these materials are considered capillary microreactors and are suitable for photoreaction screening and probing [87]. Among these materials, PFA is more frequently used and a tutorial guide for constructing a PFA-based microreactor for photocatalysis can be found in the literature [104]. On the basis of this, a similar photoreactor (CAP-µR) was fabricated.

The PFA tubing (i.d. 0.8 mm, o.d. 1.6 mm) with a total reaction volume of 4 mL (2 mL each) was wrapped on borosilicate glass tubes in a shape of a helix and connected with flangeless fittings obtained from IDEX Health & Science (Fig. 2-2b). The rest of the reactor (e.g., infusion tubing) was carefully covered with aluminum foil to prevent extra exposure and inaccurate residence time. The reacting region was fully irradiated by 40 pieces of high-power LEDs with the peak emission at $\lambda$=465 nm (purchased from TRU Components, forward current 350 mA, forward voltage 3.4 V, angle 110°) that were glued on Bosch aluminum profiles (10 profiles with 4 LEDs each, Fig. 2-2d). In this way, it is effective to keep the LED working at optimal conditions and to remove peripheral heat even with long-term irradiation (Fig. 2-2e). The Bosch aluminum profiles were secured at the indicated positions to ensure standardized illumination. The assembled capillary was placed at a distance of 2 cm from the LEDs (Fig. 2-2c). These LEDs were connected in series and powered by a dimmable 100 W constant current mode LED driver (purchased from Meanwell). The emissive light intensity was modulated by the external variable resistance of the driver depending on the output current provided (Fig. 2-2f), resulting in a maximum irradiation power of 47.6 W. The strategy adopted here can attenuate the photon flux density arriving at the system without changing the spectral irradiance distribution of the LEDs (Fig. 2-2g). In addition, two direct current (DC) axial fans were positioned at one side of the test bench (Fig. 2-2c), connected to NI 9475 digital output channels, and controlled by a LabVIEW program. The introduction of air cooling here ensures that the photochemical reaction is free from the effects of temperature. The resulting test bench (Fig. 2-2a) were used for chemical kinetic research.

The presence of the Bosch profiles in this test bench acts as an efficient heat sink and is capable of getting rid of the peripheral heating due to LED irradiation. In addition, the constant operation of two axial cooling fans within the CAP-μR keeps the operating temperature stable and close to room temperature. Therefore, the effect of temperature on the photoreaction performed on this platform is negligible.

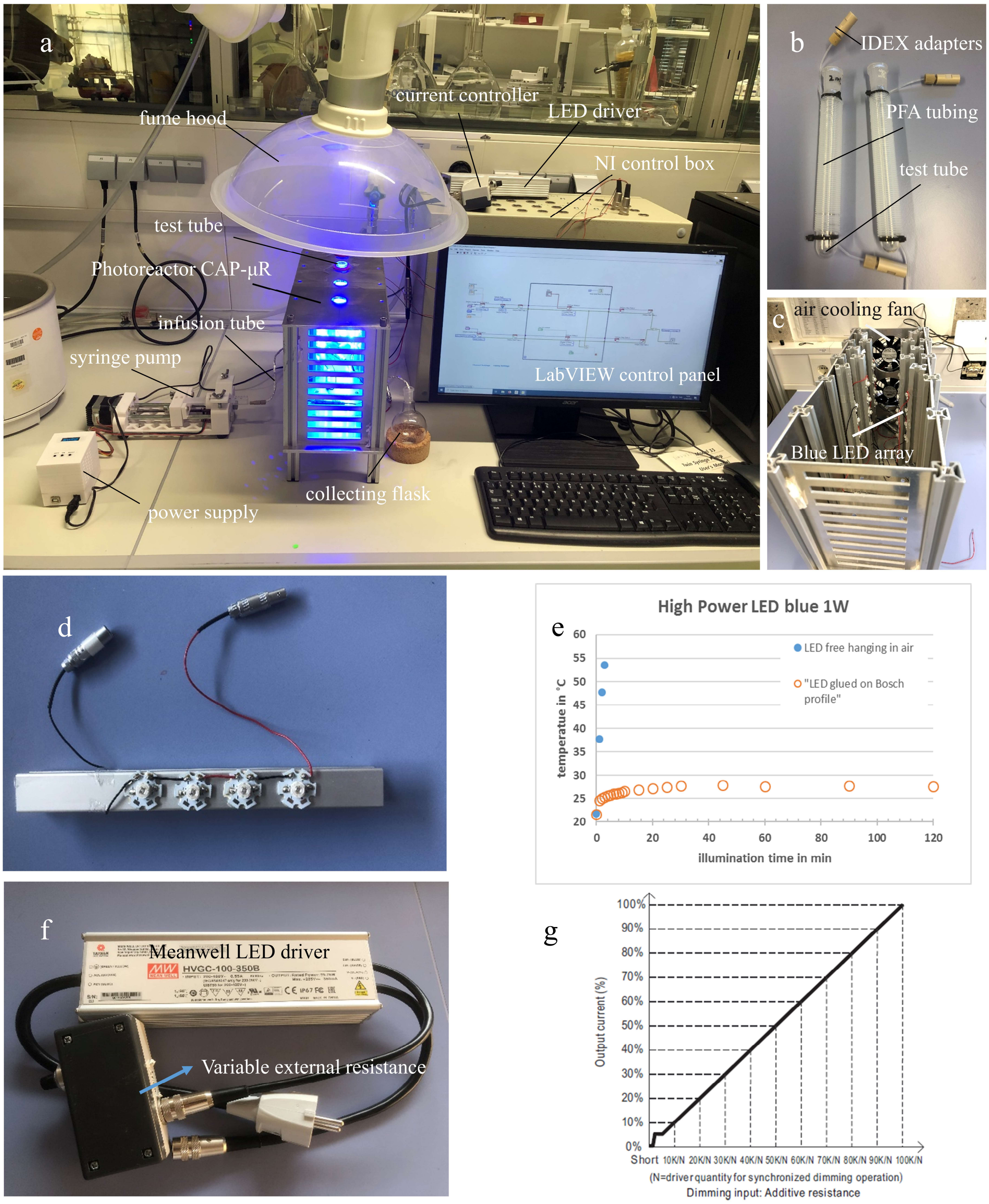

Figure 2-2 The experimental test bench of the CAP-μR for photochemical kinetics studies. a) The assembled continuous flow system b) PFA capillary microreactor used in the study c) The front view of the CAP-μR, Bosch Profile secured at indicated locations. (d) LEDs glued on Bosch Profile (e) The plot of measured LED temperature versus illumination time (f) 100 W Meanwell constant current mode LED driver and variable external resistance (g) The plot of dimmable output current versus resistance, data from the manufacturer

## 2.3 *In situ* infrared photoreactor (PHO-µR) design

Some strategies and challenges regarding combing microfluidics and FTIR spectroscopy have been generalized, providing a guide for the reactor design [51]. But even so, there has never been a relevant discussion in the literature on designing an *in situ* IR micro-photoreactor, which requires taking both photoreaction and infrared sensing into consideration. For this reason, a detailed design of the photoreactor is still required to meet research needs in this thriving field.

### 2.3.1 Microchannel

The first issue to be addressed in the development of infrared-compatible microfluidic devices is the choice of the patterning channels and how they can be combined with infrared transparent materials to form a well-sealed reacting cell. However, the aforementioned materials (PTFE, FEP, PFA) are not IR-transparent but have some degree of IR absorption, making them unsuitable for IR measurements [105]. Therefore, it is impractical to use a single material for the fabrication of *in situ* IR microfluidic photoreactor. As a consequence, hybrid materials need to be used for device design. Spectrochemical IR mapping in a thin polydimethylsiloxane (PDMS) based microfluidic device with a transparent calcium fluoride ($CaF_2$) backbone window has been disclosed, but the PDMS itself can interfere with IR absorption and has a limited temperature and solvent compatibility scope [106]. It is further reported that *in situ* IR spectroscopy can be applied to a simple $CaF_2$-encapsulated flow cell to obtain spatially and temporally resolved IR spectra representing the variation of chemical composition along the length of the reactor [53]. However, the small internal volume of the flow cell may not fully cover the observation period of slow kinetic photoreactions, as this requires a longer residence time and slower flow rate. Slower flow rates favor molecular diffusion, but not mixing by vortices. It is reported that enhancing mixing appears as a significant challenge for coupling an efficient chemical process with an *in situ* IR spectroscopy analysis, mapping, or imaging. In some cases, even dedicated micromixers are necessary to be incorporated [51]. These considerations may lead to a partial loss of chemical information. Moreover, microimaging FTIR in a photoresist channel of a Corning 7740 glass-encapsulated silicon microfluidic device with a synchrotron source has been demonstrated [107]. The transparent region of silicon, however, is limited and is not fully transparent in the visible region, which hinders the application of this material in photoreactors. Besides, the pricy cost of silicon is also not conducive to industrial production. Although the three cases mentioned above give some inspirations for the selection of the microchannel (i.e., the use of different materials to construct microchannels and matching IR windows), none of them fully covers the requirements of an *in situ* IR microfluidic photoreactor.

Meanwhile, the photochemical reaction itself is very special. The reaction only takes place in illuminated regions. On the contrary, in non-illuminated areas, the reaction itself can be seen as stagnant, i.e., immediate quenching occurs, due to the absence of incident photons in the reaction system. However, when the feed stream re-enters the illuminated zone, the reaction proceeds immediately due to the very quick activation and propagation period of the photocatalyst. The alternation of bright and dark regions in photocatalysis can therefore be approximated as a catalytic process taking place in a fixed-bed reactor, where the chemical reaction takes place only in the region where the catalyst is deposited. Due to the specific mechanism of photochemical reactions, inline IR measurements are virtually indistinguishable from *in situ* measurements. *In situ* sensing can also be considered by connecting an adjacent infrared detection zone (non-illuminated zone) after the reaction zone (illuminated zone). Consequently, it is possible to consider the infrared detection area separately from the photoreaction area, as the actual progress of the reaction is not affected when carrying out the infrared detection, thus reducing the complexity of reactor design. If only the photoreactive area is considered, in this scenario, stainless steel would be a good candidate for the construction of the microchannel due to its cheap price, easy processability, good chemical resistance, and optical reflectivity. To make maximum use of the incident light, the depth of the microchannel was chosen to be 2 mm since the actual penetration path is empirically below this value [91]. Using additive manufacturing techniques, a milled meandering microchannel with a comparatively large volume can be constructed. The design of the infrared detection cell will be discussed later as it is also relevant to the specific FTIR method implemented.

### 2.3.2 Options of glass window for the PHO-μR

Another critical component of the photoreactor is the optical window. In theory, the window should possess good transparency for both the (UV) visible and the mid-IR range in order to couple the infrared spectroscopy with microfluidics for photochemical applications. However, this is a daunting challenge, and so far no material has been reported to cover this range completely. As is shown in Fig. 2-3 for the (UV) visible range, conventional microfabrication materials such as silica glasses are not infrared transparent. Therefore, they are not able to cover a wide range of wavelength of infrared spectra, (i.e., between 400 and 4000 $cm^{-1}$, the conventional spectral range provided by benchtop FTIR), where the majority of the organic moieties absorption band is located. Other materials such as $CaF_2$, sapphire, ZnSe, or silicon have good transparency in the near-to-mid-infrared region, but sapphire has a degree of spectral loss in the mid-infrared range. In addition, the latter two materials are opaque to some extent in the visible range where photochemical reactions normally take place. Hence, equally, the material challenges from the optical windows naturally suggest the separation of infrared sensing and photochemical reactions. As mentioned earlier, one can place the infrared window adjacent to the photochemical window, and position them in sequence to achieve *in situ* IR measurement. This makes the reactor design less difficult. Only the selection of the most suitable material in the respective area needs to be considered. For the visible range, silica is one of the suitable options and the corresponding microfabrication technology is well established. As for the infrared range, $CaF_2$ should be the candidate since its application with microfluidic reactors has been realized [53, 106].

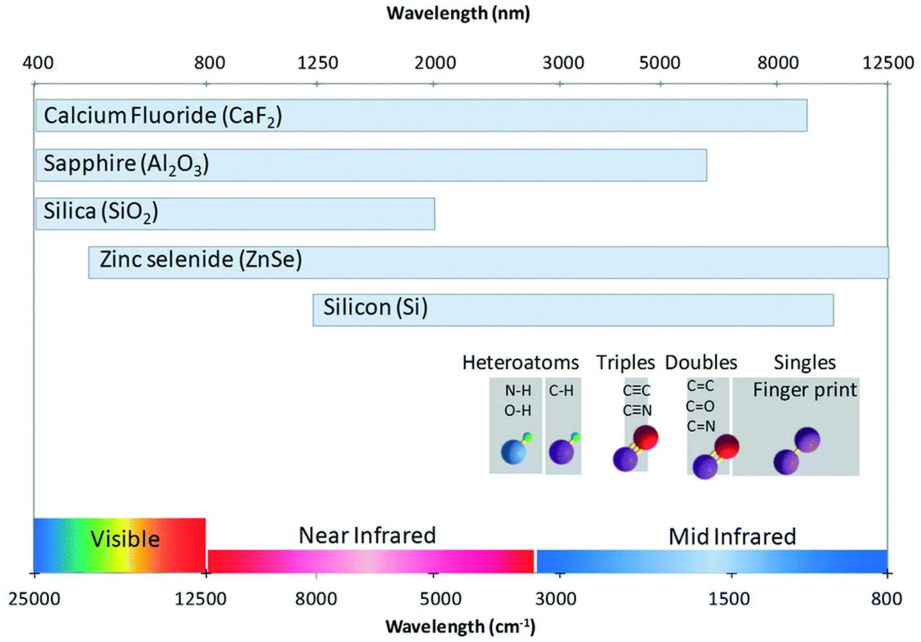

Figure 2-3 The transparent domain of frequently used materials in the visible-to-mid-infrared region and the dominant region of conventional chemical bond stretching spectra. (adapted from ref. [51] Copyright 2016 The Royal Society of Chemistry)

### 2.3.3 Lighting system

In the proposed *in situ* photoreactor, two different light sources had to be incorporated into the system, thus significantly increasing the complexity of the reactor design. In this respect, the lighting system needs to be split and considered separately. At the same time, colleagues from IMTEK at the University of Freiburg provided the matching miniaturized infrared detector and light source. Therefore, only the selection and construction of the lighting system for the chemical reaction section is considered here.

In most designs of photochemical microfluidic platforms, the light source is placed directly above the microchannel to ensure that the entire flow channel is irradiated [108-112]. There is, of course, a different design to this, in which the light source is incorporated directly into the microfluidic device and reflective material is introduced to ensure that the entire channel is illuminated [113]. The implementation of surface lighting rather than lateral lighting is more realistic. This could reduce the complexity of reactor design and increase the flexibility of system modification as the lighting system will exist independently of the photoreactor. The proposed lighting system consists of several high-power LEDs on a starboard (New Energy, XPEBRY-L1-0000-00R01-SB01) connected in series, powered by the same constant LED driver used in the CAP-μR, and positioned at a certain distance over the reacting window constructed of quartz glass. The chosen LED is considered to have a peak emission wavelength of 458 nm, radiant power of 625 mW at 350 mA forward current, and a broad viewing angle of 135 degrees as described by the supplier. The use of LEDs with different peak wavelengths in the CAP-μR and PHO-μR is intended for the subsequent validation of the generic chemical models obtained, as the conversion of a photoreaction is highly dependent on the light source used. These LEDs were placed in the designated positions on the stainless-steel board (SSB) using thermal adhesive. A 2060 V-type aluminum profile serving as a heat sink was fixed to the reverse side of the plate, where circulating cooling water can go through the drilled holes of the profile for efficient heat exchange (Fig. 2-4c). Besides, in order to make the lighting system as flexible as possible, a pulley system was integrated with the profile to construct a flexible lighting module that can be used for horizontal and vertical adjustment of the LED positions (Fig. 2-4a). By using 3D printing technology, suitable supports were customized as intermediaries between the pulleys and the aluminum profiles. Finally, the lighting module with a sandwich-like structure was constructed as shown in Figure 2-4b.

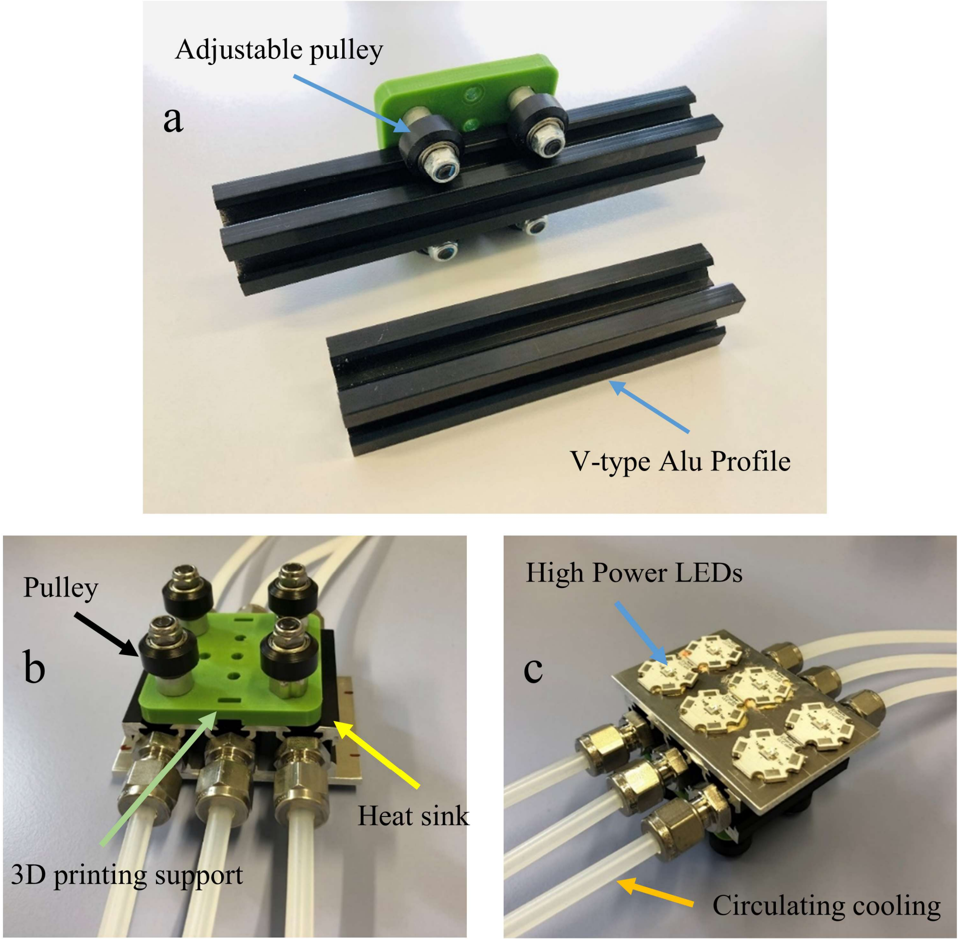

Figure 2-4 LED-based lighting module. a) A pulley system allowing the flexible positioning of the lighting module. b) The back view of the sandwich-structured LED lighting module. c) The front view of the sandwich-structured LED lighting module, 6 LEDs connected in series on (stainless-steel board) SSB.

### 2.3.4 Infrared cell design for the PHO-µR

In compliance with the previous work of Wang et al [77], the transmission mode of FTIR was used as the characterization method. The transmission mode has a plethora of advantages such as easy implementation, good spatial resolution, and capability of analyzing a width of areas. Nevertheless, technical bottlenecks make it difficult for miniaturized FTIR to cover the entire spectrial ranges for conventional characterization (400-4000 cm$^{-1}$, i.e. 2.5-25 µm). For this reason, the selected detection area needs to be split to meet the needs of different purposes, which depend on the vibrational frequencies of chemical moieties. For instance, the characteristic stretching vibration of amides, aldehydes, and azides lie in the frequency around 1650 cm$^{-1}$, 1730 cm$^{-1}$, and 2140 cm$^{-1}$, respectively [114]. In order to cover as much of the characterization region in the NIR to mid-IR as possible, the response regions of the mini-IR sensors were split into four parts with four different bandwidths, of which the decision was made with the help of the project team member from University of Freiburg. Therefore, the microfluidic photoreactor should also allocate functional areas that could embed four IR cells to correspond to the different bandwidths of the detectors. In this way, infrared mapping can be realized, which refers to multiple individual region spectra acquisition and further recombination to obtain a spatial image of the interrogated reaction stream circulating within the microchannel [51]. As the reaction and infrared cells are separated, infrared images at different residence times can be obtained by varying the flow rate, resulting in generating time- and spatially resolved infrared profiles. Such informative profiles can in turn show the progress of a photoreaction. By tuning different operating conditions, high throughput experimental screening can be achieved. Different from the earlier work of Wang [77], $CaF_2$ was employed to fabricate the infrared cell to couple the transmission FTIR analysis with the microfluidic system. The infrared cell was constructed from composite material, with the calcium fluoride glass placed above and below the milled stainless steel (SS) microfluidic channels, which are then sealed at the top and bottom with O-ring seals. To ensure that sufficient chemical information is obtained, the square sampling window had an area of approximately 25 $mm^2$. Moreover, the penetration depth of infrared sensing also matters. It is recommended that a shallow channel be used with a depth of less than ten micrometers to work in aqueous solutions [51]. However, this may lead to a high pressure drop inside the channel. High pressure drop can cause fatal experimental problems, not only regarding the compatibility of the reactants with the pressure in the channel (for gas-liquid reactions, the solubility of the gas varies with the operating pressure), but also regarding the critical pressure that the fabricated material can withstand (potential damage of the fragile $CaF_2$), the microfabrication process (sealing issues throughout the device), and the overall process handling (ensuring continuous injection). To ensure a consistent pressure drop within the microchannel and ease the microfabrication process, the depth of the infrared cell was initially designed to be the same (2 mm) as that of the microchannel. Possible, further adjustments to the depth were to be made based on experimental results. Alternatively, the issue could be addressed by increasing the sensitivity of the infrared detector. Fig. 2-5 shows the cross-sectional view of the infrared inspection cell design.

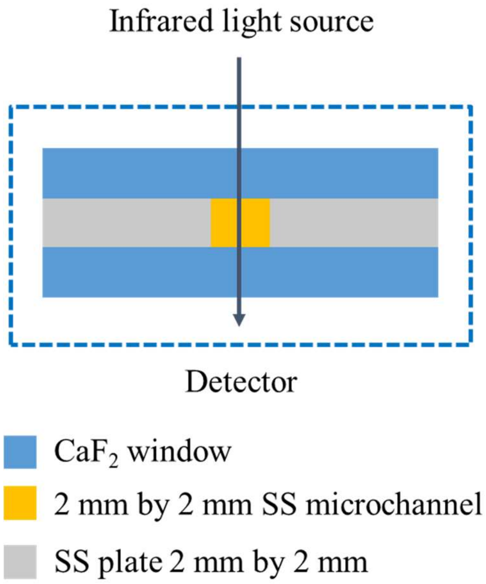

Figure 2-5 Cross-sectional section of an infrared cell

### 2.3.5 Final design of the PHO-µR and the microfluidic system for sensorless assembly

Based on the discussions in the previous two subsections, a novel microfluidic photoreactor (PHO-µR) containing four infrared detection regions and three optical reaction regions was finally designed and constructed. Fig. 2-6 shows the schematic view of the reactor design. Details on the dimensions of the optical glasses used can be found in Figure A1-A3 in the Appendix.

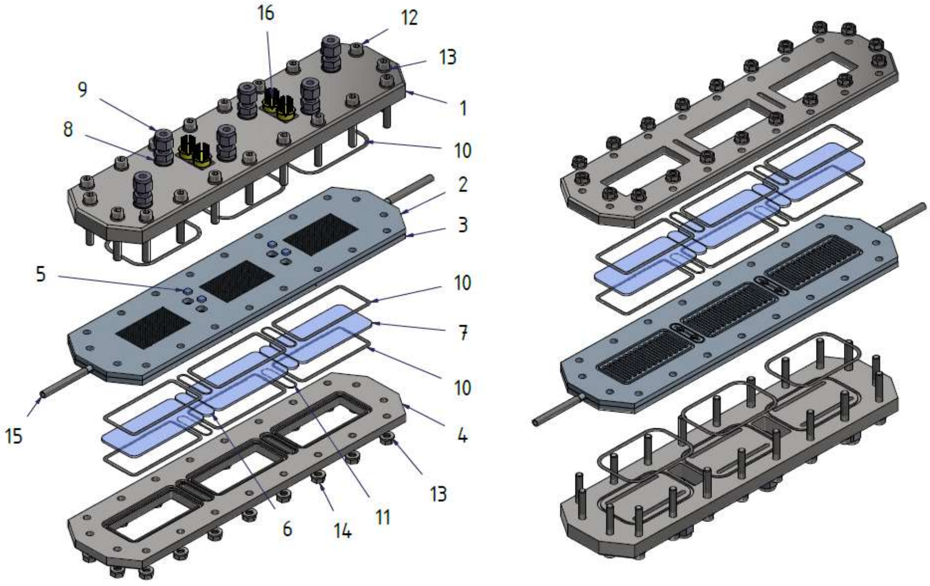

Figure 2-6 Schematical overview of the novel micro-photoreactor design (PHO-µR). Back view of the reactor (left) and top view (right). 1) Microreactor baseplate, 2) Temperature control plate, 3) Milled stainless-steel board (MSSB) meandering plate for photochemical reaction, 4) Cover plate, 5) IR-grade $CaF_2$ glass window positioned on the bottom of MSSB, 6) $CaF_2$ glass window on the top of MSSB, 7) SQ-1 quartz glass for visible light gathering and transmission, 8) RS sealing washer, 9) Swagelok screwdriver, 10 & 11) O-rings, 12) Hexagon socket screw, 13) Washer, 14) Hexagon nut, 15) 6 mm inlet or outlet pipe 16) infrared microsensor obtained from Freiburg

The reactor covers a big reaction volume of 8.61 mL, capable of collecting kinetic data and achieving considerable conversion no matter for fast or slow photoreactions. Different from a simple planar slab photoreactor containing narrow microchannels, the whole reaction region is divided into three identical zones in order to achieve continuous operations and process intensification through *in situ* infrared detection techniques. A sensing and monitoring zone is preserved between two subsequent reaction zones, which will incorporate two infrared sensors of different bandwidths. *In situ* infrared mapping is possible since the degree of photoreaction conversion varies due to different exposure times of the feed stream passing through the inspection area within the microchannel. Each reacting region consists of a meandering microfluidic channel with a cross-sectional dimension of 2 mm by 2 mm, a depth of 2 mm, and a total volume of 2.87 mL, made of reflective milled stainless-steel board (MSSB). On the backside of each microfluidic channel, a heat exchanger is incorporated. The meandering channel is covered by a 2 mm thick customized optical quartz glass window (SQ-1 grade, purchased from Hellma Optics). For the infrared inspection cell, two smaller $CaF_2$ windows (IR grade, purchased from Hellma Optics) are glued on the back side of the MSSB, while a larger and oval-shaped $CaF_2$ window is placed on the top. Special sensors are placed in a square recess in the back of the reactor. O-rings grooves surrounding the flow channel are used to properly seal the reactor with correspondingly sized O-rings. The peripheral hexagonal screws and nuts are used for securing the reactor. The fully assembled microreactor has reacting windows of 75 mm × 31 mm for each area. Fig. 2-7a-c shows the actually manufactured photoreactor and the assembled sensorless microfluidic system.

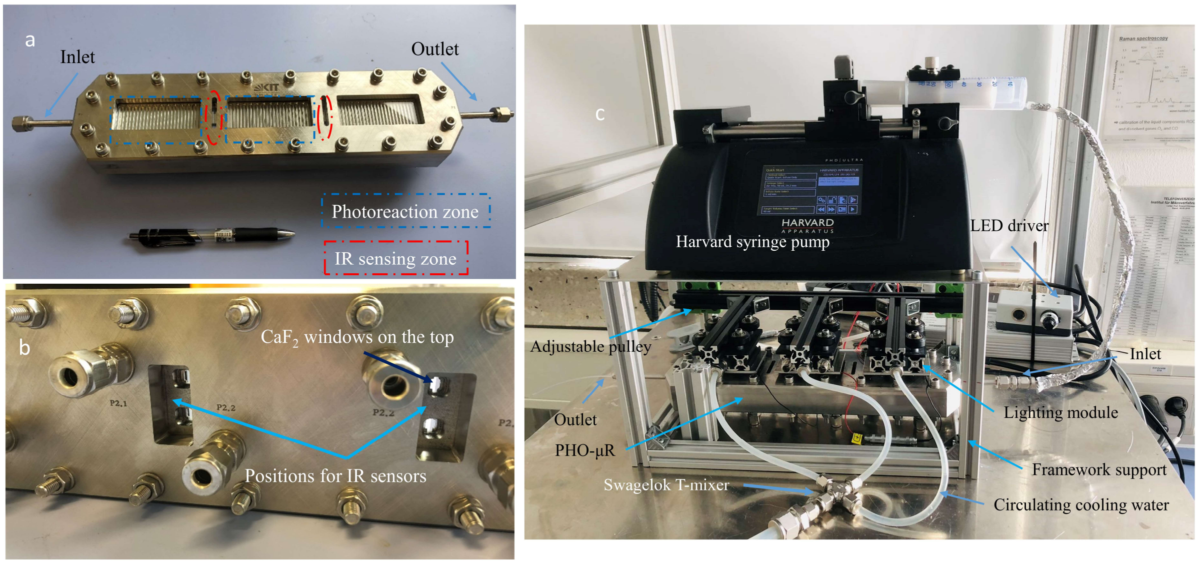

Figure 2-7 a) Front view of the PHO-μR. b) Back view of the PHO-μR. c) The assembled sensorless microfluidic system for photocatalysis.

## 2.4 Interim summary and conclusion

Two different, dimmable, and standardized photoreactor test benches were designed and built for kinetic experiments and subsequent in situ IR sensing applications. The construction of the CAP-μR follows the general principles of reactor design as mentioned in the literature, while the design of the PHO-μR is quite innovative. Due to the specific nature of the photoreaction, the PHO-μR is split into three reaction zones and also preserves infrared detection zones between subsequent reaction zones. The design of the PHO-μR takes into account both photoreaction and infrared detection, and the required materials for each region are discussed. The introduction of a pulley system makes the lighting module more flexible so that an arbitrary LED-to-reactor distance can be specified. In the subsequent chapters, the performance of the built reactors and their applications in photocatalytic reactions are highlighted.

# 3 Photon flux calibration of the CAP-μR and the PHO-μR

The photon flux is one of the key parameters of the photoreactor and also one of the most important criteria for evaluating the performance of the photoreactor. It implicitly indicates how many photons the photoreactor can receive over time. In the proposed photoreactors intended for application in homogeneous reactions, the photon flux calibration experiments should precede kinetic studies and reaction simulations. However, the actual incident photon fluxes of microfluidic reactors are hardly accessed by radiometers as the transmission effect needs to be considered. Alternatively, chemical actinometers have been developed and widely adopted for the determination of photon fluxes entering in microfluidic photocatalytic systems. These chemicals undergo photochemical conversions with a fixed quantum yield over a wide spectral range in relation to the number of photons absorbed [115, 116]. Both potassium ferrioxalate and Reinecke’s salt have been reported as practical actinometers for the determination of photon fluxes under visible light irradiation in microreactors [109, 117-119].

The actual photon flux reaching the photoreactor depends to a large extent on the nature of the material (e.g. light source, microchannel composition, reaction mixture, etc.) and the optical path (i.e., depending on whether reflection is included in the analytical model). Due to the different light paths inside the proposed photocatalytic test benches, the incident photon flux should be carefully calculated. Some fundamentals with respect to the photochemical engineering perspective have been reported, introducing how to solve radiative transport equations with the 1D analytical model. These cases include the use of the traditional Lambert-beer law for collimated light sources and the one-dimensional (1D) Monte Carlo method for diffuse light sources [95, 119]. Meanwhile, a revised model considering the reflection phenomenon has also been introduced [109]. In the CAP-μR, the FPA tubing can be regarded as having negligible transparent walls as it has good transparency and allows more than 95% of the visible light to pass through. In addition, reports have shown that the radiative transfer within similar capillary microchannels can be reduced to a one-dimensional problem and estimated using a constant irradiation profile over the whole cross-section of the capillary [117, 118, 120]. However, in the PHO-μR, the stainless steel microchannel is able to partially reflect the incident light, thereby enhancing the overall light intensity received by the photoreactor. In addition, due to the diffuse nature of LEDs, the actual light emission is closer to Lambertian [121]. Therefore, the collimated emission hypothesis is no longer valid and may lead to an overestimation of the actual photon flux of the reactor and introduce considerable errors in the post-processing [109]. In the following sections, the experimental results of the photon flux calibration were processed using the diffuse 1D Monte Carlo method according to the corresponding actual optical paths in the two test benches. In this way, the obtained results can be more realistic.

## 3.1 Light intensity determination in the CAP-μR

### 3.1.1 Photon flux calibration with potassium ferrioxalate

Potassium ferrioxalate, is recommended as one of the most commonly used and sensitive chemical actinometers in the UV and visible range (photoactive up to about 500 nm) for determining photon fluxes [116]. The stoichiometry of the ferrioxalate photolysis (Scheme 3-1) and quantum yields over a broad spectral domain were determined by Parker et. al in 1956 [122]. The complexation of ferrous ions produced with 1,10-phenanthroline results in a strong red mixture, whose strong absorbance appears at 510 nm. The conversion of photolysis can be back-calculated from the external calibration curve with known $Fe^{2+}$ concentration.

$$2[Fe(C_2O_4)_3]^{3-} \xrightarrow{hv} 2Fe(C_2O_4) + 3[C_2O_4]^{2-} + 2CO_2$$

Scheme 3-1 Ferrioxalate photolysis in sulfuric acid

The photolysis rate can be expressed in Eq. 3-1, using the 1D Monte Carlo analytical solution of the radiative transfer equation as recommended by Rochatte et al [119]. The absorption probability $p_{(\Omega)}$ can be further simplified in Eq. 3-2 for diffuse emission since the by-products in this experiment are absorbing at shorter wavelength, and only the reactant gives contribution to the photon absorption.

$$-\frac{dC_{act}}{dt} = \Phi \frac{q_\lambda}{V_R} \cdot p_{(\Omega)} \tag{3-1}$$

$$p_{(\Omega)} = \left[1 + exp\left(-C_{act}E_{act,\lambda}L\right)\left(C_{act}E_{act,\lambda}L - 1\right) + \left(C_{act}E_{act,\lambda}L\right)^2 Ei\left(-C_{act}E_{act,\lambda}L\right)\right] \tag{3-2}$$

where $C_{act}$ stands for the used actinometer concentration (mol·m$^{-3}$) and $E_{act,\lambda}$ stands for the Napierian absorption coefficient of the actinometer at wavelength of interest (L$^{-1}$·mol·cm$^{-1}$). $q_\lambda$ represents the amounts of photons absorbed in the reaction volume (einstein·s$^{-1}$), $L$ is the light path of the microreactor (m). $\Phi$ is the quantum yield at the wavelength of interest and $V_R$ is the volume of the microreactor (m$^3$). The value of $p_{(\Omega)}$ can be returned by MATLAB R2019a.

#### 3.1.1.1 The calibration curve of ferrous ions

The optical properties of an actinometer to be used should be determined before calculating the photon absorption probability $p_{(\Omega)}$. The calibration curve of ferrous ions (Fig. 3-1) was adapted from the work of Kant et al [123], using the same UV-Vis spectrometer (Agilent 8453) in the Institute for Micro Process Engineering (IMVT). The slope of the returned calibration curve is 11119.12675 L$^{-1}$·mol·cm$^{-1}$, representing the molar attenuation coefficient of the complexation product between the ferrous ion and 1,10-phenanthroline, whose value is close to those reported in the literature [115, 117, 124].

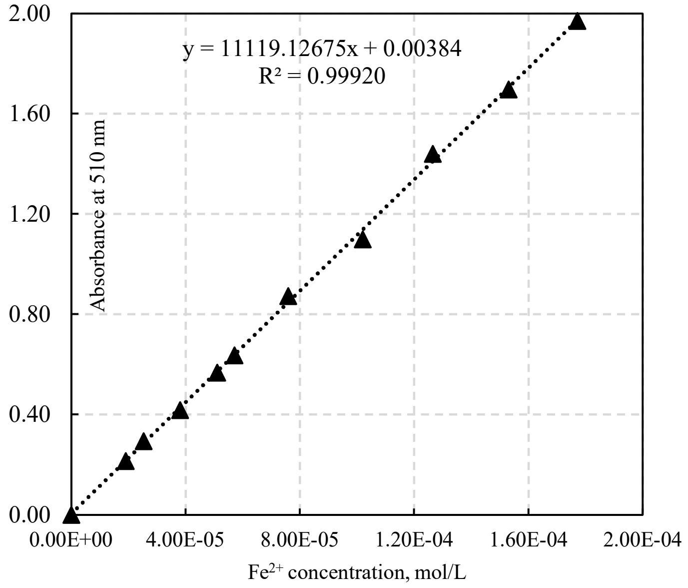

Figure 3-1 Calibration curve of ferrous ions (Fe$^{2+}$)

#### 3.1.1.2 Determination of the optical properties of potassium ferrioxalate

The optical properties regarding the Napierian absorption coefficient were obtained by dissolving potassium trioxalatoferrate(III) trihydrate $K_3[Fe(C_2O_4)_3 \cdot 3H_2O]$ in 0.05 M sulphuric acid to prepare a 0.1 mM solution. The quantum yields of a 6 mM ferrioxalate solution were procured from literature [116] and fitted using a 6th-order polynomial algorithm in Origin. An estimated quantum yield of 0.95 at 465 nm was found according to the orange dash-dot fitting light in Fig. 3-2. Meanwhile, the Napierian absorption coefficient of the used ferrioxalate was found to be 68.39 L·mol$^{-1}$·cm$^{-1}$ at 465 nm.

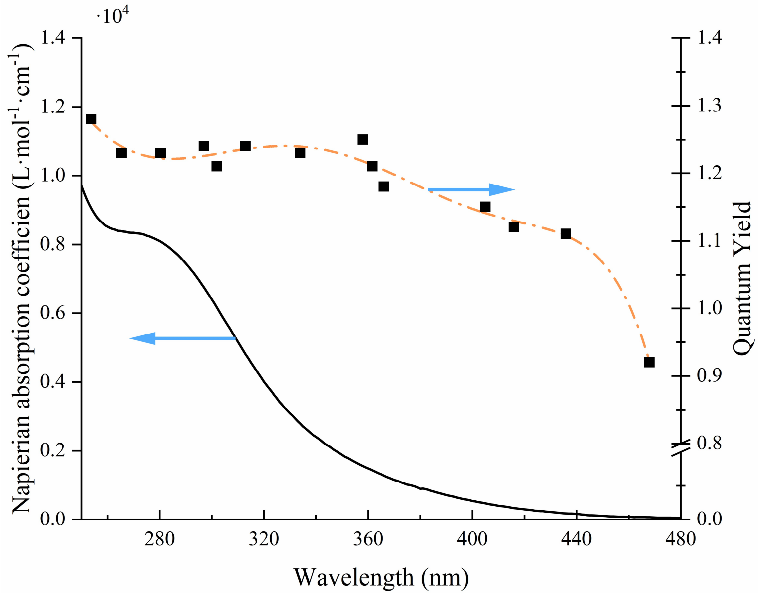

Figure 3-2 The plot of the Napierian absorption coefficient of $K_3[Fe(C_2O_4)_3{\cdot}3H_2O]$ (solid line, derived from 0.1 mM solution) and the estimated quantum yield of 0.006 M ferrioxalate over the investigated wavelength range (orange dash-dot line).

#### 3.1.1.3 Experimental procedure

The LEDs were turned on for at least 30 min prior to each experiment to make sure that the LED current was stable. Two axial cooling fans were running throughout the test. For the spectrophotometric test, a 6 mM ferrioxalate solution was used in the calibration experiment in order to get rid of clogging. For each experiment, approximately 0.2948 g of potassium trioxalatoferrate (III) trihydrate $K_3[Fe(C_2O_4)_3 \cdot 3H_2O]$ (0.6 mmol) was dissolved in 0.05 M $H_2SO_4$ and freshly prepared in a foil-covered 100 mL volumetric flask. The resulting solution was magnetically stirred for at least 30 min and preserved in a dark room to avoid its decomposition. The solution was drawn with a 100 mL Hamilton gas-tight syringe and mounted on a Harvard PHD Ultra 2000 syringe pump. The solution was then pumped through the CAP-μR (internal volume 4 mL) with set residence times of 12 s, 16 s, 20 s, 24 s and 28 s. After three times residence times elapsed (12 mL), the photolysis mixture was collected in a foil-covered dark brown vial and preserved in a dark cabinet. 1 mL ($V_1$) of irradiated samples was firstly diluted with deionized water in a 10 mL ($V_2$) volumetric flask. Then another 4 mL ($V_3$) of diluted samples were mixed with 3 mL of 0.1 wt% 1,10-phenanthroline solution, 5 mL of buffer solution (prepared with 60 mL 0.5 M sulphuric acid, 100 mL of 1 M sodium acetate) and 8 mL of water in a 20 mL ($V_4$) volumetric flasks. Finally, the mixtures were made up to 20 mL, and samples were stirred for at least 30 minutes to guarantee the completion of the complexation. The process was replicated three times in order to get good reproducibility. The absorbance of the resulting dark red solution was recorded at 510 nm. The diluting factor $D_F$ (Eq. 3-3) in these cases was 50. Then, conversion was calculated as indicated by Eq. 3-4.

$$D_F = \frac{V_2}{V_1}\frac{V_4}{V_3} \qquad 3\text{-}3$$

$$X = \frac{C_{\mathrm{Fe}^{2+}}}{C_{0\mathrm{Fe}^{3+}}} = \frac{1}{C_{0\mathrm{Fe}^{3+}}}\frac{A_{510}}{f_{\mathrm{Fe}^{2+}}}D_F \qquad 3\text{-}4$$

Where $A_{510}$ is the absorbance of the mixture, $f_{\mathrm{Fe}^{2+}}$ is the slope of the calibration curve, and $C_{0\mathrm{Fe}^{2+}}$ is the initial concentration of ferrioxalate solution, 6 mM.

#### 3.1.1.4 Calibrated light intensities in the CAP-μR using potassium ferrioxalate

The returned conversions were used to calculate the actual concentration of ferrioxalate in the capillary reactor. Photon flux calibrations were carried out under four different light intensities with 100%, 80%, 60%, and 40% power output of the LED driver. All of the experimental data were shown in Fig. 3-3. The initial photolysis rates under different intensities were returned by a 2nd order polynomial fitting in Origin as recommended by Shen et al [125]. The standard deviation shows good reproducibility of data.

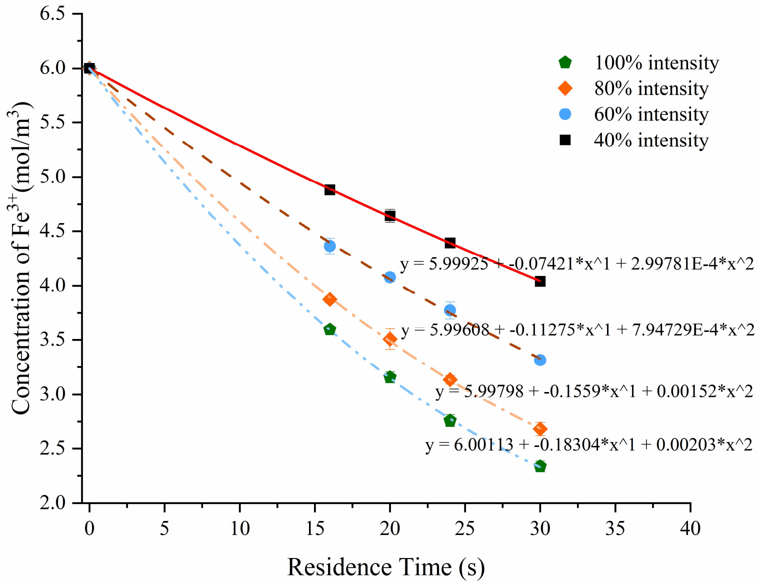

Figure 3-3 Concentration of the ferrioxalate actinometer versus residence time in the capillary microreactor CAP-μR at different light intensities using a 100W Meanwell constant current mode LED driver.

With the initial photolysis rate at hand, the incident radiation can be derived from Eq. 3-1. In this case, the light path $L$ is equal to its internal diameter of the PFA tubing (0.8 mm). The reactor's volume $V_R$ is equal to its internal volume (4 mL). As a result, the calculated $p_{(\Omega)}$ value of potassium ferrioxalate in the CAP-μR was found to be 0.0672. Therefore, the return values of $q_\lambda$ were found to be 1.15E-05, 9.77E-06, 7.07E-06, and 4.65E-06 einstein·$s^{-1}$ for 100%, 80%, 60%, and 40% power output, respectively. In order to convert the units into average surface light intensity $I$ (W/m$^2$), the Einstein-Planck equation was adopted for the unit conversion, which denotes how much energy is conveyed by one photon. The transformation is shown in Eq. 3-5 and 3-6.

$$E_\lambda = \frac{hc}{\lambda} \tag{3-5}$$

$$I = \frac{q_\lambda N_A E_\lambda}{A_{cap}} \tag{3-6}$$

Where $h$ is Planck's constant ($6.63\times10^{-34}$ J·s), $c$ is the speed of light ($3\times10^8$ m/s), and λ is the maximum emitted wavelength of the used LED (465 nm), $N_A$ is Avogadro's number ($6.02\times10^{23}$), $A_{cap}$ is the irradiated area of the CAP-μR. Table 3-1 summarizes the resulting average surface light intensities received by the reactor, ranging from 59.99 W/m$^2$ to 147.98 W/m$^2$. All of these values remain within the weak photon absorption region [87].

Table 3-1 Calibrated light intensities in the CAP-μR using potassium ferrioxalate

| Power output | Initial slope | $p_{(\Omega)}$ | $q_\lambda$ (einstein·s$^{-1}$) | light intensity $I$ (W/m$^2$) |
|---|---|---|---|---|
| 100% | -0.18304 | 0.0672 | 1.15E-05 | 147.98 |
| 80% | -0.1559 | 0.0672 | 9.77E-06 | 126.03 |
| 60% | -0.11275 | 0.0672 | 7.07E-06 | 91.15 |
| 40% | -0.07421 | 0.0672 | 4.65E-06 | 59.99 |

### 3.1.2 Photon flux calibration with Reinecke's salt in the CAP-µR

As recommended by Rochatte et al, Reinecke's salt was also adopted in the calibration experiment [119]. Solving the analytical solution of the 1D Monte Carlo method by replacing Reinecke's salt with potassium ferrioxalate has never been reported before. Therefore, experiments to calibrate the photon flux inside the CAP-µR using the Reinecke's salt were carried out to confirm the correctness of the results obtained in section 3.1.1. The photodissociation of the Reinecke's salt can be expressed in the following scheme:

$$[Cr(NH_3)_2(NCS)_4]^- + H_2O \longrightarrow [Cr(NH_3)_2(NCS)_3H_2O] + NCS^-$$

$$[Cr(NH_3)_2(NCS)_3H_2O] + H_2O \longrightarrow [Cr(NH_3)_2(NCS)_2(H_2O)_2]^+ + NCS^-$$

Scheme 3-2 Photodissocation mechanism of Reinecke's salt

One should note that the absorption of the by-product, $[Cr(NH_3)_2(NCS)_3(H_2O)]$, has the same order of magnitude as the reactant. In addition, it was demonstrated that under acidic conditions, the by-products could further hydrolyze with water in a subsequent step [126]. It is necessary to ensure that the first reaction in Scheme 3-2 is dominant. It is therefore recommended that the photoconversion should be below 30% in order to get good linearity from the fitting plot [119]. When taking the initial rate of photodissociation into consideration, the rate expression is similar to Eq. 3-2, because the contribution of the by-product is negligible, and the model is therefore simplified. The only thing that needs to be replaced in the equation is the optical properties of the used actinometer.

#### 3.1.2.1 Optical properties of Reinecke's salt

The optical properties of Reinecke's salt were procured from Rochatte et al [119]. The Napierian absorption coefficient at different wavelengths was fitted with a 6-order polynomial in Origin (Fig. 3-4). A value of 9.96 $m^2 \cdot mol^{-1}$ was found at 465 nm. A reference quantum yield of 0.30 at 465 nm was adopted according to Wegner et al [127].

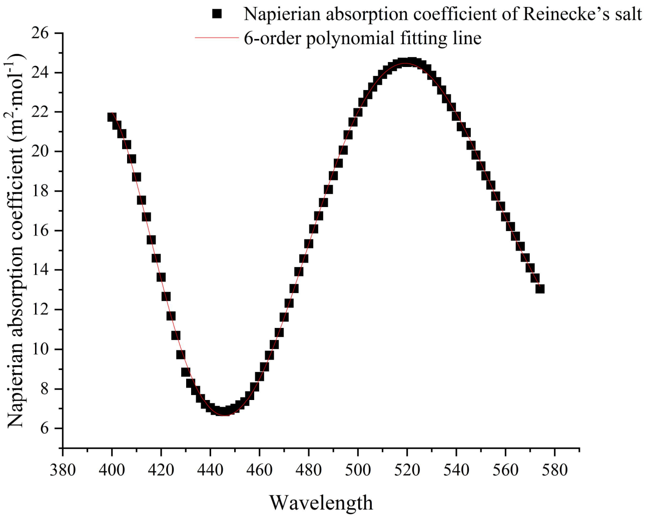

Figure 3-4 Napierian absorption coefficient of Reinecke's salt at different wavelengths. Scatter points were procured from ref. [119].

### 3.1.2.2 Experimental procedure

The LEDs were turned on for at least 30 min prior to each experiment to make sure that the LED current was stable. Two axial cooling fans were running throughout the test. For the spectrophotometric test, the preparation of the actinometer solution was done according to Radjagobalou et al in a dark room [128]. Reinecke's salt monohydrate was purchased from VWR (CAS: 13573-17-6; purity ≥93.0%; 354,41g/mol). The first step is permuting $NH^{4+}$ by $K^+$ ions. For this, a suitable quantity of Reinecke's salt was dissolved in a solution of 0.1 mol·L$^{-1}$ potassium hydroxide to produce a 15 mM solution at room temperature. The obtained pH after permutation was close to 13 as indicated by the pH paper. The solution was stirred mechanically using a glass rod to complete ammonia stripping. Next, a few drops of concentrated sulphuric acid (98%) were slowly added to the solution, and the pH was then adjusted to a range of 4-5. Another iron salt solution was prepared with a composition of 0.1 mol · L$^{-1}$ of Iron(III) nitrate nonahydrate $Fe(NO_3)_3·9H_2O$ in 0.5 mol·L$^{-1}$ of nitric acid $HNO_3$ (63%). All of these solutions were freshly prepared each time and stored in a dark cabinet prior to spectrophotometric tests. The prepared solution was drawn with a 100 mL Hamilton gas-tight syringe and mounted on a Harvard PHD Ultra 2000 syringe pump, which pumped the solution through the CAP-μR (internal volume 4 mL) with set residence times ranging between 12 and 32 seconds depending on the current output of the LED driver. The tested power output here was the same as stated before. After three residence times elapsed (corresponding to a volume of 12 mL), the mixture was collected in a foil-covered dark brown vial and preserved in a dark cabinet. 1 mL of irradiated samples was first transferred by a pipette in a 20 mL volumetric flask. Then another 3 mL of ferric solution was added and finally distilled water to make the solution up to 20 mL. Due to the non-negligible thermal pathway, i.e. Reinecke salts can react slowly with water, samples were stirred only for 5 minutes and quickly transferred to a cuvette to complete the spectroscopic test. The final pH value of the analyte was close to 1. The absorbance at 450 nm was recorded with an Agilent 8453 UV-Vis spectrometer to determine the concentration of released thiocyanate ions. The dilution factor in these cases was 20. The process was replicated three times in order to check for reproducibility. Finally, the concentration of $NCS^-$ was determined by using Eq. 3-7.

$$C_{NCS^-} = \frac{D_F}{L}\frac{A_{450}}{\varepsilon_{[Fe(NCS)]^{2+}}} \tag{3-7}$$

Where $L$ is the light path of the microreactor (0.8 mm); $\varepsilon_{[Fe(NCS)]^{2+}}$ ($L \cdot mol^{-1} \cdot cm^{-1}$) is the decadic molar absorption coefficient of $[Fe(NCS)]^{2+}$ measured at 450 nm. A reference value of 3400 $L \cdot mol^{-1} \cdot cm^{-1}$ was adopted in this study according to the literature [128, 129]. $A_{450}$ is the absorbance value at 450 nm.

### 3.1.2.3 Calibrated light intensities in the CAP-μR using Reinecke's salt

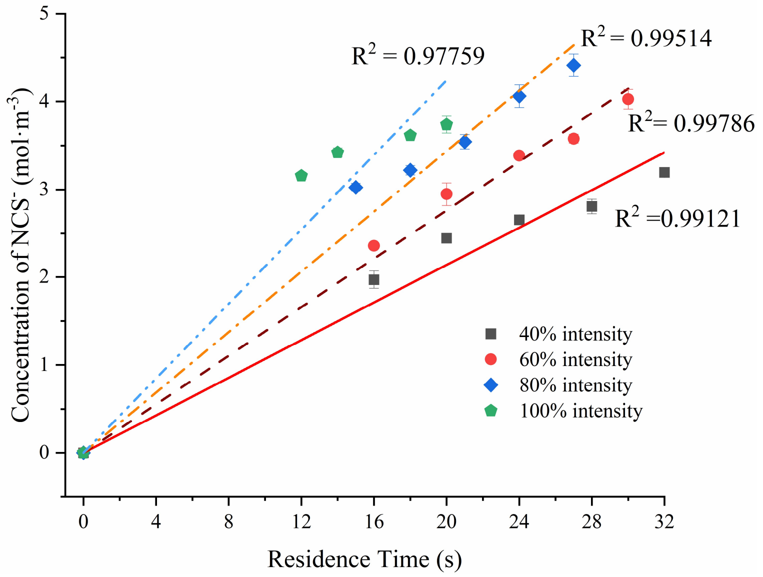

Figure 3-5 Plots of the concentration of $NCS^-$ versus residence time in the capillary microreactor at different light intensities using a 100W Meanwell constant current mode LED driver.

Fig. 3-5 summarizes the calibration results using Reinecke's salt. In fact, the linearity of the fitting line is not good under the strongest power output (100%) due to a higher conversion (>30%). Some deviations that appeared are caused by rapid hydrolysis during the post-processing. This is detrimental to the results since the second step in Scheme 3-

2 also contributes to the formation of $NCS^-$, which may result in erroneous evaluation. Good linearity can be observed with diminished power output ( ≤ 80%). Further prolonging the residence time under this light intensity produces strong fluctuations of data, resulting in poor reproducibility, which implies the further hydrolysis of the by-product is dominant. Overall, the standard deviation shows good reproducibility of the collected data. However, residence times of these spectroscopic tests should be carefully designed to suppress further hydrolysis. With the initial dissociation rate at hand, the incident photon fluxes under different light intensities were calculated with the same equations (Eq 3-2 and Eq. 3-6). The calculated $p_{(\Omega)}$ value of Reinecke's salt was found to be 0.2423 in MATLAB R2019a. Table 3-2 summarizes the resulting average surface light intensities received by the CAP-μR, ranging from 75.59 W/m$^2$ to 149.91 W/m$^2$.

Table 3-2 Calibrated light intensities in the CAP-μR using Reinecke's salt

| Power output | Initial slope | $\boldsymbol{p}_{(\Omega)}$ | $\boldsymbol{q}_{\lambda}$ (einstein·s$^{-1}$) | light intensity $\boldsymbol{I}$ (W/m$^2$) |
|---|---|---|---|---|
| 100% | 0.21203 | 0.2423 | 1.16E-05 | 149.91 |
| 80% | 0.17182 | 0.2423 | 9.42E-06 | 121.48 |
| 60% | 0.13818 | 0.2423 | 7.58E-06 | 97.69 |
| 40% | 0.10692 | 0.2423 | 5.86E-06 | 75.59 |

### 3.1.3 Comparison of the results of the two different actinometers

The results of the mean incident photon fluxes from the two different chemical actinometers are summarized in Table 3-3. From this, it is clear that there is only a small difference in the 40% output results, while the rest show almost the same value. However, one should note that the rapid hydrolysis of Reinecke's salt during the post-processing may become a problematic issue especially if the conversion is high. Using a diluted concentration of ferrioxalate solution (6 mM) allows to get rid of clogging in the PFA capillary, which makes the results more stable and reliable in comparison. Moreover, the standard deviation of the experimental values obtained from potassium ferrioxalate was smaller than those from Reinecke's salt, implying less error introduced. Therefore, the results of potassium ferrioxalate were ultimately chosen as the standard. Hence, the correctness of replacing Reinecke's salt with potassium ferrioxalate in the 1D Monte Carlo analysis to calculate the probability of light absorption has been confirmed.

Table 3-3 Determining the mean incident photon flux using ferrioxalate actinometer and Reinecke's salt actinometer

| Radiation Power | Initial slope | Results from ferrioxalate (einstein.s$^{-1}$) | Initial slope | Results from Reinecke's salt (einstein.s$^{-1}$) |
|---|---|---|---|---|
| 40% | -0.07421 | 4.65E-06 | 0.10692 | 5.86E-06 |
| 60% | -0.11275 | 7.07E-06 | 0.13818 | 7.58E-06 |
| 80% | -0.1559 | 9.77E-06 | 0.17182 | 9.42E-06 |
| 100% | -0.18304 | 1.15E-05 | 0.21203 | 1.16E-05 |

## 3.2 Light intensity determination in the PHO-μR

The optimum LED configuration of the PHO-μR is yet to be determined. As a preliminary test, a distance of 8 mm was set between the LEDs and the microchannel in the PHO-μR, which is the minimum physical distance allowed due to the geometric limitation of the microreactor itself. According to the inverse square law of light, this gives the maximum incident radiation reaching the reactor [87]. A 6 LED board (458 nm) shown in Fig. 2-4c was employed in the calibration experiments. Only one of the reaction regions was tested because the reactor has three identical zones. The rest of them were carefully covered with aluminum foil to avoid unnecessary light exposure. Potassium ferrioxalate was selected as the chemical actinometer, and the light intensity in the PHO-μR was determined using a similar procedure as described in section 3.1.1. Due to the different peak emission wavelengths of the LEDs being used in two test rigs, the optical properties of potassium ferrioxalate should be calibrated from the UV-Vis spectrum accordingly.

### 3.2.1 Light path description

The path of light is related to the optical properties of the material. In contrast to some polymer materials that have good transmittance, such as FEP and PFA, light is partially reflected if an opaque material with an emissivity of less than 1 is used. As a result, the actual light path is altered. This is the time when the contribution of the reflection has to be taken into account. Stainless steel is a reflective material with an emissivity of less than 1 [130]. This is the case with the PHO-μR's stainless steel sculpted meandering microchannels. Therefore, the actual path of the light inside the PHO-μR should be comprehensively analyzed prior to the spectrophotometric experiments. Rochatte et al. did not take reflections into consideration in their analytical 1D Monte Carlo model. Luckily, Radjagobalou and co-workers have extended the scope of the model and applied it to a reflective material. They have demonstrated that part of the light can be reflected in an engraved channel in an aluminum flat plate where the FEP tubing was placed [109]. In their model, the reflectance of stainless steel is also included and added as the sink term at the right side of the rate equation. This revised 1D Monte Carlo method allows the reflection effects to be addressed in a photoreactor. The case is very close to the microfluidic photoreactor built in this work. Therefore, this modified model is adopted to properly describe the path of light in the PHO-μR.

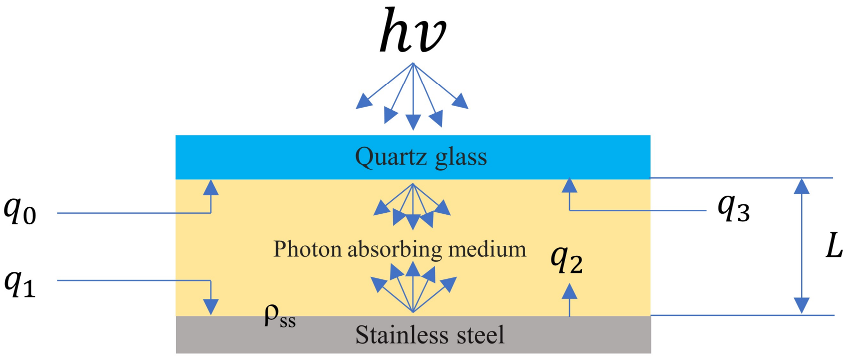

Scheme 3-3 Schematic representation of the light path inside the PHO-μR for diffuse incidence. The optical path length $L$ is equal to the channel depth of the PHO-μR.

Scheme 3-3 illustrates the actual path of the light inside the PHO-μR. $q_0$ (einstein·s$^{-1}$) represents the mean internal incident photon flux reaching the microreactor. $q_1$ (einstein·s$^{-1}$) represents that part of the mean incident photon flux that was not absorbed by the reaction medium and thus arrived at the stainless-steel surface. $q_2$ (einstein·s$^{-1}$) stands for the mean incident photon flux reflected by the stainless steel. $q_3$ (einstein·s$^{-1}$) stands for the mean reflected photon flux that was not absorbed by the reaction medium and thus reached the internal surface of the quartz glass. $L$ is the optical path length corresponding to the microchannel's depth. $\rho_{ss}$ is the reflection coefficient between the interface of the reacting medium and the stainless steel plate, which can be calculated by Eq. 3-11 according to Howell et al [131]. The revised model of potassium ferrioxalate photoconversion can be expressed in Eq. 3-8. $p_{(\Omega)}$ is the absorption probability of the used actinometer, representing the fraction of light absorption. $q_{(\Omega)}$ is the transmission probability, representing the fraction of light transmission. The summation of $q_0$ and $q_2$ stands for the mean volumetric photon absorption $q_\lambda$ over the microreactor.

$$-\frac{dC_{Fe^{2+}}}{dt} = \Phi\frac{q_0}{V_R}\cdot p_{(\Omega)}(1+q_{(\Omega)}\rho_{ss}) \qquad 3\text{-}8$$

$$p_{(\Omega)} = \left[1 + exp\left(-C_{act}E_{act,\lambda}L\right)\left(C_{act}E_{act,\lambda}L - 1\right) + \left(C_{act}E_{act,\lambda}L\right)^2 Ei\left(-C_{act}E_{act,\lambda}L\right)\right] \qquad 3\text{-}9$$

$$q_{(\Omega)} = 1 - p_{(\Omega)} \qquad 3\text{-}10$$

$$\rho_{ss} = 2\int_0^{\frac{\pi}{2}} \rho_{ss}(\theta)\, sin(\theta)\, cos(\theta)\, .\, d\theta \qquad 3\text{-}11$$

$$q_1 = q_0 q_{(\Omega)} \qquad 3\text{-}12$$

$$q_2 = q_1\rho_{ss} = q_0 q_{(\Omega)}\rho_{ss} \qquad 3\text{-}13$$

$$q_3 = q_2 q_{(\Omega)} = q_0 {q_{(\Omega)}}^2\rho_{ss} \qquad 3\text{-}14$$

$$q_\lambda = q_0 + q_2 \qquad 3\text{-}15$$

### 3.2.2 Experimental procedure

The LEDs were turned on for at least 30 min prior to each experiment to make sure that the LED current was stable. The liquid circulating cooler with a set cooling bath temperature of 15 degree Celsius was operated the whole time during the test. The cooling liquid was continuously flown through the heat sink of the LED board, as it allows sufficient surface-to-surface heat conduction with the LEDs. This action can ensure that the high-power LEDs are free from spectrum shift. For the spectrophotometric test, suitable quantities of potassium trioxalatoferrate(III) trihydrate $K_3[Fe(C_2O_4)_3 \cdot 3H_2O]$ (around 0.6 mmol) were dissolved in 0.05 M $H_2SO_4$ and freshly prepared in a foil-covered 100 mL volumetric flask to prepare a 6 mM solution. The resulting solution was magnetically stirred for at least 30 min and preserved in a dark room to avoid its decomposition. The solution was drawn with a 100 mL Hamilton gas-tight syringe and mounted on a Harvard PHD Ultra 2000 syringe pump. The solution was then pumped through the whole PHO-μR (illuminating volume of 2.87 mL in the case) with set residence times of 8 s, 10 s, 12 s, 14 s and 16 s. After three residence times elapsed (9 mL liquid volume in this case), the photolysis mixture was collected in a foil-covered dark brown vial and preserved in a dark cabinet. 0.5 mL of sample was mixed with 3 mL of 0.1 wt% 1,10-phenanthroline solution, 5 mL of buffer solution (prepared with 60 mL 0.5 M sulphuric acid, 100 mL of 1 M sodium acetate) and finally mad up to 20 mL with distilled water in a 20 mL volumetric flask. The diluting factor in the test was 40. Samples were stirred for 30 minutes to guarantee the completion of the complexation. The process was replicated three times in order to check for reproducibility. The absorbance of the resulting red solution was recorded at 510 nm. As illustrated before, a seond-order polynomial fitting was used in Origin to find the initial slope. The returned data under different light intensities are shown in Figure 3-6.

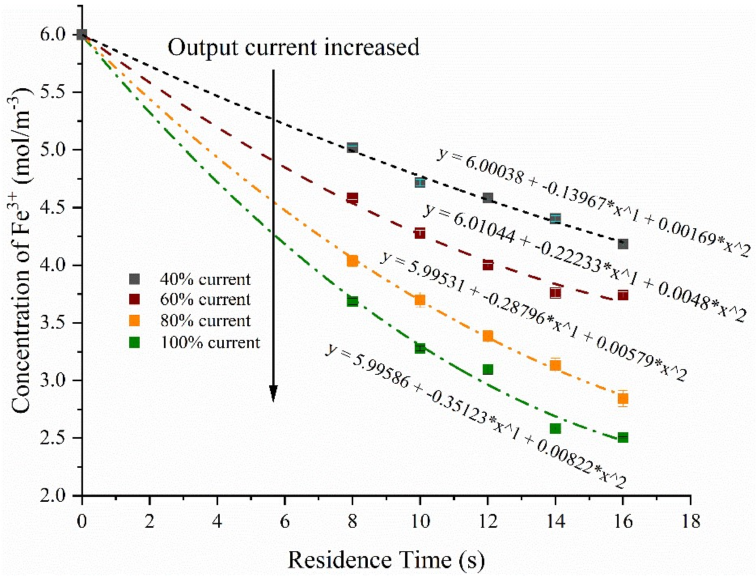

Figure 3-6 Plots of the concentration of the ferrioxalate actinometer versus residence time in the meandering microreactor PHO-μR at different light intensities using a 100W Meanwell constant current mode LED driver.

With the initial photolysis rate at hand, the mean volumetric photon absorption $q_\lambda$ can be derived from Eq. 3-15. In this case, the Napierian absorption coefficient of a value of 78.05 L·mol$^{-1}$·cm$^{-1}$ and an estimated quantum yield of 1.02 were found at 458 nm from Fig. 3-2. Meanwhile, the optical path length in the PHO-μR corresponds to the microchannel's depth (2 mm). The volume $V_R$ is equal to the illuminated volume (2.87 mL). As a result, the value of $p_{(\Omega)}$ was found to be 0.1916 in the PHO-μR. Therefore, the return values of $q_\lambda$ were found to be 5.16E-06, 4.23E-06, 3.27E-06, and 2.05E-06 einstein·s$^{-1}$ for 100%, 80%, 60%, and 40% power output, respectively. Table 3-4 summarizes the resulting average surface light intensities received by the microreactor, ranging from 374.30 W/m$^2$ to 941.27 W/m$^2$. Apparently, these values exceed the weak photon absorption region [87].

Table 3-4 Calibrated light intensities in the PHO-μR using potassium ferrioxalate

| Power output | Initial slope | $p_{(\Omega)}$ | $q_\lambda$ (einstein·s$^{-1}$) | light intensity $I$ (W/m$^2$) |
|---|---|---|---|---|
| 100% | -0.35123 | 0.1916 | 5.16E-06 | 941.27 |
| 80% | -0.28796 | 0.1916 | 4.23E-06 | 771.71 |
| 60% | -0.22233 | 0.1916 | 3.27E-06 | 595.83 |
| 40% | -0.13967 | 0.1916 | 2.05E-06 | 374.30 |

## 3.3 Comparsion between the CAP-μR and the PHO-μR

Some parameters are of great importance in the evaluation of the photoreactor. In this study, four of the most important parameters with respect to optical path length, absorption probability, illuminated area, and strongest light intensity were chosen to compare the performance of the CAP-μR and PHO-μR. Table 3-5 summarzies the results of these parameters for the two different test benches. From this, it is clear that the increase of the optical path length is beneficial to the absorption probability $p_{(\Omega)}$. The effect is more obvious when the optical path length changed from 0.8 mm to 2 mm as the $p_{(\Omega)}$ value increases proportionally to the optical path length. For the CAP-μR, the illuminated area is an order of magnitude larger than for the PHO-μR, which endows the CAP-μR a more uniform light distribution but a smaller average surface light intensity. In contrast, the average surface light intensity of the PHO-μR is 6.3 times higher than that of the CAP-μR. The higher the average surface light intensity inside the photoreactor, the better it is for increasing the space time yield of the reaction and thus for reducing the production time. From this point of view, the PHO-μR is preferable for process intensification.

Table 3-5 The comparison of several key parameters between the CAP-μR and the PHO-μR

| Photoreactor | Optical Path (mm) | Absorption probability $\boldsymbol{p}_{(\boldsymbol{\Omega})}$ | Illuminating area (mm$^2$) | Strongest surface intensity (W/m$^2$) |
|---|---|---|---|---|
| **CAP-μR** | 0.8 | 0.0672 | 19999.881 | 147.98 |
| **PHO-μR** | 2 | 0.1916 | 1435.34 | 941.27 |

## 3.4 Interim summary and conclusion

In this chapter, two different and common chemical actinometers, potassium ferrioxalate and Reinecke's salt were used for the photon flux calibration experiments. Instead of using classical Lambert-beer law describing collimated emission, the 1D Monte Carlo method was employed to calculate the absorption probability $p_{(\Omega)}$ since the LED emission is closer to Lambertian distribution, thus deriving the average surface light intensity arriving at the microreactors. The returned results between two different actinometers in the CAP-μR were almost the same, demonstrating this kind of analytical method can also be applied to potassium ferrioxalate. Because of the smaller standard deviation of the results obtained with the ferrioxalate solution, this actinometer was further used to calibrate the light intensity in the PHO-μR. The contribution of the reflection in the PHO-μR was included in the analytical model, as the optical light path in the microreactor is altered. By comparison, one finds that the strongest average surface light intensity in the CAP-μR still remains in the weak absorption region. However, all of the tested light intensities in the PHO-μR exceed this threshold, indicating stronger irradiance level. The volume-to-surface ratio of the CAP-μR is much bigger than that of the PHO-μR, resulting in a smaller but more homogeneous irradiation. Meanwhile, the spotlight effect is much better in the PHO-μR, even though the illuminated area is much smaller compared to the CAP-μR, but the average surface light intensity received is several times higher than that of the CAP-μR. Knowing these properties for the two different photoreactors is helpful for the modelling of the photoreaction kinetics in the subsequent work.

# 4 Model reaction to achieve a proof-of concept of *in situ* sensing in microchannel photoreactors

The indole skeleton is one of the most widely distributed heterocycles and is present in many natural products, biologically active compounds, and pharmaceuticals. Its derivatives express diverse benefits such as anticancer, antifungal, antimicrobial, and anti-inflammatory activity and represent important building blocks often used for the preparation of other related heterocycles [132, 133]. Conventional synthetic procedures for indole synthesis often involve harsh reaction conditions and suffer from side reactions, producing substantial waste [134, 135]. As a consequence, the development of new methodologies employing facile, eco-friendly, and atom-economical reactions is considered imperative [136]. The production of functionalized indoles and related heterocycles using a photocatalytic protocol is highly advocated for its advantages of mild operating conditions and reduced reagent consumption [137]. Meanwhile, the direct photo conversion from simple molecular structures to complex indole structures opens up a new route to bypass the laborious preparation and purification processes, making it one of the most suitable options for the preparation of highly functionalized indole derivatives [138-140]. However, most of these applications remain in traditional batch synthesis, and there is a gap in the area of flow photochemistry.

On the other hand, the rapidly developing micro technology in flow chemistry has great potential in accelerating indole photosynthesis as it is able to achieve improved mixing, more efficient mass and heat transport, and uniform illumination conditions, thereby exponentially reducing the completion period, together with satisfactory conversion [141]. The integration of microreactor technologies with photochemical synthesis also serves as a powerful tool for the estimation of reaction kinetics and for scale-up of photoreactions, allowing intrinsic rate constants to be extracted from experimental results both in homogeneous and heterogeneous photocatalysis [125, 142]. The parameters derived from kinetic studies can be employed for the assessment of process intensification and the establishment of optimum operating conditions in flow. Nevertheless, most of the photochemical reactions towards indoles are reported for the synthesis in batch operations, and examples of their synthesis under flow conditions are still scarce, let alone the associated chemical kinetic studies. The reaction kinetics do not only allow conclusions on possible reaction mechanisms, which may lead to a better understanding of the process, but also help to optimize the operating conditions of the process and to identify critical factors in process control. The contributions of this part can bridge between macroscopic and microscopic perspectives in photocatalytic research and help to propose a plausible reaction mechanism. Recently, a novel photochemical reaction involving a visible-light-induced 1,3-acyl shift to produce highly functionalized indole derivatives (Scheme 4-1) was introduced by project team member from IBCS-FMS, KIT [143]. Fluorine-labeled acylamide precursors are able to generate 3-acyl indole skeletons with the help of the iridium photocatalyst under blue light irradiation. However, understanding of the photocatalytic indole synthesis from a reaction engineering perspective is still limited.

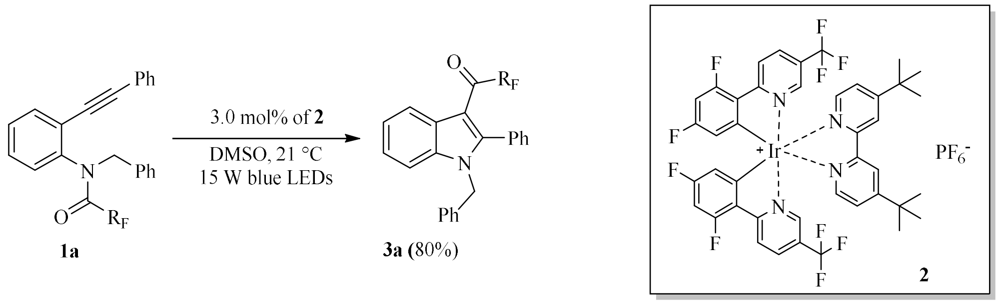

Scheme 4-1 Photochemical cyclization of F-tagged o-alkynylated N-alkyl-N-acylamides to 3-acylindoles [143].

Within the framework of the ProMiSe project, the findings in organic photoredox reaction specified the concrete objectives of this study and the research content below was developed with the help of the project team member Helena Simek Tosino. In this chapter, one of the probe reactions for this application was used to extract the photoreaction's kinetic parameters and to compare the performance of the two different test benches (CAP-μR and PHO-μR). In addition, several dimensionless parameters ($Pe$, and $Da_I$, as well as $Da_{II}$) were employed to evaluate the influence of operating parameters on the photochemical performance in the capillary microreactor, and a simplified reactor model was proposed in order to get the intrinsic rate constant independent of the reactor geometry and the incident photon flux. In addition, a kinetic model was developed and employed in CFD simulations (COMSOL) to reproduce the process observed in the two different test benches. The simulations in this section start with the most straightforward conditions (i.e., uniform illumination in the CAP-μR), and then extend to a more complex case, (i.e., employing the obtained intrinsic rate constants from kinetic evaluation as inputs and considering the radiation field distribution over the microfluidic channel in the PHO-μR). The proposed model is transferred between two test benches and validated with experimental results. The interpretation of these observations allowed the identification of the critical factors affecting the optimization of the reaction and the intensification of the process, and this way sets ground for scaling up the technology.

## 4.1 Kinetic study in the CAP-µR

Initially, the kinetic study of photocyclization was performed in the CAP-µR to collect the kinetic parameters, which includes part of results that have been published [144]. The photoconversion of F-tagged o-alkynylated N-alkyl-N-acylamide **1a** (25 mM solution in acetone) to the indole product **3a** was chosen as the probe reaction (Scheme 4-2), and a reported optimal catalyst loading of 3 mol% Ir[dF(CF$_3$)ppy]$_2$(dtbpy)(PF$_6$) **2** was employed according to the condition screening in batch synthesis. The starting material **1a** N-benzyl-2,2,3,3,4,4,5,5,6,6,7,7,8,8,8-pentadecafluoro-N-(2-(phenylethynyl)phenyl)octanamide was prepared and purified by the methods that had been reported in detail somewhere else [143]. The Iridium photocatalyst Ir[dF(CF$_3$)ppy]$_2$(dtbpy)(PF$_6$) **2** was purchased from Merck and used without further purification. Dry acetone was purchased from VWR and used under inert atmosphere each time. To be as precise as possible in determining the yield, acetone was used as solvent since it could easily be evaporated compared to DMSO, which allowed us to avoid the possible loss of material in the post-processing. The experimental work reported in this subsection was done together with the project team member Helena Šimek Tosino. All the experiments in this subsection were performed in the capillary test bench shown in Fig. 2-2.

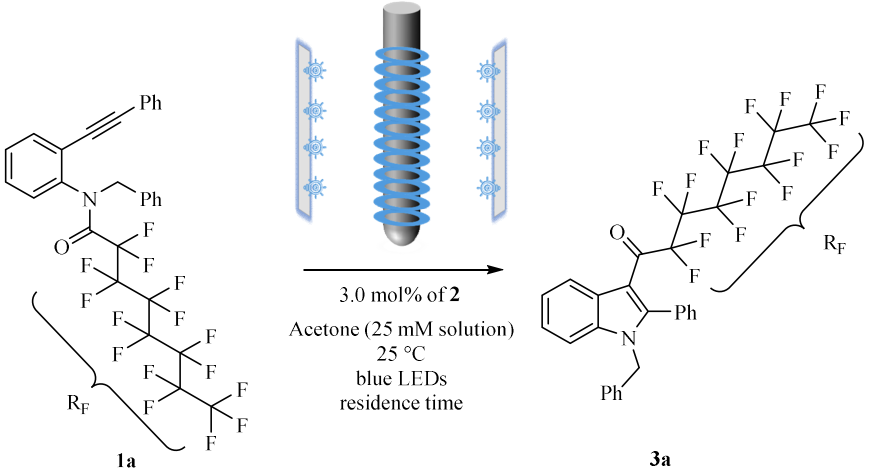

Scheme 4-2 Visible-light-induced cyclization of F-tagged o-alkynylated N-alkyl-N-acylamide **1a** to indole **3a**.

### 4.1.1 Experimental procedure

Experiments in flow were evaluated by varying the flow rate Q (resulting in a mean hydrodynamic residence time ranging from 5 to 180 min) and the incident radiation power P (four intensity levels, from 40%-100%). The radiation power adopted here corresponds to what we used in the photon flux calibration experiments. This ensures that the light intensity in the test was carefully calibrated. The LEDs were modulated and turned on for at least 30 min prior to each experiment to make sure that the LED current was stable. During the tests, two axial cooling fans were running at all times to get rid of the radiative heating and to keep the reaction as close to isothermal as possible.

The reaction solution was prepared as follows: around 70 mg of starting material **1a** (ca. 0.1 mmol) was weighed and transferred into a round bottom flask. 4 mL of dry acetone was added, followed by a PTFE magnetic stirring bar. The solution was continuously stirred until homogeneous. Then, 3.6 mg of Iridium photocatalyst **2** (3 mol%) was added carefully, and the solution was stirred until homogeneous again. The resulting solution was freshly prepared each time and withdrawn by a 10 mL HSW syringe. The syringe was mounted on a calibrated syringe pump. Different from a recommended steady-state operation in flow by Britton et al [145], the infusion process in the experiments was quasi-continuous [96, 146]. The solution was injected into the infusion tubing via syringe and eventually pumped through the irradiated region. When the syringe was empty, an extra 8 mL of fresh acetone was loaded as carrier liquid and mounted on the syringe pump again to continue the infusion process in order to collect the complete reaction mixture. Due to the characteristics of the laminar flow, the effect of diffusion in the axial direction was negligible and the carrier fluid more or less acted as a piston that pushes the reaction fluid through the photoreactor. This is backed by a Reynolds number in the range of 1.5 to 52.7 and a Dean Number in the range of 0.23 to 8.2, indicating stable laminar flow and negligible wavy perturbations [147, 148]. In addition, the estimated Bodenstein number was in a range of 90-3240, indicating the flow can be considered as a plug flow. Detail calculation is presented in the following subsection. The replacement of the syringe took only a few seconds, and the LEDs were switched off once the all the mixture had been collected. The iridium photocatalyst was then stripped from the mixture to give the crude product for NMR measurements. 1H NMR spectra were recorded on a Bruker Ascend 400 MHz to determine the conversion of crude product. Scheme 4-3 shows the diagram of the CAP-μR test bench for kinetic studies.

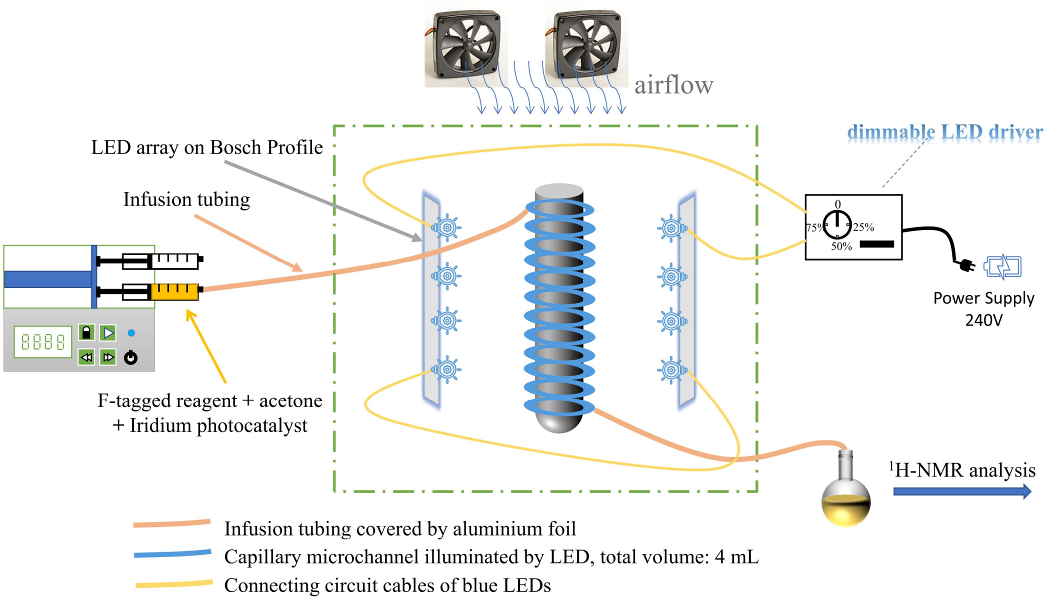

Scheme 4-3 Schematic representation of the kinetic studies of the photocyclization in the CAP-μR

### 4.1.2 Experimental evaluation of kinetic parameters

The effect of the residence time and incident light intensity on the NMR yield, which was calculated by the ratio of the collected substrate and product in the stock solution, was investigated by varying the total volumetric flow rate of the reaction solution and the total energy output of the LEDs in the CAP-μR. After post-processing, the conversions were derived from the 1H NMR spectrum by peak integration. For this reaction, there is no by-product produced. Therefore, the conversion is equal to the reaction yield. As shown in Fig. 4-1, an overview of the experimental results for a residence time ranging from 5 to 180 minutes and four levels of light intensity at 465 nm is provided. With an increase in light intensity from 40% to 100%, there is a significant surge in yield with increasing residence time. When the residence time was 120 minutes, the yield was almost doubled by using 100% intensity instead of 40% light intensity, resulting in a conversion of 55% and 29%, respectively. This ratio decreased slightly when the residence time was extended to 180 minutes (63% and 38%, respectively). This is reasonable as the reaction rate drops due to diluted substrate concentration. On the other hand, the weaker light intensity results in a smaller local concentration of activated species and reduced effective molecular collision, therefore a decreased value in curvature in the reaction profile under weakened irradiation can be observed. With the reaction profile at hand, the rate constants under different irradiation levels can be derived.

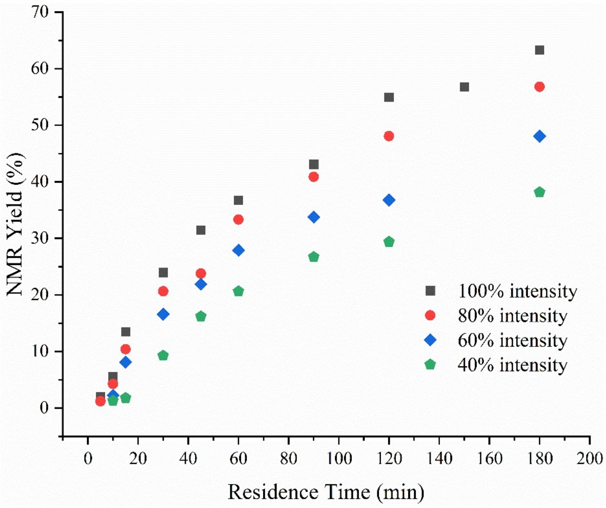

Figure 4-1 The effect of residence time on NMR yield at different light intensities, reaction condition: 25 mM N-benzyl-2,2,3,3,4,4,5,5,6,6,7,7,8,8,8-pentadecafluoro-N-(2-(phenylethynyl)phenyl)octanamide **1a**, 3 mol% Ir[dF($CF_3$)ppy]$_2$(dtbpy)($PF_6$) **2** in anhydrous acetone, 465 nm blue LED illumination, the reaction temperature was set at room temperature, 25±3 °C. (adapted from ref. [144] Copyright 2024 The Royal Society of Chemistry)

Assuming the photoreaction was conducted in an isothermal, constant volume plug flow reactor and uniform photon absorption everywhere in the reaction volume, the reaction kinetics can be expressed in Eq. 4-1. By integration, the relationship between concentration and residence time can be derived in Eq. 4-2 to 4-4, standing for zero, first, and neither zero nor first order mechanism assumptions, respectively.

$$\tau = \int_{C_{A0}}^{C_A} \frac{-dC_A}{r} = \int_{C_{A0}}^{C_A} \frac{-dC_A}{K_{app}{C_A}^n} \tag{4-1}$$

$$C_A = C_{A0} - K_{app}\tau \tag{4-2}$$

$$C_A = C_{A0} \times exp\,(-K_{app}\tau) \tag{4-3}$$

$$C_A = [(n-1)K_{app}\tau + C_{A0}^{1-n}]^{\frac{1}{1-n}} \tag{4-4}$$

The value of $K_{app}$ under the strongest irradiation level (100% energy output) was first evaluated from the experimental results by minimizing the residual sum of squares (*RSS*, formulated in Eq. 4-5) according to the corresponding reaction order assumptions. In addition, the values of $C_A$ at different residence times and light intensities were backward calculated by the NMR yield shown in Fig. 4-1.

$$RSS(n, K_{app}) = \sum \left(c_{A,model} - c_{A,exp}\right)^2 \longrightarrow min \tag{4-5}$$

The regression of the kinetic parameters ($n$, and $K_{app}$) was processed with the software package MATLAB R2019a, and nonlinear curve fitting was operated with the least-squares solver *lsqcurfit*. Table 4-1 summarizes the obtained parameter estimates for of $n$

and $K_{app}$, as well as the residual sum of squares $RSS$. Based on the data, a zero or first order kinetics with regard to the substrate concentration is much less likely than a second order kinetics (entry 1-3 of Table 4-1). Following the same strategy, the apparent rate constants under different irradiation levels were obtained as 0.3799, 0.3123, 0.2096, 0.1519 $M^{-1} \cdot min^{-1}$, standing for 100%, 80%, 60% and 40% energy output (entry 3-6 of Table 4-1), respectively. In addition, Fig. 4-2a shows the good fit of the experimental data obtained with different light intensity by the second-order kinetics. Moreover, the variation of the substrate concentration with residence time predicted by the proposed reaction kinetic model is shown in Fig. 4-2b, which is also well matched by the experimental results obtained with different light intensity and residence time, except for very short residence time. The latter may be explained by a departure from the plug flow situation at short residence times as indicated by the calculated value of the Bo number dropping below 100 for a residence time of 5 min. For all other residence times, the plug flow model can describe the process adequately.

Table 4-1 Estimated kinetic parameters based on *RSS* analysis using MATLAB *lsqcurfit* solver

| **Entry** | **Light intensity (%)** | **Equation assumption** | **Fitting order (n)** | $K_{app}$ | **unit** | ***RSS*** |
|---|---|---|---|---|---|---|
| **1** | 100 | $C_A = C_{A0} - K_{app}\tau$ | 0 | 1.08E-04 | $M \cdot min^{-1}$ | 4.85E-05 |
| **2** | 100 | $C_A = C_{A0} \times \exp(-K_{app}\tau)$ | 1 | 0.0065 | $min^{-1}$ | 1.23E-05 |
| **3** | 100 | $C_A = [(n-1)K_{app}\tau + C_{A0}^{1-n}]^{\frac{1}{1-n}}$ | 2.0018 | 0.3799 | $M^{-1} \cdot min^{-1}$ | 2.42E-06 |
| **4** | 80 | | 2.0021 | 0.3123 | | 1.17E-06 |
| **5** | 60 | | 1.9979 | 0.2096 | | 2.62E-06 |
| **6** | 40 | | 2.0012 | 0.1519 | | 2.82E-06 |

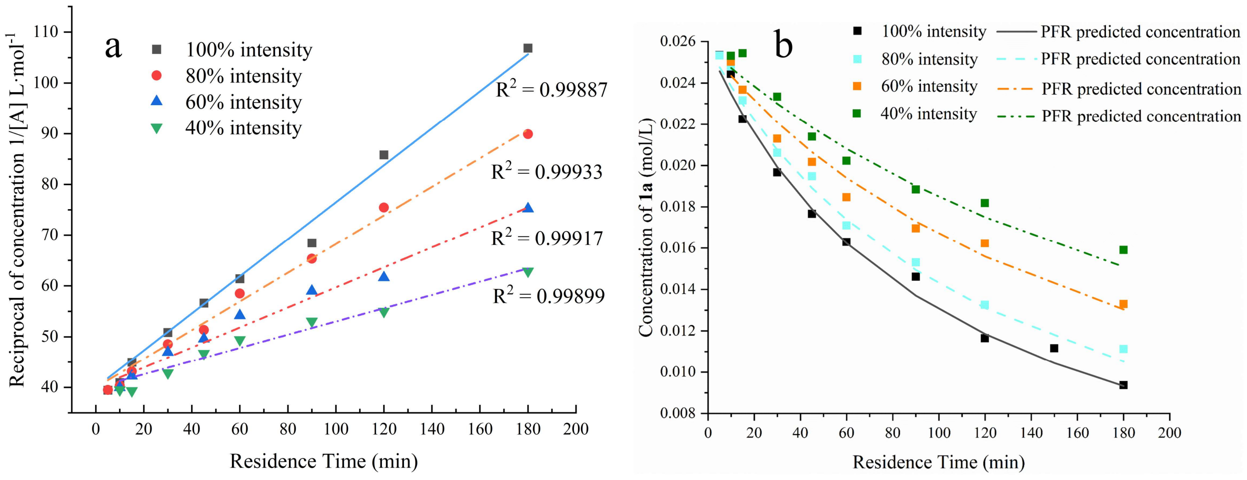

Figure 4-2 a) Validation of the second order reaction assumption by plotting the reciprocal of **1a** concentration versus residence time. b) Comparison of PFR model predicted and experimental **1a** concentration under different light intensities. Conditions: 25 mM F-tagged acylamide **1a**, 3 mol% $Ir[dF(CF_3)ppy]_2(dtbpy)(PF_6)$ **2** in anhydrous acetone, 465 nm blue LED illumination, the reaction temperature was set at room temperature (25±3 °C) with the LED energy output ranging from 40%-100%. (adapted from ref. [144] Copyright 2024 The Royal Society of Chemistry)

### 4.1.3 Mass transfer diagnosis for the CAP-µR

Several dimensionless numbers are recommended and employed to evaluate the operation conditions in microreactors from a reaction engineering point of view, giving a tutorial guide for people stepping toward flow photochemistry and scale-up studies [95, 149]. The Péclet number (Pe, diffusion time $\tau_d$ to flow time $\tau$ ratio) and the Damköhler numbers ($Da_I$, flow time scale $\tau$ to chemical time scale $\tau_r$ ratio and $Da_{II}$, diffusion time scale $\tau_d$ to chemical time scale $\tau_r$ ratio) were employed as useful dimensionless values to characterize the mass transport within the capillary microreactor. Specifically, the characteristic chemical reaction time $\tau_r$ can be estimated from $Da_I$ since in a convective flow system, its value is equal to the product of the apparent rate constant multiplied by the $n$-1 order of the initial substrate concentration and the residence time $\tau$. In addition, the validity of the plug flow model in the rate expression (Eq. 4-1, see section 4.1.2) was examined by the Bodenstein number ($Bo$), which describes the degree of back mixing by axial diffusion as well as by non-uniform flow velocity [150, 151]. The expressions are shown in Eq. 4-6 and Eq. 4-7.

$$Bo = \frac{\bar{u} L_{cap}}{D_{\mathrm{ax}}} \tag{4-6}$$

$$D_{\mathrm{ax}} = D + \frac{\bar{u}^2 {d_h}^2}{192 D} \tag{4-7}$$

where $\bar{u}$, $L_{cap}$, $D_{\mathrm{ax}}$, $D$, $d_h$ represent the average velocity, length of the capillary microreactor, Taylor dispersion coefficient, the diffusivity of the substrate **1a**, and the hydraulic diameter. The diffusivity of **1a** is not available in the literature. Even though the Wilke–Chang equation is the most frequently used one for estimating solute diffusivity in liquid phase systems, the estimated value introduces an uncertain typically of 10% [152, 153]. For the simplification of the evaluation, a reference diffusivity $D$ of $10^{-9}$ $m^2 \cdot s^{-1}$ as reported in the literature was adopted for the evaluation [154]. The estimated values of $Bo$ varied between 90 to 3240 when the set residence time was in the range of 5 to 180 min. $Bo \gg 100$ indicates a nearly ideal plug flow behavior [155, 156]. For a residence time of 5 minutes, the returned $Bo$ value bellows 100, therefore moderate deviations from the plug flow assumption are likely. At least, it cannot be excluded for experiments at short residence times around 5-10 minutes.

Table 4-2 below lists the calculated dimensionless numbers for the operating conditions covered in this study.

Table 4-2 Characteristic time and relative dimensionless numbers in this study

| **Name** | **Symbol** | **Expression** | **Values** |
|---|---|---|---|
| Residence time | $\tau$ | $\tau = \frac{V_R}{Q}$ | 5-180 min |
| Radial diffusion time | $\tau_d$ | $\tau_d = \frac{{d_h}^2}{D}$ | 10.7 min |
| Characteristic chemical reaction time | $\tau_r$ | $\tau_r = \frac{1}{K_{app}C_0^{n-1}}$ | 263 - 105 min |
| Péclet number | $Pe$ | $Pe = \frac{\tau_d}{\tau}$ | 2.14 - 0.059 |
| Damköhler I number | $Da_I$ | $Da_I = \frac{\tau}{\tau_r} = K_{app}C_0^{n-1}\tau$ | 0.048 - 1.71 |
| Damköhler II number | $Da_{II}$ | $Da_{II} = \frac{\tau_d}{\tau_r}$ | 0.10 - 0.041 |
| Bodenstein number | $Bo$ | $Bo = \frac{\overline{u}L_{cap}}{D_{\mathrm{ax}}}$ | 90-3240 |

For the second-order reaction ($n$=2), $\tau_r$ is estimated to be 105 min, which corresponds to the case of the highest reaction rate and the minimum value of $\tau_r$ in the kinetic study. In this context, the estimated value of $Da_{II}$ is always much smaller than 1. As a result, as long as the Péclet number is less than 1 (for cases where the experimental residence time is higher than 10.7 min), the operation conditions always fall in the ideal operating domain where radial concentration gradients can be neglected and the concentration is rather homogeneous at the outlet [149, 157]. Conversely, when the Péclet number exceeds 1 (i.e., the case of experimental residence times of 5 or 10 minutes), radial concentration gradients caused by the laminar velocity profile cannot be ignored, resulting in an inhomogeneous concentration distribution at the outlet. These findings are consistent with the fact in Figure 4-2b that the 5-minute and 10-minute scatter points always appear on the upper side of the plug flow model fitting line. Fig. 4-3 presents a diagram associated with the corresponding dimensionless numbers listed in Table 4-2 of this study. The region A stands for the condition that the reaction mixture is overexposed to the irradiation, and the effect of light attenuation cannot be ignored. The region B stands for the condition that both velocity field and reaction kinetics contribute to the generation of concentration gradients within the microreactor. Region C is the recommend operating domain as a homogeneous concentration distribution can be expected at the outlet. Specifically, for the operating regime located in the upper triangle of this region, high conversion can be achieved in the microreactor [149]. Region D represents the situation that a heterogeneous velocity field is the predominant cause of the concentration gradient inside the microchannel. Most of the operating conditions covered in this study are located in region C, only two cases (for a residence time of 5 or 10 minutes) appear in region D.

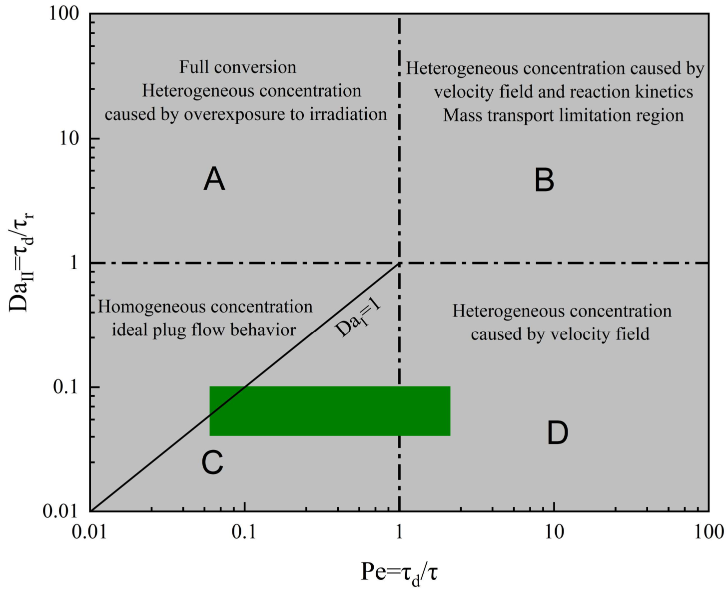

Figure 4-3 Damköhler II-Péclet number diagram representing the mass transport phenomenon inside the microchannel. Green rectangle represents the operation conditions implemented in the present work. (adapted from ref. [144] Copyright 2024 The Royal Society of Chemistry)

### 4.1.4 Relationship between apparent rate constant and surface light intensity

As demonstrated before, the strongest average surface light intensity in the CAP-μR still remains in the weak photon absorption region. Therefore, the relationship between the apparent rate constant and the average surface light intensity should be linear. Fig. 4-4 demonstrates that the apparent rate constant shows good linearity with the average surface light intensity, which follows the trend of weak photon absorption [87]. Obviously, since the reaction rate is proportional to the incident light intensity, the strong light irradiation significantly accelerated the reaction rate and greatly reduced the completion time compared to the traditional batch synthesis. In this scenario, the photon absorption of the 3 mol% iridium photocatalyst **2** is still weak in the CAP-μR due to the short light path (0.8 mm). Even though the 3 mol% of photocatalyst loading was found optimal in the batch synthesis, this does not hold for the CAP-μR [143]. This is also a testament to process intensification, as uniform irradiation can be achieved in the microreactor, resulting in drastically reduced irradiation time. Whereas the same condition is difficult to achieve in conventional batch synthesis. To further increase the productivity of the CAP-μR, more light sources should be incorporated into the system to achieve photon saturation conditions.

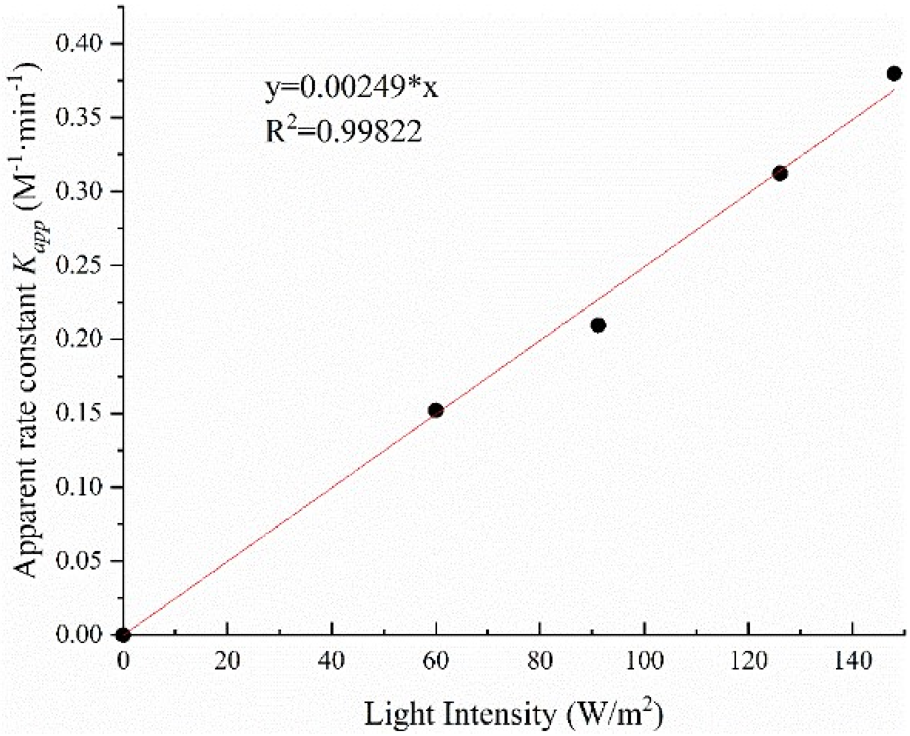

Figure 4-4 Relationship between apparent rate constant and irradiation light intensity in the CAP-μR.

### 4.1.5 Quantum yield determination

The quantum yield of a photochemical reaction is another important parameter that shows the capability of photon absorption, which can be described as the ratio of moles of products produced dived by moles of photons absorbed (Eq. 4-8).

$$\Phi = \frac{moles\ of\ produts\ produced}{moles\ of\ photons\ absorbed} \tag{4-8}$$

The calculation of the moles of photons absorbed requires the optical properties of the Ir photocatalyst to be determined. A series of concentrations (from 0.1 mM to 1 mM) of the photocatalyst was prepared in dry acetone for use in obtaining their UV-Vis spectrum (Fig. 4-5a). The solutions were characterized with an Agilent 8453 UV-Vis spectrometer in a 10 mm path length cuvette. The molar absorption coefficient of the photocatalyst at 465 nm was found to be 209.11 L·mol$^{-1}$·cm$^{-1}$ (Fig. 4-5b).

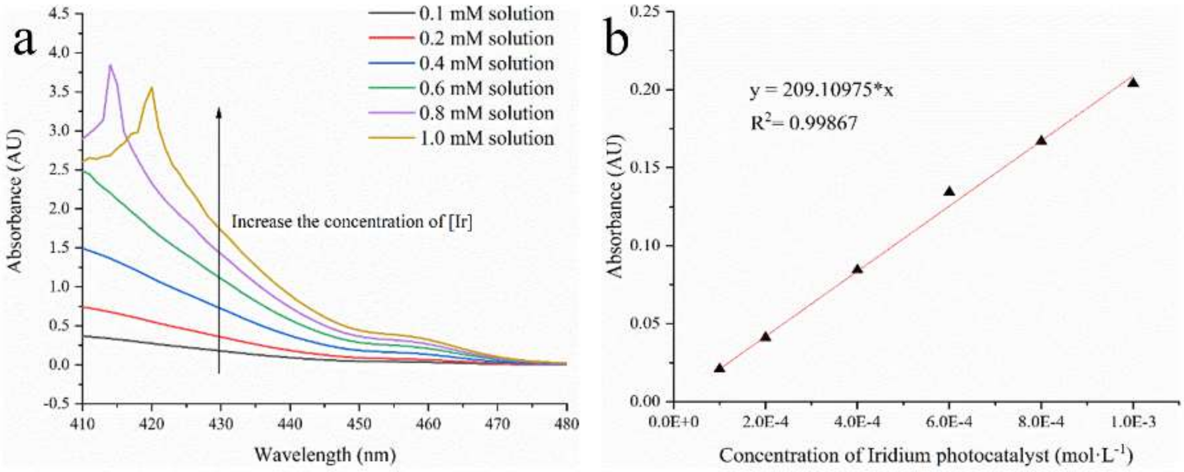

Figure 4-5 a) UV-Vis spectrum of the iridium photocatalyst in a 10 mm depth cuvette. b) Determination of the molar absorption coefficient of the iridium photocatalyst **2** at 465 nm.

In the proposed photocyclization reaction, the iridium photocatalyst can be considered the only photon-absorbing species in the reaction mixture. As a result, the absorption probability of the photocatalyst $p_{(\Omega)}$ can be similarly deduced from Eq. 3-2 by replacing the corresponding concentration and Napierian absorption coefficient, whose value was found to be 0.0591. Together with the mean incident photon flux $q_\lambda$ determined by the potassium ferrioxalate, the absorbed photon flux can be deduced. Table 4-3 summarizes the mean photon flux absorbed by the iridium photocatalyst **2** in the CAP-μR.

Table 4-3 Evaluation of the mean incident photon flux of diffuse emission absorbed by the iridium photocatalyst **2** in the CAP-μR

| Radiation Power | Incident photon flux $q_\lambda$ (einstein·s$^{-1}$) | Photon flux absorbed by the photocatalyst **2** (einstein·s$^{-1}$) |
|---|---|---|
| 100% | 1.15E-05 | 6.78E-07 |
| 80% | 9.77E-06 | 5.78E-07 |
| 60% | 7.07E-06 | 4.18E-07 |
| 40% | 4.65E-06 | 2.75E-07 |

With the absorbed photon flux in hand, the actual number of photons propagating the reaction can be calculated by multiplying it with the corresponding residence time to calculate the quantum yield. Fig. 4-6a shows the quantum yield profile over the residence time, where the same trend can be observed with different incident photon fluxes in flow experiments: the value increases sharply in the low conversion region and then decreases slowly as the reaction goes. For different light intensities, the stronger the intensity used in the experiment, the smaller the quantum yield will get in the same period. To figure out why this happens, the UV-Vis spectra of all species were measured (Fig. 4-6b). It became clear that the indole product contributes a trivial but noticeable photon absorption around the wavelength of 465 nm. Therefore, a fraction of photons will be allocated to the product and then absorbed as the reaction proceeds, resulting in fewer photons being absorbed by the iridium photocatalyst, thereby lowering reaction rate. The competition between the photocatalyst and the indole product is quite interesting in this photoreaction. Faster reaction rates can be observed at lower conversions, while at higher conversions the reaction seems to be slowed down. This kind of acceleration at low conversion reveals the incompatibility between the photocatalyst and the product to some extent. To sum up, higher conversions are always accompanied by diminished quantum yields in this photochemical transformation, making the photon absorption less effective.

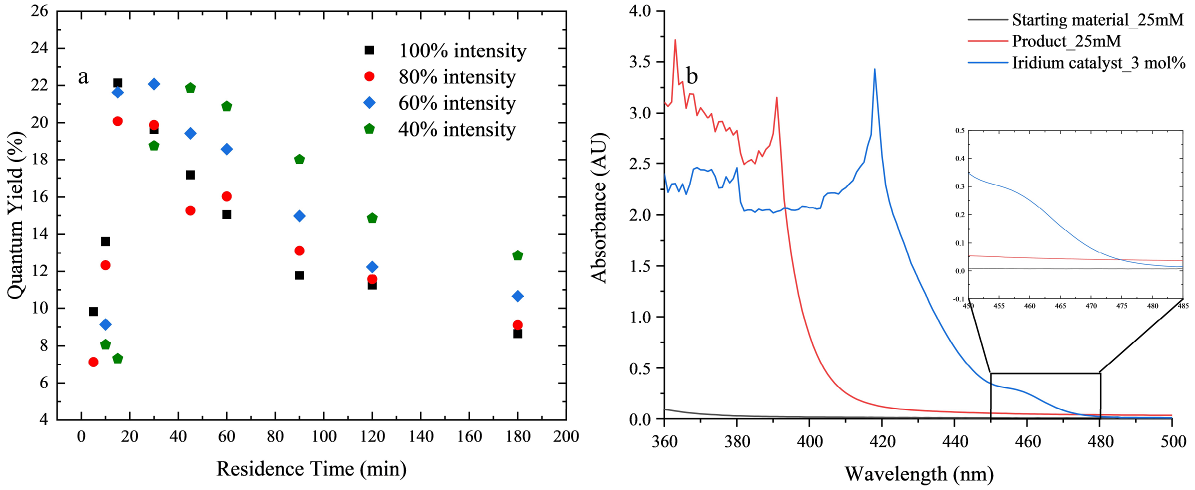

Figure 4-6 a) Plot of quantum yield versus residence time at different light intensities under 465 nm LED illumination. b) UV-vis spectra of all species in the reaction mixture. (adapted from ref. [144] Copyright 2024 The Royal Society of Chemistry)

### 4.1.6 Process intensification in microreactors

The space-time yield (STY) is commonly used to compare the performance of chemical reactors, which can be defined as in Eq. 4-9. As a result, STY values of 5.275 mmol$\cdot L^{-1} \cdot h^{-1}$, 4.735 mmol$\cdot L^{-1} \cdot h^{-1}$, 4.007 mmol$\cdot L^{-1} \cdot h^{-1}$ and 3.181 mmol$\cdot L^{-1} \cdot h^{-1}$ were calculated for the highest mean hydrodynamic residence time (3 hours) in this study with a decrease in light intensity from 100% to 40% (Fig. 4-1).

$$STY = \frac{Desired\ prodcut\ quantity}{Reactor\ volume \cdot time} (\text{mol} \cdot L^{-1} \cdot h^{-1}) \qquad 4\text{-}9$$

The photochemical transformation carried out in the proposed capillary microreactor is significantly accelerated, as a yield of 63% was achieved with a mean hydrodynamic residence time of only 3 hours under strongest irradiation compared to the batch result that required 48 hours to get a comparable conversion [143]. However, one should note that the calculated probability density function $p_{(\Omega)}$ of the iridium photocatalyst is still quite small (0.0591 in this study), which results in low photon efficiency. The photon efficiency of this photoreaction can be improved by changing some parameters with respect to the reactor geometry or reaction conditions, thus improving the STY further. Firstly, for a given photoreactor, the concentration of the photocatalyst used can be moderately increased, which is the most straightforward way to improve the $p_{(\Omega)}$ value of the used photocatalyst. However, blindly increasing the concentration of the photocatalyst is not an economically feasible solution since photon saturation conditions in the photoreactor should also be considered [87]. In addition, an increase of the optical path of the photoreactor would be another option to increase the $p_{(\Omega)}$ value as its value is proportional to the actual optical path $L$. In addition to increasing the $p_{(\Omega)}$ value of the used photocatalyst, an enhancement of the incident photon flux in the microreactor should also be considered, which can be achieved by narrowing the space between the light source and the microchannel or introducing photon reflection. It should be noted that when the light source is very close to the microchannel, it is difficult to ensure that the thermal path of the photoreaction can be free from the peripheral heating caused by irradiation, which may result in impaired conversion or selectivity [158]. The strategy of "introducing photon reflection" can be done by encapsulating the capillary microreactor into a reflective material graved microchannel [109].

### 4.1.7 Interim conclusion

In this section, the continuous-flow photocyclization of an F-tagged aniline derivate to the indole derivate was performed in the CAP-μR under 465 nm blue LED illumination. The flow operating conditions were optimized based on optimal catalyst loading in batch synthesis, and acetone was chosen as analytical friendly solvent. Through a kinetic study, some parameters were determined in order to find the reaction order. The effects of residence time and light intensity on the reaction yield were screened. The reaction order was determined by the integral method and regressed with RSS evaluation in MATLAB, which resulted in a value of 2. The light absorption of the photocatalyst in the CAP-μR remained weak because the apparent rate constant was still proportional to the incident photon flux, even when operating at 100% power output. The UV-Vis spectra of all species in the reaction mixture indicate the phenomenon of competing photon absorption, as the indole product influences the absorption of photons in the process. At the beginning, the quantum yield is much higher and most of the photons will be absorbed by the iridium photocatalyst. However, it decreases as the reaction proceeds. The combination of microreactors and photochemistry greatly speeds up the reaction rate, thereby significantly reducing the time required for the reaction and increasing the space-time yield. Moreover, a general overview of improving the space-time yield of photochemical applications in microreactors is provided. Further investigations should aim to increase the optical thickness (perform the same reaction in PHO-μR, for example) and make maximum use of the incident light for this photochemical transformation. In addition, the effect of the radiation distribution will continue to be analyzed in depth in the following section.

## 4.2 2D axisymmetric reaction simulation of the CAP-μR

### 4.2.1 Simplified reactor model for the photocyclization reaction in the CAP-μR

As is known, the kinetic of photochemical transformations is strongly dependent on the incident photon flux, and a classical rate expression is shown in Eq. 4-10.

$$k = \alpha I^{\beta} \tag{4-10}$$

Where $k$ is the reaction rate constant, $\alpha$ is a constant depending on the type of photochemistry (i.e., the reaction order), $I$ is the incident light intensity (W·m$^{-2}$), and $\beta$ is a constant depending on the photon flux. For lower light intensities (estimated below 200-250 W·m$^{-2}$), $\beta$ is equal to 1.0 implying a linear increase of $k$ with the increase of $I$, which refers to the A-B region in Fig. 4-7 [87].

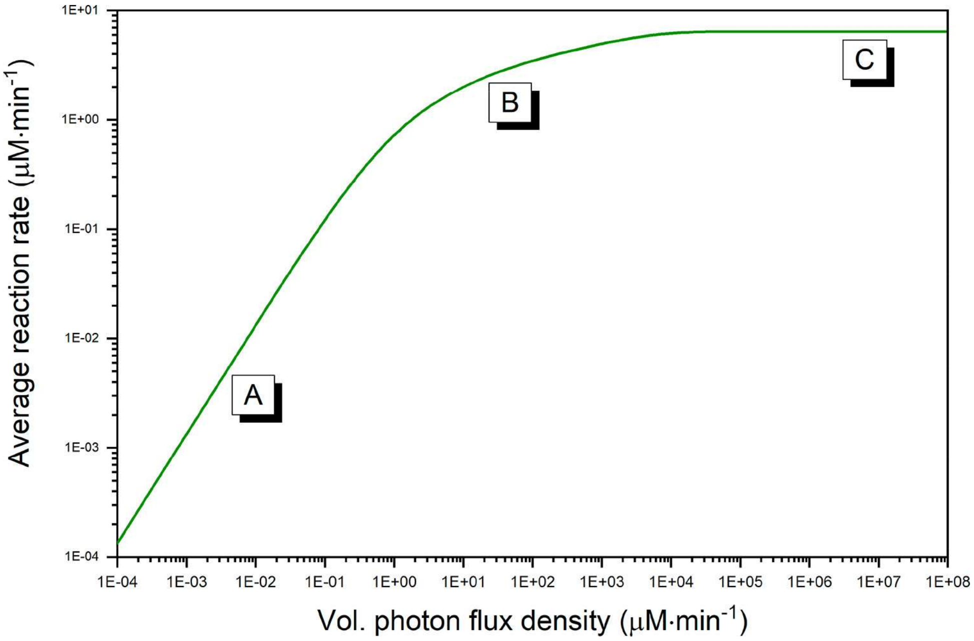

Figure 4-7 Profile of the average reaction rate in a certain time interval against the incident photon flux. (A) A linear region where $\beta$ is 1.0 at lower light intensities and the reaction is photon limited in the reactor. (B) A nonlinear region where $\beta$ is around 0.5 at intermediate light intensities and kinetic limitations appear in the reactor. (C) A constant region where $\beta$ is 0 and kinetic limitations are present in the reactor due to photon saturation. Figure adapted from [87].

The development of the reactor model requires the confirmation of the values of α and β. In the previous study, the reaction order of the photocyclization and the mean incident photon flux arriving at the CAP-μR were determined experimentally. Therefore, a suitable reactor model can be proposed to get a better understanding of this photoreaction. As characterized before, the larger illuminated area of the CAP-μR enables a more homogeneous illumination with a maximum light intensity of approximately 148.0 W/m$^2$. Besides, reports have shown that the radiative transfer within similar capillary microreactors can be reduced to a one-dimensional problem and the system can be simplified assuming a constant irradiation profile over the whole cross-section of the capillary [95, 120, 149]. Moreover, the effective incident radiation absorption of the photocatalyst can be evaluated by solving the radiative transfer equation (RTE) with a 1D Monte Carlo method calibrated with chemical actinometry [119]. Such a strategy provides the opportunity to decouple the radiation transport from the reaction kinetics and delineate the interactions with the photocatalyst. Meanwhile, the strongest light intensity (147.98 W/m$^2$) available in the CAP-μR still remains in the weak absorption region (200.0-250 W/m$^2$) [87]. As a consequence, the reaction rate increases linearly with the incident light intensity in the model. It is assumed that the conditions of monochromatic diffuse light emission, non-emission and non-scattering of the reaction medium, uniform irradiation, as well as weak photon absorption are all valid. A complete simplified reactor model including the reactor geometry and the incident photon flux could be proposed as follows (Eq 4-11 to Eq. 4-15), which is similar to that proposed by Satuf et al [142]

$$r = -\frac{dC_A}{dt} = k_{intr}\frac{S_{irrad}}{V_R}\langle \mathcal{A}_{\lambda}^{e} \rangle {C_A}^{n} = k_{intr}\cdot a_{light}\cdot q_{in}\cdot p_{(\Omega\_Ir)}\cdot {C_A}^{n} \tag{4-11}$$

$$a_{light} = \frac{S_{irrad}}{V_R} \tag{4-12}$$

$$p_{(\Omega\_Ir)} = \frac{C_{cat}E_{cat,\lambda}}{k_{tot,\lambda}}\left[1 + exp\left(-k_{tot,\lambda}L\right)\left(k_{tot,\lambda}L - 1\right) + \left(k_{tot,\lambda}L\right)^2 Ei\left(-k_{tot,\lambda}L\right)\right] \tag{4-13}$$

$$k_{tot,\lambda} = \sum_{i=1}^{n} C_i E_{i,\lambda} \tag{4-14}$$

$$k = k_{intr}\cdot a_{light}\cdot q_{in}\cdot p_{(\Omega\_Ir)} \tag{4-15}$$

$k_{intr}$ represents the intrinsic rate constant and is independent of the photon flux density. $S_{irrad}$ is the irradiated area of the microreactor. $V_R$ is the reactor's volume. $\langle \mathcal{A}_{\lambda}^{e} \rangle$ denotes the mean surface rate of photon absorption (MSRA) at specified wavelength λ. $C_A$ is the cross-sectional bulk concentration of the starting material **1a**. $n$ is the reaction order. $a_{light}$ is the ratio between the irradiated surface $S_{irrad}$ and the reactor volume $V_R$. $q_{in}$ is the mean incident photon flux density received by the microreactor's wall (CAP-μR), and $p_{(\Omega\_Ir)}$ represents the fraction of light absorbed by the photocatalyst. The latter requires the RTE to be solved by the 1D Monte Carlo method for diffuse emission (Eq. 4-13). $n$ is the reaction order with regard to the substrate concentration. $C_{cat}$ is the concentration of the photocatalyst. $E_{cat,\lambda}$ represents the Napierian absorption coefficient of the photocatalyst. $k_{tot,\lambda}$ is the summation of the total absorbance of all species in the reaction. $L$ is the light path, corresponding to the inner diameter of the PFA tubing (0.8 mm).

$Ei(x)$ is the exponential integral function.

Based on the results from the kinetic study, a reaction order of two was found for the substrate concentration (i.e.,$n = 2$). Therefore, the value of $k$ is finally replaced by the product of $k_{intr}$, $a_{light}$, $q_{in}$, $p_{(\Omega\_Ir)}$, and the square of $C_A$ in the proposed model (Eq. 4-16). The value of $k$ corresponds to the apparent rate constant $K_{app}$ obtained in the kinetic study (see section 4.1.2). The values of $a_{light}$ and $p_{(\Omega\_Ir)}$ are geometry dependent and should be evaluated and calibrated before use. To further simplify the model, the photocatalyst is considered the only photon-absorbing species in this transformation, and the contributions of photon absorption from the reactant and product are negligible. The value of $p_{(\Omega\_Ir)}$ is thereby fixed (0.0591 in this case) and considered to be a constant. The reaction rate is positively correlated with the incident photon flux density (Eq. 4-17).

$$r = -\frac{dC_A}{dt} = \frac{dC_B}{dt} = k{C_A}^2 \qquad 4\text{-}16$$

$$k \propto a_{light} \cdot q_{in} \cdot p_{(\Omega\_Ir)} \qquad 4\text{-}17$$

### 4.2.2 Mathematical modelling and computational procedure

From the Bo value analysis (see section 4.1.3), one finds that the plug flow model may not equally well cover all experimental conditions. On the other hand, the yield obtained from the experiments is an integral value including certain variations due to the fact that the flow had to be stopped when the empty syringe was recharged with fresh solvent, whereas the results given by plug flow model correspond to strictly steady-state operation. In order to confirm the feasibility of the plug flow assumption and to validate the correctness of the previously proposed reactor model, a more detailed reactor simulation was performed, which combined the fluid dynamics and the reaction kinetics for a dynamic simulation to predict the experimental cumulative conversions. For isothermal photoreaction, the RTE can be decoupled from the reaction simulation to simplify the reactor model. The numerical simulations were processed with a finite element method based on the commercial CFD software COMSOL® Multiphysics (version 6.0), using the coupled physical interfaces of the laminar flow (*spf*), transport of diluted species (*tds*), chemistry (*chem*), and reacting flow (*rfd*) modules. Since the system is assumed to be homogeneous, the reaction term coupled from the chem interface was applied to the entire simulation domain of the *tds* interface in COMSOL. By analyzing the results of simulations and experiments, the key factors influencing process intensification were determined.

#### 4.2.2.1 Computational domain and discretized grids

As the experiments were carried out in cylindrical tubing, a 2D axisymmetric problem can well describe the process when the effect of gravity and momentum transport are neglected. In this scenario, the reactor model was reduced to 2D axisymmetric as shown in Figure 4-8. The process belongs to the strictly laminar region with the Reynolds number ranging from 1.5 to 52.7 and the calculated Dean number ranging from 0.23 to 8.2, representing negligible wavy perturbations [147, 148]. The computational domain was discretized in a total of $2\times10^5$ elements using a structured mesh with an element ratio of 0.01 (100 elements in total, reverse direction) at the inlet boundary, resulting in a dense mesh near the wall. The setting here can adequately capture the boundary layer effect in fluid flow. All geometric parameters in the simulation correspond to the actual dimensions in use. The simulations were performed under the same operating conditions as the flow experiments.

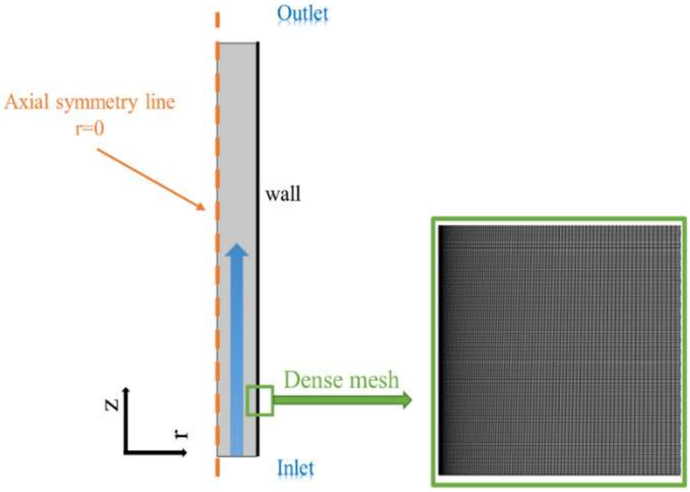

Figure 4-8 Simulation domain and grid for describing the 2D axisymmetric model of the CAP-μR. r:z arbitrarily set to 2000:1 in the detail picture on the left for the scale of better visibility.

### 4.2.2.2 Governing equations and boundary conditions

Due to the existence of the infusion tubing in the CAP-μR, it is reasonable to assume that the flow is fully developed when entering the irradiated region. The fluid density was represented by the solvent's density as the transport of diluted species interface was used. The fluid field in the CAP-μR was obtained by solving the 2D steady-state Navier-Stokes equation for incompressible Newtonian fluids (Eq. 4-18 and 4-19):

$$\rho(u\cdot\nabla)u = \nabla\cdot[-pI + \mu(\nabla u + (\nabla u)\mathrm{T}) - \frac{2\mu}{3}(\nabla\cdot u)I] \quad 4\text{-}18$$

$$\rho\nabla\cdot u = 0 \quad 4\text{-}19$$

Where $u$ is the fluid velocity, $p$ is the pressure, and $I$ is the identity tensor. Fluid density ρ was assumed equal to the density of acetone at ambient temperature, 298 K, with a value of 784.4 kg·m$^{-3}$, and a viscosity $\mu = 3.16\times10^{-4}$ Pa·s were used in the calculation. The imposed boundary conditions for solving the differential equations were: uniform average inlet velocity (calculated from the corresponding volumetric flow rate), zero pressure at the outlet, axial symmetric condition at the center line, and zero fluid velocity at the wall (no-slip condition). The numerically solved velocity field $u$ was then obtained.

Since the experimentally obtained NMR yield were cumulative results, a transient simulation was performed in order to be comparable to the experimental system. The determining velocity field $u$ was employed to derive the concentration field according to the complete transient advection-diffusion equation, where a sink term for the chemical reaction was incorporated on the right-hand side of the equation. As discussed in section 4.1.2, the reaction order was found to be two, and various apparent rate constants under different light intensities were determined experimentally. Even though the indole product **3a** has been proven to have a certain degree of photon competition in the photochemical transformation (see section 4.1.5), its contribution remains negligible in this study. Even at complete conversion, the photon absorption of the product is still an order of magnitude smaller than that of the photocatalyst **2**. Therefore, within the range of experimental conditions covered (under 100% energy output, the maximum conversion is only 63% at a residence time of 180 minutes), the process can be considered as homogeneous. The corresponding apparent rate constants derived from section 4.1.2 were used in the source term on the right-hand side of the diffusion and convection equation (Eq. 4-20), i.e., the apparent rate constants were assumed to be independent of the position in the capillary:

$$\frac{\partial c_i}{\partial t} + \nabla \cdot (-D_i \nabla c_i) + u \cdot \nabla c_i = K_{app} c_i^2 \qquad \text{4-20}$$

In Eq. 4-20, $c_i(x, phi, z)$ represents the local concentration of species $i$ at each point within the reacting channel, whereas the capital $C_i$ in Eq. 4-11 and 4-16 is on behalf of the average concentration of species $i$ in the channel's cross-section, where the subscript A represents the starting material **1a**. A reference diffusivity D of 10$^{-9}$ m$^2$·s$^{-1}$ was adopted both for the starting material **1a** and indole product **3a**. To properly capture the reality of the process and achieve good convergence, the following boundary conditions were imposed: uniform concentration $C_{i\_\mathrm{in}}$ at the inlet prior to the injection of fresh solvent, after which this value became 0, zero diffusive flux at the outlet, axial symmetric condition at the center line, insulating conditions at the wall (no flux).

#### 4.2.2.3 Computational procedure

All numerical simulations were processed with a finite element method based on the commercial CFD software COMSOL® Multiphysics (version 6.0), using the coupled physical interfaces of the laminar flow (*spf*), transport of diluted species (*tds*), chemistry (*chem*) and reacting flow (*rfd*) modules. The iterative solver GMRES with a residual tolerance of 0.001 was used in the stationary fluid flow computation and considered as the convergence criterion. First of all, the parametric sweep function was used for parallel computation to obtain stationary solutions of the velocity fields of different residence times (5-180 min). Then, the resulting velocity fields were transferred for multiphysics coupling of chemistry, diluted species transport, and reacting flow in a transient study. Next, a step pulse describing a gradually increased concentration of the starting material **1a** from 0 mol·m$^{-3}$ to 25 mol·m$^{-3}$ was introduced at the inlet, which starts from 0 to 1 with a transition zone of 0.01s. Subsequently, after 4 mL of the reaction mixture had filled the tube, fresh solvent was introduced at the inlet to continue the process. In this scenario, a time-dependent study coupling mass transfer, chemistry, and reacting flow was carried out by the direct solver PARDISO to investigate the concentration field of all species. The BDF algorithm was employed for the variable time-stepping when solving the transient problem. An integration function was used to calculate the molar flow of the product **3a** as a function of time at the outlet. Therefore, the accumulated yield could be reproduced through numerical simulations, taking into account the effects of back-diffusion caused by the introduction of the fresh solvent.

#### 4.2.2.4 Sensitivity study

A grid independence study was executed by adopting a finer grid with 6×10$^5$ elements in addition to ensure that the results for the velocity and concentration fields converge to the same values and are independent of grid resolution. In addition, a higher diffusivity (10$^{-8}$ m$^2$·s$^{-1}$) of the species was adopted in the numerical simulation, which is the recommended maximum reference diffusivity in liquid phase according to Stokes–Einstein equation.

### 4.2.3 Numerical simulation results

In order to get cumulative conversion from numerical simulations, the cross-sectional product molar flux density at the outlet of the capillary over time $\vec{J_p}(t)$ was extracted. The product molar flow as a function of time at the outlet $n_p(t)$ could be plotted as the integral of the product flux density over the cross-sectional area of the capillary (Eq. 4-21). To properly calculate the cumulative conversion from simulations, the overall number of moles of product produced $n_p$ was calculated by the summation of the product molar flow over computing time $t_c$, in which time in the equation is set to the moment when the product concentration at the outlet stably approached zero (Eq. 4-22). $n_p$ is the moles of indole product **3a** generated, and $n_{s0}$ is the moles of starting material **1a** employed in each experiment, with a fixed value of 0.1 mmol. From batch results, no by-products were produced as indicated by the TLC, therefore the selectivity of the reaction was considered 100%, and the yield is equal to conversion [143].

$$n_p(t) = \int_{\Omega} \vec{j}_p(t)dA \tag{4-21}$$

$$n_p = \int_0^{t_c} n_p(t)dt \tag{4-22}$$

$$X = \frac{n_p}{n_{s0}} \tag{4-23}$$

### 4.2.3.1 Sensitivity results

As an illustrative case, the result of 180 min residence time was used to compare the difference between the coarse and finer mesh (Fig. 4-9). Both grids gave almost the same molar flow as a function of time at the outlet as two curves (black and orange) were nearly overlapping each other over most of the region, even though marginal differences appeared in the velocity field. The predicted accumulative yields were generally close to each other with a relatively small deviation (62.65% for coarser grid and 62.68% for finer grid). Meanwhile, the predicted value of the coarser grid (62.65%) was already very close to the experimental value (63.30%), indicating that the simulation was able to reproduce this experimental process. Hence, to save computation time, the coarser grid ($2\times10^5$ elements) was used for the rest of numerical simulations.

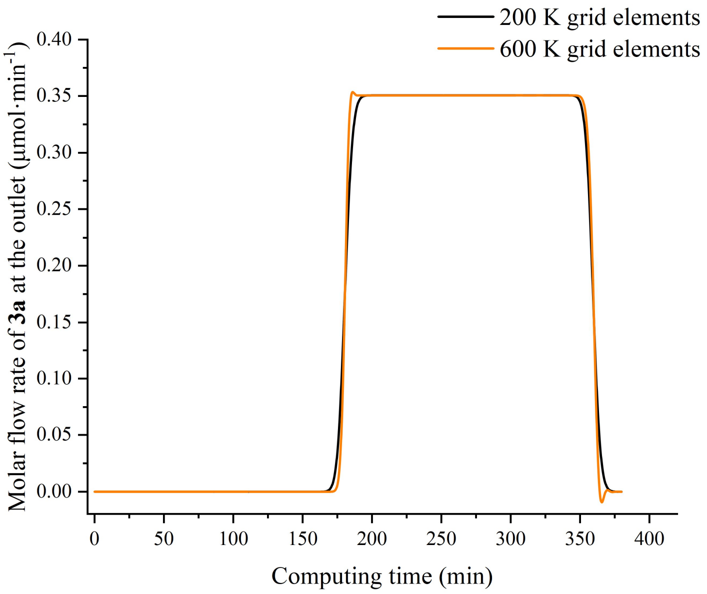

Figure 4-9 Grid sensitivity test: predicted molar flow of the product **3a** as a function of time at the outlet for a set residence time of 180 min under 100% light irradiation.

In addition, cumulative yields are affected by the possible dilution effect at the outlet due to the introduction of fresh solvent. The difference between the results for the larger and the smaller reference diffusivity was compared for a given experimental condition of 180 minutes, i.e., the case where the interdiffusion of fresh solvent and reaction mixture has the greatest impact on the experimental conversion (Fig. 4-10). Similarly, the molar flow rate at the outlet as a function of time essentially overlaps, despite the fact that the reference diffusivity value differs by an order of magnitude. In addition, one can find out that a larger diffusivity value accelerates the process into a steady state (orange curve) and the outlet fluid remains in steady state for a longer period of time. At the same time, due to the larger diffusivity, the actual time affected by the interdiffusion of the fresh solvent and the reaction mixture (13 min) is only half of what it would be in the case of a smaller diffusivity (27 min). Nevertheless, there is hardly any difference between the two from the results of the numerical simulations (i.e., the comparison of cumulative conversion between two cases). The integral values of the area under the curve are almost equal, resulting in an estimated conversion of 62.79% for the larger reference diffusivity and 62.65% for the smaller reference diffusivity. However, the larger reference diffusivity value requires longer computation times to obtain converged computational results. Consequently, the smaller diffusivity value was employed in all predictions. The strategies adopted here ensure the accuracy of the results and reduce the computational cost.

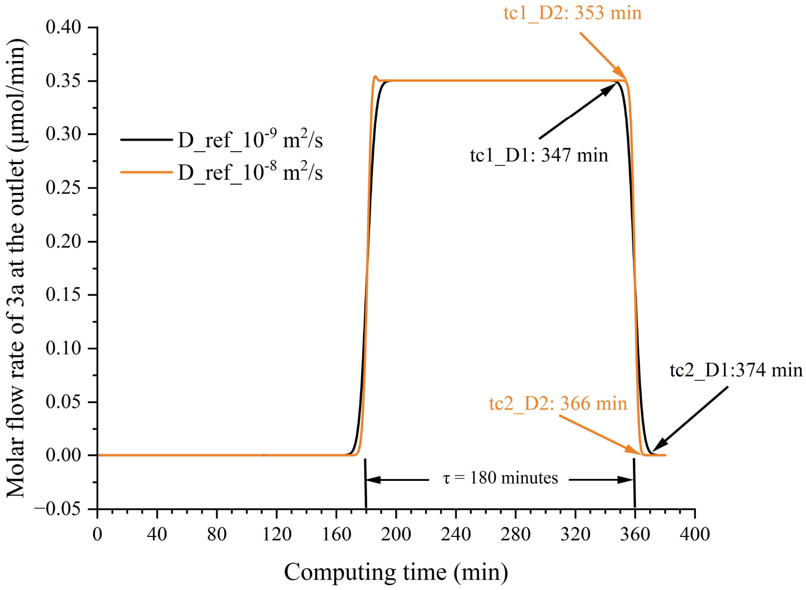

Figure 4-10 Reference diffusivity value sensitivity test: predicted molar flow of the product **3a** as a function of time at the outlet for a set residence time of 180 min under 100% light irradiation. tc1_D1 stands for the critical steady-state time (i.e., the outlet concentration is about to decline due to the influence of interdiffusion), smaller reference diffusivity; tc1_D2 stands for the critical steady-state time, larger reference diffusivity. tc2_D1 stands for the critical time when the concentration of the product at the outlet is zero, smaller reference diffusivity; tc2_D2 stands for the critical time when the concentration of the product at the outlet is zero, larger reference diffusivity.

#### 4.2.3.2 Overview of numerical predictions

The predicted molar flow rate of **3a** as a function of time at the outlet for different light intensities of 40-100% irradiation can be found in Fig. A4-A7 in the Appendix. Table A1 lists the area under the curves of Fig. A4-A7 for different light intensities, which stands for the total moles of product that could be collected (Eq. 4-22) and the predicted cumulative conversion (Eq. 4-23). As shown in a parity plot given in Fig. 4-11a, almost all data points fall inside the $\pm 10\%$ region, indicating that the majority of simulation results match the experimental results well, but there are still some deviations in the red dashed box and purple dash-dot box. On one hand, the errors in the red dashed box were caused by short residence times. The calculated diffusion time ($\tau_d$, the characteristic radial diffusion time, i.e., a time estimated for the reactants to reach the wall by diffusion) is 640 s, which exceeds the experimental residence times (5 or 10 min) in this region. This corresponds to the case where the radial Péclet number $Pe\_r$ exceeds 1 and the radial diffusion is insufficient to eliminate the concentration gradients in radial direction generated by the gradient of the flow velocity. This was not accounted for in the simplified plug flow model used for establishing the reaction kinetics. In such context, the product will be accumulated near the wall, leading a concentration gradient in radial direction (black and red line of Fig. 4-11b, the corresponding operating conditions are located in region D of Fig. 4-3 in section 4.1.3). It results in lower experimental conversions and an overestimation of the predicted values in the red dashed box. The finding is in line with the mass transport diagnostics in section 4.1.3. In such conditions, extra micro mixing elements should be incorporated into the system to promote radial mixing. For extended residence times, the radial concentration gradients decrease and eventually the concentration field becomes uniform over the cross-section of the channel (Fig. 4-11b). On the other hand, the bias in the purple dash-dot box was caused by photon competition, since a fraction of light gets absorbed by the indole product, as indicated in the UV-Vis spectra of all the species in the mixture (see Fig. 4-6b). The trends in the parity plot also follow the conclusion from quantum yield determination: as the reaction proceeds, the fraction of photons absorbed by the cumulative product in the reaction mixture cannot be ignored, thence the probability density function $p_{(\Omega\_Ir)}$ of the iridium photocatalyst calculated according to Eq. 4-13 actually decreases, resulting in a decrease of the reaction rate. At the same time, the overall incident photon flux arriving at the CAP-μR and the apparent rate constants adopted in the simplified COMSOL simulation were macroscopic mean values, which did not take the photon absorption of the indole product into consideration. Therefore, the hypothesis that the photocatalyst is the only absorbing species is no longer valid in reality. In such context, the scatter points in the polarity diagram first appear on the upper side of the diagonal line due to the existence of the radial concentration gradient, and then move downward to the opposite side of the diagonal line due to the acceleration of the photoreaction in the initial stage, and eventually crosses the diagonal line to the top side of the polarity plot again due to non-negligible photon competition (Fig. 4-11a). The comparison between experiments, plug flow model and COMSOL simulation results is shown in Fig. 4-11c. The predicted conversion for residence times of 5 and 10 minutes were overestimated due to the existence of mass transport limitation. Furthermore, the conversion predicted by the plug flow model always surpasses the cumulative conversion obtained by COMSOL simulations. It can deduce that the relative deviation between the predicted yields from the plug flow model and from the COMSOL simulation was consistently less than 5% in the absence of mass transport limitations, i.e., the residence time is larger than 15 minutes. In addition, the transient COMSOL simulation can be used to invert the kinetic parameters for steady-state plug flow conditions by extracting the outlet concentration when it reaches a constant. The invert calculation resulted in a corrected apparent rate constant of 0.3803, 0.3121, 0.2095 and 0.1517 $M^{-1}\cdot min^{-1}$, standing for a decrease in LED output from

100% to 40%, respectively. Results showed that relative errors of apparent rate constants between established reaction kinetics in section 4.1.2 and steady-state plug flow model from COMSOL inversion calculation are rather small (Fig. 4-11d). Relative errors between two values are kept within 0.15%. Therefore, the system error induced by the interdiffusion of the fresh solvent and the reaction mixture was negligible and acceptable, and the plug flow assumption was acceptable for establishing the kinetic model. As a consequence, once the operation conditions fall within the ideal operating domain where both the $Pe$ and $Da_{II}$ values are less than 1, the plug flow model can be used to predict the conversion in the CAP-μR.

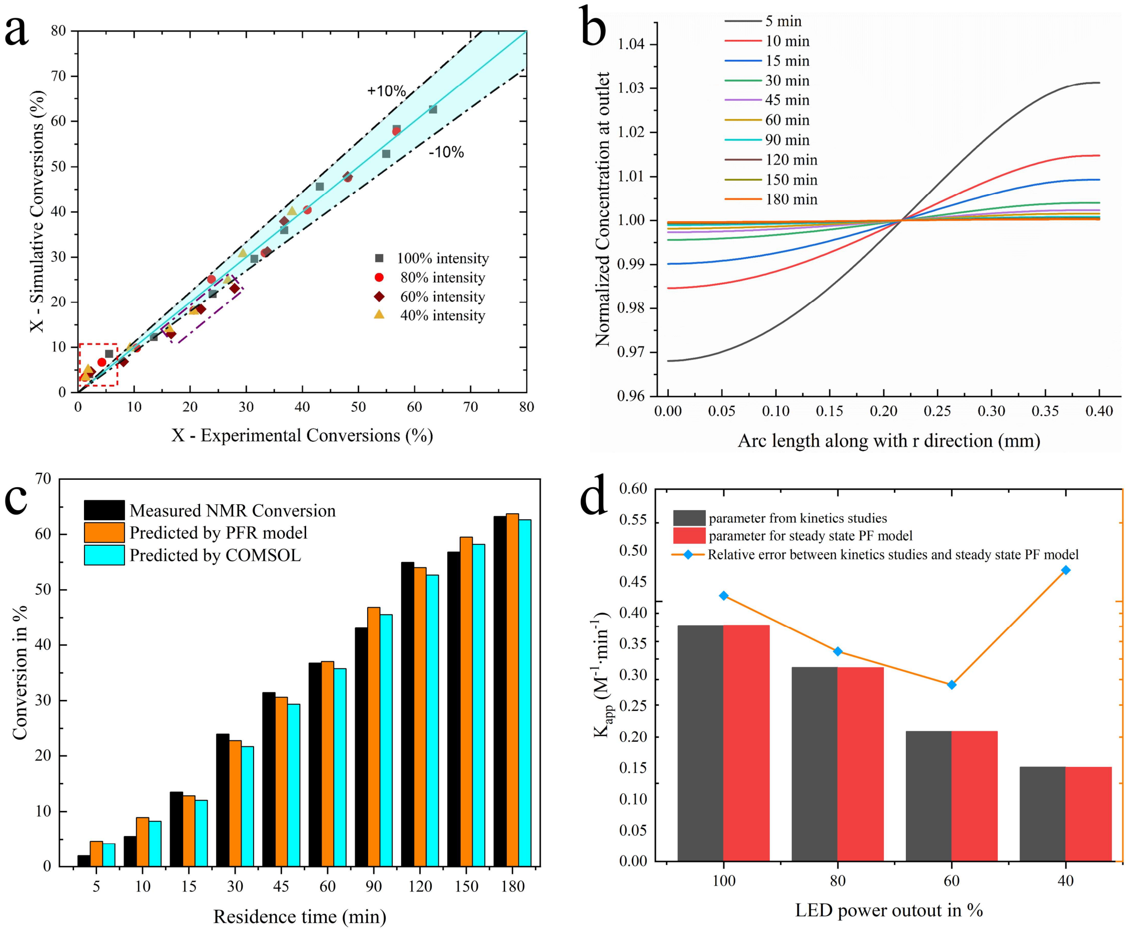

Figure 4-11 (a) Comparison of the predicted cumulative conversions from COMSOL (coarse grid) and experimental conversions in a polarity plot for different light intensities in the capillary microreactor. (b) Plot of the normalized outlet concentration of the product along the r direction at steady state under 100% irradiation output, 47.6 W. (c) Comparison of conversions between experiments, the plug flow model and COMSOL simulations (coarse grid) under 100% irradiation output. (d) Histogram of the apparent rate constant from kinetics studies and steady state plug flow model from COMSOL inversion calculations.

### 4.2.4 Extraction of the intrinsic rate constant

The results from the 2D axisymmetric simulation reproduce the process quite well, thereby demonstrating that the kinetic parameters established in section 4.1 are reasonable and acceptable. The value of $p_{(\Omega\_Ir)}$ at the chosen concentration (3 mol%) was calculated by MATLAB R2019a and found to be 0.0591 in the PHO-μR (optical path 0.8 mm). Since the reaction rate is proportional to the received light intensity (Eq. 4-15), the intrinsic rate constant of the photoreaction can be extracted by plotting the apparent rate constant against the product of $a_{ligh}$ , $q_{in}$ and $p_{(\Omega\_Ir)}$. As a result, the intrinsic rate constant $k_{intr}$ can be derived from Eq. 4-15 assuming that the probability density function $p_{(\Omega\_Ir)}$ of iridium photocatalyst is constant. One obtains a value of 36.24 $L^2 \cdot mol^{-1} \cdot einstein^{-1}$ (Fig. 4-12).

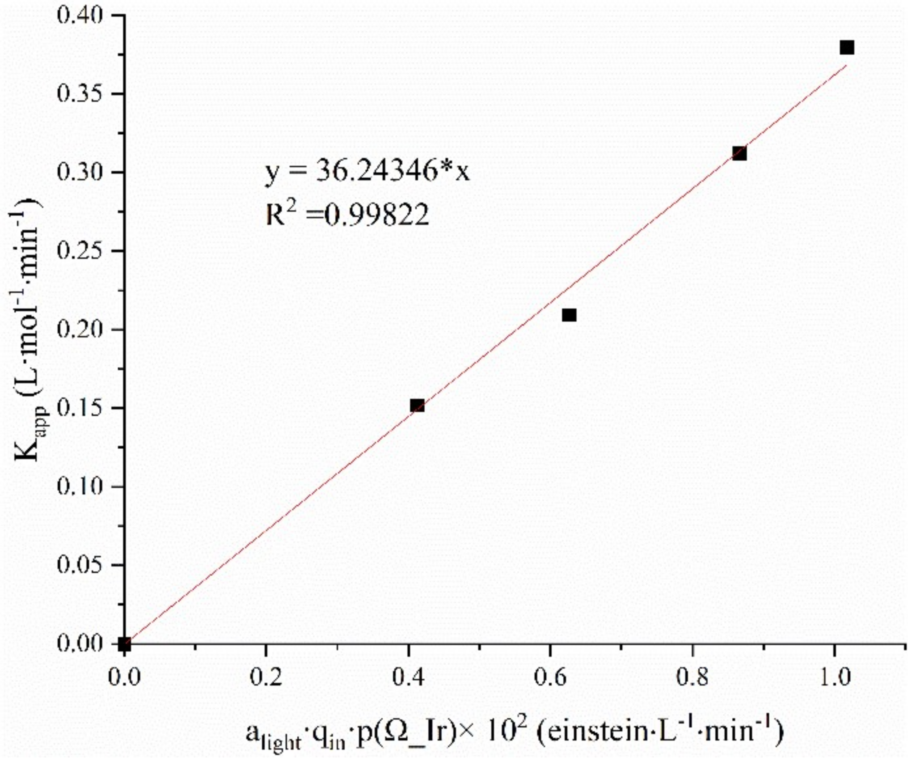

Figure 4-12 Extraction of the intrinsic rate constant of the photoreaction. (adapted from ref. [144] Copyright 2024 The Royal Society of Chemistry)

### 4.2.5 Interim conclusion

In this section, a two-dimensional axisymmetric model was proposed to describe the photochemical process in the CAP-μR. A uniform transversal irradiance hypothesis was adopted due to the large illuminating area of the CAP-μR, and the apparent rate constants from *RSS* regression in MATLAB were used in the simulation. The derived Bodenstein numbers for the actual operating conditions show that the plug flow assumption is acceptable for the simulation in most of experimental space, as it captures the pseudo-homogeneous photocatalysis process very well and the experimental yields are in good agreement with the simulation results. The scatters in the parity plot indicate that even though the indole product affects the photon absorption of the photocatalyst to some extent, the reaction generally follows the principle of homogeneous photocatalysis. In order to obtain uniform bulk concentrations and achieve high conversions in the CAP-μR, the residence time should be greater than 60 min.

Moreover, the intrinsic rate constant of the photoreaction was found, resulting in 36.24 $L^2 \cdot mol^{-1} \cdot einstein^{-1}$. This value should be independent of the incident light intensity and the geometry of the photoreactor. To further confirm the correctness of this conclusion, the same reaction was also performed in the PHO-μR, which has a more demanding channel geometry together with an unsymmetrical illumination and reaches higher incident light intensities.

## 4.3 Three-dimensional, spatially resolved multiphysics simulation of the PHO-μR

Since the CAP-μR has a large illumination surface area per volume, and the light shines on the capillary over the whole circumference. It is reasonable to assume that the irradiation over the capillary is homogenous. A uniform transversal irradiance profile can then be employed in the reaction model to address the linear light attenuation effects by the 1D Monte Carlo method. In fact, the actual surface irradiance and homogeneity of the radiation field are highly dependent on the LED configuration of the microreactor system. In general, the distance between the LEDs and the microchannel should be relatively small to cover all of the reaction regions inside the system and make the photon distribution over the microchannel as uniform as possible [98, 110]. However, due to the limited emission angle, Lambertian power distribution, and quasi-point source nature of the LEDs, homogeneous illumination is yet difficult to achieve in a micro-structured photoreactor if the position of the LEDs is not carefully designed [98, 112, 113, 159, 160]. This results in a scattered photon distribution where some points receive higher local illumination while the places in the edge are barely irradiated due to the short distance between the LED and microchannel. In contrast, putting the LED far away from the microchannel may lead to lost irradiation and wasted energy (Fig. 4-13). Therefore, the optimal positioning of the reactor and the light sources should be determined in advance to minimize radiation loss and maximize photon capture efficiency.

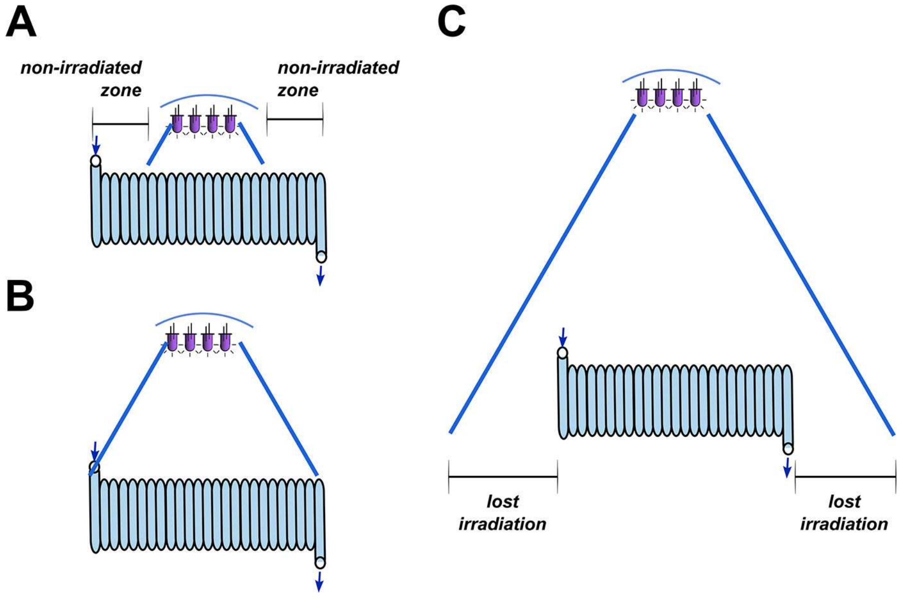

Figure 4-13 Minimizing radiation loss and maximizing photon capture efficiency by tuning the LED-to-reactor distance. (A) The light source is not capable of covering the reactor dimensions, and only part of the reaction volume is illuminated. (B) Optimal positioning of the reactor and light source so that the entire reaction volume is fully utilized. (C) The light source is positioned too far away from the microchannel, resulting in a considerable loss of irradiation. Figure is adapted from [87].

In this scenario, the radiation field varies with different LED-to-reactor distances, and the irradiation homogeneity must not be ignored as uncertainties in spatial illumination and inhomogeneity in irradiance obscure kinetic studies and may lead to an erroneous analysis of kinetic parameters, particularly the "local volumetric rate of photon absorption" (LVRPA), which is a key factor affecting the local reaction kinetics. In other words, the local reaction rate is highly dependent on the incident radiation field. To get the radiation distribution and further obtain the actual concentration distribution of the reactants in the microchannel, the Radiative Transfer Equation (RTE) must be solved for the concrete system geometry embedded in an optimization strategy, this allows one to find the optimal positioning of the LEDs relative to the microfluidic channel by simulation. Several simplified analytical models using algebraic equations like the two-flux model (TFM) [161], four-flux model (FFM) [162], and six-flux model (SFM) [163] have been proposed to solve the radiation distribution over a flat slab geometry. The mathematical results from these algebraic equations, although applicable to planar geometry, may occasionally be misinterpreted in a complex geometry, particularly in a meandering microchannel where the photocatalyst is partially deposited. Furthermore, none of them takes into account the reflection at the walls of the microchannel, as this would complicate the algebraic equations, yet is indeed the case one needs to address in the PHO-μR.

Alternatively, to capture the radiation distribution over these geometries properly, other kinds of solutions based on the finite volume method (FVM) or statistical Monte Carlo method (MCM) are considered. Both methods have been demonstrated to adequately capture the photon transfer features in the NETmix photocatalytic reactor. The incident radiation flux over the catalytic surface is well presented under different illumination mechanisms denominated as back-side illumination (BSI) and front-side illumination (FSI), respectively [110, 160]. It has been demonstrated that computational fluid dynamics (CFD) is capable of providing reliable irradiance predictions for different configurations of LED-based photoreactor design, making it serve as a promising tool for optimization, scale-up, and validation of the proposed photocatalytic system [111, 164-167]. Furthermore, it can integrate all the multiphysics phenomena involved in the photo transformation such as fluid dynamics, species transport, radiation transport, and reaction kinetics. Once the radiation field over the geometry of interest is determined, the resulting values of the LVRPA can be accessed at arbitrary locations of the simulated geometry, and the local reaction rate as well as the concentration field can be easily derived based on the corresponding kinetic parameters. Although radiation fields can be obtained from these CFD tools, predictions of reactant concentration fields in photoreactors using multiphysics coupling are rarely reported.

In this section, the commercial CFD software (COMSOL Multiphysics, version 6.0) based on the finite element method (FEM) was chosen to perform spatially resolved reaction simulations based on the radiative transfer simulation of the PHO-μR to assess the irradiance homogeneity, spatial illuminance distribution over the microchannel, and suitable LED configurations. Under the branch of the heat transfer module, the Discrete Ordinary Method (DOM) was chosen to get the radiation distribution over the geometry of interest, which is known to provide accurate predictions if the angular discretization of the simulation is sufficient [111]. The received irradiance values over the surface of the microchannel in the PHO-μR were carefully iterated with experimental data from chemical actinometry to be as faithful as possible to the actual situation [110]. The following reaction simulations were performed to get the spatially resolved concentration field based on kinetic studies that are described in section 4.1. In the end, the proposed reaction model was validated with experimental results.

## 4.3.1 Radiative transfer modelling to find optimal LED configurations

### 4.3.1.1 Discrete Ordinate Method (DOM)

The DOM is able to convert the integral-differential RTE into a set of algebraic equations to capture the photon transport process, which can be solved using several default built-in quadrature sets that represent the direction of light propagation in COMSOL. The governing equations in the simulation can be expressed by Eq. 4-24 and 4-25.

$$S_i \cdot \nabla I_i = \kappa I_b(T) - (\kappa + \sigma_s) I_i + \frac{\sigma_s}{4\pi} \sum_{j=1}^{N} \omega_j I_j \varphi(S_j, S_i) \qquad \text{4-24}$$

$$G = \sum_{j=1}^{N} \omega_j I_j \qquad \text{4-25}$$

where $S_i$ is the $i^{th}$ discrete ordinate, $I_i$ is the $i^{th}$ component of the radiative intensity, $I_b$ is the black body radiation intensity ($\mathrm{W \cdot m^{-2} \cdot sr^{-1}}$), κ ($m^{-1}$) and $\sigma_s$ ($m^{-1}$) represent absorption and scattering coefficients of the reaction media, respectively, $\omega_j$ is the quadrature weight, $\varphi(\Omega_j, \Omega_i)$ is the scattering phase function, and G ($\mathrm{W \cdot m^{-2}}$) is the incident radiation at a given point. The angular discretization should be sufficient to avoid “ray effects”, which means that the radiant intensity tends to be concentrated in the discrete directions dictated by the built-in quadrature set. An inadequate discretization will lead to misinterpretation of the photon transfer, especially for simulating LED emission. Solving the RTE for each wavelength of the LED emission spectra is extremely computationally expensive, therefore only the wavelength of 458 nm (peak wavelength of using LED) was considered here.

#### 4.3.1.2 Simulative domain and boundary settings

To simulate the distribution of the radiation inside the meandering channel, the actual geometry was carefully reproduced in the model to consider the exact parameters of the PHO-μR, and the resulting 3D model was discretized into a sufficient number of elements. Since the reactor has three identical reaction zones, the simulation will be performed in only one of the zones. In the PHO-μR, the thickness of the meandering channel is 2 mm, and the reactor window can be considered a 75 mm × 31 mm × 2 mm rectangle. A cylindrical structure with a radius of 1.5 mm and height of 1.2 mm (adapted from the supplier's datasheet) was used to represent the top LED geometry. The diffuse surface emitting model was adopted for the emitting LED array with the settings of peripheral transparent walls and external irradiation on the bottom. The air space between the LEDs and the internal surface of the quartz window was represented by a rectangle that matches the window geometry and the specified LED-to-reactor height $h_L$, of which the domain was treated as a diactinic medium assuming that there is no absorption, no scattering, and no emission. The quartz glass window that gathers and transmits photons to the reaction medium was considered to have a transmission ratio of 0.93 according to the supplier's datasheet. The thickness of the quartz glass was considered to be zero [111]. Meanwhile, the milled meandering channel was considered as highly polished opaque surfaces with an emissivity of 0.093 at ambient temperature [130]. Structured meshes were created for the LEDs while unstructured meshes were created for the air domain and the meandering channel. A typical discretized domain ($h_L$=8 mm) for RTE simulation in this study can be found in Fig. 4-14.

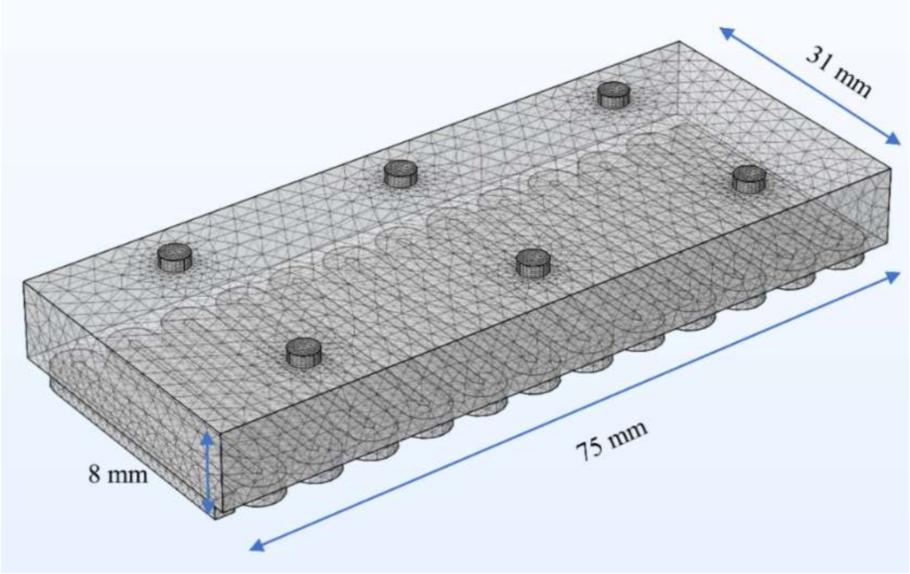

Figure 4-14 Simulative domain for radiation field prediction. 6 LED configuration with a minimum available LED-to-reactor distance of 8 mm. The LED positioning adopted here aligns with the same setting for photon flux calibration experiments.

In the simulation, the temperature was fixed to 1 K in all domains as well as boundaries to inactivate the ambient thermal emission, reducing the computational cost [111]. In addition, the number of discrete directions of the light will define the precision of the results. To get good resolution solution and balance the computational cost, the light was discretized into 80 directions using the built-in S8 Level Symmetric Even quadrature set.

#### 4.3.1.3 Grid dependency study

A grid dependency study was carried out to find an optimal meshing that suits the RTE simulations. The aforementioned domain was finally discretized into finite elements ranging from 33 K to 65 K grid elements by varying the set parameters. As the discretized grids reached the maximum computing capacity of the computer, a finer grid was specified only near the LED and over the meandering channel. A nonlocal coupling general extrusion operator (genext1) in COMSOL was employed to extract the radiation field and map it to the actual meandering microfluidic channel. Scaled residuals for DOM simulations were decreased below $10^{-3}$ to consider a converged solution. The simulations were performed on a workstation equipped with an Intel(R) Xeon(R) CPU E5-2670 0@ 2.60GHz using Windows 10, 64 bits with 128 GB RAM memory.

At the beginning, a quick test to determine an ideal discretized grid for the RTE simulation was performed. A 6 aligned LED configuration with a reference LED-to-reactor distance of 8 mm was chosen, which is the actual LED configuration that was adopted in the photon flux calibration experiments. A reference intensity of 11840 W·m$^{-2}$ was used as the incident intensity on the LED surface. The average incident radiation $\bar{I}$ over the microchannel surface (Eq. 4-26) and the calculation time. A typical stationary RTE simulation takes around 5-6 hours to converge.

$$\bar{I} = \frac{1}{N}\sum_{j=1}^{N}\int_{4\pi} I(\Omega)d\Omega \qquad 4\text{-}26$$

Fig. 4-15 shows that an increase in the number of simulated grid elements leads to a rapid surge in computing time. The more grid elements, the higher the average irradiance on the microchannel surface, which finally reached an almost stable value around 1500 $\mathrm{W/m^2}$. To balance the resolution with the calculation time, a grid of around 60.9 K elements was used for all RTE simulations in this study. This number of grid elements results in an average cell volume of 0.35 $\mathrm{mm^3}$.

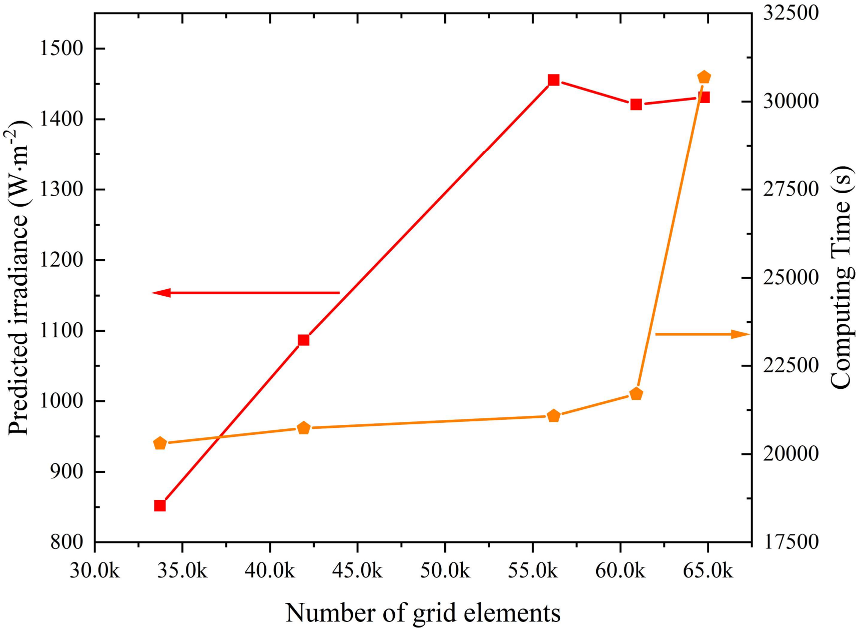

Figure 4-15 Grid dependency study. A reference intensity of 11840 W·m$^{-2}$ was employed in the test as the incident intensity of the LED surface. 6 aligned arrangements of LED, $h_L$ equal to 8 mm.

#### 4.3.1.4 Proposed LED configurations and simulated cases

In the following simulations, several LED configurations were proposed to find the optimal LED arrangement. The number of LEDs used varies from 4 to 8, depending on the geometric constraints of the reaction window. Four different layouts were considered as shown in Fig. 4-16. Five levels of LED-to-reactor distance were screened for the system studied: 8, 10, 12, 15 and 20 mm, respectively. Therefore, a total of 20 cases were simulated and compared to find the optimal design, with the parameters shown in Tab 4-4.

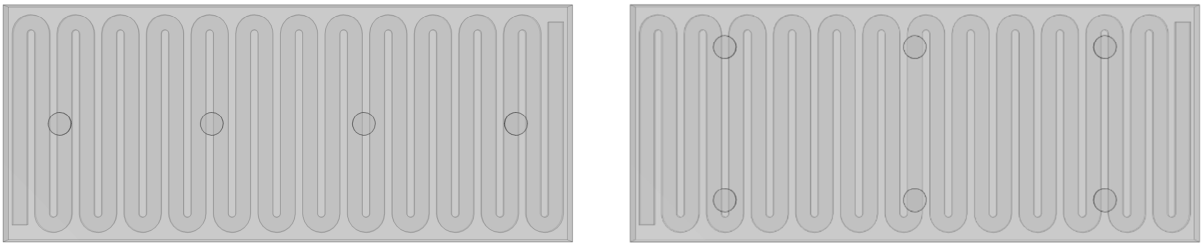

(a) 4 aligned LEDs (b) 6 aligned LEDs

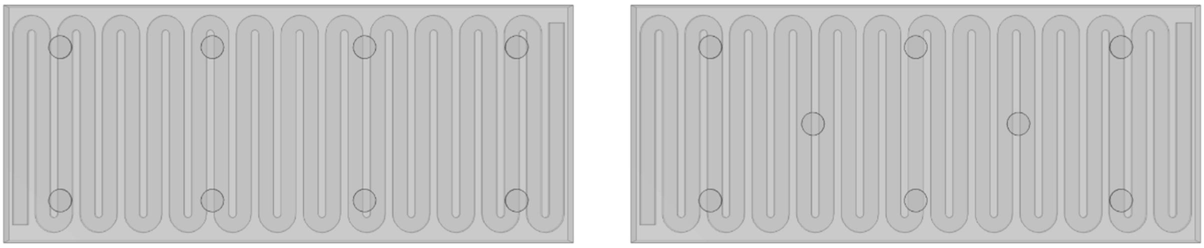

(c) 8 aligned LEDs (d) 8 staggered LEDs

Figure 4-16 Proposed LED configurations

Table 4-4 Evaluated cases for RTE simulation

| Case | LEDs amounts | Arrangement | $\boldsymbol{h_L}$ (mm) | Case | LEDs amounts | Arrangement | $\boldsymbol{h_L}$ (mm) |
|---|---|---|---|---|---|---|---|
| 1 | 4 | aligned | 8 | 11 | 8 | aligned | 8 |
| 2 | 4 | aligned | 10 | 12 | 8 | aligned | 10 |
| 3 | 4 | aligned | 12 | 13 | 8 | aligned | 12 |
| 4 | 4 | aligned | 15 | 14 | 8 | aligned | 15 |
| 5 | 4 | aligned | 20 | 15 | 8 | aligned | 20 |
| 6 | 6 | aligned | 8 | 16 | 8 | Staggered | 8 |
| 7 | 6 | aligned | 10 | 17 | 8 | Staggered | 10 |
| 8 | 6 | aligned | 12 | 18 | 8 | Staggered | 12 |
| 9 | 6 | aligned | 15 | 19 | 8 | Staggered | 15 |
| 10 | 6 | aligned | 20 | 20 | 8 | Staggered | 20 |

To properly capture the irradiance level of each LED configuration, an iterative method was employed to calibrate the average incident radiation on the inner side of the reactor window using chemical actinometry [110]. The actual light path in the PHO-μR is described in Scheme 3-3. In theory, the incident light intensity inside the reactor's surface should be the summation of $q_0$ and $q_3$. To further simplify the model and make it compatible with the analytical solution from the 1D Monte Carlo method, it was assumed that the absorption probability $p_{(\Omega)}$ of light in the path of reflection is negligible and the light will not attenuate along the reflection path. Thereby the iterated incident light intensity should be consistent with what we obtained in the calibration experiments.

Based on the result from the photon flux calibration, the average incident light intensity received on the microchannel's surface was found to be 941.27 W·m$^{-2}$ under the strongest driver current output (case 6 of Table 4-4). By performing stepwise iterative calculations, the value representing the average surface light intensity on the microchannel derived from the RTE simulations should therefore be close to this value. The value set here acts as the internal boundary condition inside the PHO-μR. The calibrated surface emission intensity of each LED was found to be 7620 W·m$^{-2}$ after several iterations. This value was therefore chosen as the new boundary condition in all RTE simulations, in line with all cases specified in Table 4-4.

The reactor's performance was evaluated based on the average incident radiation over the microchannel surface $\bar{E}$, the energy efficiency η, the global deviation of the irradiance $\bar{\sigma}$, and the heterogeneity factor $\hat{I}$. The respective expressions are given in Eq. 4-27 to Eq. 4-29.

$$\eta = \frac{A_{\mu R} \cdot \bar{E}}{N_L P_L} \qquad 4\text{-}27$$

$$\bar{\sigma} = \frac{\sqrt{\frac{1}{N}\sum_{m=1}^{N}(E - \bar{E})^2}}{\bar{E}} \qquad 4\text{-}28$$

$$\hat{I} = \frac{\sigma_{sam}}{\bar{E}} = \frac{\sqrt{(E-\bar{E})^2}}{\bar{E}} \qquad 4\text{-}29$$

where $E$ and $\bar{E}$ (W·m$^{-2}$) represent the local and average irradiance value, respectively. $A_{\mu R}$ (m$^2$) is the irradiated area of the PHO-μR. $N_L$ is the number of LEDs used. $P_L$ (W) is the emitted power by each LED. $m$ is the position index over the microchannel. $\bar{\sigma}$ is the global deviation of illumination heterogeneity. $\sigma_{sam}$ is the irradiance deviation of a single position and $\hat{I}$ is the heterogeneity factor.

The average irradiance level $\bar{E}$ and the energy efficiency $\eta$ are of significance for designing an illumination system, indicating the amounts of photons available for the photoreaction. $\bar{\sigma}$ evaluates the overall performance of the designed illumination system while $\hat{I}$ is used to indicate how the photons are spatially distributed and to what extent the illumination deviates over the illuminated domain. Higher $\bar{\sigma}$ values indicate more heterogeneity in the radiation distribution. Obviously, the optimal LED configuration should maximize $\bar{E}$ and $\eta$, while minimizing $\bar{\sigma}$.

#### 4.3.1.5 Predicted radiation field

Fig. 4-17 shows the average irradiance received at the inner surface of the microchannel for each of the proposed configurations. Each line denotes the irradiance level of one of the simulated arrangements at each LED-to-channel spacing. The solid lines stand for an aligned setting and the dash-dot line represents a staggered system. As expected, irradiance values decrease with an increase of spatial distances and increase along with the number of LEDs, among which the staggered system produces slightly higher irradiance values for the same number of LEDs. The increment in irradiance between two different arrangements is more distinguishable for smaller LED-to-reactor distances. The systems simulated gave irradiance values ranging from 415.63 W·m$^{-2}$ to 1294.10 W·m$^{-2}$.

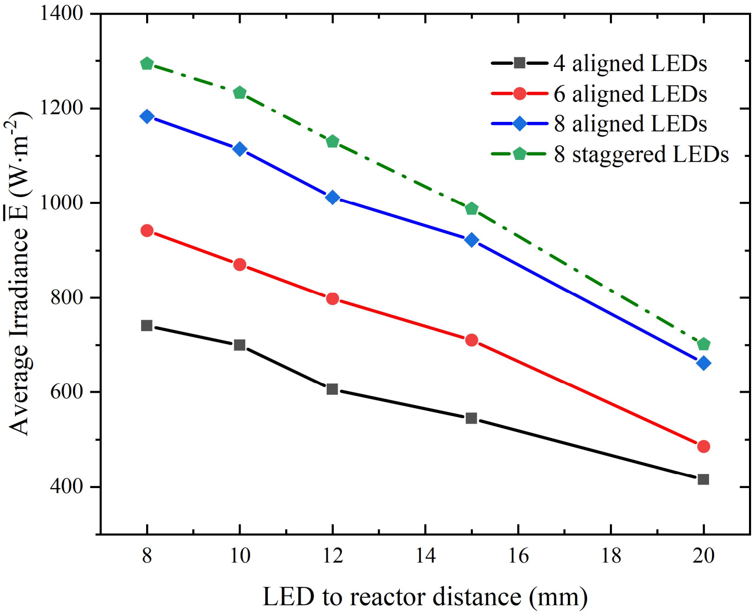

Figure 4-17 Irradiance level obtained from RTE simulation. Black solid (4 LEDs, aligned cases 1-5), red solid (6 LEDs, aligned cases 6-10), blue solid (8 LEDs, aligned cases 11-15), Olive dash-dot (8 LEDs, staggered cases 1-5). Refer to Table 4-4.

In Figure 4-18, the energy efficiency of the proposed lighting system is plotted versus the spacing. The configuration of 4 aligned LEDs always gives the highest energy efficiency, while the 6 aligned LED configuration at a distance of 20 mm shows the worst efficiency of all cases evaluated. The configuration of 8 aligned LEDs yields a lower energy efficiency than 6 LEDs at LED-to-reactor distances inferior to 15 mm, but this value is exceeded in reverse at a spacing of 20 mm. The staggered system results in a moderate efficiency value, which is higher for the corresponding aligned system. Overall, a clear linear decreasing trend can be observed with increasing distance. Analogous to the irradiance, the energy efficiency is lower for the aligned system, and both give the highest values at smaller spacing. Increasing the number of LEDs does not help to improve the energy efficiency, whilst the arrangement of the LEDs has a great influence on it. For 8 LED configurations, the energy efficiency reaches its maximum of around 35% for a distance of 8 mm and remains at its minimum at approximately 20% for a distance of 20 mm. Interestingly, all LED configurations give similar predicted values at the maximum distance (20 mm), except for 4 LEDs. In summary, the systems simulated are able to achieve 18.50%-42.42% energy absorption, giving an implicit indication of how many photons can be activated by the photocatalyst.

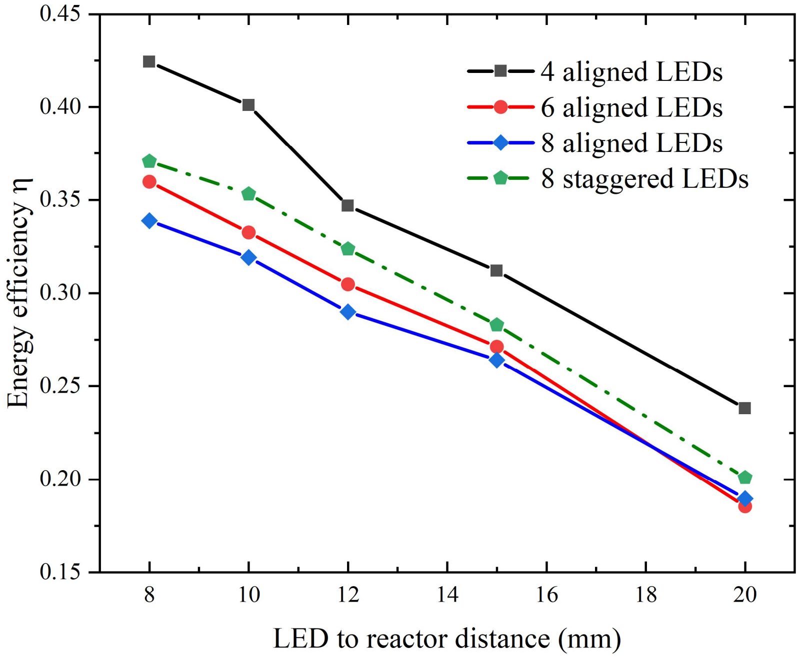

Figure 4-18 Energy efficiency of the simulated cases. Black solid (4 LEDs, aligned cases 1-5), red solid (6 LEDs, aligned cases 6-10), blue solid (8 LEDs, aligned cases 11-15), Olive dash-dot (8 LEDs, staggered cases 1-5). Refer to Table 4-4.

The degree of radiation homogeneity inside the reactor domain is also a parameter of interest. Hence, the global deviation of the irradiance at the inner surface of the microchannel for each of the proposed configurations was analyzed. Fig. 4-19 shows the global deviation obtained for each LED configuration, representing the degree of heterogeneity. The smaller the resulting value, the better the homogeneity of the system. Obviously, smaller deviation values appear with larger numbers of LEDs for the same arrangement type, implying more uniform illumination within the channel. An increased number of LEDs leads to a higher LED coverage and thus to a more uniform irradiation.

4 LEDs always gave the worst homogeneity due to poor LED coverage. In addition, the staggered system produces higher uniformity for the same number of LEDs when the distance exceeds 8 mm. Such differences become more pronounced when the distance from the LED to the reactor reaches 20 mm. In the cases investigated, the overall deviation in illumination heterogeneity increases with increasing LED-to-reactor distance. The trends here are in agreement with finding of Matiazzo et al. who reported that an increase in the LED-to-reactor distance leads to an increase in illuminance heterogeneity when 28 LEDs are incorporated in the system [160]. To make the illumination inside the microchannel as homogeneous as possible, a distance of 8 mm would be the best choice.

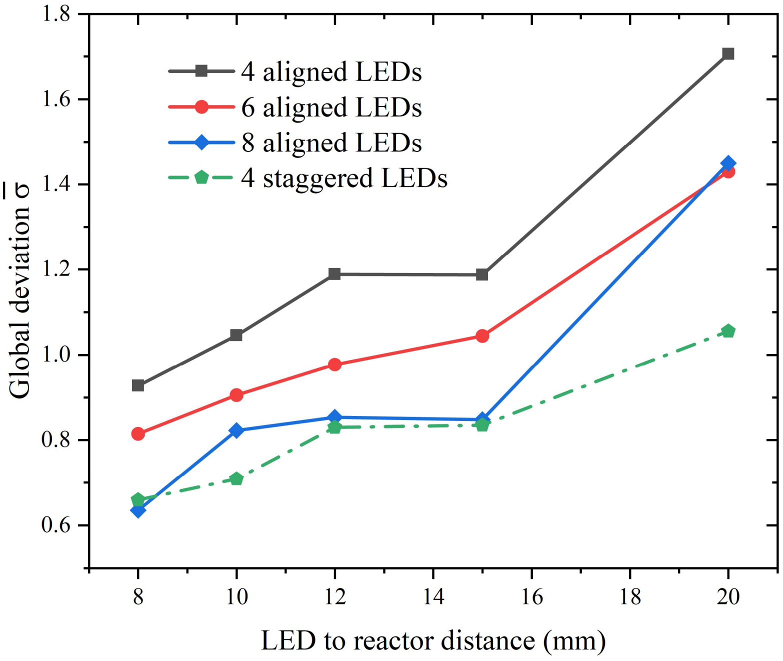

Figure 4-19 Global irradiance deviation of the simulated cases. Black solid (4 LEDs, aligned cases 1-5), red solid (6 LEDs, aligned cases 6-10), blue solid (8 LEDs, aligned cases 11-15), Olive dash-dot (8 LEDs, staggered cases 1-5). Refer to Table 4-4.

Fig. 4-20 shows the irradiance contour plots on the microchannel surface for different LED arrangements at a LED-to-reactor distance of 8 mm, analyzing the heterogeneity factor $\hat{I}$ (Eq. 4-29) weighted by the average irradiance. Several hot spots can be clearly observed in these contour maps, where the local irradiance is several times higher than the average. This is due to the nature of the DOM method as the light is concentrated in discrete directions specified by the quadrature sets. The locations of the hot spots are highly dependent on the geometric arrangement of the LEDs. The more LEDs are used, the more hotspots will appear. The presence of a hot spot will lead to a faster reaction rate and create a concentration gradient around it. Increasing the spatial distance between the

LED and the microchannel is not conducive to improving irradiation uniformity, as some blank areas representing dark areas appear in the contour map (Fig. A8-A11). Due to the diffuse nature of the LEDs, these areas receive very little radiation. From the kinetic point of view, almost no reaction will happen here. An ideal photoreactor design should avoid dark areas as much as possible and make sure the reacting region is fully illuminated. Taking into account at the same time the irradiance level, energy efficiency, and global deviation in irradiance and radiation uniformity, a distance of 8 mm would be the best choice for positioning the LEDs. Meanwhile, due to the diffuse nature of the LEDs, the more LEDs incorporated into the system, the more homogeneous the irradiance will get. From this perspective, using miniaturized LED light sources and having them distributed along the path of the microchannel would be a good option [98].

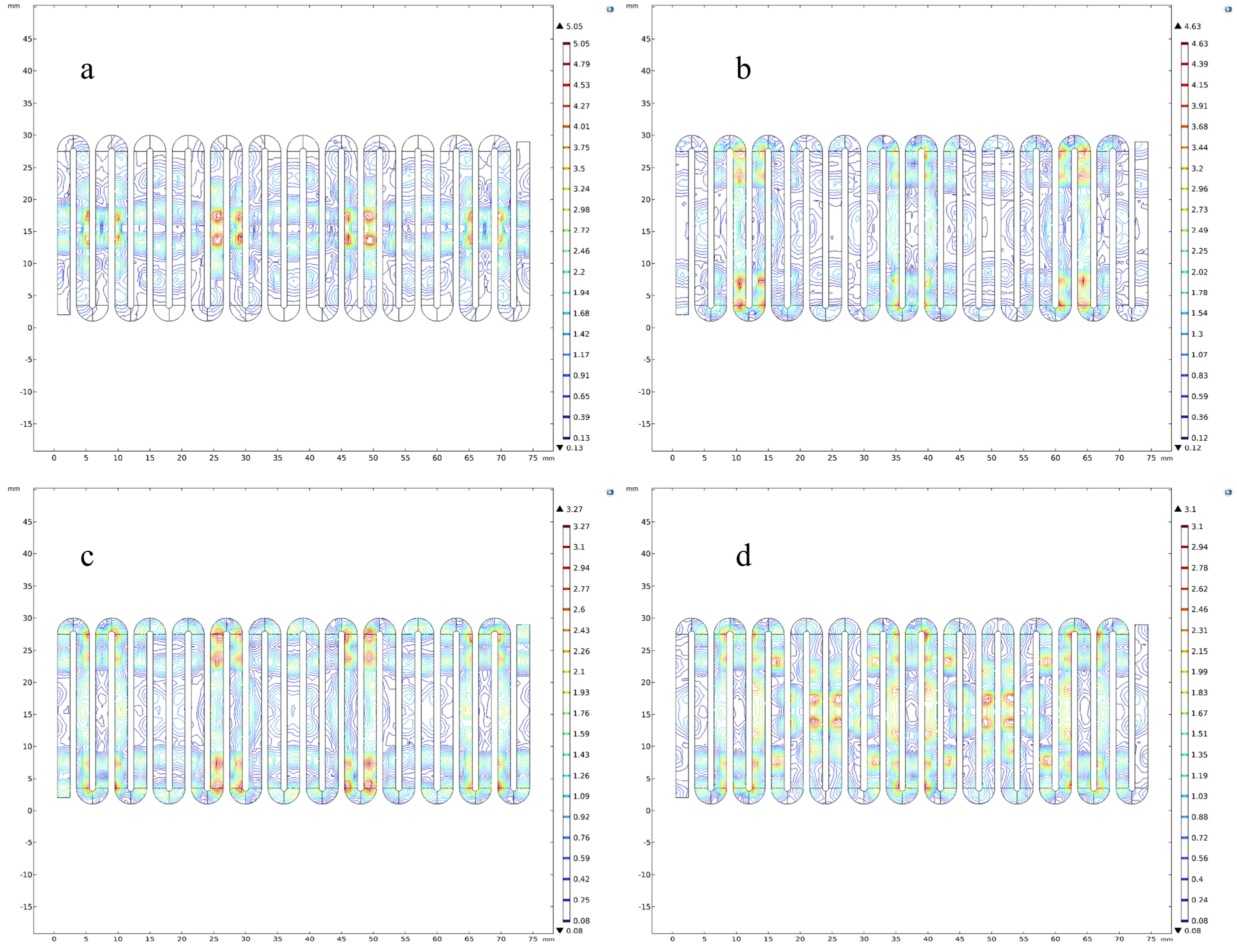

Figure 4-20 Irradiance contour plots of the microchannel surface at a LED-to-reactor distance of 8 mm. a) 4 aligned LEDs, case 1 of Table 4-4. b) 6 aligned LEDs, case 6 of Table 4-4. c) 8 aligned LEDs, case 11 of Table 4-4. d) 8 staggered LEDs, case 16 of Table 4-4.

### 4.3.2 Spatially resolved concentration prediction

#### 4.3.2.1 Reaction simulation model

Since the radiation fields of different LED configurations were obtained, the concentration field can be predicted by linking the radiation field with the reaction kinetics described in section 4.1. The iridium photocatalyst can be considered to be the only photon-absorbing species in the reaction mixture, as is demonstrated that the photon absorption of the reactant and product are negligible at the concentration level applied, and the process can still be treated as homogeneous according to a 2D axisymmetric simulation (Fig. 4-11a). Therefore, the optical properties of the photocatalyst were adopted at the peak emission wavelength of the used LED (458 nm), and the light scattering effect of the reaction media was ignored in the simulation. Due to the shift in the peak emission wavelength of the LED, the optical properties of the iridium photocatalyst used should be redefined. With the calibration curve at hand (Fig. 4-5a), the molar absorption coefficient of the photocatalyst at 458 nm was found to be 363.91 L·mol$^{-1}$·cm$^{-1}$ (Fig. 4-21).

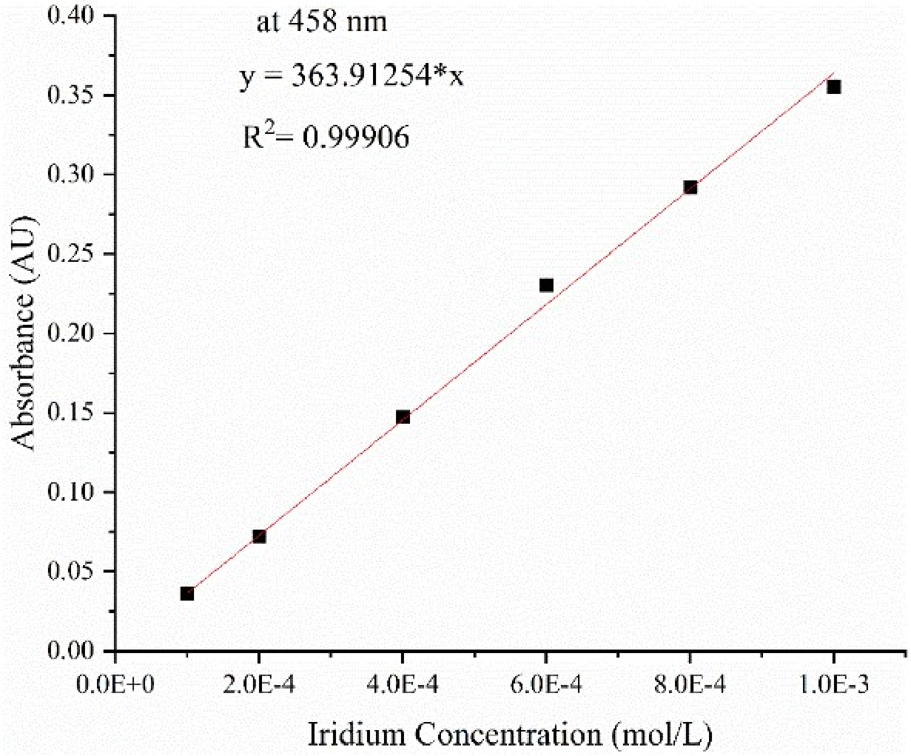

Figure 4-21 Determination of the molar absorption coefficient at 465 nm

The second-order photocatalytic process was simulated under isothermal and steady state conditions. The reaction mixture in laminar flow regime was considered as an incompressible Newtonian fluid. The numerical solution of the concentration field was obtained by solving the mass, momentum and species conservation equations from Eq. 4-30 to Eq. 4-32. Equation 4-33 was introduced to take advantage of the radiation field obtained from the RTE simulation and the intrinsic rate constant procured from the kinetic study.

$$\rho(u \cdot \nabla)u = \nabla \cdot [-pI + \mu(\nabla u + (\nabla u)\mathrm{T}) - \tfrac{2\mu}{3}(\nabla \cdot u)I] \qquad 4\text{-}30$$

$$\rho\nabla \cdot u = 0 \qquad 4\text{-}31$$

$$\nabla \cdot (-D_i \nabla c_i) + u \cdot \nabla c_i = R_i \qquad 4\text{-}32$$

$$R_i = \frac{-dC_{an}}{dt} = k_{intr}\frac{LVREA}{E_\lambda}C_{an}^{\;2} \qquad 4\text{-}33$$

$$LVREA = kappa_s \times G \qquad 4\text{-}34$$

$$E_\lambda = N_{\mathrm{A}}\frac{hc}{\lambda} \qquad 4\text{-}35$$

$$kappa_s = C_{Ir} \times E_{Ir,\lambda} \qquad 4\text{-}36$$

where ρ ($\mathrm{kg \cdot m^{-3}}$) represents the fluid density, $u$ ($\mathrm{m \cdot s^{-1}}$) is the velocity field, $p$ (Pa) represents pressure, and $I$ is the identity tensor. $\mu$ (Pa·s) is the dynamic viscosity, $D_i$ ($\mathrm{m^2 \cdot s^{-1}}$) stands for diffusivity of species $i$, $c_i$ is the concentration of species $i$, $R_i$ ($\mathrm{mol \cdot m^{-3} \cdot s^{-1}}$) is the reaction rate of species $i$, $k_{\mathrm{intr}}$ ($\mathrm{m^6 \cdot mol^{-1} \cdot mol_{photon}^{-1}}$) is the intrinsic rate constant, where the unit of $\mathrm{mol_{photon}}$ is equal to “einstein” used in the kinetic study. LVRPA ($\mathrm{W \cdot m^{-3}}$) is the local volumetric rate of photon absorption that is linearly related to the apparent rate constant at weak photon absorption. $\mathrm{E_\lambda}$ ($\mathrm{J \cdot mol_{photon}^{-1}}$) is the energy conveyed by one mole of photons at wavelength λ (nm). $C_{an}$ stands for the local concentration of the F-tagged aniline precursor **1a**. $kappa_s$ ($\mathrm{m^{-1}}$) is the optical thickness of the photocatalyst at wavelength $\lambda$. G ($\mathrm{W \cdot m^{-2}}$) represents the incident radiation at each point over the microchannel solved by the RTE equation. $\mathrm{N_A}$ is the Avogadro constant. $h$ is known as the Planck constant. $c$ ($\mathrm{m \cdot s^{-1}}$) is the speed of light. $\lambda$ (nm) stands for the peak emission wavelength of the LED (458 in this case). $C_{Ir}$ is the concentration of the iridium photocatalyst **2** in the experiments. $E_{Ir,\lambda}$ represents the Napierian absorption coefficient of the iridium photocatalyst at the wavelength of interest.

The unit of the light intensity derived from the RTE simulation is watt per square meter ($\mathrm{W/m^2}$). By linking this value with the Einstein-Planck relationship (Eq. 4-35), the unit can be properly converted and used in the rate expression (Eq. 4-34).

#### 4.3.2.2 Boundary conditions

The flow was considered fully developed using the average velocity of the fluid at the inlet, and zero-gauge pressure at the reactor outlet. Inflow conditions were equal to the inlet concentrations. The reactor’s walls were set as no slip walls, and zero diffusive molar flux was employed for all species. The mass transport was prescribed to be dominated by convection at the outlet.

$$\bar{u} = \frac{Q_{in}}{A} \tag{4-37}$$

$$c_i = c_{0,i} \tag{4-38}$$

$$n \cdot (D_i \nabla c_i) = 0 \tag{4-39}$$

In addition, an iterative method was adopted to simulate the whole reaction region inside the reactor since this is composed of three subsequent reaction zones. As a result, the average concentration at the outlet of the previous simulation domain was reused as the inlet concentration for the next one (Eq. 4-40). The syntax of the operation in COMSOL uses the built-in “withsol” operator.

$$c_{i\_in,idex} = \bar{c}_{i\_out,\ idex\text{-}1} \tag{4-40}$$

where $\bar{u}$ represents the average inlet velocity, $A$ is the cross-sectional area of the microchannel in the PHO-μR, $Q_{in}$ is the volumetric flow rate , $c_{i\_in}$ is the inlet concentration of species $i$, $idex$ is the index factor (1, 2, 3 stands for the 1st, 2nd and 3rd simulative domain), $\bar{c}_{i\_out}$ is the average outlet concentration of species $i$. The conditions for reaction simulations are summarized in Table 4-5.

Table 4-5 Conditions for the CFD modelling

| | |
|---|---|
| Residence time | 5 min |
| Pressure outlet | Atmospheric |
| Inlet concentration of aniline precursors **1a** | 25 mol $\cdot\, m^{-3}$ |
| Inlet concentration of indole product **3a** | 0 mol $\cdot\, m^{-3}$ |
| Reaction rate expression | $R_i = k_{intr} \frac{LVRPA}{E_\lambda} \mathrm{C}_{\mathrm{an}}^{2}$ |

### 4.3.2.3 Simulative domain and grid dependency

To ensure that the radiation field is correctly mapped onto the microstructure channel, the domain for reaction simulation was replicated from the same geometry as it was used in the RTE simulation. The operation of radiation field mapping can be performed with the built-in “withsol” operator in COMSOL, either. Another finer structured mesh was created for the species transport simulations and the results converged at approximately 846,000 grid elements.

### 4.3.2.4 Predicted concentration field

To evaluate how the LED configuration influences the photocyclization process inside the PHO-μR, reaction simulations were performed by linking fluid dynamics, species transport and radiation fields in each illumination system. Firstly, the velocity field under steady state was calculated and then used as input for the species transport study. The integration of the radiation field with reaction kinetics is achieved by introducing a variable named with "LVRPA" in COMSOL. A reference distance of 8 mm was set since this gave the highest radiation homogeneity. An intrinsic rate constant of 36.24 $L^2 \cdot mol^{-1} \cdot mol_{photon}^{-1}$ was adopted in Eq. 4-33, employing the conclusion described in section 4.2.4. The CFD simulations were performed with the same conditions as indicated in Table 4-5, except for the radiation field. Figure 4-22 depicts the distribution of the concentration field in a given unit cell for four different LED arrangements. For a kinetically controlled process (i.e., short residence time), distinct concentration gradients can be observed near the hot-spots for each configuration, which results in a highly inhomogeneous concentration distribution inside the microchannel. Evidently, stronger irradiance contributes to the increased LVRPA, which leads to the observation that 4 aligned LEDs system provides the lowest concentration values whilst the 8 staggered LEDs system generates the highest concentration values. The concentration distribution inside the microchannel is also consistent with its radiation field and light uniformity, i.e., the 4 aligned LEDs configuration gives the most pronounced concentration gradients, while the 8 staggered LEDs system has a relatively uniform concentration gradient. Moreover, the photon attenuation and light reflection effect can be observed here either. A higher concentration of products appeared close to the optical glass side and the bottom surface of the microchannel.

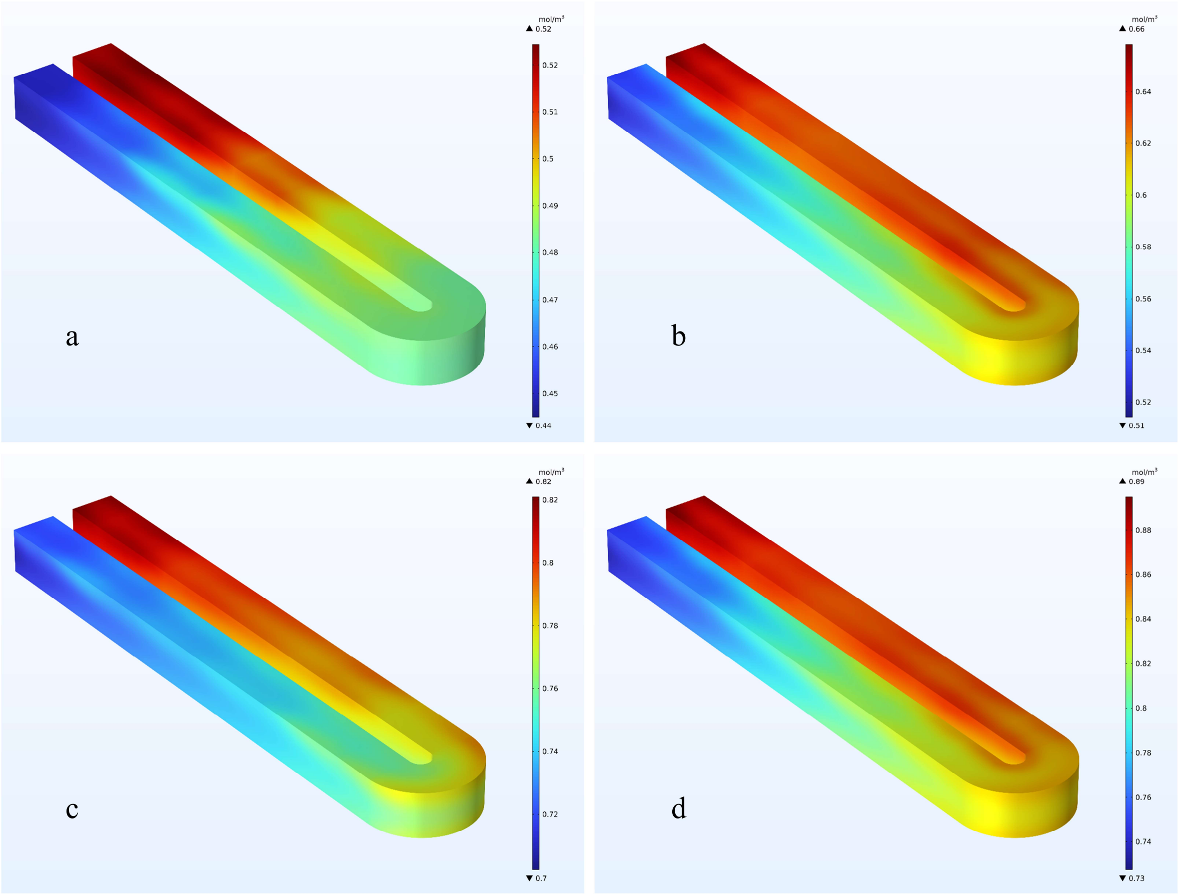

Figure 4-22 Predicted concentration fields in a section of the microchannel. a) 4 aligned LEDs, case 1 of Table 4-4. b) 6 aligned LEDs, case 6 of Table 4-4. c) 8 aligned LEDs, case 11 of Table 4-4. d) 8 staggered LEDs, case 16 of Table 4-4. Conditions specified in Table 4-5.

A zoom-in view of Figure 4-22b is shown in Figure 4-23b. Interestingly, the concentration values are higher on the upper and lower surfaces at the bend of the microchannel, while the values are smaller in the center of the channel. On one hand, due to the given short residence time, this process is kinetically controlled, and the different velocity fields result in distinct concentration gradients along the vertical direction of the microchannel. On the other hand, the LVRPA on the bottom side of the microchannel is enhanced due to the photon reflection inside the PHO-μR, causing a faster local reaction rate and higher local product concentration. The discrepancy here captures well the nature of the fluid dynamics, reaction kinetics, and photon reflection phenomenon inside the channel, where the velocity field inside the channel exhibits a parabolic distribution (Fig. 4-23a) due to laminar flow, resulting in a longer residence time close to the wall, and therefore a higher local concentration. If the same reaction is performed in a non-reflective photoreactor (e.g., PDMS), where photon reflection is not considered in the simulation, the concentration field will be strictly related to the radiation field, while the effect of the velocity field on the concentration field will be almost negligible (Figure 4-23c).

Consequently, the indole product will accumulate near the optical side and the concentration will decrease along the increasing photon penetration path since it is assumed that all the photons will be completely absorbed at the bottom of the microchannel. This proves that the radiation field in the photoreactor has a very important effect on the concentration distribution. An ambiguous assessment of the radiation field will result in the inability to correctly access the spatially resolved information within the microchannel. This is especially the case when uniform irradiation is not easily obtained in photoreactors, and the effect of reflection cannot be ignored.

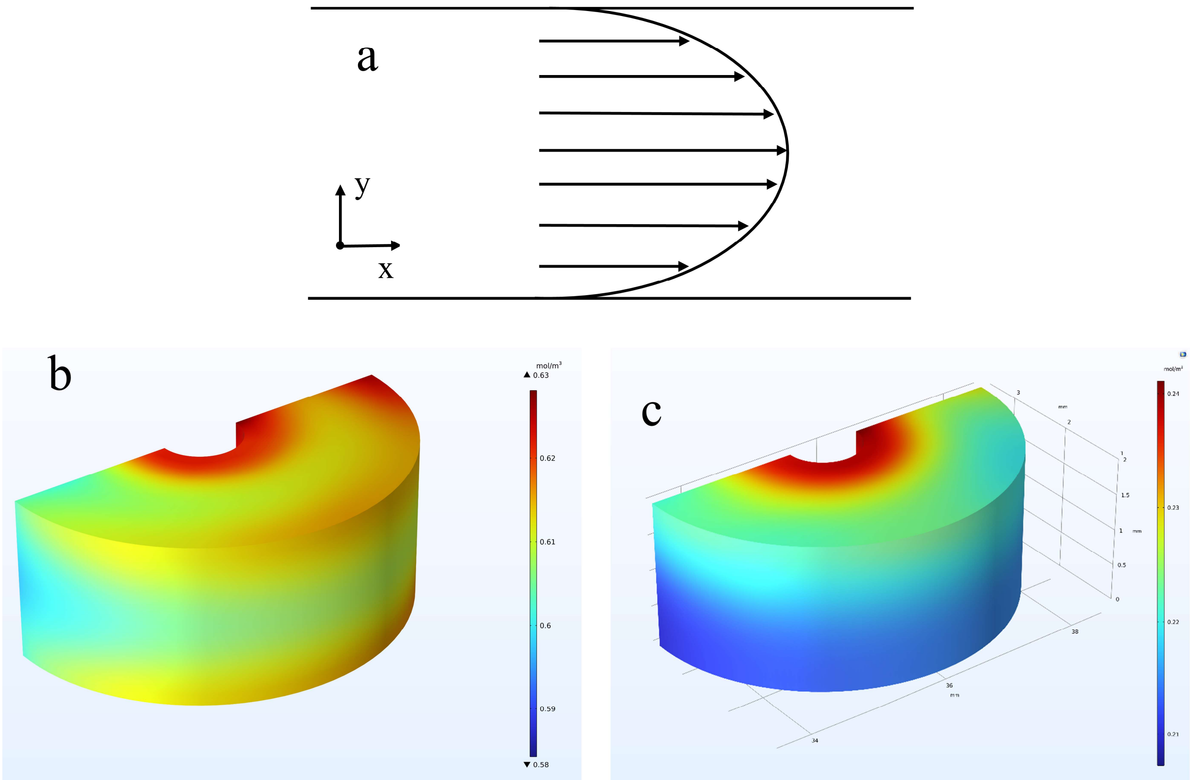

Figure 4-23 (a) The parabolic velocity distribution due to laminar flow (b) Zoom-in plot of the predicted concentration field in the partial microchannel. 6 aligned LEDs, case 6 of Table 4-4, with reflection, the emissivity of stainless-steel plate in simulation is considered to be 0.092. (c) Zoom-in plot of the predicted concentration field in the microchannel. 6 aligned LEDs, case 6 of Table 4-4, without reflection, the emissivity of stainless-steel plate in simulation is considered to be 1.

Besides, CFD simulation is also helpful for finding suitable operating conditions in flow. The effects of residence time on the concentration field were studied. Figure 4-24 shows a typical zoomed-in plot of the effect of residence time on the concentration field for the 6 aligned LEDs configurations. It is observed that for a short residence time of 5 min, a strong concentration gradient appears within the channel (Fig. 4-24a). If the residence time is extended, the situation becomes completely different. When the residence time is 60 minutes, the concentration gradient in the microchannel is significantly reduced and a more uniform concentration distribution can be achieved (Fig. 4-24b). Further extension of the residence time did not result in a more noticeable change. This change reveals a shift in the photochemical reaction process from kinetic control to diffusion control. For a kinetically controlled process, the concentration field is highly dependent on the radiation field, since the effect of diffusion is limited, leading to a non-uniform concentration distribution along the microchannel. In contrast, if the residence time is long enough, the diffusion inside the channel is sufficient, thereby creating a more uniform concentration profile. Integrating the radiation field with the reaction kinetics is beneficial to restore the real situation of the chemical reaction inside the channel as much as possible. By variation of the residence time in CFD simulations, it is possible to find the right operating conditions while avoiding mass transfer resistance in the microchannel as much as possible.

Predicted concentration field: t_res 5 min

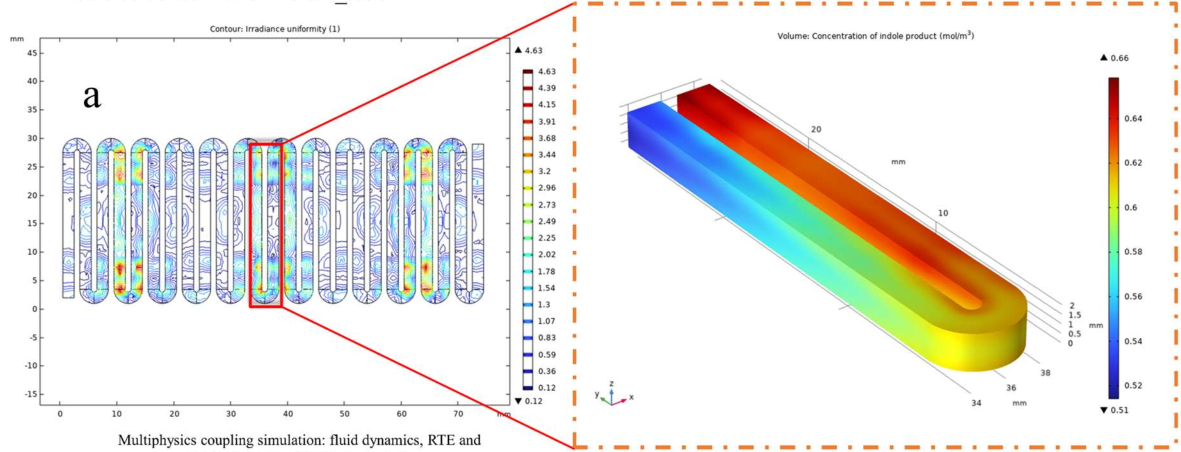

Multiphysics coupling simulation: fluid dynamics, RTE and species transport, 3D stationary study

Predicted concentration field: t_res 60 min

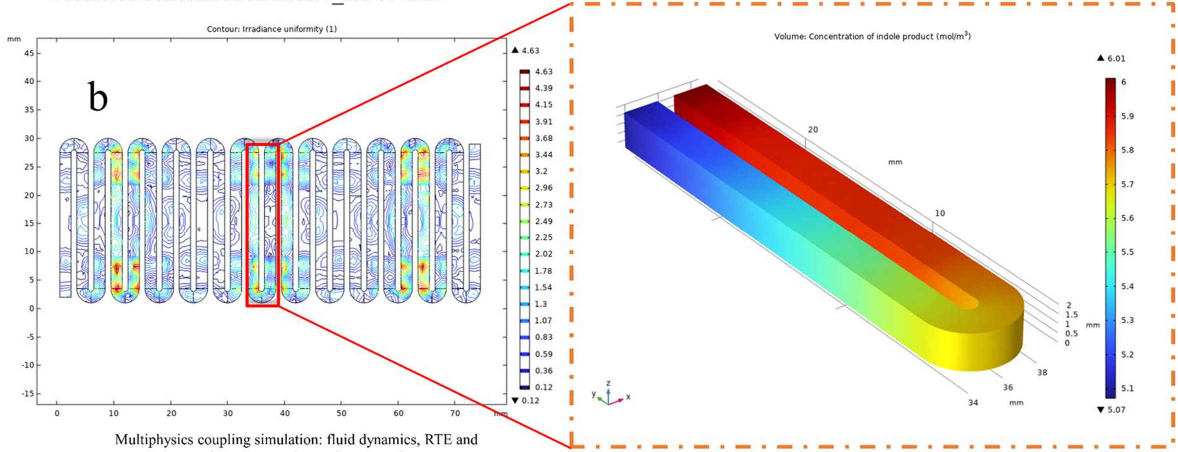

Multiphysics coupling simulation: fluid dynamics, RTE and species transport, 3D stationary study

Figure 4-24 (a) Zoom-in concentration plot for 6 LEDs configuration at a distance of 8 mm. The residence time for reaction simulation was set to 5 min. (b) Zoom-in concentration plot for 6 aligned LED configuration at a distance of 8 mm. The residence time for reaction simulation was set to 60 min.

### 4.3.3 Model validation

#### 4.3.3.1 Design of validation experiments

For a homogeneous photocatalytic process, the radiation field in the reactor should be as homogeneous as possible to ensure that the conversion is uniform everywhere in the microchannel, thus minimizing undesired concentration gradients within the channel. According to the simulation results, the 8-staggered LED arrangement turned out to be the most ideal candidate for the final LED board design since the maximum irradiance level and minimum global deviation are obtained, even though the energy efficiency is moderate. However, due to the geometrical constraints of the reactor and the LEDs themselves, the LEDs on the edges will overlap between two adjacent boards, resulting in an inconsistent radiation distribution and erroneous evaluation of the system. Finally, for the LED board, the 6 aligned LEDs arrangement was ultimately selected as this showed the second-best performance.

For photocatalysis, the light intensity arriving at the photoreactor is of great importance to the kinetics. As the light intensity increases, the relationship between the reaction rate and the photon flux density will gradually transition from a linear correlation to a root-mean-square correlation, and finally become independent of the photon flux under photon saturation conditions [87]. In order to transfer the reaction model from two-dimensional to three-dimensional simulations using the intrinsic rate constants derived from the kinetic study, and to validate the model between two different test benches, the weak photon absorption conditions of the studied system should be ensured. In this scenario, the local reaction rate is linearly related to the light intensity and the assumption of Eq. 4-33 is still valid. Therefore, validation experiments were carefully designed and performed with the chosen LED configuration (case 6 of Table 4-4) and reduced LED power output (40%) to ensure weak photon absorption conditions, corresponding to a calibrated average surface irradiance value around 374 $W \cdot m^{-2}$. The residence time for the validation experiments was set between 30 min and 180 min in each simulative region, which resulted in a total residence time between 90 min and 540 min in the PHO-μR.

#### 4.3.3.2 Experimental procedures

The current was modulated by the LED driver and set to a power output of 40%. The radiative power used here is consistent with the one used in the photon flux calibration experiments and with the boundary condition set in the reaction simulation. The LEDs were fixed at a distance of 8 mm from the microchannel and turned on for at least 30 minutes prior to each experiment to ensure a stable current. A circulating cooler was running throughout tests to get rid of the radiative heating and prevent the LEDs from wavelength shifting. Thus, keeping the reaction as close to isothermal as possible.

To complete the steady-state operation, the solution was prepared in a volume of 35 mL, which is consistent with the stationary study settings for the reaction simulation. The reaction solution was prepared as follows: around 600.0 mg of starting material **1a** (0.8844 mol, 1.00 equiv) was weighed and transferred into a round bottom flask. 35 mL of dry acetone was added, followed by a PTFE magnetic stirring bar. The solution was continuously stirred until homogeneous. Then, 34.30 mg of the iridium photocatalyst **2** (3 mol%) was added and stirred until homogeneous again. The solution was freshly prepared each time and withdrawn by a 50 mL HSW syringe (piston diameter 29.20 mm). The syringe was mounted on a Harvard syringe pump (PHD ultra). Then, the reaction mixture was pumped through the meandering microchannel and irradiated with blue LEDs in the PHO-μR. Finally, the reaction mixtures were collected 3 times under steady state after 2.5 times residence volumes elapsed. The yield of each sample was analyzed by 1H-NMR.

#### 4.3.3.3 Comparison between reaction and simulation

Table 4-6 summarizes the conditions for the validation experiments and compares the results between simulations and experiments (three times average) at the residence time of 120 min and 180 min, respectively. Between these two data sets, the relative errors between simulations and experimental data acquired were equivalent to 3.26% and 3.81%. Such small relative errors indicate that the spatially resolved reaction simulation considering radiation distribution can reproduce the actual photochemical transformation well.

Table 4-6 Conditions for validation experiments

| | | |
|---|---|---|
| Total power output (40%) | 7.2 W | 7.2 W |
| Calibrated average incident radiation | 374 W·m$^{-2}$ | 374 W·m$^{-2}$ |
| Residence time for domain | 120 min | 180 min |
| $\overline{\boldsymbol{X_{Exp}}}$ [a] | 61.42% | 71.43% |
| $\boldsymbol{X_{CFD}}$ | 59.42% | 68.71% |
| Relative error (%) | 3.26 | 3.81 |

a) The experimental yield $\boldsymbol{X_{Exp}}$ is the average of three samples under steady state.

Besides, to ensure the correctness of the validation data, the NMR yield of different residence times ranging from 30 min to 180 min can be found in Table 4-7. $\boldsymbol{X_{CFD}}$ is the predicted yield from multiphysics-coupled reaction simulations. $\boldsymbol{X_{Exp}}$ is the yield of each sample from 1H-NMR measurement while $\overline{\boldsymbol{X_{Exp}}}$ is its mean value. Good reproducibility is easily obtained by steady-state operation except for a residence time of 180 min. Such inconsistency in the 180 min data may be attributed to the high volatility of acetone, causing the product to accumulate at the outlet and not be fully collected. Nevertheless, the good linearity between the inverse of the concentration and the residence time shows the correctness of collecting data (Fig. 4-25), which is consistent with the $2^{nd}$ order reaction.

Table 4-7 Comparison of results between validation experiments and simulations

| Residence Time [a] (min) | $\boldsymbol{X_{CFD}}$ (%) | $\boldsymbol{X_{Exp}}$ (%) |  |  | $\overline{\boldsymbol{X_{Exp}}}$(%) |
|---|---|---|---|---|---|
| 30 | 26.84 | 35.48 | 35.69 | 35.28 | 35.48 |
| 45 | 35.49 | 47.51 | 47.78 | 47.78 | 47.69 |
| 60 | 42.25 | 53.70 | 53.60 | 53.38 | 53.56 |
| 120 | 59.42 | 61.01 | 61.64 | 61.61 | 61.42 |
| 180 | 68.71 | 68.85 | 75.12 | 70.33 | 71.43 |

a. The residence time refers to the actual set residence time of the individual reaction regions, rather than the whole reaction domain of PHO-μR.

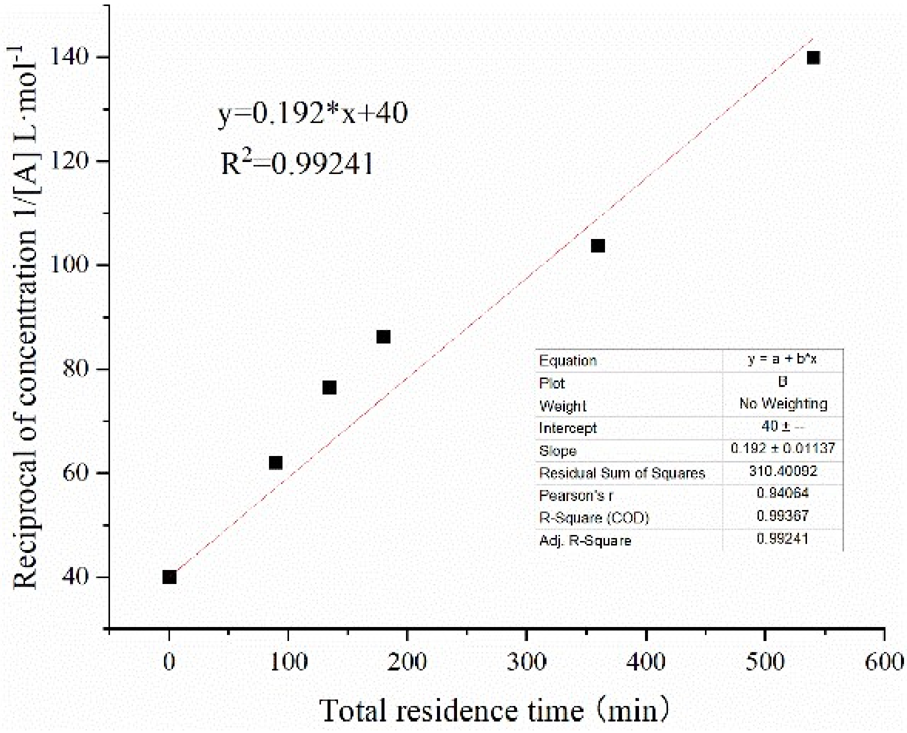

Figure 4-25 Linear relationship between the inverse of substrate concentration and residence time for validation experiments in PHO-μR.

However, it is still important to mention here that a huge deviation between simulations and experiments can be observed for the first three datasets in Table 4-7. This may be attributed to a faster reaction rate of the photoreaction at low conversions. As the reaction progresses and the conversion increases, the product will absorb more photons, thus decelerating the reaction rate. This effect was caused by the competition for photon absorption between the photocatalyst and the indole product becoming non-negligible during the reaction process. Furthermore, the intrinsic rate constant used here is derived from the apparent rate constant, which is a macroscopic average value. In fact, the intrinsic rate constant adopted in the spatially resolved reaction simulation is also an average value. The process is simplified and only homogeneous photocatalysis is considered. Therefore, reaction acceleration is possible at the initial stage of the photochemical process, while reaction deceleration is realistic at the later stage of the reaction due to photon competition. As a result, the experimental conversions were always larger than prediction in this region. The trend here is similar to the 2D axisymmetric simulations presented in Fig. 4-11a (in the purple dash-dot rectangle region, the actual yield exceeds the simulated value, and the error is also more than 10%). The situations correspond to the first three datasets in Table 4-7. Nevertheless, simulations at higher conversion conditions are more consistent with experimental results. Thus, the model used for the RTE simulations is successfully validated.

### 4.3.4 Interim conclusion

The incident radiation field in the PHO-μR was successfully evaluated by the DOM method in COMSOL, which served as a useful tool to find the optimal LED configurations for photoreactor test benches. The numbers of LEDs used, the arrangement of the LEDs, as well as the LED-to-reactor spacing were comprehensively studied considering 20 different cases in the CFD simulations. The resulting irradiance level, energy efficiency, global light heterogeneity, as well as incident radiation distribution over the reactor's window were systematically analyzed. The proposed systems provided average surface irradiance ranging from 415.63 $W \cdot m^{-2}$ to 1294.10 $W \cdot m^{-2}$, with energy efficiencies between 18.50% and 42.42%. A suitable LED-to-reactor distance of 8 mm was determined, which allowed to achieve the highest irradiance level and least light heterogeneity in the PHO-μR. With this LED-to-reactor distance, it is possible to achieve as homogeneous illumination as possible in this special reactor.

In addition, the radiation fields of different LED configurations were integrated with CFD simulations to get spatially resolved reaction predictions. The photocyclization process considering the radiation distribution was simulated for 4 different LED configurations with 5 LED-to-reactor distances, giving a total of 20 cases. Light attenuation phenomena, the presence of local hotspots caused by diffuse illumination, and boundary layer effects due to laminar flow are reflected in detail from the concentration plots in the simulations, which give a microscopic view of the actual process. Moreover, the reaction simulations are also able to observe the shift of the process from kinetic to diffusion control.

Finally, considering geometric constraints and balancing the optical performance of various configurations, the 6 aligned LEDs arrangement was identified as the best choice for the actual LED board and employed in the validation experiments. The intrinsic rate constant procured from the kinetic study was used in this fully coupled simulation, and the model was validated with experiments. As discussed earlier, the proposed reactor model is more suitable for higher conversion cases, and the experimental results for a residence time of 120 minutes and 180 minutes matched well with simulations with a relative tolerance below 5%, showing the correctness of the proposed model in turn. The kinetic model proposed here is helpful to scale up this reaction. In addition, the model needs further refinement to get a better understanding of the photon competition between the indole product and the photocatalyst, and the acceleration phenomenon at the initial stage of the reaction.

## 4.4 Productivity investigation of the PHO-µR

The discussion in subsection 4.3 has confirmed the most appropriate LED configuration and the optimal LED-to-reactor distance. The next step was to increase the productivity of the PHO-µR and to find the optimal operating conditions in flow. The experimental conditions employed were almost identical to those described in section 4.3.3.2, except that the operating power output of the LEDs was 100%, which resulted in an actual energy output of 6 W per reaction zone and a total energy output of 18 W for the constructed microfluidic system. According to the results of the 3D simulations, the axial concentration gradient of the indole product in the microchannel does not change significantly at residence times longer than 60 minutes, indicating the reaction is about to reach equilibrium. It is therefore highly likely that the optimum operating conditions will be found at a residence time of less than 60 minutes. The residence time for productivity investigation is therefore set below 60 minutes. In addition, DMSO was also employed as the solvent because it is reported as the best choice for this photochemical transformation [143]. Table 4-8 summarizes the experimental results on the residence time and the chosen solvent.

Table 4-8 Conditions for productivity tests

| Entry | Residence time[a] | Solvent | Power output | Calibrated radiation | NMR yield[b] |
|---|---|---|---|---|---|
| 1 | 15 min | Dry acetone | 18 W | 941.27 W/m$^2$ | 41% |
| 2 | 30 min | Dry acetone | 18 W | 941.27 W/m$^2$ | 75% |
| 3 | 60 min | Dry acetone | 18 W | 941.27 W/m$^2$ | 75% |
| 4 | 30 min | DMSO | 18 W | 941.27 W/m$^2$ | 72% |
| 5 | 60 min | DMSO | 18 W | 941.27 W/m$^2$ | 87% |

a) This refers to the actual set residence time of the individual reaction regions. b) The NMR yield is the average of three samples under steady state.

The NMR yield increased from 41% to 87% as the residence time increases from 15 to 60 minutes. Interestingly, the result yield with acetone as solvent did not increase further after 30 minutes. This confirms the hypothesis that the photoreaction may be approaching equilibrium when the axial concentration gradient within the microchannel is negligible. The optimal residence time for the experiment can be obtained near this critical time threshold. However, the situation is inconsistent with the result when DMSO was used as the solvent. An increase in NMR yield was observed from 72% to 87% as the residence time was increased from 30 to 60 minutes. This may be attributed to the solvent effect of the reaction, and one should also note that complete conversion is hardly achieved in acetone in batch photosynthesis. Meanwhile, a higher conversion would be theoretically obtained with DMSO as the solvent. However, the difference in the viscosity of the two solvents could affect the diffusion and convection processes of the photoreaction. This would account for the fact that the NMR yield with acetone as solvent is slightly higher than that with DMSO in the experiment with a residence time of 30 min. Furthermore, the productivity was greatly enhanced in the PHO-μR (75% for 90-minute residence times) compared to the results acquired in the CAP-μR (63% for 180-minute residence times), which requires 47.6 W of energy output, while the latter requires only 18 W of energy output. The calculated photochemical space time yield value (PSTY, calculated by STY divide by the power of the light sources) in the PHO-μR reached 0.6944 mmol$\cdot L^{-1} \cdot h^{-1} \cdot W^{-1}$, which is 6-fold higher than the same value in the CAP-μR (0.1108 mmol$\cdot L^{-1} \cdot h^{-1} \cdot W^{-1}$). Performing the same photoreaction in the PHO-μR therefore results in higher productivity and reduced energy consumption.

## 4.5 System commissioning with mini-IR sensors

### 4.5.1 Installation of mini-IR sensors on the PHO-µR

With the optimal LED configuration at hand, the final step was to combine the miniaturized infrared sensor from Freiburg with the PHO-µR for *in situ* IR detection. This requires considering both the geometrical limitations of the lighting module, the micro photoreactor, the infrared lighting module, and the infrared sensors. The infrared detection module should be added to the reaction system in a way that does not affect the configuration of the reaction lighting system as much as possible. Apart from the design of the infrared sensors and infrared light source themselves, the dimensions of the individual components are known, and their corresponding 3D models can be found online, so Autodesk Inventor® 2022 was used to quickly debug and design realistic and feasible component assemblies. Accordingly, the successfully commissioned bracket design could be exported and manufactured using 3D printing technology. As previously envisaged, the infrared light sources and infrared detectors are to be placed between two adjacent reaction regions. Due to the eventual use of transmission mode for infrared detection, the infrared light source needs to be aligned with the sensor to minimize system errors due to actions such as disassembly and reassembly. This is also a part of system standardization. Furthermore, in order to keep the LED configuration consistent with the best results derived from the RTE simulations, the actual infrared sensor was placed in a different position from the original design presented in Fig. 2-6. It has been found that placing the infrared light source at the backside of the reactor and the sensor on the top is the most logical design, meaning that in this configuration, visible and infrared light travel in opposite directions. Figure 4-26a shows the designed prototype with the reaction lighting module deliberately placed away from the IR bracket for better visualization. In this configuration, the reaction lighting module does not overlap with the 3D-printed sensor bracket, thus ensuring the radiation of each reaction area is identical and its distribution is consistent with the RTE simulation. It also means one can use the reaction model proposed in section 4.3.2 for yield prediction and compare it with the results obtained from IR inspection for process control. In addition, the 3D-printed bracket[1] was fabricated to accommodate both the infrared light sources and the infrared sensors, where the sensors are placed on the top while the light sources are on the bottom (Fig. 4-26b). The light sources and sensors are designed as plug-in structures. The infrared bracket is

---

[1] The prototype of the bracket received help from project team member David Ilioaë, personal communication.

secured with screws and nuts to ensure the infrared light is aligned with the infrared detector. The plug-in design also allows the infrared detection system to be as flexible as possible, as the type of sensor used can be substituted, depending on the range in which the characteristic IR absorption peaks of the photoreaction appear.

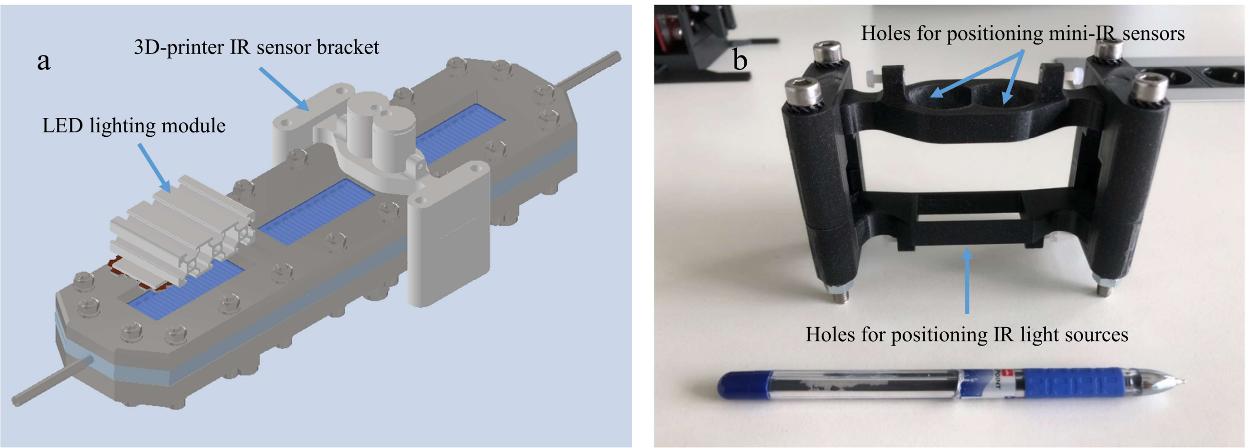

Figure 4-26 a) 3D design and positioning of the PHO-μR, LED lighting module, and 3D printing IR sensor bracket for microfluidic platform assembly in Autodesk Inventor. b) Figure of the 3D printing IR sensor bracket.

### 4.5.2 Software development

Previously designed dimmable lighting systems were manually controlled via external LED drivers with variable resistors. Such a design is not very convenient for process control. Since the LED driver used has pulse width modulation (PWM) signal conditioning, the actual output current of the LED driver could be adjusted by changing the duty cycle of the signal, thus adjusting the light intensity received by the PHO-μR. Similar process control can be performed via LabVIEW to regulate a variety of different system inputs. Simple LED switching can be done using the Boolean control in LabVIEW, while dimmable current outputs can be achieved by PWM control. Likewise, real-time temperature control can be automated. All possible modules for process control were clarified and developed. Therefore, a National instruments (NI) control box made of a 9189 CompactDAQ chassis was assembled for process control, containing two NI 9475 digital output modules, two NI 9481 relay modules, and one NI 9216 RTD module (Fig. 4-27). Typically, the LEDs used are powered by 350 mA constant LED drivers in the NI box, allowing them to operate properly at their rated current. If the light intensity of the system needs to be adjusted, the Meanwell LED driver should be used, the output of which needs to be connected to the counter output module of the NI control box for programmed control, rather than using an external variable resistor. The designed control system can also provide 8 channels of temperature monitoring, using several PT 100 RTD sensors.

All the above functions were implemented via LabVIEW codes. Moreover, the project team members from Freiburg Universities have provided the control program for the infrared sensors. As a result, several programmable software packages for the *in situ* microfluidic photoreactor were developed.

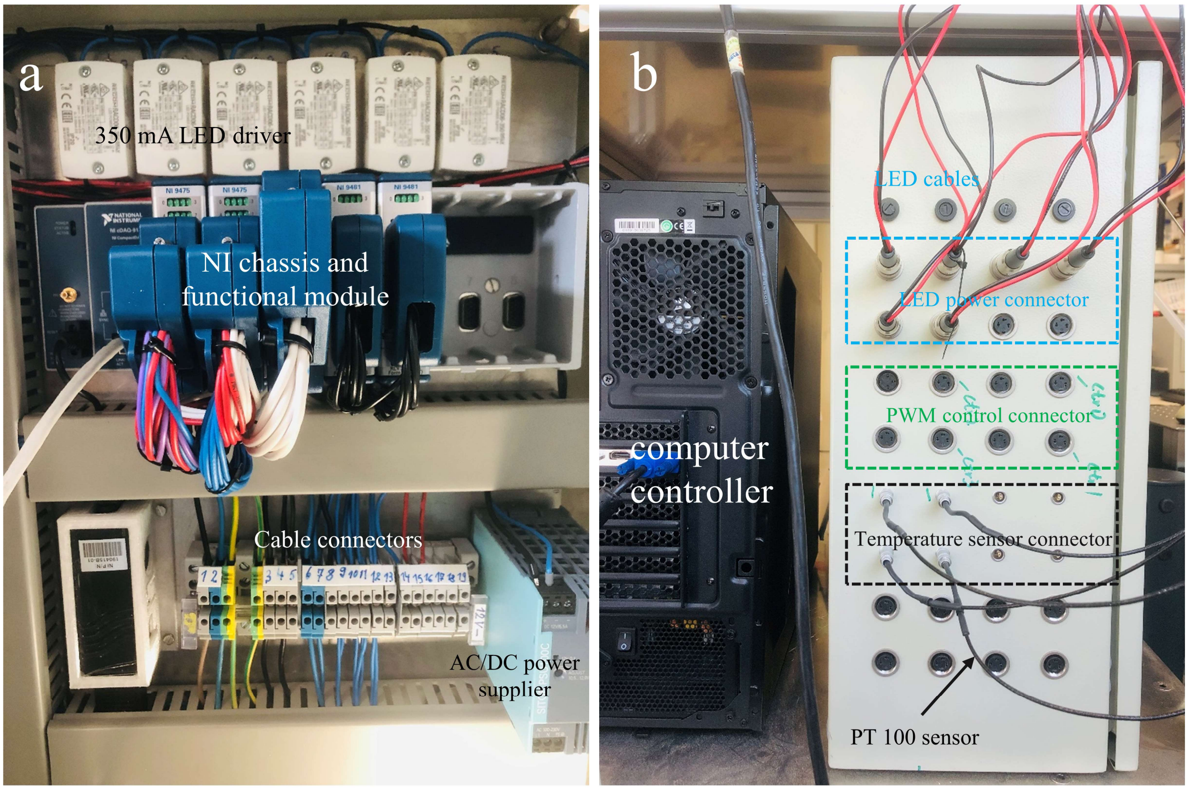

Figure 4-27 Details of NI control box. a) The NI control box made of 9189 CompactDAQ chassis and NI 9475 digital output modules, NI 9481 relay modules, and NI 9216 RTD module. 4 channels of counter output are available. b) Side view of the NI box, including plugs for LED, PWM, and PT 100 sensor connections.

### 4.5.3 Proof-of-concept

In conjunction with previous simulation works, a compact, robust, and standardized microfluidic system for *in situ* infrared sensing shown in Figure 4-28 was assembled, which was successfully integrated with the mini-IR sensors[2] from IMTEK at the University of Freiburg. The reactor assembly takes both photoreaction and infrared detection into account and has adjustable light source position, and independent and identical illumination areas to ensure that the most possible uniform irradiation is achieved. Besides, the light intensity arriving at the photoreactor can be modulated by the PWM signal in the LabVIEW program. Meanwhile, the introduction of the 3D-printed sensor bracket has enabled the combination of infrared technology with the microfluidic photoreactor (PHO-µR), thus making *in situ* infrared detection of photoreactions possible.

---

[2] Miniaturized optical sensors for microfluidic system assembly were designed by project team member David Ilioaë from IMTEK, Freiburg

To this end, the proof-of-concept "*in situ* infrared detection of photoreactions in microfluidic reactors" has been demonstrated. This would be the first case to show the feasibility of the integration among optical sensors, photoreactions, and microreactors. With the help of the developed software package, process intensification and control were achieved. At the same time, the modular design of the individual components has proven the feasibility of building a standardized microfluidic photochemical platform.

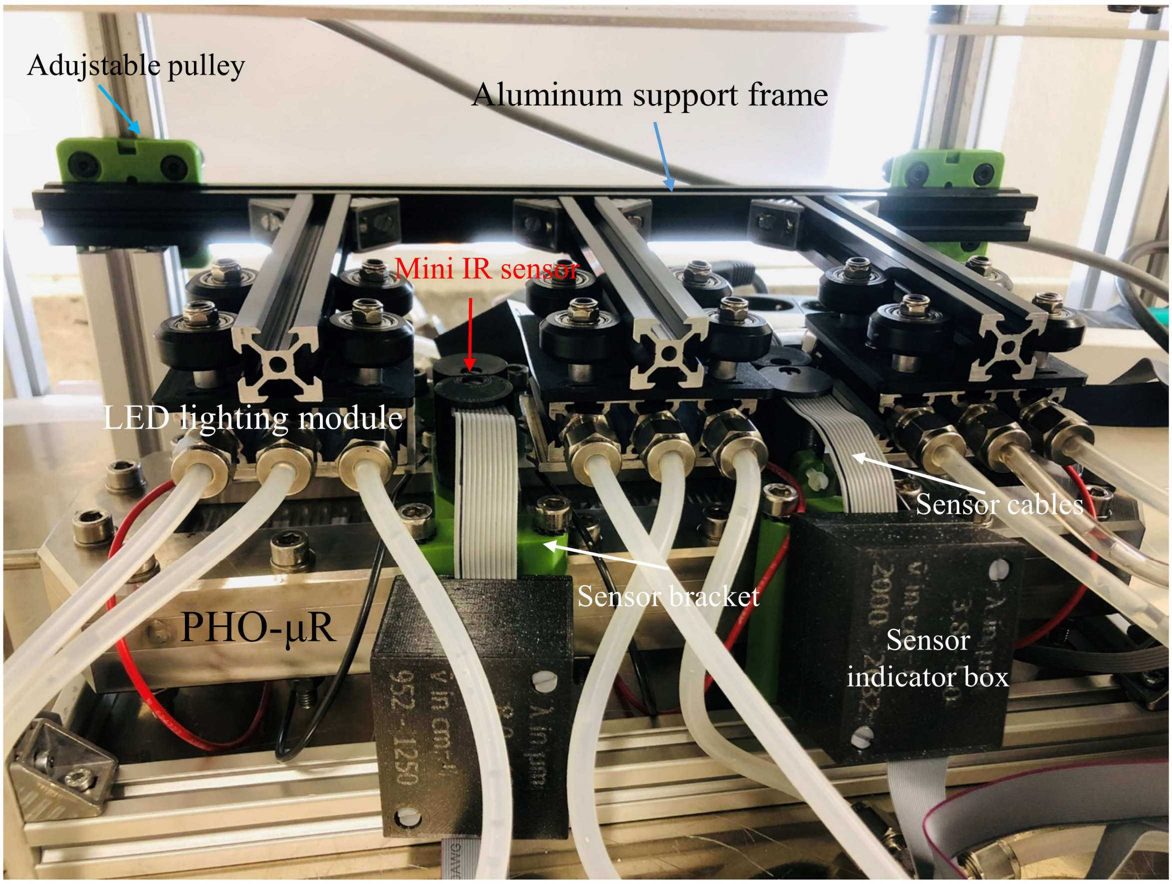

Figure 4-28 The standardized microfluidic photocatalytic system for *in situ* infrared sensing application. The assembly design follows the results from Multiphysics reaction simulation.

### 4.5.4 Remaining challenges and possible solutions

Although the proof of concept has been confirmed, the sensitivity of the sensors used turned out to be insufficient. With the help of project team members from IBCS at KIT and IMTEK at the University of Freiburg[3], the performance of the miniaturized infrared sensor was first evaluated by a 0.5 $mol{\cdot}L^{-1}$ 2-Iodoaniline solution with a penetration depth of 0.1 mm. Fig. 4-29 shows the spectrum obtained from the IMTEK IR sensor and the spectrum obtained from a benchtop Bruker ALPHA ATR-FTIR. Although it was possible to observe similar trends near 1320, 1480, and 1630 $cm^{-1}$ in the IR spectra, the characteristic absorption peaks of certain regions of the iodoaniline were masked, which makes the spectra comparison not meaningful. Besides, increasing the penetration depth of the infrared cell is detrimental to optical measurements, which is the case for the PHO-μR in its initial design (2 mm penetration depth). As the Lambert-Beer law indicates, due to the increased penetration depth a large part of the light will be absorbed by the chemicals in the mixture, and only a small part is able to be transmitted and then received by the IR detector. The reduced intensity of the light received by the IR detector leaves a non-negligible gap in the obtained spectrum, making it difficult to obtain meaningful spectra in order to distinguish between before and after the photochemical reaction. Moreover, another challenge comes from the photochemical reactions themselves. In general, not only one reactant is involved in photochemical transformations. Including several components in a mixture may cause difficulties in spectral differentiation. Attempting to improve the sensitivity of the sensor would be one option to make this kind of IR detection practically relevant and applicable. Nevertheless, this objective is daunting, challenging, and requires further improvements.

---

[3] The spectrum measurement received the help from project team members Helena Simek Tosino and David Ilioaë.

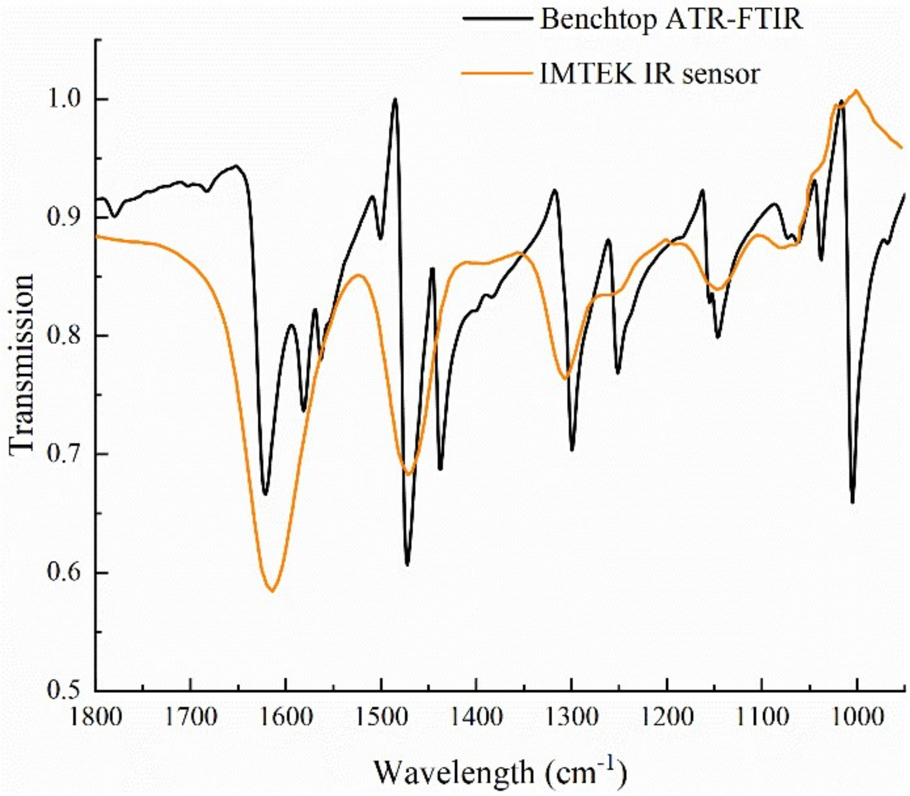

Figure 4-29 Comparison of the infrared spectrum obtained from the IMTEK IR sensor and a benchtop Bruker ALPHA ATR-FTIR instrument. Black, the spectra prepared from solid samples. Orange, the spectra measured by a 0.5 mol·L$^{-1}$ 2-Iodaniline solution in acetonitrile, measured with a penetration depth of 0.1 mm.

Another attempt to circumvent the dilemma is to reduce the penetration depth of the infrared cell of the PHO-µR. It is possible to reduce the penetration depth of the cell from 2 mm to 0.2 mm or even less with 3D printed spacers or suitable O-rings to compensate for the voids due to modifications (Fig. 4-30), but the feasibility is still questionable. On one hand, the appropriate cell penetration depth for the infrared sensor to be useful has not yet been determined, depending on the sensitivity of the sensor and the chemicals used for inspection. On the other hand, modifying the reactor design is time-consuming and carries the risk of damage to the optical glass. Due to time restrictions, it was not possible to modify the PHO-µR in this work. Future investigations must address this question.

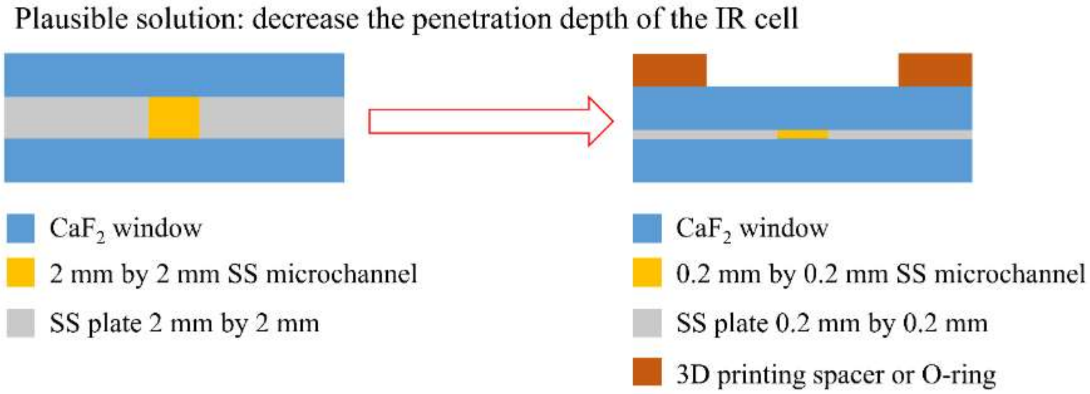

Figure 4-30 Proposed solution to increase the feasibility of in situ infrared sensing by decreasing the penetration depth of the infrared cell in the PHO-μR.

## 4.6 Interim summary

In summary, the visible-light-induced photocyclization of an F-tagged aniline derivative to the corresponding 3-acylindole was chosen as a model reaction and was successfully transferred and implemented in flow photochemistry. On one hand, a kinetic study of this photochemical transformation was carried out in the CAP-μR to get kinetic parameters and build up a reaction model. The influences of residence time and light intensities on the reaction yield were determined by NMR spectroscopy. The reaction order was found to be two, and the apparent rate constant under different light intensities were calculated. The study of the quantum yield of the reaction revealed a photon competition mechanism during the process since part of the light is absorbed by the indole product. In addition, a 2D axisymmetric reactor model was developed to reproduce the process in the CAP-μR, which can predict the yield quite well. A uniform transversal irradiance profile was adopted in the model to simplify the process. A linear relationship between the apparent rate constant and the photon flux of the photoreactor was assumed in the reaction rate expression because the incident light intensity received by CAP-μR was still weak. As a result, the geometry-independent intrinsic rate constant was extracted from the obtained kinetic parameters. Moreover, some dimensionless parameters with respect to process intensification were evaluated and the operating conditions in the CAP-μR were comprehensively analyzed.

On the other hand, the reactor model was extended to the more complex case of the PHO-μR where the radiation field inside the microchannel was considered. Thus, the actual geometry was considered in a 3D model. The discrete ordinate method (DOM) was employed to get the spatially resolved radiation distribution, taking the reflection of the stainless-steel channel into consideration. 20 different possible LEDs configurations were systematically studied and compared based on their performance, including irradiance level, energy efficiency, global deviation of the local irradiance, as well as heterogeneity factor. Thereby the most efficient LED configuration was found. Meanwhile, the resulting radiation field was coupled with fluidic dynamics and reaction kinetics to predict the concentration distribution of the product. In the proposed reaction rate expression, the intrinsic rate constant procured from the kinetic study was employed. This comprehensive model was analyzed in detail and was shown to capture photon reflection and laminar flow phenomena well. This coupled multiphysics simulation combining radiation fields provides a microscopic view to help researchers to get a better understanding of factors limiting the reaction process. Moreover, the model was experimentally validated, and the reaction profile followed the same pattern of secondary order reactions. Although some of the results show large deviations from the simulated results, such deviations were also observed in the 2D simulations attributed to the fact that the intrinsic rate constant was derived from a macroscopic average, which does not describe well the photon competition phenomena between the photocatalyst and the indole product. With the help of parameter screening in reaction simulation, a suitable operating residence time of 60 min for each reaction region was found. The implementation of the same photoreaction in the PHO-μR gave improved productivity and reduced energy consumption.

To sum up, a generic reaction kinetics model applicable to the condition of weak photon absorption of the photocatalyst was successfully developed and transferred between two different microfluidic platforms using different light sources (Fig. 4-31). The reactor model starts with a simple two-dimensional problem, assuming a uniform irradiance profile, and gradually increases in difficulty to three dimensions, taking into account the diffuse emission nature of LEDs. The reaction kinetics established in the CAP-μR were successfully used as input to predict the conversion of the product in the PHO-μR. Although the proposed model still has some shortcomings, it can roughly predict the yield of the photoreaction. Subsequent work may be carried out on model refinement, e.g., taking into account photon competition effects.

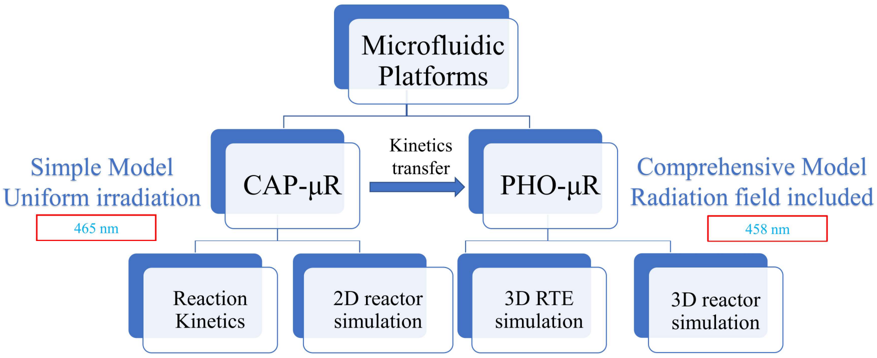

Figure 4-31 Overview of proposed reactor models between two different microfluidic platforms

At the end of this chapter, the integration of the optical infrared sensor, the photoreaction, and the microfluidic photoreactor has been realized. The LED configuration for the standardized assembled system follows the results from the RTE simulation in the subsection of Chapter 4.3 to maximize its potential and make the irradiation inside the reactor as homogeneous as possible. A 3D-printed infrared sensor bracket was designed and employed in the assembly to secure alignment of the infrared light source and infrared sensors. Software packages with different purposes of process control were developed to reduce manual operations. Even though the performance of the sensor is still far from expectation, the proof-of-concept of "*in situ* infrared sensing of photoreactions in a microfluidic photoreactor" was basically realized.

# 5 Summary and outlook

The focus of this dissertation was on the integration of infrared sensors, photocatalysis, and microfluidic reactors for process control. Two different, standardized microfluidic photoreactors (CAP-µR and PHO-µR) and their corresponding photocatalytic platforms were built and the photocyclization of the F-tagged o-alkynylated N-alkyl-N-acylamides **1a**[4] to 3-acylindoles **3a**[5] was chosen as the probe reaction to develop a generic reactor model. The PHO-µR was used to integrate the miniaturized infrared sensors from IMTEK at the University of Freiburg, demonstrating for the first time the proof-of-concept for *in situ* infrared sensing of photoreactions in microreactors.

The main achievement of the study on the reactor design is the development of a novel, special, and compact *in situ* photoreactor (PHO-µR) containing three separate reaction regions and four reserved infrared detection regions. The actual light path inside the reactor was comprehensively analyzed and the photon flux received by the reactor was calibrated with potassium ferrioxalate actinometry using a 1D Monte Carlo method. The maximum mean surface irradiance received was found to be quite strong, with a value of 941.27 W/m$^2$. Due to the deepening of the penetrating light path, the absorption probability of the potassium ferrioxalate actinometry increased from 0.0672 to 0.1916 compared to the more conventional CAP-µR used for the evaluation of the reaction kinetics. This also indicates a more efficient energy utilization in the PHO-µR.

The main achievement of the research into the kinetics in the CAP-µR is the extraction of the intrinsic rate constant of the chosen photoreaction and the development of a simplified reactor model. The concentration profiles under four different levels of light intensity were analyzed and the reaction order was found to be two with the help of the *RSS* evaluation method in MATLAB. Consequently, four different apparent rate constants were derived. They were found to be linearly related to the incident light intensity, indicating the reaction rate being located in the weak absorption region. By plotting the resulting constant against the product of the absorption probability of the iridium photocatalyst, the specific irradiated surface, and the photon flux received by the CAP-µR, the intrinsic rate constant was found to be 36.24 $L^2 \cdot mol^{-1} \cdot einstein^{-1}$. In addition, a 2D axisymmetric model was developed to reproduce the process in the capillary, and several dimensionless parameters were employed to analyze the flow operating conditions. The model starts with the simplest case, assuming a transversal irradiance profile in the CAP-

---

[4] The structure of **1a** is presented in Scheme 4-2

[5] The structure of **3a** is presented in Scheme 4-2

μR due to its symmetry. The predicted conversions generally match with the experimental values quite well where the majority of scatters are located within 10% tolerance. Some predictions seem to be biased by mass transport limitations occurring inside the channel, in which case the Péclet number $Pe$ exceeds 1. Besides, the photon competition between the iridium photocatalyst and the photon-absorbing indole product also contribute to the deviations. Nevertheless, the 2D simulation can still capture the photocatalytic process quite well, and in most cases the Bodenstein number $Bo$ are still located in the plug flow region.

Moreover, an iterative DOM method based on the results of photon flux calibration was used to provide a 3D spatially resolved radiation field prediction of the PHO-μR. By analyzing the irradiance level, energy efficiency, and global deviation, a LED-to-reactor distance of 8 mm was found to be optimal. The 3D reactor model was developed by incorporating the extracted intrinsic rate constant from the kinetic study in CAP-μR and the radiation field from the RTE simulation in the PHO-μR into the reaction rate expression term in the governing equation, thus giving spatially resolved concentration profiles in the microchannel. The predicted concentration fields are found to be highly dependent on the radiation field, where a higher local product concentration appears around the hotspot of the irradiation field. The simulations show both the phenomenon of photon attenuation, laminar flow, and light reflection. Interestingly, the fluid field has a negligible contribution to the concentration field if no reflections occur in the photoreactor. In addition, a shift from kinetic to diffusion control was observed through simulations. Besides, the axial concentration gradient inside the microchannel has no significant changes if the set residence time is more than 60 minutes. The correctness of the simulation was verified by validation experiments, which were carried out under the weakest photon flux tested to guarantee the linearity between the local rate constant and the incident irradiation, thereby ensuring that the actual reaction rate agrees with the rate expression in the simulation. Despite some deviations, the tendency is consistent with the results of the 2D simulations. The predictions are broadly consistent with experimental results of moderate conversion at longer residence times. Thus, the reactor model was validated, which in turn, shows the reliability of the RTE simulation. In this context, the reaction kinetics model was successfully transferred between two different microfluidic platforms. Further simulation work could consider the photon competition contribution of the indole product in the reaction rate term. Besides, with the guide from simulations, the productivity was predicted for residence times below 60 minutes. A residence time of

30 min was found to be optimal using dry acetone as the solvent. In this context, the calculated STY value of the PHO-μR is 37.50 mmol$\cdot L^{-1} \cdot h^{-1}$, which is 7 times higher than that of the CAP-μR. One should note that the solvent effect plays an important role in the photoreaction as complete conversion is never achieved in acetone, while the reaction in DMSO is more competitive. Further studies could focus on the use of DMSO as a solvent for the optimization of the chosen photoreaction and continuation work should be performed in DMSO to obtain the most suitable operating conditions for scale-up purposes.

In line with the conclusions from RTE simulations (i.e. the 6 aligned LED configuration as the final LED board design), a compatible 3D-printed IR sensor holder was designed and constructed to utilize the miniature IR sensor. Meanwhile, a versatile software package was developed to control the inputs of the assembled microfluidic system, thereby achieving programmable process control. Finally, the integration between the infrared sensors, the microfluidic reactor (PHO-μR), and photocatalysis has been basically achieved, which shows the proof-of-concept of *in situ* sensing of photoreactions in microreactors. Even though the sensors did not work as expected, future extensions of the work may focus on increasing the sensitivity of the infrared sensor or decreasing the penetration depth of the infrared cell of the PHO-μR. It is worth noting that addressing the conflict between the depth of the reaction channel and the infrared cell is a crucial issue for microfluidic *in situ* photoreactor design. A deeper reaction channel is beneficial to the photoreaction since more photons can be utilized to promote conversion while it is detrimental for optical sensing because it is difficult to obtain high-resolution spectra due to excessive spectral absorption of analytes. Due to time restrictions, relevant modifications can be made to verify the feasibility of this scheme in subsequent studies. Another unignorable challenge comes from sealing because the inconsistent pressure drop may break fragile construction materials, especially transparent windows for the photoreactor. This will lead to unsustainable use of the equipment. The compatibility of construction materials for *in situ* photoreactors is a prominent obstacle in engineering. Ultimately, using this kind of *in situ* detection technique in a photoreactor requires a compromise in reactor design, the use of smaller internal volumes, for instance. It should also be pointed out that the choice of a model photoreaction for the *in situ* IR sensing application is highly empirically dependent, which is now an inevitable step in this interdisciplinary field.

With the prototype of the *in situ* photoreactor and off-the-shelf software packages at hand, future extensions of this work may focus on incorporating other optical techniques for process evaluation and control. Hence, a compact, robust, and versatile microfluidic photocatalytic platform with real-time monitoring and feedback control is foreseeable and is expected in the near future.

# Nomenclature

### Symbols

| | |
|---|---|
| $C$ | Bulk concentration ($mol \cdot m^{-3}$) |
| $\Phi$ | Quantum yield (1) |
| $V_R$ | Reaction volume of the photoreactor ($m^3$) |
| $q_\lambda$ | Overall incident photon flux received by a photoreactor at a given wavelength ($einstein \cdot s^{-1}$) |
| $p_{(\Omega)}$ | Absorption probability of species $i$ (1) |
| $E_{i,\lambda}$ | Napierian absorption coefficient of species $i$ at a given wavelength λ ($L^{-1} \cdot mol \cdot cm^{-1}$) |
| $L$ | Optical penetration path in the photoreactor ($m$) |
| $D_F$ | Diluting factor in the actinometer experiments (1) |
| $C_{\mathrm{Fe}^{2+}}$ | Concentration of ferrous ions ($mol \cdot m^{-3}$) |
| $C_{0\mathrm{Fe}^{3+}}$ | Initial concentration of ferrioxalate solution ($mol \cdot m^{-3}$) |
| $A_{510}$ | UV-Vis absorbance of the samples at 510 nm (1) |
| $f_{\mathrm{Fe}^{2+}}$ | Slope of the calibration curve for the complexation of ferrous ions with 1,10-phenanthroline (1) |
| X | Conversion (1) |
| $E_\lambda$ | Energy conveyed by photons at given wavelength ($\mathrm{J \cdot mol_{photon}}^{-1}$) |
| $h$ | Planck's constant ($\mathrm{J} \cdot s$) |
| $c$ | Speed of the light ($m \cdot s^{-1}$) |
| $N_A$ | Avogadro's number |
| $A_{cap}$ | Irradiated area of the CAP-μR ($m^2$) |
| $A_{450}$ | UV-Vis absorbance of the samples at 450 nm (1) |
| $\varepsilon_{[Fe(NCS)]^{2+}}$ | Decadic molar absorption coefficient of $[\mathrm{Fe(NCS)}]^{2+}$ at 450 nm ($L^{-1} \cdot mol \cdot cm^{-1}$) |
| $q_{(\Omega)}$ | Transmission probability (1) |
| $\rho_{ss}$ | Reflection coefficient between the interface (1) |
| $K_{app}$ | Apparent rate constant ($\mathrm{M^{-1} \cdot min^{-1}}$) |

| | |
|---|---|
| $k_{intr}$ | Intrinsic rate constant of the photoreaction (L$^{2}$·mol$^{-1}$·$einstein^{-1}$) |
| $q_{in}$ | Incident photon flux density received at the wall of the CAP-µR ($einstein \cdot m^{-2} \cdot s^{-1}$) |
| $S_{irrad}$ | Irradiated area of the CAP-µR ($m^{2}$) |
| $a_{light}$ | Specific irradiated surface of the CAP-µR ($m^{-1}$) |
| $\langle \mathcal{A}_{\lambda}^{e} \rangle$ | Mean surface rate of photon absorption at specified wavelength λ at the CAP-µR ($einstein \cdot m^{-2} \cdot s^{-1}$) |
| $p_{(\Omega\_Ir)}$ | Absorption probability of the iridium photocatalyst **2** |
| $\rho$ | Density of solvent used ($kg \cdot m^{-3}$) |
| $u$ | Velocity field |
| $\mu$ | Viscosity of the solvent used ($Pa \cdot s$) |
| $I$ | Identity tensor |
| $D_i$ | Diffusivity of species $i$ ($m^{2} \cdot s^{-1}$) |
| $c_i$ | Local concentration of species $i$ ($mol \cdot m^{-3}$) |
| $\vec{j}_p(t)$ | Normal molar flux density of the indole product as a function of time at the outlet of the CAP-µR |
| $\Omega$ | Spatial domain of the integral function |
| $n_p$ | Predicted overall moles of the indole product produced ($mol$) |
| $t_c$ | Computing time for the 2D transient study |
| $Q$ | Experimental set flow rate in the CAP-µR test bench ($m^{3} \cdot min^{-1}$) |
| $\bar{u}$ | Average flow velocity ($m \cdot s^{-1}$) |
| $D_{\mathrm{ax}}$ | Taylor dispersion coefficient ($m^{2} \cdot s^{-1}$) |
| $d_h$ | Hydraulic diameter ($m$) |
| $\tau$ | Residence time (min) |
| $S_i$ | The $i^{th}$ discrete ordinate |
| $I_i$ | The $i^{th}$ component of the radiative intensity |
| $I_b$ | Black body radiation intensity (W·m$^{-2}$ · sr$^{-1}$) |
| $\kappa$ | Absorption coefficient of the reaction medium ($m^{-1}$) |
| $\sigma_s$ | Scattering coefficients of the reaction medium ($m^{-1}$) |
| $\varphi(\Omega_j, \Omega_i)$ | Scattering phase function |

| | |
|---|---|
| $\omega_j$ | Quadrature weight |
| $G$ | Local incident radiation at a given point ($W \cdot m^{-2}$) |
| $E$ | Local irradiance value ($W \cdot m^{-2}$) |
| $\bar{E}$ | Average irradiance value ($W \cdot m^{-2}$) |
| η | Energy efficiency (1) |
| $A_{\mu R}$ | Irradiated area of the PHO-µR ($m^2$) |
| $N_L$ | Number of the LEDs used in the simulation (1) |
| $P_L$ | Emitted power by each LED (W) |
| $\bar{\sigma}$ | Global deviation of illumination heterogeneity (1) |
| $\sigma_{sam}$ | Irradiance deviation of a single sample (1) |
| $\hat{I}$ | Heterogeneity factor (1) |
| $kappa_s$ | Optical thickness of the iridium photocatalyst **2** at wavelength λ ($m^{-1}$) |
| $X_{Exp}$ | Yield of each sample from 1H-NMR measurement (1) |
| $\overline{\boldsymbol{X_{Exp}}}$ | Average value of $X_{Exp}$ for three replicates (1) |
| $\boldsymbol{X_{CFD}}$ | Predicted yield from multiphysics-coupled reaction simulations (1) |

**Subscripts and superscripts**

| | |
|---|---|
| act | The chemical actinometer used in the photon flux calibration |
| λ | Peak wavelength emitted by the using LEDs in photoreactors ($m$) |
| cap | Capillary microreactor CAP-µR |
| $i$ | Species in the mixture |
| $A0$ | Initial concentration of **1a** in the kinetic study |
| $\alpha$ | Constant related to the type of photoreaction |
| $\beta$ | Constant related to the light intensity received by the system |
| $tot$ | Summation of the contribution of components in the mixture |
| $n$ | Reaction order on substrate's concentration |
| $r, phi, z$ | Velocity vectors in the 2D axisymmetric simulation |
| $in$ | Inlet |
| $out$ | Outlet |
| $p$ | Predicted product **3a** |
| $s0$ | Initial value of starting material **1a** |

| | |
|---|---|
| $d$ | Radial |
| $\mu R$ | Microfluidic photoreactor PHO-μR |
| $sam$ | Sample point for RTE evaluation |
| an | F-tagged aniline precursor **1a** |
| Ir | Iridium photocatalyst **2** |
| $idex$ | Index number for iterative calculation |

# References

[1] A.K. Au, W. Huynh, L.F. Horowitz, A. Folch, 3D-Printed Microfluidics, Angewandte Chemie International Edition 55(12) (2016) 3862-3881. https://doi.org/10.1002/anie.201504382.
[2] R. Amin, S. Knowlton, A. Hart, B. Yenilmez, F. Ghaderinezhad, S. Katebifar, M. Messina, A. Khademhosseini, S. Tasoglu, 3D-printed microfluidic devices, Biofabrication 8(2) (2016) 022001. https://doi.org/10.1088/1758-5090/8/2/022001.
[3] M.P. Sealy, G. Madireddy, R.E. Williams, P. Rao, M. Toursangsaraki, Hybrid Processes in Additive Manufacturing, Journal of Manufacturing Science and Engineering 140(6) (2018). https://doi.org/10.1115/1.4038644.
[4] Y. He, Y. Wu, J.-z. Fu, Q. Gao, J.-j. Qiu, Developments of 3D Printing Microfluidics and Applications in Chemistry and Biology: a Review, Electroanalysis 28(8) (2016) 1658-1678. https://doi.org/10.1002/elan.201600043.
[5] C. Parra-Cabrera, C. Achille, S. Kuhn, R. Ameloot, 3D printing in chemical engineering and catalytic technology: structured catalysts, mixers and reactors, Chemical Society Reviews 47(1) (2018) 209-230. https://doi.org/10.1039/C7CS00631D.
[6] X. Hou, Y.S. Zhang, G.T.-d. Santiago, M.M. Alvarez, J. Ribas, S.J. Jonas, P.S. Weiss, A.M. Andrews, J. Aizenberg, A. Khademhosseini, Interplay between materials and microfluidics, Nature Reviews Materials 2(5) (2017) 17016. https://doi.org/10.1038/natrevmats.2017.16.
[7] A.-G. Niculescu, C. Chircov, A.C. Bîrcă, A.M. Grumezescu, Fabrication and Applications of Microfluidic Devices: A Review, International Journal of Molecular Sciences 22(4) (2021) 2011. https://doi.org/10.3390/ijms22042011.
[8] K. Ren, J. Zhou, H. Wu, Materials for Microfluidic Chip Fabrication, Accounts of Chemical Research 46(11) (2013) 2396-2406. https://doi.org/10.1021/ar300314s.
[9] P.N. Nge, C.I. Rogers, A.T. Woolley, Advances in Microfluidic Materials, Functions, Integration, and Applications, Chemical Reviews 113(4) (2013) 2550-2583. https://doi.org/10.1021/cr300337x.
[10] J. Wegner, S. Ceylan, A. Kirschning, Flow Chemistry – A Key Enabling Technology for (Multistep) Organic Synthesis, Advanced Synthesis & Catalysis 354(1) (2012) 17-57. https://doi.org/10.1002/adsc.201100584.
[11] Y. Su, N.J.W. Straathof, V. Hessel, T. Noël, Photochemical Transformations Accelerated in Continuous-Flow Reactors: Basic Concepts and Applications, Chemistry – A European Journal 20(34) (2014) 10562-10589. https://doi.org/10.1002/chem.201400283.
[12] A.M. Nightingale, C.L. Leong, R.A. Burnish, S.-u. Hassan, Y. Zhang, G.F. Clough, M.G. Boutelle, D. Voegeli, X. Niu, Monitoring biomolecule concentrations in tissue using a wearable droplet microfluidic-based sensor, Nature Communications 10(1) (2019) 2741. https://doi.org/10.1038/s41467-019-10401-y.
[13] L.-J. Pan, J.-W. Tu, H.-T. Ma, Y.-J. Yang, Z.-Q. Tian, D.-W. Pang, Z.-L. Zhang, Controllable synthesis of nanocrystals in droplet reactors, Lab on a Chip 18(1) (2018) 41-56. https://doi.org/10.1039/C7LC00800G.
[14] G. Tofighi, H. Lichtenberg, J. Pesek, T.L. Sheppard, W. Wang, L. Schöttner, G. Rinke, R. Dittmeyer, J.-D. Grunwaldt, Continuous microfluidic synthesis of colloidal ultrasmall gold nanoparticles: in situ study of the early reaction stages and application for catalysis, Reaction Chemistry & Engineering 2(6) (2017) 876-884. https://doi.org/10.1039/C7RE00114B.
[15] R. Porta, M. Benaglia, A. Puglisi, Flow Chemistry: Recent Developments in the Synthesis of Pharmaceutical Products, Organic Process Research & Development 20(1) (2016) 2-25. https://doi.org/10.1021/acs.oprd.5b00325.
[16] A. Adamo, R.L. Beingessner, M. Behnam, J. Chen, T.F. Jamison, K.F. Jensen, J.-C.M.

Monbaliu, A.S. Myerson, E.M. Revalor, D.R. Snead, T. Stelzer, N. Weeranoppanant, S.Y. Wong, P. Zhang, On-demand continuous-flow production of pharmaceuticals in a compact, reconfigurable system, Science 352(6281) (2016) 61-67. https://doi.org/10.1126/science.aaf1337.

[17] C.-W. Chi, A.R. Ahmed, Z. Dereli-Korkut, S. Wang, Microfluidic cell chips for high-throughput drug screening, Bioanalysis 8(9) (2016) 921-937. https://doi.org/10.4155/bio-2016-0028.

[18] P. Zhou, J. He, L. Huang, Z. Yu, Z. Su, X. Shi, J. Zhou, Microfluidic High-Throughput Platforms for Discovery of Novel Materials, Nanomaterials 10(12) (2020) 2514. https://doi.org/10.3390/nano10122514.

[19] P. Gruber, M.P.C. Marques, N. Szita, T. Mayr, Integration and application of optical chemical sensors in microbioreactors, Lab on a Chip 17(16) (2017) 2693-2712. https://doi.org/10.1039/C7LC00538E.

[20] B. Kuswandi, Nuriman, J. Huskens, W. Verboom, Optical sensing systems for microfluidic devices: A review, Analytica Chimica Acta 601(2) (2007) 141-155. https://doi.org/10.1016/j.aca.2007.08.046.

[21] S. Urban, B.J. Deschner, L.L. Trinkies, J. Kieninger, M. Kraut, R. Dittmeyer, G.A. Urban, A. Weltin, In Situ Mapping of H2, O2, and H2O2 in Microreactors: A Parallel, Selective Multianalyte Detection Method, ACS Sensors 6(4) (2021) 1583-1594. https://doi.org/10.1021/acssensors.0c02509.

[22] T. Eifert, K. Eisen, M. Maiwald, C. Herwig, Current and future requirements to industrial analytical infrastructure—part 2: smart sensors, Analytical and Bioanalytical Chemistry 412(9) (2020) 2037-2045. https://doi.org/10.1007/s00216-020-02421-1.

[23] K.F. Jensen, Flow chemistry—Microreaction technology comes of age, AIChE Journal 63(3) (2017) 858-869. https://doi.org/10.1002/aic.15642.

[24] B.P. Mason, K.E. Price, J.L. Steinbacher, A.R. Bogdan, D.T. McQuade, Greener Approaches to Organic Synthesis Using Microreactor Technology, Chemical Reviews 107(6) (2007) 2300-2318. https://doi.org/10.1021/cr050944c.

[25] I. Pupeza, M. Huber, M. Trubetskov, W. Schweinberger, S.A. Hussain, C. Hofer, K. Fritsch, M. Poetzlberger, L. Vamos, E. Fill, T. Amotchkina, K.V. Kepesidis, A. Apolonski, N. Karpowicz, V. Pervak, O. Pronin, F. Fleischmann, A. Azzeer, M. Žigman, F. Krausz, Field-resolved infrared spectroscopy of biological systems, Nature 577(7788) (2020) 52-59. https://doi.org/10.1038/s41586-019-1850-7.

[26] D. Cambié, C. Bottecchia, N.J.W. Straathof, V. Hessel, T. Noël, Applications of Continuous-Flow Photochemistry in Organic Synthesis, Material Science, and Water Treatment, Chemical Reviews 116(17) (2016) 10276-10341. https://doi.org/10.1021/acs.chemrev.5b00707.

[27] D. Webb, T.F. Jamison, Continuous flow multi-step organic synthesis, Chemical Science 1(6) (2010) 675-680. https://doi.org/10.1039/C0SC00381F.

[28] B.J. Reizman, K.F. Jensen, Feedback in Flow for Accelerated Reaction Development, Accounts of Chemical Research 49(9) (2016) 1786-1796. https://doi.org/10.1021/acs.accounts.6b00261.

[29] S. Bordawekar, A. Chanda, A.M. Daly, A.W. Garrett, J.P. Higgins, M.A. LaPack, T.D. Maloney, J. Morgado, S. Mukherjee, J.D. Orr, G.L. Reid, III, B.-S. Yang, H.W. Ward, II, Industry Perspectives on Process Analytical Technology: Tools and Applications in API Manufacturing, Organic Process Research & Development 19(9) (2015) 1174-1185. https://doi.org/10.1021/acs.oprd.5b00088.

[30] J.J. Haven, T. Junkers, Online Monitoring of Polymerizations: Current Status, Eur J Org Chem 2017(44) (2017) 6474-6482. https://doi.org/10.1002/ejoc.201700851.

[31] G.A. Price, D. Mallik, M.G. Organ, Process analytical tools for flow analysis: A perspective, Journal of Flow Chemistry JFChem 7(3-4) (2017) 82-86.

https://doi.org/10.1556/1846.2017.00032.
[32] V. Sans, L. Cronin, Towards dial-a-molecule by integrating continuous flow, analytics and self-optimisation, Chemical Society Reviews 45(8) (2016) 2032-2043. https://doi.org/10.1039/C5CS00793C.
[33] J.P. McMullen, K.F. Jensen, Integrated Microreactors for Reaction Automation: New Approaches to Reaction Development, Annual Review of Analytical Chemistry 3(1) (2010) 19-42. https://doi.org/10.1146/annurev.anchem.111808.073718.
[34] K. Eisen, T. Eifert, C. Herwig, M. Maiwald, Current and future requirements to industrial analytical infrastructure—part 1: process analytical laboratories, Analytical and Bioanalytical Chemistry 412(9) (2020) 2027-2035. https://doi.org/10.1007/s00216-020-02420-2.
[35] P. Sagmeister, R. Lebl, I. Castillo, J. Rehrl, J. Kruisz, M. Sipek, M. Horn, S. Sacher, D. Cantillo, J.D. Williams, C.O. Kappe, Advanced Real-Time Process Analytics for Multistep Synthesis in Continuous Flow**, Angewandte Chemie International Edition 60(15) (2021) 8139-8148. https://doi.org/10.1002/anie.202016007.
[36] M. Baumann, Integrating continuous flow synthesis with in-line analysis and data generation, Organic & Biomolecular Chemistry 16(33) (2018) 5946-5954. https://doi.org/10.1039/C8OB01437J.
[37] Z. Wang, Y. Zhang, B. Liu, K. Wu, S. Thevuthasan, D.R. Baer, Z. Zhu, X.Y. Yu, F. Wang, In Situ Mass Spectrometric Monitoring of the Dynamic Electrochemical Process at the Electrode-Electrolyte Interface: a SIMS Approach, Anal Chem 89(1) (2017) 960-965. https://doi.org/10.1021/acs.analchem.6b04189.
[38] J. Li, H. Šimek, D. Ilioae, N. Jung, S. Bräse, H. Zappe, R. Dittmeyer, B.P. Ladewig, In situ sensors for flow reactors – a review, Reaction Chemistry & Engineering 6(9) (2021) 1497-1507. https://doi.org/10.1039/D1RE00038A.
[39] R. Chung, J.E. Hein, The More, The Better: Simultaneous In Situ Reaction Monitoring Provides Rapid Mechanistic and Kinetic Insight, Topics in Catalysis 60(8) (2017) 594-608. https://doi.org/10.1007/s11244-017-0737-9.
[40] G. Finch, A. Yilmaz, M. Utz, An optimised detector for in-situ high-resolution NMR in microfluidic devices, Journal of Magnetic Resonance 262 (2016) 73-80. https://doi.org/10.1016/j.jmr.2015.11.011.
[41] J. Bart, A.J. Kolkman, A.J. Oosthoek-de Vries, K. Koch, P.J. Nieuwland, H. Janssen, J. van Bentum, K.A.M. Ampt, F.P.J.T. Rutjes, S.S. Wijmenga, H. Gardeniers, A.P.M. Kentgens, A Microfluidic High-Resolution NMR Flow Probe, Journal of the American Chemical Society 131(14) (2009) 5014-5015. https://doi.org/10.1021/ja900389x.
[42] A.J. Oosthoek-de Vries, J. Bart, R.M. Tiggelaar, J.W.G. Janssen, P.J.M. van Bentum, H.J.G.E. Gardeniers, A.P.M. Kentgens, Continuous Flow 1H and 13C NMR Spectroscopy in Microfluidic Stripline NMR Chips, Analytical Chemistry 89(4) (2017) 2296-2303. https://doi.org/10.1021/acs.analchem.6b03784.
[43] J. Smits, J.T. Damron, P. Kehayias, A.F. McDowell, N. Mosavian, I. Fescenko, N. Ristoff, A. Laraoui, A. Jarmola, V.M. Acosta, Two-dimensional nuclear magnetic resonance spectroscopy with a microfluidic diamond quantum sensor, Science Advances 5(7) (2019) eaaw7895. https://doi.org/10.1126/sciadv.aaw7895.
[44] J. Eills, W. Hale, M. Sharma, M. Rossetto, M.H. Levitt, M. Utz, High-Resolution Nuclear Magnetic Resonance Spectroscopy with Picomole Sensitivity by Hyperpolarization on a Chip, Journal of the American Chemical Society 141(25) (2019) 9955-9963. https://doi.org/10.1021/jacs.9b03507.
[45] P.F. Silva, M. Jouda, J.G. Korvink, Geometrically-differential NMR in a stripline front-end, Journal of Magnetic Resonance 310 (2020) 106659. https://doi.org/10.1016/j.jmr.2019.106659.
[46] O. Nassar, M. Jouda, M. Rapp, D. Mager, J.G. Korvink, N. MacKinnon, Integrated impedance sensing of liquid sample plug flow enables automated high throughput NMR

spectroscopy, Microsystems & Nanoengineering 7(1) (2021) 30. https://doi.org/10.1038/s41378-021-00253-2.
[47] H. Davoodi, N. Nordin, L. Bordonali, J.G. Korvink, N. MacKinnon, V. Badilita, An NMR-compatible microfluidic platform enabling in situ electrochemistry, Lab on a Chip 20(17) (2020) 3202-3212. https://doi.org/10.1039/D0LC00364F.
[48] J.G. Korvink, N. MacKinnon, V. Badilita, M. Jouda, "Small is beautiful" in NMR, Journal of Magnetic Resonance 306 (2019) 112-117. https://doi.org/10.1016/j.jmr.2019.07.012.
[49] B. Ahmed-Omer, E. Sliwinski, J.P. Cerroti, S.V. Ley, Continuous Processing and Efficient in Situ Reaction Monitoring of a Hypervalent Iodine(III) Mediated Cyclopropanation Using Benchtop NMR Spectroscopy, Organic Process Research & Development 20(9) (2016) 1603-1614. https://doi.org/10.1021/acs.oprd.6b00177.
[50] M.V. Gomez, A. Juan, F. Jiménez-Márquez, A. de la Hoz, A.H. Velders, Illumination of Nanoliter-NMR Spectroscopy Chips for Real-Time Photochemical Reaction Monitoring, Analytical Chemistry 90(3) (2018) 1542-1546. https://doi.org/10.1021/acs.analchem.7b04114.
[51] A. Perro, G. Lebourdon, S. Henry, S. Lecomte, L. Servant, S. Marre, Combining microfluidics and FT-IR spectroscopy: towards spatially resolved information on chemical processes, Reaction Chemistry & Engineering 1(6) (2016) 577-594. https://doi.org/10.1039/C6RE00127K.
[52] K.L.A. Chan, X. Niu, A.J. de Mello, S.G. Kazarian, Rapid prototyping of microfluidic devices for integrating with FT-IR spectroscopic imaging, Lab on a Chip 10(16) (2010) 2170-2174. https://doi.org/10.1039/C004246C.
[53] E. Gross, X.-Z. Shu, S. Alayoglu, H.A. Bechtel, M.C. Martin, F.D. Toste, G.A. Somorjai, In Situ IR and X-ray High Spatial-Resolution Microspectroscopy Measurements of Multistep Organic Transformation in Flow Microreactor Catalyzed by Au Nanoclusters, Journal of the American Chemical Society 136(9) (2014) 3624-3629. https://doi.org/10.1021/ja412740p.
[54] L. Zhang, M. Lohrasbi, U. Tumuluri, S.S.C. Chuang, Asymmetric Hydrogenation of α-Amino Ester Probed by FTIR Spectroscopy, Organic Process Research & Development 20(9) (2016) 1668-1676. https://doi.org/10.1021/acs.oprd.6b00222.
[55] A. Pawlowska-Zygarowicz, R. Kukawka, H. Maciejewski, M. Smiglak, Optimization and intensification of hydrosilylation reactions using a microreactor system, New Journal of Chemistry 42(18) (2018) 15332-15339. https://doi.org/10.1039/C8NJ01167B.
[56] J.-C. Dong, X.-G. Zhang, V. Briega-Martos, X. Jin, J. Yang, S. Chen, Z.-L. Yang, D.-Y. Wu, J.M. Feliu, C.T. Williams, Z.-Q. Tian, J.-F. Li, In situ Raman spectroscopic evidence for oxygen reduction reaction intermediates at platinum single-crystal surfaces, Nature Energy 4(1) (2019) 60-67. https://doi.org/10.1038/s41560-018-0292-z.
[57] J. Yu, M. Yang, Z. Li, C. Liu, Y. Wei, C. Zhang, B. Man, F. Lei, Hierarchical Particle-In-Quasicavity Architecture for Ultratrace In Situ Raman Sensing and Its Application in Real-Time Monitoring of Toxic Pollutants, Analytical Chemistry 92(21) (2020) 14754-14761. https://doi.org/10.1021/acs.analchem.0c03375.
[58] T.A. Meier, R.J. Beulig, E. Klinge, M. Fuss, S. Ohla, D. Belder, On-chip monitoring of chemical syntheses in microdroplets via surface-enhanced Raman spectroscopy, Chemical Communications 51(41) (2015) 8588-8591. https://doi.org/10.1039/C4CC09595B.
[59] N.E. Leadbeater, R.J. Smith, T.M. Barnard, Using in situ Raman monitoring as a tool for rapid optimisation and scale-up of microwave-promoted organic synthesis: esterification as an example, Organic & Biomolecular Chemistry 5(5) (2007) 822-825. https://doi.org/10.1039/B615597A.
[60] E. Cao, M. Sankar, S. Firth, K.F. Lam, D. Bethell, D.K. Knight, G.J. Hutchings, P.F. McMillan, A. Gavriilidis, Reaction and Raman spectroscopic studies of alcohol oxidation on gold–palladium catalysts in microstructured reactors, Chemical Engineering Journal 167(2)

(2011) 734-743. https://doi.org/10.1016/j.cej.2010.08.082.
[61] B.A. Rizkin, R.L. Hartman, Catalytic activity of Pd/hydrophilic phosphine ligand in the interface of an aqueous-phase Cu-free Sonogashira coupling, Reaction Chemistry & Engineering 3(3) (2018) 251-257. https://doi.org/10.1039/C8RE00021B.
[62] Y. Jiang, J. Huang, V.R. Reddy Marthala, Y.S. Ooi, J. Weitkamp, M. Hunger, In situ MAS NMR–UV/Vis investigation of H-SAPO-34 catalysts partially coked in the methanol-to-olefin conversion under continuous-flow conditions and of their regeneration, Microporous and Mesoporous Materials 105(1) (2007) 132-139. https://doi.org/10.1016/j.micromeso.2007.05.028.
[63] Y. Bu, J.W.H. Niemantsverdriet, H.O.A. Fredriksson, Cu Model Catalyst Dynamics and CO Oxidation Kinetics Studied by Simultaneous in Situ UV–Vis and Mass Spectroscopy, ACS Catalysis 6(5) (2016) 2867-2876. https://doi.org/10.1021/acscatal.5b02861.
[64] D.L. Browne, S. Wright, B.J. Deadman, S. Dunnage, I.R. Baxendale, R.M. Turner, S.V. Ley, Continuous flow reaction monitoring using an on-line miniature mass spectrometer, Rapid Communications in Mass Spectrometry 26(17) (2012) 1999-2010. https://doi.org/10.1002/rcm.6312.
[65] L. Yang, Z. Zhu, X.-Y. Yu, S. Thevuthasan, J.P. Cowin, Performance of a microfluidic device for in situ ToF-SIMS analysis of selected organic molecules at aqueous surfaces, Analytical Methods 5(10) (2013) 2515-2522. https://doi.org/10.1039/C3AY26513G.
[66] L. Yang, Z. Zhu, X.-Y. Yu, E. Rodek, L. Saraf, T. Thevuthasan, J.P. Cowin, In situ SEM and ToF-SIMS analysis of IgG conjugated gold nanoparticles at aqueous surfaces, Surface and Interface Analysis 46(4) (2014) 224-228. https://doi.org/10.1002/sia.5252.
[67] K. Sai Krishna, C.V. Navin, S. Biswas, V. Singh, K. Ham, G.L. Bovenkamp, C.S. Theegala, J.T. Miller, J.J. Spivey, C.S.S.R. Kumar, Millifluidics for Time-resolved Mapping of the Growth of Gold Nanostructures, Journal of the American Chemical Society 135(14) (2013) 5450-5456. https://doi.org/10.1021/ja400434c.
[68] A. Tsoukalou, P.M. Abdala, D. Stoian, X. Huang, M.-G. Willinger, A. Fedorov, C.R. Müller, Structural Evolution and Dynamics of an In2O3 Catalyst for CO2 Hydrogenation to Methanol: An Operando XAS-XRD and In Situ TEM Study, Journal of the American Chemical Society 141(34) (2019) 13497-13505. https://doi.org/10.1021/jacs.9b04873.
[69] Z. Li, Z. Qi, S. Wang, T. Ma, L. Zhou, Z. Wu, X. Luan, F.-Y. Lin, M. Chen, J.T. Miller, H. Xin, W. Huang, Y. Wu, In Situ Formed Pt3Ti Nanoparticles on a Two-Dimensional Transition Metal Carbide (MXene) Used as Efficient Catalysts for Hydrogen Evolution Reactions, Nano Letters 19(8) (2019) 5102-5108. https://doi.org/10.1021/acs.nanolett.9b01381.
[70] I. Lignos, R. Maceiczyk, A.J. deMello, Microfluidic Technology: Uncovering the Mechanisms of Nanocrystal Nucleation and Growth, Accounts of Chemical Research 50(5) (2017) 1248-1257. https://doi.org/10.1021/acs.accounts.7b00088.
[71] Z. Yang, T. Albrow-Owen, H. Cui, J. Alexander-Webber, F. Gu, X. Wang, T.-C. Wu, M. Zhuge, C. Williams, P. Wang, A.V. Zayats, W. Cai, L. Dai, S. Hofmann, M. Overend, L. Tong, Q. Yang, Z. Sun, T. Hasan, Single-nanowire spectrometers, Science 365(6457) (2019) 1017-1020. https://doi.org/10.1126/science.aax8814.
[72] G.E.M. Crisenza, P. Melchiorre, Chemistry glows green with photoredox catalysis, Nature Communications 11(1) (2020) 803. https://doi.org/10.1038/s41467-019-13887-8.
[73] F. Parrino, M. Bellardita, E.I. García-López, G. Marcì, V. Loddo, L. Palmisano, Heterogeneous Photocatalysis for Selective Formation of High-Value-Added Molecules: Some Chemical and Engineering Aspects, ACS Catalysis 8(12) (2018) 11191-11225. https://doi.org/10.1021/acscatal.8b03093.
[74] L. Yuan, Y.-J. Xu, Photocatalytic conversion of CO2 into value-added and renewable fuels, Applied Surface Science 342 (2015) 154-167. https://doi.org/10.1016/j.apsusc.2015.03.050.

[75] S. Kampouri, K.C. Stylianou, Dual-Functional Photocatalysis for Simultaneous Hydrogen Production and Oxidation of Organic Substances, ACS Catalysis 9(5) (2019) 4247-4270. https://doi.org/10.1021/acscatal.9b00332.
[76] D. Hebrault, A.J. Rein, B. Wittkamp, Chemical Knowledge via In Situ Analytics: Advancing Quality and Sustainability, ACS Sustainable Chemistry & Engineering 10(16) (2022) 5072-5077. https://doi.org/10.1021/acssuschemeng.2c00292.
[77] Z. Wang, P.H. Cu-Nguyen, H. Zappe, A two-step Fabry-Perot filter array in mid-infrared wavelength range for integration with photochemical microreactors, Sensors and Actuators A: Physical 311 (2020) 112047. https://doi.org/10.1016/j.sna.2020.112047.
[78] FOR 2383: Assessing and Controlling Dynamic Local Process Conditions in Microreactors via Novel Integrated Microsensors. https://gepris.dfg.de/gepris/projekt/274353615?language=en.
[79] N.A. Romero, D.A. Nicewicz, Organic Photoredox Catalysis, Chemical Reviews 116(17) (2016) 10075-10166. https://doi.org/10.1021/acs.chemrev.6b00057.
[80] K.L. Skubi, T.R. Blum, T.P. Yoon, Dual Catalysis Strategies in Photochemical Synthesis, Chemical Reviews 116(17) (2016) 10035-10074. https://doi.org/10.1021/acs.chemrev.6b00018.
[81] X.J. Lang, J.C. Zhao, X.D. Chen, Cooperative photoredox catalysis, Chemical Society Reviews 45(11) (2016) 3026-3038. https://doi.org/10.1039/c5cs00659g.
[82] A. Tlili, S. Lakhdar, Acridinium Salts and Cyanoarenes as Powerful Photocatalysts: Opportunities in Organic Synthesis, Angew Chem Int Edit 60(36) (2021) 19526-19549. https://doi.org/10.1002/anie.202102262.
[83] V.I. Supranovich, V.V. Levin, A.D. Dilman, Radical Addition to N-Tosylimines via C–H Activation Induced by Decatungstate Photocatalyst, Org Lett 21(11) (2019) 4271-4274. https://doi.org/10.1021/acs.orglett.9b01450.
[84] D. Mazzarella, A. Pulcinella, L. Bovy, R. Broersma, T. Noël, Rapid and Direct Photocatalytic C(sp3)−H Acylation and Arylation in Flow, Angewandte Chemie International Edition 60(39) (2021) 21277-21282. https://doi.org/10.1002/anie.202108987.
[85] I.B. Perry, T.F. Brewer, P.J. Sarver, D.M. Schultz, D.A. DiRocco, D.W.C. MacMillan, Direct arylation of strong aliphatic C–H bonds, Nature 560(7716) (2018) 70-75. https://doi.org/10.1038/s41586-018-0366-x.
[86] P.J. Sarver, N.B. Bissonnette, D.W.C. MacMillan, Decatungstate-Catalyzed C(sp3)–H Sulfinylation: Rapid Access to Diverse Organosulfur Functionality, Journal of the American Chemical Society 143(26) (2021) 9737-9743. https://doi.org/10.1021/jacs.1c04722.
[87] L. Buglioni, F. Raymenants, A. Slattery, S.D.A. Zondag, T. Noel, Technological Innovations in Photochemistry for Organic Synthesis: Flow Chemistry, High-Throughput Experimentation, Scale-up, and Photoelectrochemistry, Chemical Reviews 122(2) (2022) 2752-2906. https://doi.org/10.1021/acs.chemrev.1c00332.
[88] A.E. Cassano, C.A. Martin, R.J. Brandi, O.M. Alfano, Photoreactor Analysis and Design: Fundamentals and Applications, Industrial & Engineering Chemistry Research 34(7) (1995) 2155-2201. https://doi.org/10.1021/ie00046a001.
[89] R. Radjagobalou, V.D.D.S. Freitas, J.-F. Blanco, F. Gros, J. Dauchet, J.-F. Cornet, K. Loubiere, A revised 1D equivalent model for the determination of incident photon flux density in a continuous-flow LED-driven spiral-shaped microreactor using the actinometry method with Reinecke's salt, Journal of Flow Chemistry 11(3) (2021) 357-367. https://doi.org/10.1007/s41981-021-00179-w.
[90] H.E. Bonfield, T. Knauber, F. Lévesque, E.G. Moschetta, F. Susanne, L.J. Edwards, Photons as a 21st century reagent, Nature Communications 11(1) (2020) 804. https://doi.org/10.1038/s41467-019-13988-4.
[91] C.C. Le, M.K. Wismer, Z.-C. Shi, R. Zhang, D.V. Conway, G. Li, P. Vachal, I.W. Davies, D.W.C. MacMillan, A General Small-Scale Reactor To Enable Standardization and

Acceleration of Photocatalytic Reactions, Acs Central Sci 3(6) (2017) 647-653. https://doi.org/10.1021/acscentsci.7b00159.
[92] D.K. Tiwari, R.A. Maurya, J.B. Nanubolu, Visible-Light/Photoredox-Mediated sp3 C-H Functionalization and Coupling of Secondary Amines with Vinyl Azides in Flow Microreactors, Chemistry – A European Journal 22(2) (2016) 526-530. https://doi.org/10.1002/chem.201504292.
[93] J.M.R. Narayanam, J.W. Tucker, C.R.J. Stephenson, Electron-Transfer Photoredox Catalysis: Development of a Tin-Free Reductive Dehalogenation Reaction, Journal of the American Chemical Society 131(25) (2009) 8756-8757. https://doi.org/10.1021/ja9033582.
[94] N.J.W. Straathof, B.J.P. Tegelbeckers, V. Hessel, X. Wang, T. Noël, A mild and fast photocatalytic trifluoromethylation of thiols in batch and continuous-flow, Chemical Science 5(12) (2014) 4768-4773. https://doi.org/10.1039/C4SC01982B.
[95] K. Loubiere, M. Oelgemoller, T. Aillet, O. Dechy-Cabaret, L. Prat, Continuous-flow photochemistry: A need for chemical engineering, Chem Eng Process 104 (2016) 120-132. https://doi.org/10.1016/j.cep.2016.02.008.
[96] U.K. Sharma, H.P.L. Gemoets, F. Schröder, T. Noël, E.V. Van der Eycken, Merger of Visible-Light Photoredox Catalysis and C–H Activation for the Room-Temperature C-2 Acylation of Indoles in Batch and Flow, ACS Catalysis 7(6) (2017) 3818-3823. https://doi.org/10.1021/acscatal.7b00840.
[97] W.-K. Jo, R.J. Tayade, New Generation Energy-Efficient Light Source for Photocatalysis: LEDs for Environmental Applications, Industrial & Engineering Chemistry Research 53(6) (2014) 2073-2084. https://doi.org/10.1021/ie404176g.
[98] A. Roibu, R.B. Morthala, M.E. Leblebici, D. Koziej, T. Van Gerven, S. Kuhn, Design and characterization of visible-light LED sources for microstructured photoreactors, Reaction Chemistry & Engineering 3(6) (2018). https://doi.org/10.1039/c8re00165k.
[99] T.D. Svejstrup, A. Chatterjee, D. Schekin, T. Wagner, J. Zach, M.J. Johansson, G. Bergonzini, B. König, Effects of Light Intensity and Reaction Temperature on Photoreactions in Commercial Photoreactors, Chemphotochem 5(9) (2021) 808-814. https://doi.org/10.1002/cptc.202100059.
[100] C.A. Hone, C.O. Kappe, Towards the Standardization of Flow Chemistry Protocols for Organic Reactions, Chemistry–Methods 1(11) (2021) 454-467. https://doi.org/10.1002/cmtd.202100059.
[101] F. Schiel, C. Peinsipp, S. Kornigg, D. Böse, A 3D-Printed Open Access Photoreactor Designed for Versatile Applications in Photoredox- and Photoelectrochemical Synthesis**, Chemphotochem 5(5) (2021) 431-437. https://doi.org/10.1002/cptc.202000291.
[102] H.E. Bonfield, K. Mercer, A. Diaz-Rodriguez, G.C. Cook, B.S.J. McKay, P. Slade, G.M. Taylor, W.X. Ooi, J.D. Williams, J.P.M. Roberts, J.A. Murphy, L. Schmermund, W. Kroutil, T. Mielke, J. Cartwright, G. Grogan, L.J. Edwards, The Right Light: De Novo Design of a Robust Modular Photochemical Reactor for Optimum Batch and Flow Chemistry, Chemphotochem 4(1) (2020) 45-51. https://doi.org/10.1002/cptc.201900203.
[103] J. Li, P. Hodapp, B.P. Ladewig, N. Jung, R. Dittmeyer, A batch photoreactor for small-scale laboratory research - a technical note, ChemRxiv. Cambridge: Cambridge Open Engage (2022). https://doi.org/10.26434/chemrxiv-2022-46w7s.
[104] N.J.W. Straathof, Y. Su, V. Hessel, T. Noël, Accelerated gas-liquid visible light photoredox catalysis with continuous-flow photochemical microreactors, Nature Protocols 11(1) (2016) 10-21. https://doi.org/10.1038/nprot.2015.113.
[105] A.M.S. Galante, O.L. Galante, L.L. Campos, Study on application of PTFE, FEP and PFA fluoropolymers on radiation dosimetry, Nuclear Instruments and Methods in Physics Research Section A: Accelerators, Spectrometers, Detectors and Associated Equipment 619(1) (2010) 177-180. https://doi.org/10.1016/j.nima.2009.10.103.
[106] M.V. Barich, A.T. Krummel, Polymeric Infrared Compatible Microfluidic Devices for

Spectrochemical Analysis, Analytical Chemistry 85(21) (2013) 10000-10003. https://doi.org/10.1021/ac4026016.
[107] I.P. Silverwood, N. Al-Rifai, E. Cao, D.J. Nelson, A. Chutia, P.P. Wells, S.P. Nolan, M.D. Frogley, G. Cinque, A. Gavriilidis, C.R.A. Catlow, Towards microfluidic reactors for in situ synchrotron infrared studies, Review of Scientific Instruments 87(2) (2016) 024101. https://doi.org/10.1063/1.4941825.
[108] X. Zhan, C. Yan, Y. Zhang, G. Rinke, G. Rabsch, M. Klumpp, A.I. Schäfer, R. Dittmeyer, Investigation of the reaction kinetics of photocatalytic pollutant degradation under defined conditions with inkjet-printed TiO2 films – from batch to a novel continuous-flow microreactor, Reaction Chemistry & Engineering 5(9) (2020) 1658-1670. https://doi.org/10.1039/D0RE00238K.
[109] R. Radjagobalou, V.D.D. Freitas, J.F. Blanco, F. Gros, J. Dauchet, J.F. Cornet, K. Loubiere, A revised 1D equivalent model for the determination of incident photon flux density in a continuous-flow LED-driven spiral-shaped microreactor using the actinometry method with Reinecke's salt, Journal of Flow Chemistry 11(3) (2021) 357-367. https://doi.org/10.1007/s41981-021-00179-w.
[110] C. Passalia, M. Flores, S.G.S. Santos, L.O. Paulista, M.D. Labas, V.J.P. Vilar, R.J. Brandi, Radiation modelling in the NETmix photocatalytic reactor: The concept of efficiencies in series, J Environ Chem Eng 8(6) (2020). https://doi.org/10.1016/j.jece.2020.104464.
[111] C. Casado, R. Timmers, A. Sergejevs, C.T. Clarke, D.W.E. Allsopp, C.R. Bowen, R. van Grieken, J. Marugan, Design and validation of a LED-based high intensity photocatalytic reactor for quantifying activity measurements, Chemical Engineering Journal 327 (2017) 1043-1055. https://doi.org/10.1016/j.cej.2017.06.167.
[112] T. Matiazzo, K. Ramaswamy, V.J.P. Vilar, N. Padoin, C. Soares, Radiation field modeling of the NETmix milli-photocatalytic reactor: Effect of LEDs position over the reactor window, Chemical Engineering Journal 429 (2022). https://doi.org/10.1016/j.cej.2021.131670.
[113] J.Y. Zhang, Y.M. Mo, A scalable light-diffusing photochemical reactor for continuous processing of photoredox reactions, Chemical Engineering Journal 435 (2022) 134889. https://doi.org/10.1016/j.cej.2022.134889.
[114]
https://chem.libretexts.org/Ancillary_Materials/Reference/Reference_Tables/Spectroscopic_Reference_Tables/Infrared_Spectroscopy_Absorption_Table.
[115] H.J. Kuhn, S.E. Braslavsky, R. Schmidt, Chemical actinometry (IUPAC Technical Report), Pure and Applied Chemistry 76(12) (2004) 2105-2146. https://doi.org/10.1351/pac200476122105.
[116] J. Rabani, H. Mamane, D. Pousty, J.R. Bolton, Practical Chemical Actinometry—A Review, Photochem Photobiol 97(5) (2021) 873-902. https://doi.org/10.1111/php.13429.
[117] T. Aillet, K. Loubiere, O. Dechy-Cabaret, L. Prat, Accurate Measurement of the Photon Flux Received Inside Two Continuous Flow Microphotoreactors by Actinometry, Int J Chem React Eng 12(1) (2014) 257-269. https://doi.org/10.1515/ijcre-2013-0121.
[118] B. Wriedt, D. Kowalczyk, D. Ziegenbalg, Experimental Determination of Photon Fluxes in Multilayer Capillary Photoreactors, Chemphotochem 2(10) (2018) 913-921. https://doi.org/10.1002/cptc.201800106.
[119] V. Rochatte, G. Dahi, A. Eskandari, J. Dauchet, F. Gros, M. Roudet, J.F. Cornet, Radiative transfer approach using Monte Carlo Method for actinometry in complex geometry and its application to Reinecke salt photodissociation within innovative pilot-scale photo(bio)reactors, Chemical Engineering Journal 308 (2017) 940-953. https://doi.org/10.1016/j.cej.2016.08.112.
[120] R.P.M. Moreira, G. Li Puma, CFD modeling of pharmaceuticals and CECs removal by

UV/H2O2 process in helical microcapillary photoreactors and evaluation of OH radical rate constants, Chemical Engineering Journal 415 (2021) 128833. https://doi.org/10.1016/j.cej.2021.128833.
[121] I. Moreno, C.C. Sun, Modeling the radiation pattern of LEDs, Opt Express 16(3) (2008) 1808-1819. https://doi.org/10.1364/Oe.16.001808.
[122] C.G. Hatchard, C.A. Parker, A New Sensitive Chemical Actinometer .2. Potassium Ferrioxalate as a Standard Chemical Actinometer, Proc R Soc Lon Ser-A 235(1203) (1956) 518-536. https://doi.org/10.1098/rspa.1956.0102.
[123] P. Kant, L.L. Trinkies, N. Gensior, D. Fischer, M. Rubin, G. Alan Ozin, R. Dittmeyer, Isophotonic reactor for the precise determination of quantum yields in gas, liquid, and multi-phase photoreactions, Chemical Engineering Journal 452 (2023) 139204. https://doi.org/10.1016/j.cej.2022.139204.
[124] K.C. Kurien, A modification to the ferrioxalate actinometer, Journal of the Chemical Society B: Physical Organic (0) (1971) 2081-2082. https://doi.org/10.1039/J29710002081.
[125] C. Shen, M.J. Shang, H. Zhang, Y.H. Su, A UV-LEDs based photomicroreactor for mechanistic insights and kinetic studies in the norbornadiene photoisomerization, Aiche Journal 66(2) (2020). https://doi.org/10.1002/aic.16841.
[126] J. Szychlinski, P. Bilski, K. Martuszewski, J. Blazejowski, Complementary Study on the Use of the Potassium Reinecke Salt as a Chemical Actinometer, Analyst 114(6) (1989) 739-741. https://doi.org/10.1039/an9891400739.
[127] E.E. Wegner, A.W. Adamson, Photochemistry of Complex Ions. III. Absolute Quantum Yields for the Photolysis of Some Aqueous Chromium(III) Complexes. Chemical Actinometry in the Long Wavelength Visible Region, Journal of the American Chemical Society 88(3) (1966) 394-404. https://doi.org/10.1021/ja00955a003.
[128] R. Radjagobalou, J.F. Blanco, V.D.D. Freitas, C. Supplis, F. Gros, O. Dechy-Cabaret, K. Loubiere, A revised experimental protocol for implementing the actinometry method with the Reinecke's salt, J Photoch Photobio A 382 (2019). https://doi.org/10.1016/j.jphotochem.2019.111934.
[129] J.-F. Cornet, A. Marty, J.-B. Gros, Revised Technique for the Determination of Mean Incident Light Fluxes on Photobioreactors, Biotechnology Progress 13(4) (1997) 408-415. https://doi.org/10.1021/bp970045c.
[130] S.I. Woods, T.M. Jung, D.R. Sears, J. Yu, Emissivity of silver and stainless steel from 80 K to 300 K: Application to ITER thermal shields, Cryogenics 60 (2014) 44-48. https://doi.org/10.1016/j.cryogenics.2014.01.002.
[131] M.P.M. John R. Howell, Robert Siegel, Thermal Radiation Heat Transfer, 5th ed., CRC Press.2010. https://doi.org/10.1201/9781439894552.
[132] N.K. Kaushik, N. Kaushik, P. Attri, N. Kumar, C.H. Kim, A.K. Verma, E.H. Choi, Biomedical Importance of Indoles, Molecules 18(6) (2013) 6620-6662. https://doi.org/10.3390/molecules18066620.
[133] P.T. Singh, M.O. Singh, Recent Progress in Biological Activities of Indole and Indole Alkaloids, Mini-Rev Med Chem 18(1) (2018) 9-25. https://doi.org/10.2174/1389557517666170807123201.
[134] D.F. Taber, P.K. Tirunahari, Indole synthesis: a review and proposed classification, Tetrahedron 67(38) (2011) 7195-7210. https://doi.org/10.1016/j.tet.2011.06.040.
[135] M. Platon, R. Amardeil, L. Djakovitch, J.-C. Hierso, Progress in palladium-based catalytic systems for the sustainable synthesis of annulated heterocycles: a focus on indole backbones, Chemical Society Reviews 41(10) (2012) 3929-3968. https://doi.org/10.1039/C2CS15350E.
[136] T.V. Sravanthi, S.L. Manju, Indoles — A promising scaffold for drug development, European Journal of Pharmaceutical Sciences 91 (2016) 1-10. https://doi.org/10.1016/j.ejps.2016.05.025.

[137] A.A. Festa, L.G. Voskressensky, E.V. Van der Eycken, Visible light-mediated chemistry of indoles and related heterocycles, Chemical Society Reviews 48(16) (2019) 4401-4423. https://doi.org/10.1039/C8CS00790J.
[138] H.J. Kim, D.C. Fabry, S. Mader, M. Rueping, Photoredox/rhodium catalysis in C–H activation for the synthesis of nitrogen containing heterocycles, Organic Chemistry Frontiers 6(14) (2019) 2319-2323. https://doi.org/10.1039/C9QO00206E.
[139] J. Zoller, D.C. Fabry, M.A. Ronge, M. Rueping, Synthesis of Indoles Using Visible Light: Photoredox Catalysis for Palladium-Catalyzed C-H Activation, Angewandte Chemie International Edition 53(48) (2014) 13264-13268. https://doi.org/10.1002/anie.201405478.
[140] P. Zhang, T. Xiao, S. Xiong, X. Dong, L. Zhou, Synthesis of 3-Acylindoles by Visible-Light Induced Intramolecular Oxidative Cyclization of o-Alkynylated N,N-Dialkylamines, Org Lett 16(12) (2014) 3264-3267. https://doi.org/10.1021/ol501276j.
[141] M. Colella, L. Degennaro, R. Luisi, Continuous Flow Synthesis of Heterocycles: A Recent Update on the Flow Synthesis of Indoles, Molecules 25(14) (2020) 3242. https://doi.org/10.3390/molecules25143242.
[142] M.L. Satuf, J. Macagno, A. Manassero, G. Bernal, P.A. Kler, C.L.A. Berli, Simple method for the assessment of intrinsic kinetic constants in photocatalytic microreactors, Applied Catalysis B: Environmental 241 (2019) 8-17. https://doi.org/10.1016/j.apcatb.2018.09.015.
[143] H. Simek Tosino, A. Jung, O. Fuhr, C. Muhle-Goll, N. Jung, S. Bräse, F-Tag Induced Acyl Shift in the Photochemical Cyclization of o-Alkynylated N-Alkyl-N-acylamides to Indoles**, Eur J Org Chem 26(11) (2023) e202201132. https://doi.org/10.1002/ejoc.202201132.
[144] J. Li, H. Šimek Tosino, B.P. Ladewig, N. Jung, S. Bräse, R. Dittmeyer, Extraction of the intrinsic rate constant for a photocyclization reaction in capillary microreactors using a simplified reactor model, Reaction Chemistry & Engineering (2024). https://doi.org/10.1039/D4RE00087K.
[145] J. Britton, T.F. Jamison, The assembly and use of continuous flow systems for chemical synthesis, Nature Protocols 12(11) (2017) 2423-2446. https://doi.org/10.1038/nprot.2017.102.
[146] T. Wan, L. Capaldo, G. Laudadio, A.V. Nyuchev, J.A. Rincón, P. García-Losada, C. Mateos, M.O. Frederick, M. Nuño, T. Noël, Decatungstate-Mediated C(sp3)–H Heteroarylation via Radical-Polar Crossover in Batch and Flow, Angewandte Chemie International Edition 60(33) (2021) 17893-17897. https://doi.org/10.1002/anie.202104682.
[147] P.M. Ligrani, A Study of Dean Vortex Development and Structure in a Curved Rectangular Channel with Aspect Ratio of 40 at Dean Numbers up to 430, NASA, 1994.
[148] M. Mansour, D. Thévenin, K.D.P. Nigam, K. Zähringer, Generally-valid optimal Reynolds and Dean numbers for efficient liquid-liquid mixing in helical pipes, Chem Eng Sci 201 (2019) 382-385. https://doi.org/10.1016/j.ces.2019.03.003.
[149] T. Aillet, K. Loubière, L. Prat, O. Dechy-Cabaret, Impact of the diffusion limitation in microphotoreactors, AIChE Journal 61(4) (2015) 1284-1299. https://doi.org/10.1002/aic.14718.
[150] A. Delparish, A. Uslu, Y.R. Cao, T. de Groot, J. van der Schaaf, T. Noel, M.F.N. D'Angelo, Boosting the valorization of biomass and green electrons to chemical building blocks: A study on the kinetics and mass transfer during the electrochemical conversion of HMF to FDCA in a microreactor, Chemical Engineering Journal 438 (2022). https://doi.org/10.1016/j.cej.2022.135393.
[151] X. Shi, S. Liu, C. Duanmu, M. Shang, M. Qiu, C. Shen, Y. Yang, Y. Su, Visible-light photooxidation of benzene to phenol in continuous-flow microreactors, Chemical Engineering Journal 420 (2021) 129976. https://doi.org/10.1016/j.cej.2021.129976.
[152] K. Miyabe, R. Isogai, Estimation of molecular diffusivity in liquid phase systems by the Wilke–Chang equation, Journal of Chromatography A 1218(38) (2011) 6639-6645.

https://doi.org/10.1016/j.chroma.2011.07.018.
[153] R.H. Perry, D.W. Green, J.O. Maloney, Perry's chemical engineers' handbook. 7th ed, 1997.
[154] Y. Cao, C. Soares, N. Padoin, T. Noël, Gas bubbles have controversial effects on Taylor flow electrochemistry, Chemical Engineering Journal 406 (2021) 126811. https://doi.org/10.1016/j.cej.2020.126811.
[155] M.T. Kreutzer, J.J.W. Bakker, F. Kapteijn, J.A. Moulijn, P.J.T. Verheijen, Scaling-up Multiphase Monolith Reactors: Linking Residence Time Distribution and Feed Maldistribution, Ind Eng Chem Res 44(14) (2005) 4898-4913. https://doi.org/10.1021/ie0492350.
[156] K.D. Nagy, B. Shen, T.F. Jamison, K.F. Jensen, Mixing and Dispersion in Small-Scale Flow Systems, Organic Process Research & Development 16(5) (2012) 976-981. https://doi.org/10.1021/op200349f.
[157] M.L. Satuf, J. Macagno, A. Manassero, G. Bernal, P.A. Kler, C.L.A. Berli, Simple method for the assessment of intrinsic kinetic constants in photocatalytic microreactors, Appl Catal B-Environ 241 (2019) 8-17. https://doi.org/10.1016/j.apcatb.2018.09.015.
[158] T.D. Svejstrup, A. Chatterjee, D. Schekin, T. Wagner, J. Zach, M.J. Johansson, G. Bergonzini, B. Konig, Effects of Light Intensity and Reaction Temperature on Photoreactions in Commercial Photoreactors, Chemphotochem 5(9) (2021) 808-814. https://doi.org/10.1002/cptc.202100059.
[159] B.M. da Costa, A.L.P. Araujo, S.P. Padrao, R.A.R. Boaventura, M.M. Dias, J.C.B. Lopes, V.J.P. Vilar, Effect of catalyst coated surface, illumination mechanism and light source in heterogeneous TiO2 photocatalysis using a mili-photoreactor for n-decane oxidation at gas phase, Chemical Engineering Journal 366 (2019) 560-568. https://doi.org/10.1016/j.cej.2019.02.122.
[160] T. Matiazzo, V.J.P. Vilar, H.G. Riella, N. Padoin, C. Soares, CFD and radiation field modeling of the NETmix milli-photocatalytic reactor for n-decane oxidation at gas phase: Effect of LEDs number and arrangement, Chemical Engineering Journal 444 (2022). https://doi.org/10.1016/j.cej.2022.136577.
[161] G.L. Puma, A. Brucato, Dimensionless analysis of slurry photocatalytic reactors using two-flux and six-flux radiation absorption-scattering models, Catal Today 122(1-2) (2007) 78-90. https://doi.org/10.1016/j.cattod.2007.01.027.
[162] O. Alvarado-Rolon, R. Natividad, R. Romero, L. Hurtado, A. Ramirez-Serrano, Modelling and Simulation of the Radiant Field in an Annular Heterogeneous Photoreactor Using a Four-Flux Model, Int J Photoenergy 2018 (2018). https://doi.org/10.1155/2018/1678385.
[163] I. Grcic, G.L. Puma, Six-flux absorption-scattering models for photocatalysis under wide-spectrum irradiation sources in annular and flat reactors using catalysts with different optical properties, Appl Catal B-Environ 211 (2017) 222-234. https://doi.org/10.1016/j.apcatb.2017.04.014.
[164] C. Casado, J. Marugan, R. Timmers, M. Munoz, R. van Grieken, Comprehensive multiphysics modeling of photocatalytic processes by computational fluid dynamics based on intrinsic kinetic parameters determined in a differential photoreactor, Chemical Engineering Journal 310 (2017) 368-380. https://doi.org/10.1016/j.cej.2016.07.081.
[165] J. Moreno, C. Casado, J. Marugan, Improved discrete ordinate method for accurate simulation radiation transport using solar and LED light sources, Chem Eng Sci 205 (2019) 151-164. https://doi.org/10.1016/j.ces.2019.04.034.
[166] J. Moreno-SanSegundo, C. Casado, J. Marugan, Enhanced numerical simulation of photocatalytic reactors with an improved solver for the radiative transfer equation, Chemical Engineering Journal 388 (2020). https://doi.org/10.1016/j.cej.2020.124183.
[167] R.P.M. Moreira, G. Li Puma, Multiphysics Computational Fluid-Dynamics (CFD)

Modeling of Annular Photocatalytic Reactors by the Discrete Ordinates Method (DOM) and the Six-Flux Model (SFM) and Evaluation of the Contaminant Intrinsic Kinetics Constants, Catal Today 361 (2021) 77-84. https://doi.org/10.1016/j.cattod.2020.01.012.

# Appendix

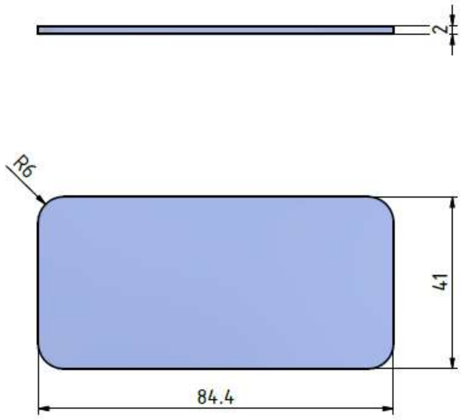

Figure A1 Dimensions of the reaction windows (SQ-1 grade) of the PHO-µR

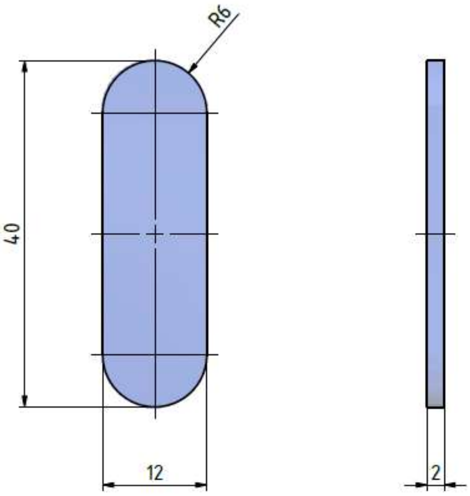

Figure A2 Dimensions of the infrared sensing top window (IR grade) of the PHO-µR

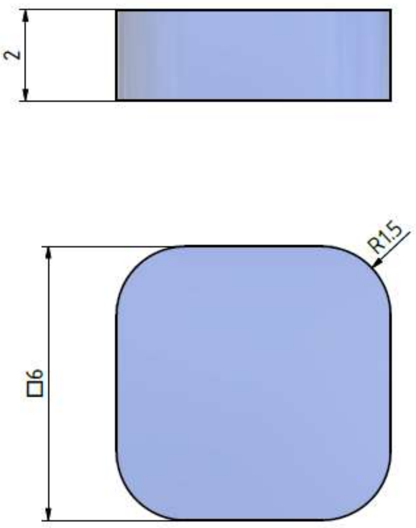

Figure A3 Dimensions of the infrared sensing back window (IR grade) of the PHO-µR

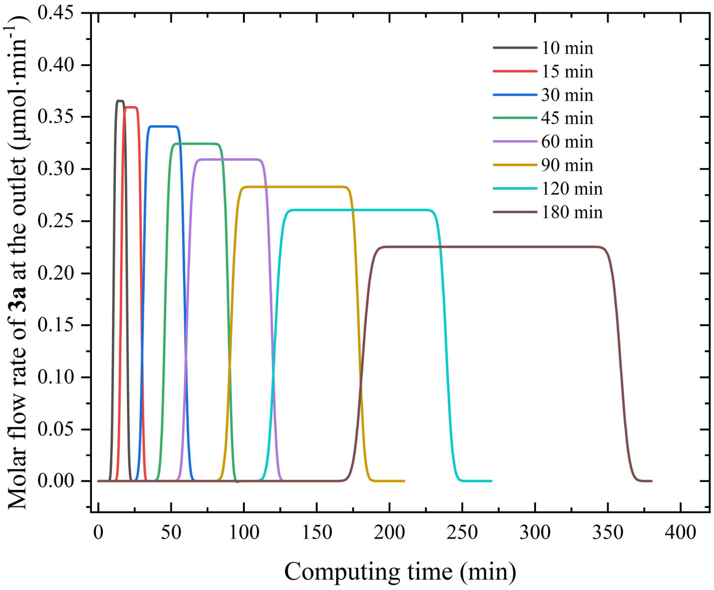

Figure A4 Predicted molar flow rate of **3a**[6] as a function of time at the outlet, 40% irradiation power, 2D axisymmetric simulation in the CAP-µR.

---

[6] The structure of **3a** is presented in Scheme 4-2

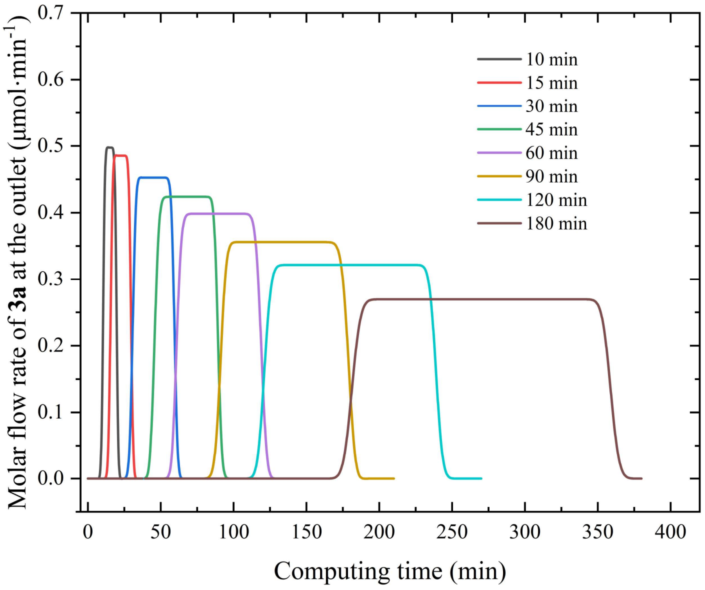

Figure A5 Predicted molar flow rate of **3a**[7] as a function of time at the outlet, 60% irradiation power, 2D axisymmetric simulation in the CAP-μR.

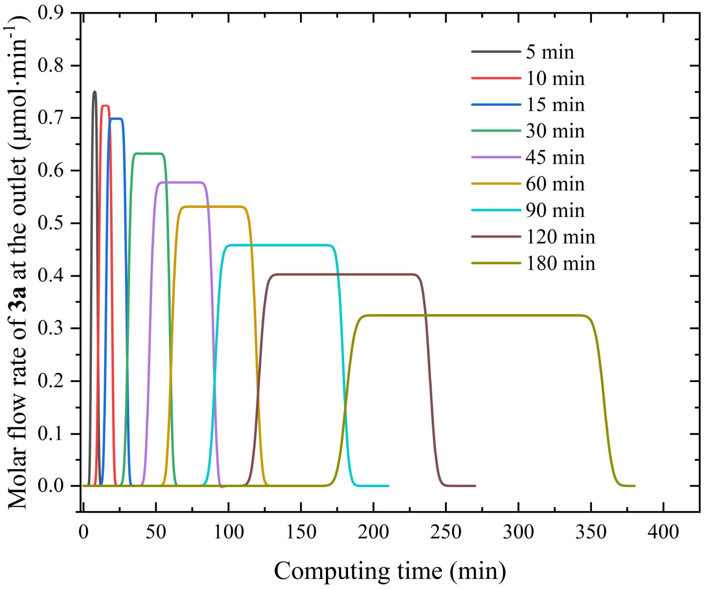

Figure A6 Predicted molar flow rate of **3a**[8] as a function of time at the outlet, 80% irradiation power, 2D axisymmetric simulation in the CAP-μR.

---

[7] The structure of **3a** is presented in Scheme 4-2

[8] The structure of **3a** is presented in Scheme 4-2

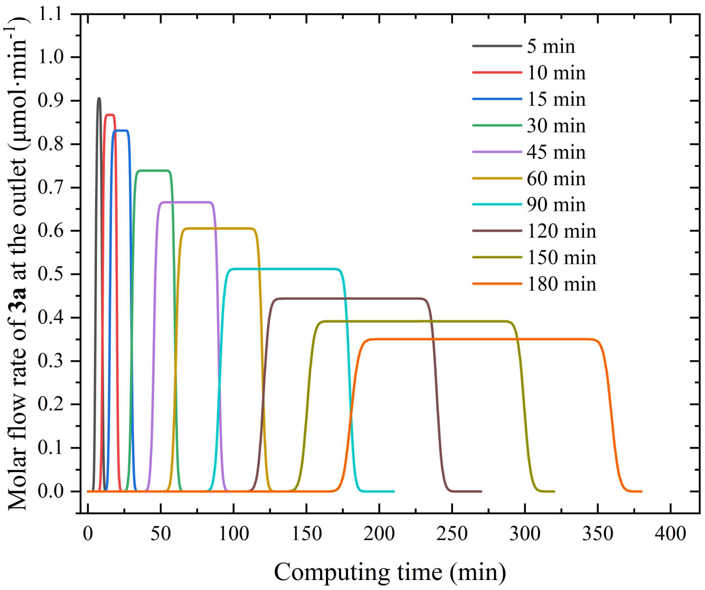

Figure A7 Predicted molar flow rate of **3a**[9] as a function of time at the outlet, 100% irradiation power, 2D axisymmetric simulation in the CAP-μR.

---

[9] The structure of **3a** is presented in Scheme 4-2

Table A1 Integral values of indole product molar fluxes as a function of time at the outlet and estimated conversions from 2D axisymmetric numerical simulation

| irradiation power | Residence Time (min) | Total mole of **3a** produced | Estimated conversion (%) |
|---|---|---|---|
| **100% output** | 5 | 4.05 µmol | 4.05 |
| | 10 | 8.55 µmol | 8.55 |
| | 15 | 12.29 µmol | 12.29 |
| | 30 | 21.90 µmol | 21.90 |
| | 45 | 29.64 µmol | 29.64 |
| | 60 | 35.96 µmol | 35.96 |
| | 90 | 45.68 µmol | 45.68 |
| | 120 | 52.84 µmol | 52.84 |
| | 150 | 58.34 µmol | 58.34 |
| | 180 | 62.65 µmol | 62.65 |
| **80% output** | 5 | 3.37 µmol | 3.37 |
| | 10 | 6.70 µmol | 6.70 |
| | 15 | 9.85 µmol | 9.85 |
| | 30 | 18.19 µmol | 18.19 |
| | 45 | 25.10 µmol | 25.10 |
| | 60 | 30.90 µmol | 30.90 |
| | 90 | 40.42 µmol | 40.42 |
| | 120 | 47.57 µmol | 47.57 |
| | 180 | 57.71 µmol | 57.71 |
| **60% output** | 10 | 4.60 µmol | 4.60 |
| | 15 | 6.84 µmol | 6.84 |
| | 30 | 12.99 µmol | 12.99 |
| | 45 | 18.43 µmol | 18.43 |
| | 60 | 23.10 µmol | 23.10 |
| | 90 | 31.20 µmol | 31.20 |
| | 120 | 37.90 µmol | 37.90 |
| | 180 | 47.86 µmol | 47.86 |
| **40% output** | 10 | 3.38 µmol | 3.38 |
| | 15 | 5.06 µmol | 5.06 |
| | 30 | 9.78 µmol | 9.78 |
| | 45 | 14.06 µmol | 14.06 |

| | | | |
|---|---|---|---|
| | 60 | 17.93 µmol | 17.93 |
| | 90 | 24.87 µmol | 24.87 |
| | 120 | 30.68 µmol | 30.68 |
| | 180 | 39.98 µmol | 39.98 |

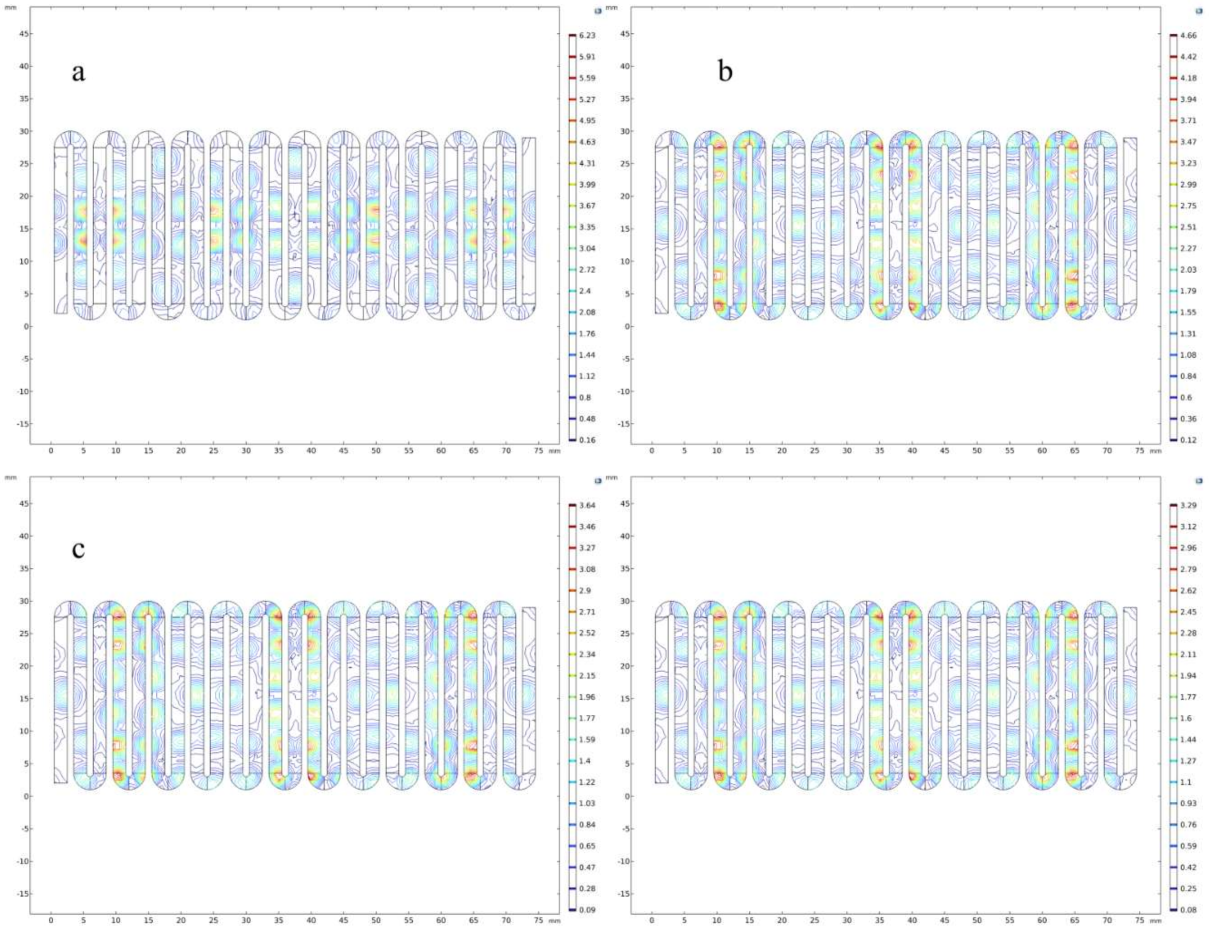

Figure A8 Irradiance contour plots on the microchannel surface at a LED-to-reactor distance of 10 mm. a) 4 aligned LEDs, case 2 of Table 4-4. b) 6 aligned LEDs, case 7 of Table 4-4. c) 8 aligned LEDs, case 12 of Table 4-4. d) 8 staggered LEDs, case 17 of Table 4-4.

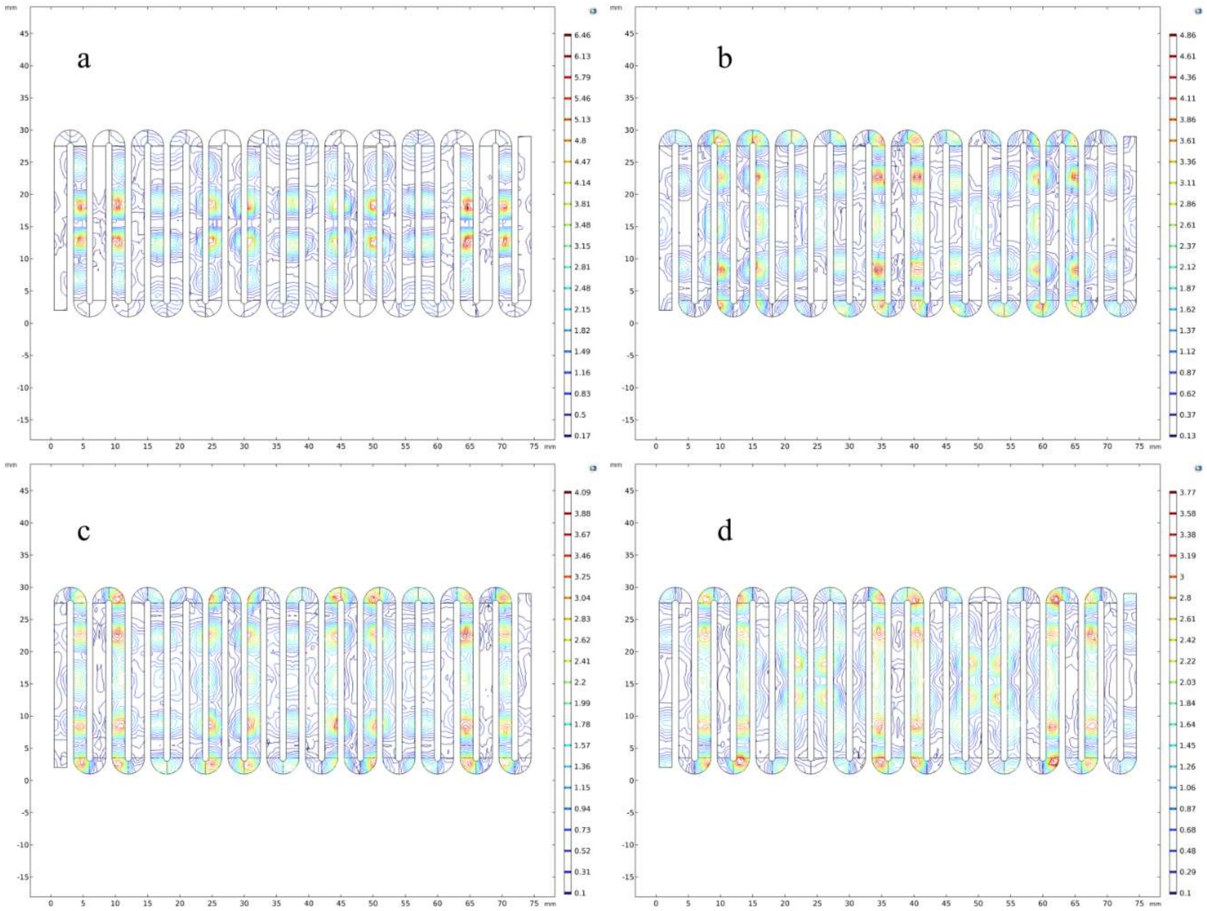

Figure A9 Irradiance contour plots on the microchannel surface at a LED-to-reactor distance of 12 mm. a) 4 aligned LEDs, case 3 of Table 4-4. b) 6 aligned LEDs, case 8 of Table 4-4. c) 8 aligned LEDs, case 13 of Table 4-4. d) 8 staggered LEDs, case 18 of Table 4-4.

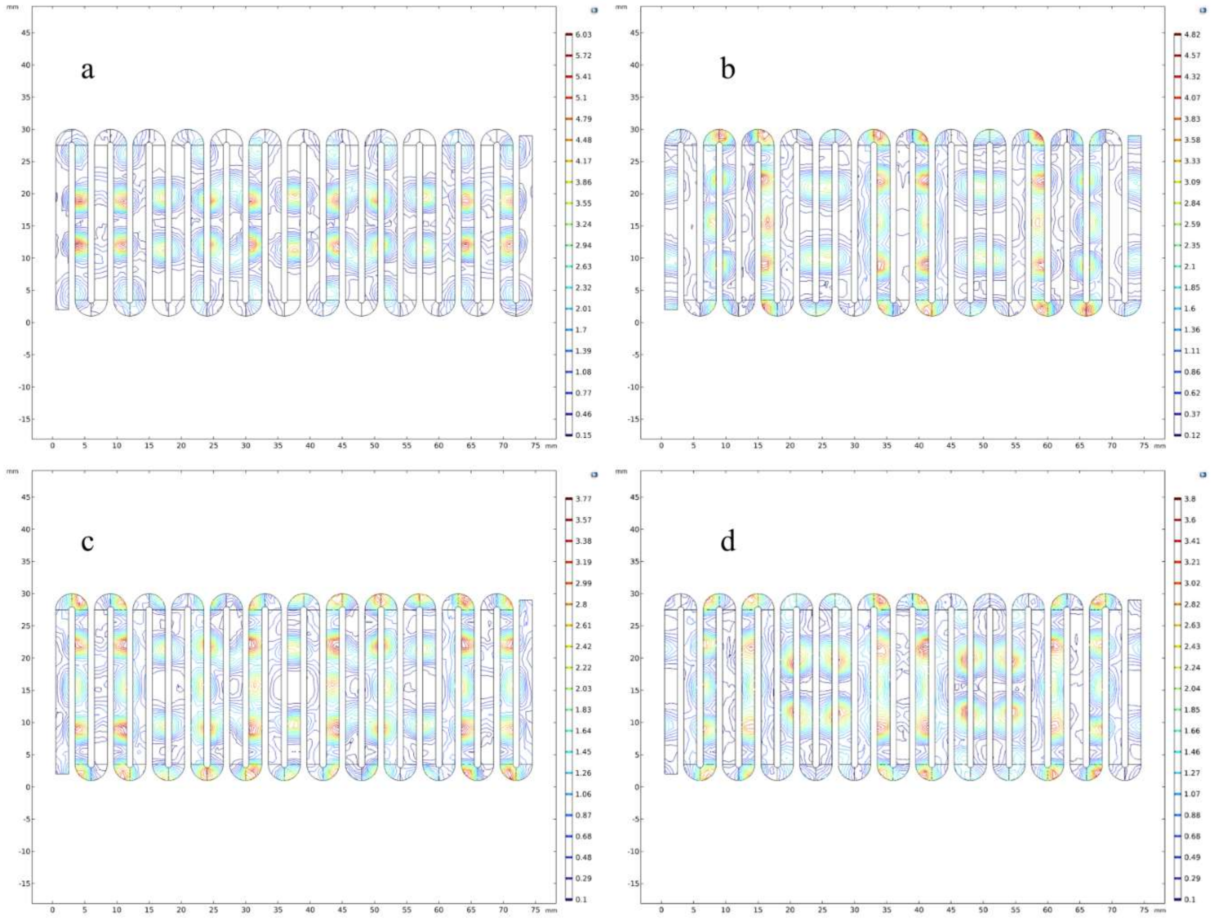

Figure A10 Irradiance contour plots on the microchannel surface at a LED-to-reactor distance of 15 mm. a) 4 aligned LEDs, case 4 of Table 4-4. b) 6 aligned LEDs, case 9 of Table 4-4. c) 8 aligned LEDs, case 14 of Table 4-4. d) 8 staggered LEDs, case 19 of Table 4-4.

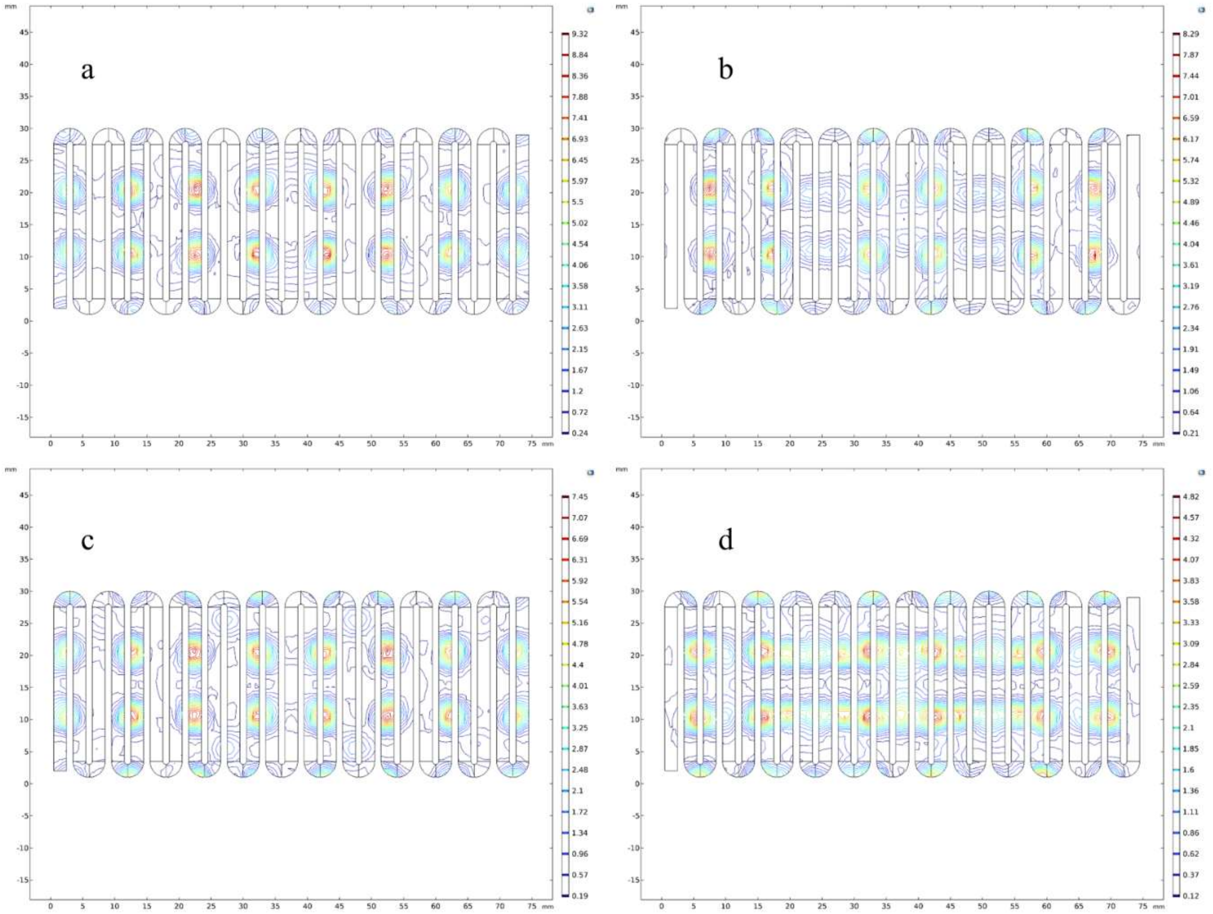

Figure A11 Irradiance contour plots on the microchannel surface at a LED-to-reactor distance of 20 mm. a) 4 aligned LEDs, case 5 of Table 4-4. b) 6 aligned LEDs, case 10 of Table 4-4. c) 8 aligned LEDs, case 15 of Table 4-4. d) 8 staggered LEDs, case 20 of Table 4-4.

# List of figures

# List of tables

# List of schemes